FEDERAL UNIVERSITY OF SANTA CATARINA
DEPARTMENT OF MECHANICAL ENGINEERING

DEVELOPMENT OF A TWO-PHASE JET HEAT SINK INTEGRATED WITH A COMPACT REFRIGERATION SYSTEM FOR ELECTRONICS COOLING

Pablo Adamoglu de Oliveira

Florianópolis (SC)

2016

Pablo Adamoglu de Oliveira

EVAPORADOR DE JATOS BIFÁSICOS INCIDENTES INTEGRADO A UM SISTEMA DE REFRIGERAÇÃO COMPACTO PARA RESFRIAMENTO DE COMPONENTES ELETRÔNICOS

Tese submetida ao Programa de Pós-Graduação em Engenharia Mecânica da Universidade Federal de Santa Catarina para a obtenção do Grau de Doutor em Engenharia Mecânica.
Orientador: Jader R. Barbosa Jr., Ph.D.

Florianópolis, SC

2016

Pablo Adamoglu de Oliveira

EVAPORADOR DE JATOS BIFÁSICOS INCIDENTES INTEGRADO A UM SISTEMA DE REFRIGERAÇÃO COMPACTO PARA RESFRIAMENTO DE COMPONENTES ELETRÔNICOS

Esta Tese foi julgada adequada para obtenção do Título de "Doutor em Engenharia Mecânica", e aprovada em sua forma final pelo Programa de Pós-Graduação em Engenharia Mecânica da Universidade Federal de Santa Catarina.

Florianópolis, 15 de Fevereiro de 2016.

_____

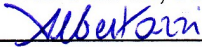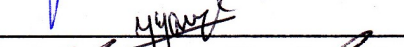Prof. Jader Riso Barbosa Jr., Ph.D. – Orientador

_____

Prof. Armando Albertazzi Gonçalves Jr., Dr. Eng. – Coordenador do Curso

BANCA EXAMINADORA

_____
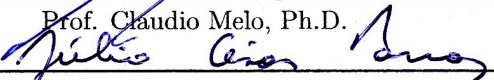
Prof. Jader Riso Barbosa Jr., Ph.D. – Presidente

_____

Prof. Gherhardt Ribatski, Dr. – Relator

_____

Prof. Jurandir Itizo Yanagihara, Dr.

_____

Prof. Alvaro Toubes Prata, Ph.D.

_____

Prof. Claudio Melo, Ph.D.

_____

Prof. Júlio César Passos, Dr.

*"Let me tell you the secret
that has led me to my goal.
My strength lies solely
in my tenacity."
(Louis Pasteur)*

*"The two most powerful warriors
are patience and time."
(Leo Tolstoy)*

To my sweet little angel,
Maria Clara (in memoriam).

Acknowledgments

I would like to express my sincere gratitude and appreciation to my advisor Prof. Jader Riso Barbosa Jr., for his guidance, encouragement and support during the development of this research work. His practical advices, inexhaustible patience and availability for questions and discussions were of primary importance throughout the different stages of this thesis.

I also would like to thank the committee: Prof. Gherhardt Ribatski, Prof. Jurandir I. Yanagihara, Prof. Alvaro T. Prata, Prof. Claudio Melo and Prof. Júlio César Passos, for agreeing to evaluate this thesis and for their suggestions and comments to improve the final version of this manuscript.

I am very grateful to Prof. Walter L. Weingaertner, for his insightful comments and constructive criticisms regarding the concept and design of the jet heat sink developed in this thesis. Besides, valuable contributions from Prof. Claudio Melo are duly acknowledged.

I am deeply grateful and indebted to my dear friend Paulo V. Trevizoli, particularly for numerous prolific discussions and invaluable technical assistance during the experimental work, which were indispensable to finish this thesis.

I owe a great debt to Rafael V. de Lima (Polo's technician), which diligent hands-on performance was crucial during the stages of construction, mounting and adjustment of the experimental apparatus.

I would like to thank Felipe S. M. Pires and Filipe V. Gaelzer, which worked under my supervision during the design of the jet heat sink and conduction of the experimental tests, respectively. Their contributions to this work and friendship are greatly appreciated. The appreciation is extended to Eduardo L. da Silva, Edilson F. Junior and Matheus S. Capovilla, for their technical assistance regarding some experimental issues, such as LabVIEW coding.

Special thanks are due to the staff and other technicians of the Polo Laboratories, especially Alexsandro dos S. Silveira, Jorge L. S. Lubas

Contents

List of Figures

List of Tables

Nomenclature

Roman symbols

a	Amplitude of the plate sinusoidal wavelength	[m]
A_c	Channel area for fluid flow	[m^2]
A_h	Skin heater area	[m^2]
A_o	Orifice cross-sectional area	[m^2]
A_s	Heated surface area	[cm^2]
A_t	Heat transfer area of the corrugated plate	[m^2]
$\bar{h}$	Specific enthalpy of the two-phase mixture	[J kg^{-1}]
$b(X)$	Systematic standard uncertainty of a generic variable	
C_f	Friction coefficient of the two-phase mixture	[-]
COP	Coefficient of performance	[-]
COP_{id}	Ideal coefficient of performance	[-]
COP_{jc}	Modified (jet-cooler) coefficient of performance	[-]
COP_{os}	Overall refrigeration system COP	[-]
D	Diameter of the impingement surface	[m]
d_h	Hydraulic diameter of the condenser flow channels	[m]
d_o	Orifice diameter	[μm]
f	Operating frequency of the compressor	[Hz]
g	Gravity acceleration	[m s^{-2}]
G_w	Mass flux of the WEG mixture	[kg m^{-2} s^{-1}]
H	Jet impingement length	[mm]

h	Specific enthalpy	[J kg^{-1}]
$\hbar_{cond}$	Condenser overall heat transfer coefficient	[W m^{-2} K^{-1}]
$\hbar_s$	Jet impingement heat transfer coefficient	[W m^{-2} K^{-1}]
h_{lv}	Latent heat of vaporization	[J kg^{-1}]
H_p	Condenser height	[m]
i	Current	[A]
k_{95}	Student's t-distribution factor	[-]
k_f	Thermal conductivity of the liquid film	[W m^{-1} K^{-1}]
k_s	Thermal conductivity of the heated surface	[W m^{-1} K^{-1}]
L_s	Impingement surface-to-RTDs' plane distance	[mm]
L_λ	Plate enlarged length per wavelength	[m]
L_o	Orifice length	[mm]
L_{pt}	Condenser (total) plate length	[m]
$\dot{m}_r$	Mass flow rate of the refrigerant (R-134a)	[kg h^{-1}]
$\dot{m}_w$	Mass flow rate of the WEG mixture	[kg h^{-1}]
N	Number of measurements in a sample distribution	[-]
N_c	Number of channels per fluid	[-]
N_λ	Number of wavelength per plate	[-]
N_t	Total number of plates of the condenser	[-]
Nu_w	Nusselt number of the WEG mixture	[-]
P	Pressure	[bar]
P_{cond}	Condensing pressure	[bar]
P_{evap}	Evaporating pressure	[bar]
Pr_f	Prandtl number of the liquid film	[-]
Pr_w	Prandtl number of the WEG mixture	[-]

q''	Heat flux	[W m^{-2}]
$\dot{Q}_c^*$	Corrected cooling capacity	[W]
$\dot{Q}_c$	Cooling capacity of the refrigeration system	[W]
$\dot{Q}_{cond}$	Condenser heat transfer rate	[W]
$\dot{Q}_{enc}$	Heat transfer rate through the enclosure walls	[W]
$\dot{Q}_{evap}$	Evaporator heat transfer rate	[W]
$\dot{Q}_p$	Heat transfer rate of a passive cooling technology	[W]
$\dot{Q}_{sh}$	Superheating heat transfer rate	[W]
$\dot{Q}_{shell}$	Heat transfer rate through the compressor shell	[W]
$\dot{Q}_{TEC}$	Cooling capacity of the thermoelectric cooler	[W]
R_a	*Apparent* thermal resistance of the active cooler	[℃ W^{-1}]
R_{amb}	Ambient (hot-side reservoir) thermal resistance	[℃ W^{-1}]
R_c	Combined reservoirs thermal resistance	[℃ W^{-1}]
$R_{cond\text{-}amb}$	Condensing fluid-to-ambient thermal resistance	[℃ W^{-1}]
Re_f	Reynolds number of the liquid film	[-]
Re_o	Reynolds number of the two-phase mixture	[-]
Re_w	Reynolds number of the WEG mixture	[-]
R_g	Gas constant for N$_2$	[Pa m^3 kg^{-1} K^{-1}]
R_{hs}	Heat sink thermal resistance	[℃ W^{-1}]
$R_{j\text{-}amb}$	Junction-to-ambient thermal resistance	[℃ W^{-1}]
$R_{j\text{-}evap}$	Junction-to-evaporating fluid thermal resistance	[℃ W^{-1}]
T_{RTD}	Temperature measured by the RTD	[℃]
s	Specific entropy	[J kg^{-1} K^{-1}]
$s(X)$	Standard deviation of a generic variable	
T	Temperature	[K]

t	Experimental test	[-]
T_{amb}^*	Effective ambient temperature	[℃]
T_{cal}	Temperature inside the calorimeter	[℃]
T_{cond}	Condensing temperature	[℃]
T_{evap}	Evaporating temperature	[℃]
T_f	Temperature of the liquid film	[℃]
T_j	Junction temperature	[℃]
T_p	Temperature of the condenser plate	[℃]
t_r	Repeatability test	[-]
T_{room}	Room temperature	[℃]
$\overline{T}_{RTD}$	Mean temperature of the RTDs in the copper block	[℃]
T_s	Impingement surface temperature	[℃]
T_{TC}	Temperature measured by the thermocouple	[℃]
T_w	Average temperature of the WEG mixture	[℃]
$T_{w,i}$	WEG mixture temperature at the condenser inlet	[℃]
U	Expanded (overall) uncertainty	
u	Combined standard uncertainty	
V	Tension	[V]
v	Specific volume	[m³ kg⁻¹]
V_o	Orifice discharge velocity	[m s⁻¹]
$V_{o,cr}$	Critical velocity of the two-phase mixture	[m s⁻¹]
$V_{o,l}$	Velocity of the liquid phase at the orifice exit	[m s⁻¹]
$\dot{W}$	Total input work rate	[W]
$\dot{W}_{ah}$	Input thermal power dissipated by the air heater	[W]
$\dot{W}_{comp}$	Electrical power consumption of the compressor	[W]

$\dot{W}_{fan}$	Electrical power consumption of a single cooler fan	[W]
$\dot{W}_{fans}$	Total electrical power consumption of the cooler fans	[W]
$\dot{W}_h$	Input thermal load dissipated by the skin heater	[W]
$\dot{W}_{sh}$	Input superheating thermal power	[W]
$We_{l,v}$	Critical Weber number	[-]
$\dot{W}_{ind}$	Indicated power	[W]
W_p	Condenser plate width	[m]
W_s	Surface width (numerical model)	[m]
X	Generic output variable (or independent parameter)	
x	Vapor mass quality	[-]

Greek symbols

α	Compressor piston displacement percentage	[%]
$\bar{\mu}$	Viscosity of the two-phase mixture	[kg m^{-1} s^{-1}]
$\bar{\rho}$	Density of the two-phase mixture	[kg m^{-3}]
$\delta_{1\text{st},\%}$	First-law (heat balance) residue percentage	[%]
$\delta_{1\text{st}}$	First-law heat balance residue	[W]
δ_{cal}	Calorimeter heat balance residue	[W]
$\delta_{cal,\%}$	Calorimeter (heat balance) residue percentage	[%]
Δh_f	Fluid friction specific energy loss	[J kg^{-1}]
δ_p	Condenser plate thickness	[m]
ΔP_{jc}	Jet cooler pressure drop	[bar]
ΔT_a	Temperature difference defined in Eq. (4.30)	[℃]
$\Delta \tau$	Time interval	[s]
ΔT_{cal}	Calorimeter temperature difference	[℃]
ΔT_s	Wall superheat of the impingement surface	[℃]

ΔT_{sup}	Refrigerant superheating degree	[℃]
η	Second-law efficiency	[-]
η^*	Second-law ratio	[-]
η_{jc}	Modified (jet-cooler) second-law efficiency	[-]
η_{min}	Minimum second-law efficiency	[-]
η_{os}	Overall refrigeration system second-law efficiency	[-]
Γ	Mass flow rate per surface width	[kg m^{-1} s^{-1}]
γ	Temperature parameter defined in Eq. (4.31)	[℃]
κ	Correction factor for the cooling capacity	[%]
λ	Wavelength of the chevron-pattern condenser plate	[m]
μ	Dynamic viscosity	[kg m^{-1} s^{-1}]
μ_f	Dynamic viscosity of the liquid film	[kg m^{-1} s^{-1}]
Φ	Surface enlargement factor	[-]
ψ	Pressure-to-temperature ratio	[Pa K^{-1}]
ρ	Density	[kg m^{-3}]
ρ_f	Density of the liquid film	[kg m^{-3}]
σ	Surface tension	[N m^{-1}]
Θ	Parameter relative difference (repeatability tests)	[%]
θ	Surface inclination angle	[°]
φ	Dummy variable	
ξ	Generic dependent variable	

Sub-scripts

cal	Calorimeter heat balance
calibr	Calibration
cf	Curve fit

$comp, i$	Compressor inlet
$comp, o$	Compressor outlet
$cond, i$	Condenser inlet
$cond, o$	Condenser outlet
eb	Energy balance
jc	Jet cooler
jc, i	Jet cooler inlet
jc, o	Jet cooler outlet
l, o	Saturated liquid conditions at the orifice exit
o	Orifice exit
ref	Reference (related to the standard uncertainty)
sat	Saturation conditions
up	Upstream conditions
v, o	Saturated vapor conditions at the orifice exit

Abreviations

BPHE	Brazed Plate Heat Exchanger
CAD	Computer Aided Design
CHF	Critical Heat Flux
COTS	Commercial-Off-The-Shelf
EDIFICE	Embedded Droplet Impingement For Integrated Cooling of Electronics
IGBT	Insulated Gate Bipolar Transistor
JFET	Junction Field Effect Transistor
MEMS	Micro Electro-Mechanical Systems
RNG	Input power range
PCB	Printed Circuit Board

PID   Proportional-Integral-Derivative

POM   Polyoxymethylene

RTD   Resistance Temperature Detector

TC   Thermocouple

TEC   Thermoelectric Cooler

TIM   Thermal Interface Material

WEG   Water-Ethylene Glycol

Abstract

        The proper functioning and reliability of electronic components depend upon adequate thermal management since high temperature is the principal vector of failure in these devices. The growing complexity of current electronic component design associated with the ever-increasing power consumption and the continuous scale reduction place thermal management of electronics as one of the most strategic challenges for technological innovation in heat transfer. Therefore, new concepts for high heat flux removal are required, such as mechanical vapor compression refrigeration, which is among the most promising active cooling technologies. This thesis presents a novel heat sink for thermal management of electronic devices. The cooler was designed to operate integrated with a compact vapor compression refrigeration system and combines the expansion device and the evaporator in a single cooling unit, thus producing a highly effective two-phase jet impingement cooling of the heated surface. An experimental apparatus was designed and built which operates with a small-scale oil-free linear compressor using R-134a as the working fluid. A purpose-built calorimeter was developed to measure the heat dissipation rate through the compressor shell, thus providing closure for the overall system energy balance. The thermal performance of both the jet impingement cooling module and the vapor compression refrigeration system were evaluated for a variety of operating conditions. In addition, a comprehensive thermodynamic analysis was performed using different performance metrics. Experiments have been carried out with single and multiple orifice configurations of the jet heat sink. The influence of the following parameters was quantified: (i) applied thermal load, (ii) orifice diameter, (iii) orifice-to-heater distance, (iv) hot reservoir temperature and (v) compressor piston displacement. At operating conditions for which the system pressure ratio ranged from 1.4 to 2.2, the two-phase jet heat sink was capable of dissipating cooling capacities of up to 160 W and 200 W from a 6.4-cm^2 surface for single and multiple orifice configurations, respectively, maintaining the temperature of the impingement surface lower than 40℃ with heat transfer coefficients ranging from around 14,000 to 16,000 W/(m^{2}K).

Resumo

    O funcionamento e a confiabilidade de componentes eletrônicos dependem do seu gerenciamento térmico visto que temperatura é o principal vetor de falha operacional nestes sistemas. A crescente complexidade no projeto de componentes eletrônicos associada ao aumento do consumo de potência e à contínua redução de escala colocam o gerenciamento térmico de dispositivos eletrônicos como um dos maiores desafios para inovação tecnológica em transferência de calor. Assim, novos conceitos são necessários tais como o emprego de sistemas de refrigeração por compressão mecânica de vapor, que estão entre as mais promissoras tecnologias de resfriamento ativo. A presente tese introduz um novo aparato para o resfriamento de componentes eletrônicos que opera integrado a um sistema de refrigeração compacto e combina o dispositivo de expansão e o evaporador em uma mesma unidade de resfriamento. A técnica de resfriamento é baseada em jatos bifásicos incidentes sobre uma superfície aquecida. Uma bancada experimental que opera com um compressor linear compacto e utiliza R-134a puro como fluido refrigerante foi projetada e construída. Um calorímetro foi desenvolvido para verificação indireta do fechamento dos balanços de energia do sistema, quantificando o calor dissipado na carcaça do compressor. Os desempenhos térmicos do evaporador de jatos bifásicos e do sistema de refrigeração foram avaliados para várias condições operacionais. Uma análise termodinâmica foi conduzida envolvendo diferentes métricas de desempenho. Experimentos foram realizados com um único bocal e com múltiplos bocais de atomização. A influência dos seguintes parâmetros foi quantificada: (i) carga térmica aplicada, (ii) diâmetro do orifício do bocal, (iii) distância do bocal à superfície de incidência, (iv) temperatura do reservatório quente e (v) deslocamento linear do pistão do compressor. Em condições de operação para as quais a razão de pressão do sistema variou de 1,4 a 2,2, o evaporador de jatos bifásicos foi capaz de remover cargas térmicas de até 160 W e 200 W em uma superfície com 6,4 cm^2 de área utilizando configurações de jatos único e múltiplos, respectivamente. Para estes casos, a temperatura da superfície foi mantida abaixo de 40℃ e coeficientes de transferência de calor de 14.000 a 16.000 W/(m^{2}K) foram atingidos.

1   *Introduction*

High heat flux cooling technologies have been under intense research over the past three decades. Cooling of high-performance computers, high-power electronic modules, hybrid/electric vehicles power equipment and advanced military avionics are among the many examples of applications of thermal management devices (MUDAWAR, 2001; CHU *et al.*, 2004; NAKAYAMA *et al.*, 2009).

The proper functioning and reliability of electronic components predominantly depends on adequate thermal management. As reported in Anandan and Ramalingam (2008), the principal vector of failure in electronic components during operation is temperature (55%), followed by vibration (20%), humidity (19%) and dust (6%). Advances in micro-fabrication of electronic circuitry have led to a continual decrease in physical dimensions allowing more circuit components per unit surface area, which severely increases the heating power density. According to the iNEMI (International Electronics Manufacturing Initiative) roadmaps, presented in Figure 1.1, contemporary microprocessors for desktop machines are designed to operate above 150 W, server and computer cluster chips are likely to exceed power dissipation of 500 W per chip, and the power dissipation of chips in automotive applications, whose dimensions are typically smaller than desktop computer and servers, is reaching 300 W with heat fluxes of 200 - 300 W/cm^2 (BAR-COHEN; HOLLOWAY, 2014).

Taking the automobile industry as an example, at the year 2010, the demand for reducing the size of IGBT (Insulated Gate Bipolar Transistor) modules for hybrid and electric vehicles was expected to increase the volumetric power rating in 10 to 50 times compared to the larger modules commonly used in railway applications. Additionally, the performance and the service life of Li-Ion battery in train and automobile applications is quite sensitive to temperature increase, i.e., the capacity is reduced from 6% to 35% when the storage temperature is raised from 0℃ to 40℃ (NAKAYAMA *et al.*, 2009).

Therefore, the growing complexity that characterizes the current design of electronic components associated with the ever-increasing power consumption and the continuous scale reduction (high packaging density) of these devices place thermal management of electronics as one of the most strategic challenges for technological innovation in heat transfer (BAR-COHEN, 2013).
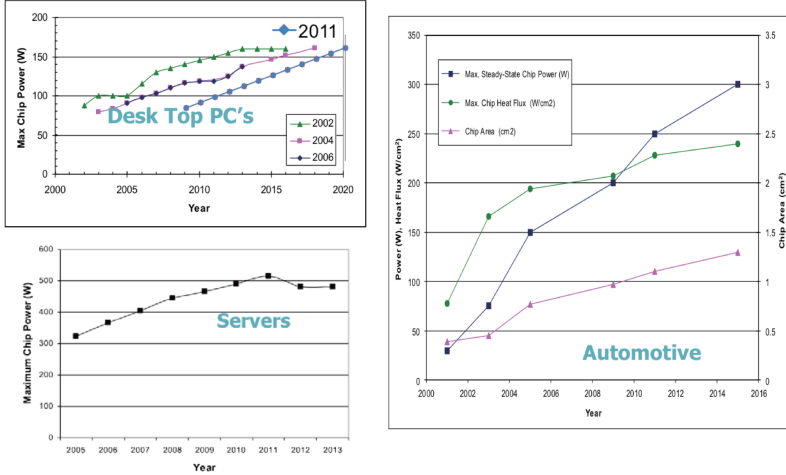
Figure 1.1 – iNEMI roadmaps for chip power dissipation. Adapted from Bar-Cohen and Holloway (2014).

Conventional techniques for thermal management of electronics encompasses (fan-finned) heat sinks and cold plates for which single-phase heat transfer with air blow or liquid flow is the main cooling mechanism. The cooling potential of a *passive* system, i.e., a cooling technology that does not rely on refrigeration, such as a heat pipe or a finned heat sink, is measured in terms of the junction-to-ambient thermal resistance as follows:

$$\dot{Q}_p = \frac{T_j - T_{amb}^*}{R_{j\text{-}amb}} \tag{1.1}$$

where $\dot{Q}_p$ is the passive heat dissipation rate, T_j is the junction temperature, T_{amb}^* is the effective ambient temperature (i.e., corrected for effects of proximity and preheating), and $R_{j\text{-}amb}$ is the thermal resistance between the junction and the ambient.

This resistance, R_{j-amb}, can be described as a network of smaller resistance elements, which are due to conduction in the several adjoining media and also due to convection of the coolant in the heat sink itself, as illustrated in Figure 1.2.
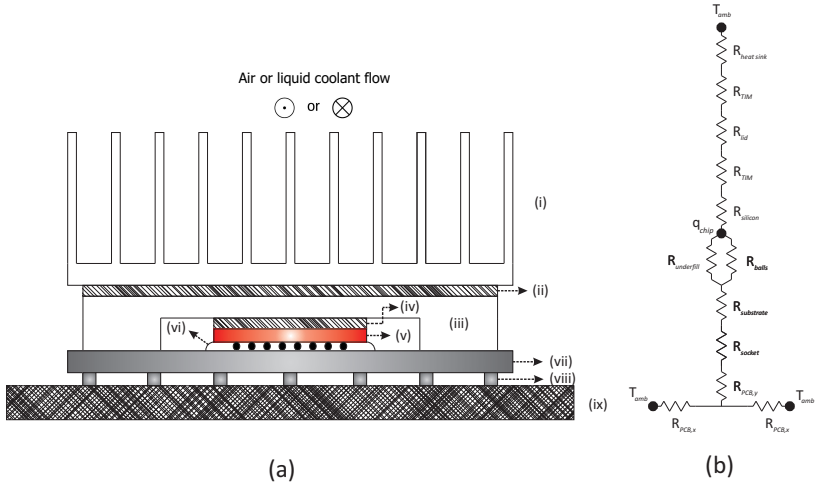
Figure 1.2 – (a) Main components and (b) thermal resistance network of a heat rejection system usually adopted in desktop computers and servers. Legend: (i) heat sink, (ii) TIM, (iii) lid, (iv) TIM, (v) silicon dye, (vi) underfill and balls, (vii) substrate, (viii) sockets, and (ix) PCB (Printed Circuit Board). Adapted from Belady (2002 apud BARBOSA *et al.*, 2012).

For a fixed junction temperature, the heat transfer rate can be increased if the thermal resistance is decreased. Kandlikar and Bapat (2007) carried out a quantitative analysis of the thermal resistances and pointed out that the thermal resistance of the thermal interface material (TIM), the conduction resistance of the substrates, and the convective resistance inside the heat sink are all crucial in determining the maximum heat dissipation rate for a given coolant fluid flow rate, chip surface and coolant inlet temperatures. Although commercial TIMs offer low thermal resistances when they are fresh (between 0.03 and 0.1 °C cm² W⁻¹), their thermal performance can be severely degraded as a result of long-term exposure to high temperatures (PRASHER; CHIU, 2009).

Because of their relatively low convective heat transfer coefficients and linear relationship between heat flux and surface-to-fluid

temperature difference, single-phase cooling schemes, particularly the air-based ones, can result in unacceptably high temperatures when subjected to high heat fluxes. In addition, the heat transfer coefficient generally increases asymptotically with the air velocity whereas the pressure drop doubles and the acoustic noise obeys a fifth order power-law. Hence, the penalties clearly outweigh the modest gains in heat transfer (WHELAN et al., 2012).

The progressive scale reduction in electronic equipment will impose an asymptotic limit on the minimization of thermal resistances (MONGIA et al., 2006; WHELAN et al., 2012; MANCIN et al., 2013). Several researchers agree that single-phase natural and forced convection cooling schemes (i.e., fan-cooled finned heat sinks and cold plates) will no longer be capable of maintaining the operating temperatures of processors and other high-power components below tolerable levels (HEYDARI, 2002; ORTEGA; BIRLE, 2006; TRUTASSANAWIN et al., 2006; CREMASCHI et al., 2007; SUNG; MUDAWAR, 2009a; WHELAN et al., 2012; MANCIN et al., 2013). Therefore, new concepts for the removal of high heat fluxes are required so as to meet the increasing demands with greater efficiencies.

The removal of highly concentrated heat loads demands cooling strategies that can offer large thermal conductances. Two-phase cooling schemes are particularly appropriate for high heat flux situations because of their high heat transfer coefficients and the steep, nonlinear relationship between heat flux and surface-to-fluid temperature difference, typical of nucleate boiling. These two attributes facilitate the removal of highly concentrated heat loads corresponding to relatively small temperature differences and significantly reduce the surface temperature and temperature fluctuations in response to changes in the heat flux. Reducing both the temperature and its fluctuations is an important operational safeguard to ensure the reliability and structural integrity of thermal management devices found in several high heat flux applications (SUNG; MUDAWAR, 2009a).

Figure 1.2 also portrays the basic configuration of a passive technology that employs *indirect liquid cooling*, i.e, a liquid coolant flowing through the finned heat sink. In this case, the cooling performance is partially determined by the convective heat transfer process. The performance also depends on the resistances of the different layers of materials (shown in the figure) separating the chip from the liquid coolant, which promote a relatively large temperature gradient when dissipating high heat fluxes. In addition to finned heat sinks, heat pipes and cold plates are also used for indirect liquid cooling (BELADY, 2001; WANG

et al., 2009). Some heat pipe applications are illustrated in Figure 1.3 (a): tube in fin (left) and embedded (right) heat pipes were used in HP's V-Class servers, tower heat pipes (top and center) were used in Convex's C3 server and a typical laptop heat pipe/spreader is shown at the bottom of the figure (BELADY, 2001). In turn, Figure 1.3 (b) depicts an indirect liquid cooling system composed of five cold plates.

(a) Heat pipe examples

(b) Liquid cold plate assembled to an electronic board
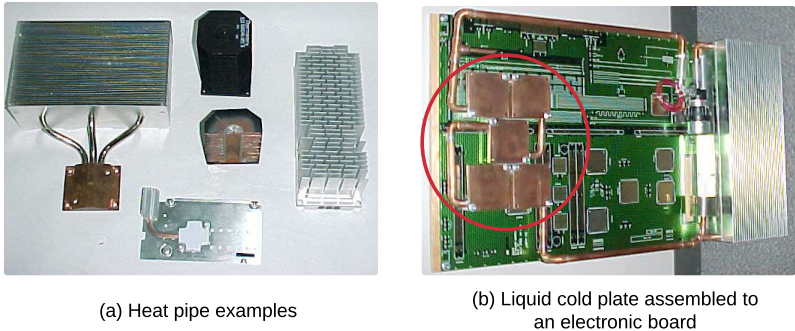
Figure 1.3 – Passive cooling technologies that employ indirect liquid cooling: (a) heat pipes and (b) cold plate. Adapted from Belady (2001)

The aforementioned thermal resistances may be completely eliminated by *direct liquid cooling* of the chip. However, bringing the cooling fluid into direct contact with the surface of the heat spreader, or the electronic component itself, limits cooling options to a few coolants such as perfluorocarbons (FCs) and hydro-fluoro-ethers (HFEs). Unfortunately, the thermophysical properties of these coolants are quite inferior to those of common coolants such as water and water-ethylene glycol mixtures (STARKE *et al.*, 2005; MUDAWAR *et al.*, 2008).

Direct liquid cooling is advantageous only when its convective thermal resistance is smaller than the sum of the convective, conductive and contact resistances of the indirect liquid cooling configuration shown in Figure 1.2. Because heat spreading plays a minor role in a direct cooling system, high-flux chips may be packaged quite close to one another, greatly reducing both the weight and the volume of the cooling system.

Given the inferior thermophysical properties of dielectric coolants and the strong dependence of cooling performance on convective resistance, the viability of a direct cooling system is highly dependent on the ability to achieve very large convective heat transfer coefficients. As shown in Figure 1.4, this goal can be realized by adopting a highly ef-

fective direct liquid immersion cooling configuration (jet impingement, saturated pool boiling and convective flow boiling) and also by capitalizing on the benefits of phase change.
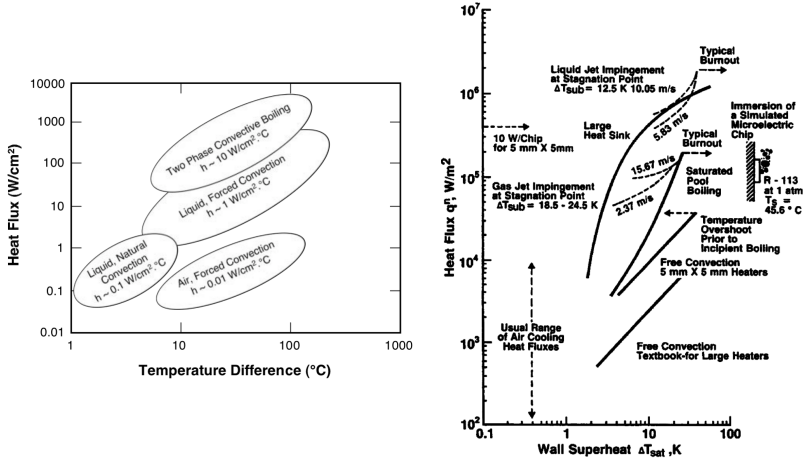
Figure 1.4 – Heat transfer potential of some existing cooling technologies for various fluids and operating conditions. Graphs on the left and right are reproduced from Mudawar *et al.* (2008) and Chu *et al.* (2004), respectively.

The coolant candidates for direct liquid cooling of microelectronic components must comply with a series of technical requirements. Firstly, the coolant must be chemically compatible with the system-specific combination of chip, chip package, substrate, and PCB materials, e.g., silicon, silicon dioxide, silicon nitride, alumina, o-rings, plastic encapsulants, solder, gold, and epoxy glass. Besides, the coolant must be (i) environmentally friendly, (ii) non-flammable, (iii) nontoxic, (iv) effective at two-phase cooling, i.e., have a large latent heat and a normal boiling point temperature in the range of 20℃ to 80℃ to avoid high-pressure confinement of the liquid-vapor mixture.

Lastly, the coolant should have appropriate thermophysical and mechanical properties such as a high-dielectric strength for electrical isolation. The FC and HFE coolants have very low wetting angles and relatively low critical pressures, thermal conductivities, and specific heats, but air solubilities approaching 50% by volume. Compared to HFE coolants, refrigerant R-134a has a higher latent heat despite its lower normal boiling point temperature, which requires a medium

pressure container (STARKE *et al.*, 2005; BAR-COHEN *et al.*, 2006).

According to Barbosa *et al.* (2012), there is a clear understanding that mechanical vapor compression refrigeration is among the most promising *active* cooling technologies (i.e., those capable of lowering the chip temperature below that of the ambient) for the next generation of electronic systems. An active cooling system (refrigerator) is a thermodynamic system that operates in a cycle to transfer energy (and entropy) from a low-temperature source to a high-temperature sink. In practice, refrigerators are conceived to transfer heat from a body or fluid and maintain it at a temperature lower than that of its surroundings. Therefore, work input is required to lift the thermal load applied on the low-temperature source. This work input plus the thermal load are rejected as heat into the ambient.

A typical single-stage vapor compression-based processor cooling system is composed of a compressor, a condenser, an expansion device, and a heat sink or cold plate evaporator, as seen in Figure 1.5.
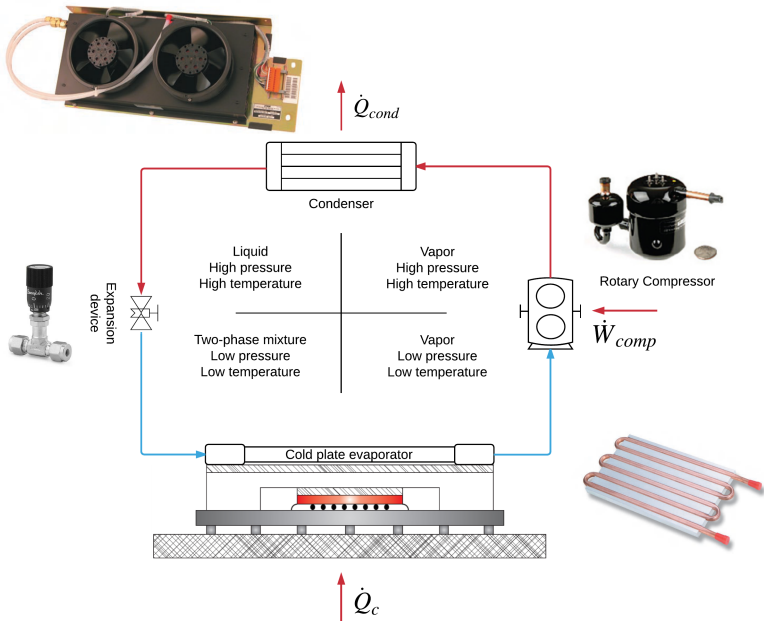
Figure 1.5 – Schematic diagram of a vapor compression cooling system for microprocessors.

The active cooling system can decrease the junction-to-ambient thermal resistance by way of dividing the thermal network into two branches: (i) the heat sink/evaporator thermal network and (ii) the condenser thermal network are such that,

$$\dot{Q}_{evap} = \frac{T_j - T_{evap}}{R_{j\text{-}evap}} \qquad (1.2)$$

$$\dot{Q}_{cond} = \dot{Q}_{evap} + \dot{W} = \frac{T_{cond} - T_{amb}^*}{R_{cond\text{-}amb}} \qquad (1.3)$$

where T_{evap} is the refrigerant evaporating temperature, T_{cond} is the refrigerant condensing temperature, $\dot{W}$ is the rate of work consumption, $\dot{Q}_{evap}$ is the evaporator heat transfer rate, $\dot{Q}_{cond}$ is the heat rejection rate, $R_{j\text{-}evap}$ encompasses the thermal resistances between the chip and the evaporating refrigerant and, lastly, $R_{cond\text{-}amb}$ is the thermal resistance between the condensing refrigerant and the ambient.

According to Phelan *et al.* (2002), the potential advantages of active cooling, in general, are the following: (i) ability to dissipate heat while maintaining a low junction temperature; (ii) higher device speed and increased reliability because of the reduced operating temperature; and (iii) expanded device lifetime because of the constant operating temperature. On the other hand, there are several issues that need to be addressed before a successful implementation of mechanical vapor compression technology for electronics cooling: (i) designing an efficient, reliable and compact compressor, (ii) developing and improving suitable cold plate evaporators, (iii) integrating the cooling system in a restricted space, (iv) resolving packaging related issues, and (v) maintaining a competitive cost for the entire system.

The compressor is certainly the most challenging component of the refrigeration system in terms of its miniaturization (JEONG, 2004). The few studies that have dealt with applications in electronics cooling were not specifically focused on the actual system miniaturization. However, they used small (but not truly miniaturized) commercially available compressors. Since some commercial compressors are designed for operating at large pressure ratios like refrigerators and other low back-pressure (LBP) systems, their performance is poor at the relatively small pressure ratios associated with the high back-pressure (HBP) conditions often desired for electronics cooling (BARBOSA, 2011).

Cooling solutions that rely on two-phase flow enhanced heat transfer, such as sprays, jets and microchannels have been attracting

the attention of the research community for a number of years (BAR-COHEN *et al.*, 2006; AGOSTINI *et al.*, 2007; KANDLIKAR; BAPAT, 2007; ANANDAN; RAMALINGAM, 2008; EBADIAN; LIN, 2011; TULLIUS *et al.*, 2011; MARCHINICHEN *et al.*, 2013; KADAM; KUMAR, 2014). In contrast with the currently available passive cooling techniques, such as heat pipes and single-phase liquid loops (RIBEIRO *et al.*, 2010), sprays, two-phase jets and boiling in micro-channels can be easily integrated with vapor compression cooling in order to achieve junction temperatures below that of the ambient (BARBOSA *et al.*, 2012).

Spray cooling is a technology with great potential to assist the thermal management of future generations of electronics and other applications involving high heat fluxes (CADER *et al.*, 2004; FABBRI *et al.*, 2005a; SHEDD, 2007; KIM, 2007; MUDAWAR *et al.*, 2008; CHENG *et al.*, 2010). It has been demonstrated as an effective way of removing high heat loads due to the small surface overheating and low mass flow rates, which are essential requirements for the thermal design of compact high-power electronic devices. Integrated mechanical vapor compression-spray cooling devices have been proposed recently in the literature (YAN *et al.*, 2010a, 2010b, 2010c; CHUNQIANG *et al.*, 2012; XU *et al.*, 2014; HOU *et al.*, 2015; CHEN *et al.*, 2015). However, as far as the present author is aware, no specific attention has been given to the potential for size reduction (miniaturization) of the cooling system (for instance, through the incorporation of a small-scale compressor).

Impinging jets are also suitable for high heat flux removal, particularly in the presence of phase change of the working fluid. When jets impinge on a surface they undergo a very large change in kinetic energy at the stagnation point. However, large temperature gradients can be formed on the target surface, unless a multi-nozzle configuration is carefully implemented. Another benefit of this cooling technique is its flexibility, as different jet impingement geometries can be achieved by utilizing different sizes, shapes and patterns of jet orifices in a cooling module (JOSHI *et al.*, 2013a, 2013b; JOSHI; DEDE, 2015). Multi-jet impingement cooling schemes have the disadvantage of reducing the local heat transfer coefficient because of the interaction between adjacent jets. The solution to this problem lies in the use of complex geometries to improve drainage of the liquid flow from the jets (BARRAU *et al.*, 2010; MUSZYNSKI; ANDRZEJCZYK, 2015).

Microchannels offer compactness, fluid inventory reduction and a very thin boundary layer during the fluid flow, which yields to very high heat flux removal. Nevertheless, if single-phase flow is present, microchannels cause a large increase in temperature along the fluid

flow path and are also responsible for a relatively large pressure drop. Impinging jets can produce comparable thermal performance to microchannels with lower pressure drops and higher volumetric flow rates, which make them more appropriate for integration to several real world applications such as cooling of power electronics in military vehicles (e.g. this could be done by integrating a cooling device with an array of impinging jets into the radiator flow loop already present in most vehicles) (MADDOX *et al.*, 2015).

1.1   Presentation of the Object of Investigation

This study proposes a new cooling unit for thermal management of electronic devices. The cooler was designed to operate integrated with a compact vapor compression refrigeration system in order to maintain the temperature of a heated surface below a specified level. A representation of the refrigeration system is presented in Figure 1.6.
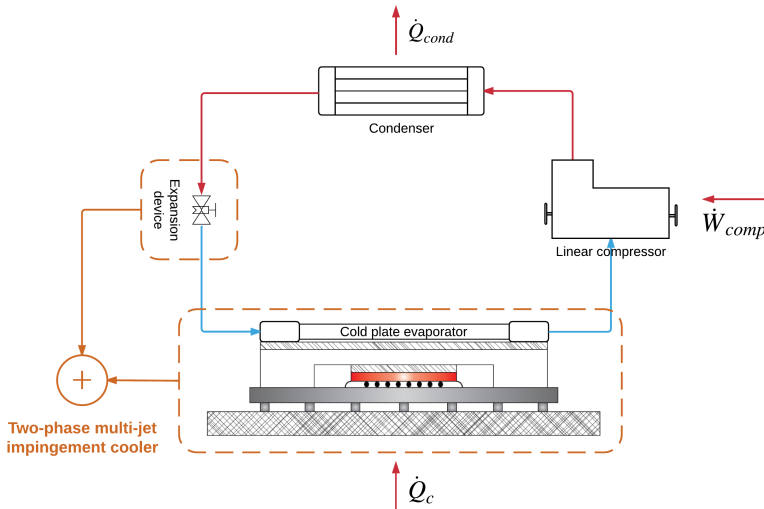
Figure 1.6 – General representation of the proposed refrigeration system and the object of investigation.

The proposed active cooling system is composed of: (i) a small-scale oil-free linear compressor, (ii) a compact condenser, and (iii) the

cooling module which is a jet-impingement-based device that combines the array of micro-orifices (the expansion device) and the evaporator/heat sink itself into a single unit. The system operates with R-134a as this was the refrigerant for which the compressor has been designed. A mixture of distilled water and ethylene glycol is used as the secondary fluid in a thermal bath coupled with the condenser.

The work presented in this thesis is at the intersection of two research areas, namely, heat transfer and fluid flow of impinging jets and design of vapor compression systems for electronics cooling. Although a detailed characterization of the flow field is not presented, the impact of the jet(s) geometry on the heat transfer coefficient behavior is quantified so that a comprehensive thermodynamic analysis of the proposed refrigeration system can be performed.

1.2 Objectives

The objective of the present thesis is to develop an innovative active thermal management device for electronics cooling that operates integrated with a compact compressor. The new module combines the expansion device and the evaporator in a single unit, thus producing a highly effective two-phase jet impingement cooling of the heater surface.

To enable the development of this research work, the following actions were pursued:

- Design and build a versatile experimental apparatus, i.e., a compact vapor compression-based refrigeration system;

- Design and build a calorimeter for the small-scale compressor in order to indirectly measure the heat dissipation rate through the shell and close the system energy balances.

- Perform experimental tests to evaluate the thermal performance of the jet impingement cooling module for a variety of operating conditions;

- Perform a complete thermodynamic analysis of the active cooling system.

1.3 Outline of the Thesis

The present thesis was divided into five chapters as follows. In Chapter 2 - *Literature Review* - a review of thermal management devices

that use direct liquid cooling techniques, particularly jet impingement, is presented. Chapter 3 - *Experimental Apparatus* - describes the design and construction of the laboratory apparatus, the experimental procedure and data processing for the experimental tests. Chapter 4 - *Experimental Analysis of the Cooling System* - presents and discusses the experimental results, performance metrics, steady-state heat transfer and thermodynamic parameters. Finally, Chapter 5 summarizes the final considerations and recommendations for future work.

2   *Literature Review*

During the last two decades, several works have reported experimental investigations of devices designed to cool compact heated surfaces. This chapter reviews the state of the art of thermal management devices for electronics cooling. The discussion is concerned only with cooling units that employ direct liquid cooling techniques, such as jet impingement cooling, hybrid cooling schemes that make use of jet impingement cooling, and spray cooling. First, a brief introduction to the fundamentals of jet impingement cooling is presented. Next, a general description of the experimental studies is given, which encompasses the working principle of the cooling module, the experimental apparatus built to test it and the principal results. The reviewed devices for high heat flux removal are organized in two categories: (i) devices integrated with closed-loop systems and (ii) devices integrated with vapor compression refrigeration systems (VCRS). Open-loop system-based experimental facilities are not addressed in this review.

2.1   Fundamentals of Jet Impingement Cooling

Liquid jet impingement offers very low thermal resistance and is relatively simple to implement, i.e., by using a straight tube or a contraction nozzle directly oriented toward the region of the heat load (LIENHARD V, 1995). Boiling happens when a liquid jet impinges on a heated surface at a temperature higher than the saturation temperature of the fluid causing heterogeneous nucleation on the surface. Common configurations in jet impingement boiling include free surface and submerged jets. In the free surface configuration, the liquid jet and the heated surface are surrounded by a gaseous environment, whereas in the submerged jet configuration, the liquid jet and the heated surface are surrounded by a liquid environment (WOMAC *et al.*, 1993; CHIEN;

CHANG, 2011; CARDENAS; NARAYANAN, 2014).

   In a single-phase free surface impinging jet, there are five differ-
ent flow regions, as portrayed in Figure 2.1 (a): (i) the stagnation zone;
(ii) the laminar boundary layer region, in which the viscous boundary
layer thickness is less than the liquid film thickness and the outer por-
tion of the liquid sheet flows nearly parallel to the wall at the incoming
jet speed; (iii) the viscous similarity region, in which the viscous ef-
fects extend through the entire liquid film and the film speed decreases
with increasing radial distance; (iv) the region of developing turbu-
lence; and (v) the region of fully turbulent flow, which may relaminar-
ize farther downstream as the liquid film speed decreases (LIENHARD
V, 1995, 2006).
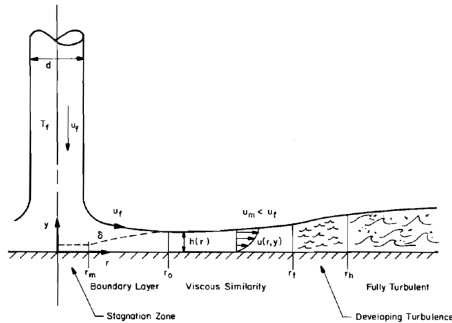
(a) Single-phase jet
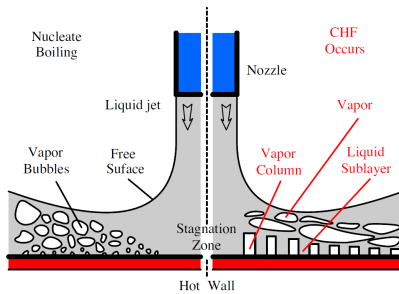
(b) Phase-changing (boiling) jet

Figure 2.1 – Fluid flow regions of free surface impinging jets. Adapted
from Lienhard (1995) (single-phase) and Qiu *et al.* (2015) (boiling).

   Regardless of the high heat transfer rate promoted in the stag-
nation zone by a single phase impinging jet, the heat transfer rate can

be considerably enhanced once boiling is involved. In a typical boiling configuration illustrated in Figure 2.1 (b), the boiling process develops from single phase forced convection to nucleate boiling, then to transition boiling, and finally to film boiling, along with the increase of wall superheat. In the nucleate boiling regime, a high heat transfer rate can be generated under a relatively low wall-to-fluid temperature difference (QIU *et al.*, 2015).

The transition from single-phase forced convection to the nucleate boiling regime is marked by the onset of nucleate boiling. The critical heat flux (CHF) may be reached at the end of the nucleate boiling region, after which the wall superheat sharply increases for a fixed wall heat flux. An abrupt decrease of the heat transfer coefficient may result in a device burn-out, as the heated wall becomes covered by a vapor blanket. Being able to accurately predict the CHF not only allows one to operate with a safe distance with respect to this limit but also helps to design and optimize robust heat transfer solutions.

If the jet is generated by the expansion of a stable (saturated or slightly sub-cooled) liquid, a liquid-vapor mixture can be produced downstream of the orifice if enough time is allowed for it to reach thermodynamic equilibrium. However, in high-speed jets, the liquid may be in a metastable (superheated) state at the orifice exit. The superheated condition implies that the temperature of the liquid is higher than its corresponding boiling temperature at its actual pressure. As the superheated liquid is accelerated through the orifice, its pressure falls below the saturation pressure and vapor may be generated inside the flow, thereby reducing its temperature. The break up of a liquid jet based in this condition of thermodynamic instability is called flash-boiling atomization (REITZ, 1990; KARAMI; ASHGRIZ, 2011).

Oza (1984) classified the break up regimes of a flash-boiling jet as external and internal, depending on the degree of superheat of the liquid. In external flashing, a liquid jet with a low degree of superheat emerges intact from the orifice and the atomization occurs some distance from the orifice exit due to rapid bubble growth. In internal flashing (or transition regime), a liquid jet with a high degree of superheat diverges immediately at the orifice exit as boiling and rapid bubble growth occurs within the injector orifice, producing an already atomized two-phase flow at the orifice exit.

Reitz (1990) observed experimentally that water jets in the so-called internal flashing regime may actually be broken up by phenomena occurring outside the nozzle due to the existence of an inner intact core, which is normally obscured by the surrounding diverging jet. However,

Reitz (1990) also argues that if the operating conditions at the orifice
exit are close enough to the saturation temperature (corresponding to
a pressure of approximately 6 bar), it is possible that the emerging jet
would be already atomized (i.e., predominantly vapor phase flow with
suspended droplets) due to boiling within the injector orifice.

        According to Lienhard (2006), turbulence in an axisymmetric jet
is carried into the radially spreading liquid film causing two primary
effects. First, it tends to increase convective heat transfer in the bound-
ary downstream of the stagnation zone as well as promotes turbulent
transition of the thin liquid sheet. Second, it disturbs the surface of
the incoming jet. In addition to the initial disturbances carried into the
thinning liquid sheet, radial spreading can produce a strong increase in
their amplitude. If the initial disturbances are large enough, the ampli-
fied disturbances can cause droplets to break free from the liquid sheet
resulting in the splattering phenomenon, which is presented in Figure
2.2. Splattering is more important for long and/or inertia-governed
jets. Strong splattering can result in atomization of 30% to 70% of
the incoming liquid. Because airborne droplets no longer contribute to
cooling the target surface, heat transfer far downstream is degraded.

(a) Schematic drawing   (b) Photographs
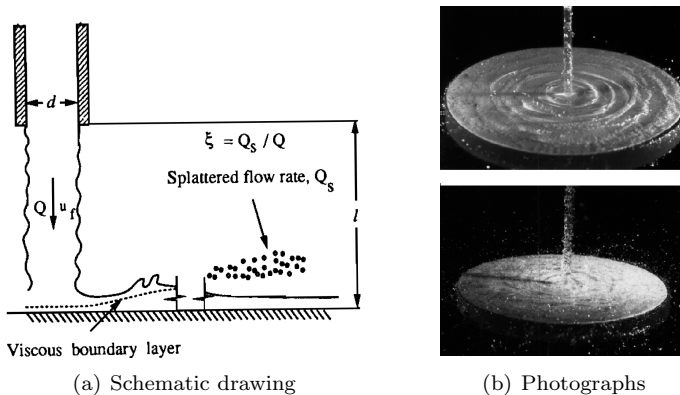
Figure 2.2 – Splattering of a turbulent jet: (a) schematic drawing and
(b) photographs. Radially traveling waves (upper right corner) and a
more intense splattering (lower right corner) are shown in (b). Adapted
from (a) Lienhard (1995) and (b) Lienhard (2006).

        Over the past two decades, liquid jet impingement cooling has
been extensively studied. The effects several parameters such as noz-
zle shape, impingement height, nozzle pitch distance, cross flow and

drainage conditions on the flow and heat transfer of single- and two-phase jet impingement have been widely reported (WOMAC *et al.*, 1993; GARIMELLA; RICE, 1995; LIENHARD V, 1995; PAN; WEBB, 1995; LIENHARD V, 2006; ROYNE; DEY, 2006; WHELAN; ROBINSON, 2009; MAHMOUDI *et al.*, 2012; LINDEMAN; SHEDD, 2013; SAN; CHEN, 2014). Qiu *et al.* (2015) presented an up-to-date comprehensive review on jet-impingement boiling heat transfer, where the effects of jet parameters (impact velocity, impact distance, jet diameter, sub-cooling and jet array) and target surface parameters (surface condition and surface aging) have been discussed in detail.

2.2 Cooling Devices Integrated with Closed-Loop Systems

In this section, several thermal management devices reported in the literature are presented according to the following categories: (i) devices exclusively based on jet impingement cooling; (ii) hybrid cooling solutions that use impinging jets; and (iii) some devices that employ the spray cooling technique.

2.2.1 Jet Impingement Cooling Devices

Oh *et al.* (1998) and Lienhard and Hadeler (1999) presented a cooling module for the removal of very high heat fluxes. The cooling module, depicted in Figure 2.3 (a), was composed of a heated faceplate, a hexagonal array of 14 tube nozzles with 5 cm in length and 2.78 mm in (inner) diameter, and a liquid manifold arrangement. Liquid water was driven into the nozzle array from the lower (higher-pressure) manifold to the upper (lower-pressure) manifold. The jets upwardly impinged on the rear side of a metallic film faceplate heated by a cooling load imposed on its forward surface. The experimental setup, shown in Figure 2.3 (b), was composed of a water reservoir, a turbine flow meter, a centrifugal pump, the cooling module, valves and pressure transducers.

In order to estimate the heat transfer coefficient, velocity and pressure fields were calculated by numerical simulations using the $k - \epsilon$ RNG turbulence model (VERSTEEG; MALALASEKERA, 1995). Experimental results, numerical studies and thermal stress analysis were reported. The heat transfer in the cooling module was dominated by the thermal resistances to the insulating film between the test heater

and the faceplate. The authors informed that the cooling unit was able to remove heat fluxes up to 1,700 W/cm^2 from an area of 10 cm^2. Besides, heat transfer coefficients of 220,000 W/m^{2}K were obtained. The jet cooling process was entirely by single-phase convection with impingement velocities of 47 m/s. Boiling was expected only for heat fluxes well above 2,000 W/cm^2.

(a) Exploded view

(b) (i) Module cross-section illustrating the fluid flow path and (ii) flow loop for module test
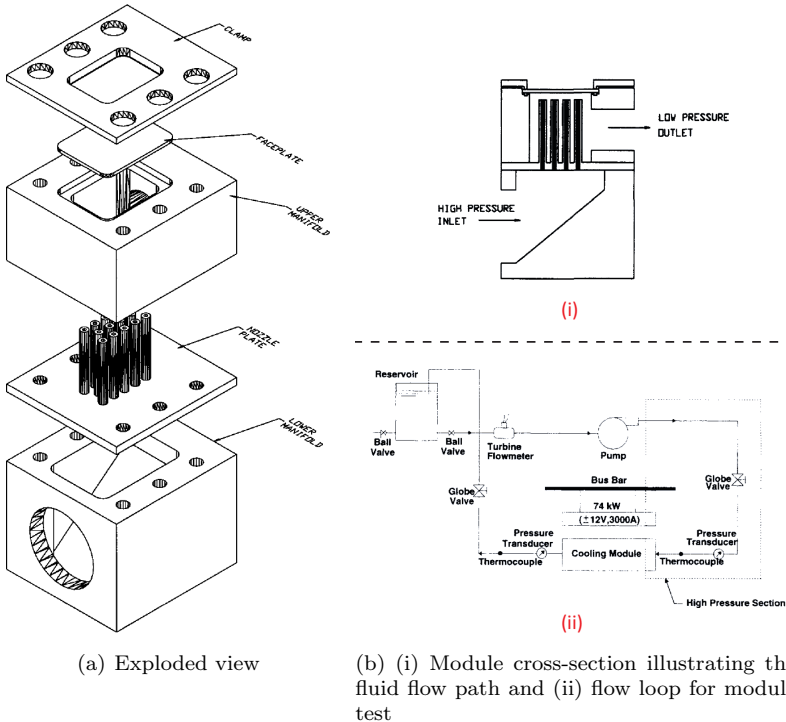
Figure 2.3 – Cooling module proposed by Oh *et al.* (1998). Adapted from Oh *et al.* (1998) and Lienhard and Hadeler (1999).

Fabbri *et al.* (2005a, 2005b) designed and tested a high power density cooling module based on the impingement of microjets. The decision of employing jet impingement cooling was supported by experimental studies (FABBRI *et al.*, 2003, 2005a, 2005b) comparing the single-phase heat transfer performance and pressure drop of liquid (water) droplet sprays produced by HAGO nozzles and microjet arrays created by orifice plates over a range of parameters suitable for electronics cooling applications. The microjet arrays were superior to the

sprays since they required less pumping power per unit of heating power removed.

The cooling unit, portrayed in Figures 2.4 (a) and (b), was composed of the three primary items: (i) an orifice plate for jet formation; (ii) a containment vessel to hold the nozzle, the heat source and the coolant (deionized water), and (iii) a pump for liquid recirculation. The container with a coupled fan also served as a heat exchanger to the ambient. Figure 2.4 (c) presents a schematic diagram of the flow loop built to test the cooling unit.
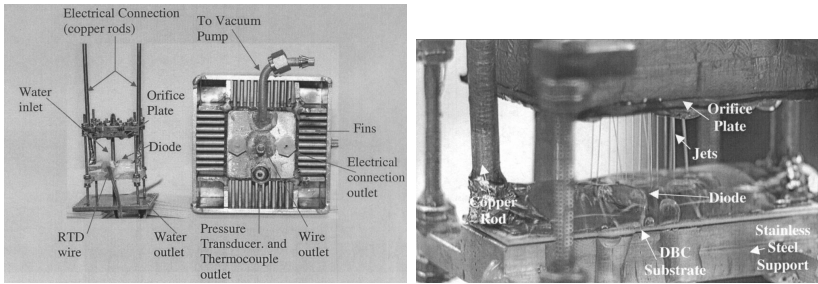
(a) Cooling module

(b) Details of the diode and the jets
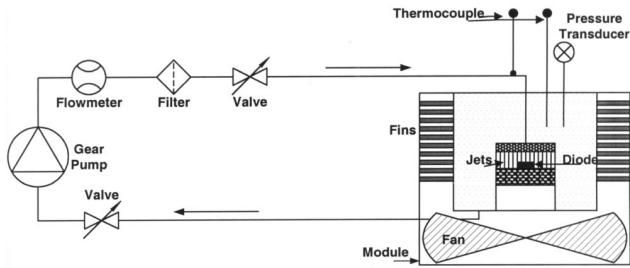
(c) Schematic diagram of the experimental facility

Figure 2.4 – Cooling module and experimental facility presented by Fabbri *et al.* (2005a, 2005b). Adapted from Fabbri *et al.* (2005a).

The orifice plate (0.5-mm thick) had 24 orifices of 140 μm in diameter, distributed in a square array pattern with 2 mm spacing. The overall dimensions of the cooling unit (including the fan cooler) were 100 mm $\times$ 100 mm $\times$ 130 mm. The orifice plate was installed on a support located above the heat source, i.e., a diode with an area of 43.5 mm^2 mounted onto a DCB (Direct Bond Copper) substrate layer, which was glued on top of a G10 insulating plate.

In order to explore the overall potential of the proposed cool-
ing concept, the experimental tests were run keeping an approximately
constant jet velocity (4.5 m/s) for both the single-phase and nucleate
boiling regimes. The module was first charged with deionized water at
room temperature. Then, the pump was started and the flow rate was
set to the desired value. Next, the internal pressure of the chamber
was reduced using a vacuum pump. At steady-state chamber con-
ditions, the vapor partial pressure was calculated using steam tables
assuming that the temperature measured in the chamber was equal to
the vapor saturation temperature at the computed vapor partial pres-
sure. Subsequently, power was supplied to the diode and the data were
recorded.

The authors reported that their device was capable of dissipating
129 W with a heat flux of 300 W/cm^2 at a surface temperature of 80℃.
It was verified that the reduction of the system pressure resulted in an
early boiling inception, thus allowing for higher heat removal rates at
lower surface temperatures. The ratio between the power consumed,
used to pump the fluid and run the fan, to the power removed from
the heater presented a decreasing tendency indicating that the cooling
process was more efficient for higher heat transfer rates removed from
the diode. The ratio values ranged from $\approx 25\%$ (less efficient case,
corresponding to 20 W) to $\approx 4.4\%$ (most efficient case, corresponding
to 129 W). The principal source of loss was that some jets did not
impinge on the diode since the area covered by the jet array was larger
than that of the diode. Therefore, part of the coolant did not remove
any heat, although it was still being pumped, which represented a waste
of the power consumed by the system.

Meyer *et al.* (2006) conducted an experimental investigation of
the performance of the cooling module shown in Figure 2.5 (a), which
operated with an array of three confined rectangular jets impacting
a 3 cm × 3 cm heated surface. Item (i) of this figure presents the
primary components of the test module: the heater block, the jet plate
and the plastic housing. Item (ii) illustrates the working fluid (FC-72
and ethanol) path, i.e., the coolant was supplied through a port at
the back of the middle plastic plate, which was followed by a diverging
plenum. A deflecting plate situated midway along the diverging plenum
caused the fluid to stagnate before reaching the jet plate and ensured
an even flow distribution among the jets. The flow was divided among
three small plenums in the jet plate, situated above each jet orifice
impinging on the surface of the heated copper block. Thereafter, the
fluid flowed horizontally away from the impingement zone and collided

with the fluid from the neighboring jets or the sidewalls. Then, it passed through four exit channels located above the collision planes, rejoining in a plenum above the jet plate before exiting the test module. Finally, item (iii) exhibits a photograph of the three tested jet plates.

Figure 2.5 (b) portrays a schematic diagram of the flow loop used to test cooling module. The liquid was circulated in the loop with the aid of a variable speed magnetically coupled pump. Subsequently, it passed through a filter, a rotameter and a fan-cooled sub-cooler before entering the test module. Exiting the test module, the two-phase mixture was routed to a reservoir for phase separation. Vapor was released to a condenser situated atop the reservoir, then it condensed and trickled down to the reservoir. The liquid was drained directly into a deaeration chamber below the reservoir. Pressure, temperature and volumetric flow rate of the coolant were the controlled parameters.
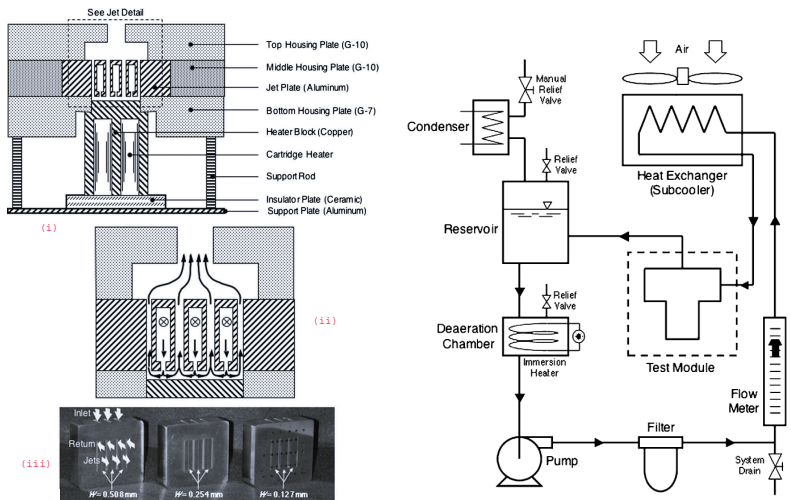
(a) Cooling module construction details: (i) components, (ii) working fluid path and (iii) photograph of the jet plates underside

(b) Schematic diagram of the flow loop

Figure 2.5 – Cooling module and experimental setup presented in the work of Meyer *et al.* (2006). Adapted from Meyer *et al.* (2006).

The effects of impingement velocity, jet width (0.127 mm, 0.254 mm and 0.508 mm for FC-72 and 1 mm for ethanol) and coolant subcooling degree (10.6℃ e 20.6℃) at the inlet of the module were explored in order to elaborate correlations for single-phase heat transfer coeffi-

cient and critical heat flux. As the three parameters mentioned above were increased the single-phase region could be extended, thus delaying the onset of boiling and enhancing CHF. For FC-72, the single-phase heat transfer coefficient increased with the impingement velocity and jet width. For the range of velocities studied, the critical heat flux was significantly affected by inlet sub-cooling since an increment of 10℃ in sub-cooling increased CHF by 26%. Tests with ethanol were run exclusively to extend the applicability range of the proposed CHF correlation.

Overall, Meyer *et al.* (2006) reported that their jet impingement cooling device was highly effective to remove heat fluxes in excess of 100 W/cm^2 as well as to maintain fairly isothermal surface conditions with spatial variation of less than 1.2℃ and 2.6℃ for single-phase and nucleate boiling regimes, respectively. At critical heat flux conditions, surface temperatures ranged from 85.1℃ to 97.3℃. A better cooling performance was achieved by decreasing the jet width for a given volumetric flow rate. For the majority of the tested conditions, the pressure drop was fairly low, even for the smallest jet width and the largest impingement velocity conditions.

Wang *et al.* (2011) proposed a submerged jet array cooling scheme as a solution for thermal management of high performance electronics. The heat transfer performance of the liquid jet array was investigated using experimental and numerical methods to generated data on the thermal management design for cooling an electronic board. The jet array was generated using a 5 mm thick metallic nozzle plate, where 285 (19 × 15) circular and sharp-edge nozzles (0.5-mm diameter and 5.5-mm pitch) were machined in a rectangular array, as shown in Figure 2.6 (a). The array was tested for an impingement height of 3 mm with the volumetric flow rate varying from 2.0 to 10.0 L/min. The heat load ranged from 500 to 2000 W over an area of 233 × 160 mm^2, corresponding to heat fluxes from 1.3 to 5.4 W/cm^2.

The experiments were conducted using a closed-loop system in which the water stored in the water tank was pumped through a rotameter to the impingement chamber inlet. After passing through the nozzle plate and impinging onto the heated surface, the liquid was drained away via the two outlets to the heat rejection unit, where the liquid was cooled down before returning to the pump. During the experimental tests, the heating power was first set at a fixed value and the flow rate was varied. Figure 2.6 (b) portrays the experimental setup used to test the proposed jet impingement-based device.

The difference between the heater surface temperature and the

liquid temperature at the inlet of the jet chamber decreased with the flow rate and increased with the heating power. The experimental Nusselt numbers agreed well with reported data from previous studies. Numerical simulations were also conducted on a 16-nozzle module using the renormalization group (RNG) $k - \epsilon$ turbulence model (VERSTEEG; MALALASEKERA, 1995) to gain insight into the temperature and velocity fields. The temperature and velocity fields were generated and the average heat transfer coefficient obtained from the numerical analysis showed good agreement with the experimental data.

(a) Nozzle plate   (b) Schematic diagram of the flow loop
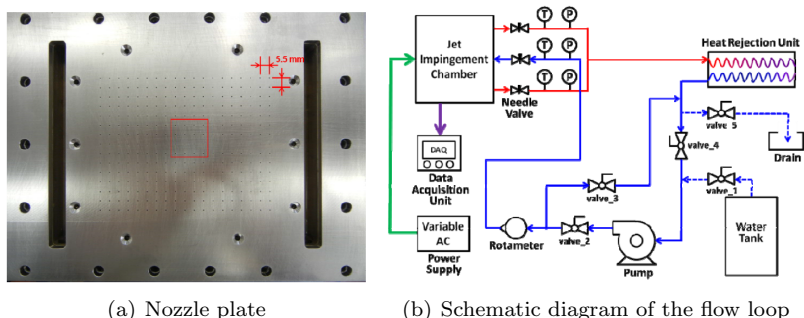
Figure 2.6 – Nozzle plate for jet generation and experimental setup reported by Wang *et al.* (2011). Adapted from Wang *et al.* (2011).

Browne *et al.* (2010, 2012) conducted experimental studies of single-phase and flow boiling heat transfer of submerged circular microjet arrays with a fabricated microdevice, shown in Figure 2.7 (a). Two staggered arrays of seventeen 112-μm diameter microjets were investigated using different nozzle spacings: 360 μm and 230 μm. The refrigerant (R-134a) flow entered into the 200-μm tall, 2-mm wide and 10-mm long chamber as a confined and submerged jet, impinged onto the thin-film square heater (1-mm side) and exited both ends through the 1-mm circular holes, as portrayed in Figure 2.7 (b).

The experimental setup is shown in Figure 2.7 (c). It was composed of a custom built test section (fixture) which housed the microdevice, a gear pump, a turbine flow meter and a by-pass with a needle valve for fine flow rate control. A concentric counter-flow heat exchanger connected to a constant-temperature bath was used to control the system temperature. An electrical preheater was used to set the temperature at the inlet of the fixture. A thin-film heater was used to provide the constant heat flux boundary condition.

(a) Microdevice and test section (fixture)   (b) Microdevice key features

(c) Schematic diagram of the experimental facility
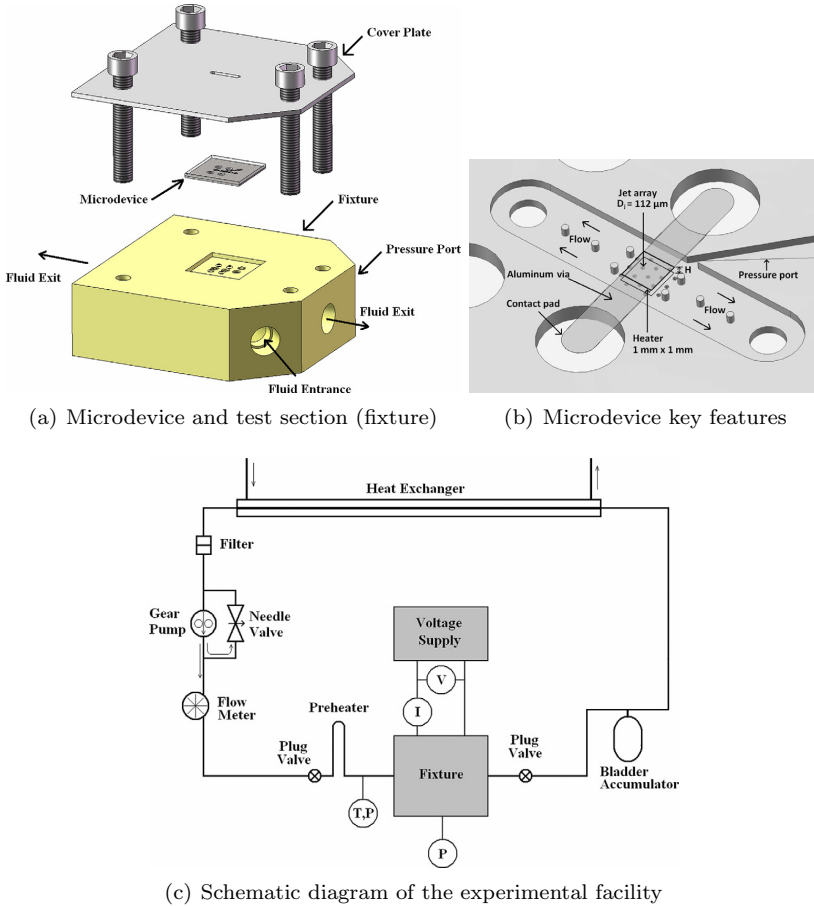
Figure 2.7 – Cooling device and experimental facility presented by Browne *et al.* (2010, 2012). Adapted from Browne *et al.* (2012).

   The authors determined the area averaged heat transfer coefficient for both single-phase and boiling regimes. The single-phase investigation was carried out over specific ranges of Reynolds (3,050 to 10,600) and Nusselt (53.6 to 128) numbers, comparing the results obtained with air and water. The experiments in the boiling regime were conducted for different values of sub-cooling degree (10, 20 and 30℃) and jet velocity (4, 7 and 10 m/s). Boiling enhanced the heat transfer process making possible for the microdevice to dissipate a maximum heat flux of 590 W/cm^2 at a wall superheat of nearly 30℃. Increasing

the jet velocity resulted in an increase of the single-phase heat transfer coefficient, onset nucleate boiling heat flux and overall heat transfer performance. Besides, a higher inlet sub-cooling increased both the heat flux at the onset nucleate boiling and the maximum dissipated heat flux. However, the inlet sub-cooling did not have a strong effect on the wall superheat at which the critical heat flux occurred.

Particularly, Browne *et al.* (2012) found out that nitrogen dissolved in the R-134a did not affect the mechanism behind the surface temperature excursion, which were likely to be dominated by surface roughness and other nucleating stability factors. Although a correlation for the two-phase heat transfer coefficient was proposed, the authors advised that it was not intended for prediction purposes because of the limited database.

Whelan *et al.* (2012) developed and tested a closed-loop liquid cooling system for thermal management of a commercially available CPU. The experimental apparatus was composed of a water delivery and a monitoring system, as well as a heater block and housing. The heater block and housing, shown in Figure 2.8 (a), were designed to emulate an Intel Pentium 4 processor. The processor cooler was a miniature jet array waterblock with an orifice plate containing 49 individual 1-mm jets spaced of 4 mm. As depicted in Figure 2.8 (b), water entered the plenum chamber and passed through the array of jets before impinging onto the upper copper surface (27.5 mm × 27.5 mm) stepped up to 28.7 mm × 28.7 mm at the base.
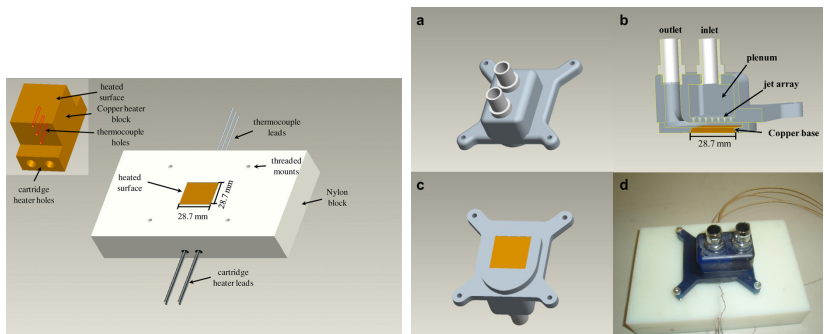
(a) Heater block and housing assembly

(b) Renderings (a - c) and picture (d) of the jet impingement waterblock

Figure 2.8 – CPU thermal management device developed by Whelan *et al.* (2012). Adapted from Whelan *et al.* (2012).

A schematic diagram of the flow loop is presented in Figure 2.9. It was composed of a variable speed pump which draw deionized water from a water reservoir. Water differential pressures and temperatures were measured at the inlet and outlet of the waterblock and heat exchanger. The heat exchanger, which acted as a condenser, consisted of two plastic inlet and outlet plenums and a tube bundle in crossflow with air over its outer surface and hot water flowing on the inside of the tubes. The waterblock was designed to have a small footprint at the board level and the remote heat exchanger was designed to dissipate the required heat load with the smallest volume for the pressure drop constraint.
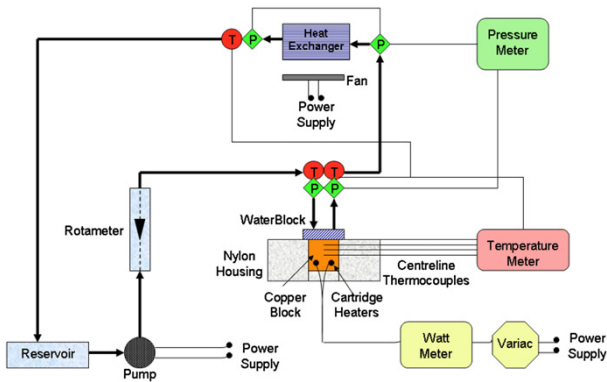
Figure 2.9 – Schematic diagram of the experimental flow loop. Adapted from Whelan *et al.* (2012).

The liquid-based cooling system successfully dissipated the required 200 W with a chip temperature of 65℃ and a waterblock base temperature of 53℃. The overall system thermal resistance decreased from 0.25 K/W at 50 W to 0.18 K/W at 200 W. A similar drop in the system thermal resistance was obtained as the liquid volumetric flow rate was increased from 2.0 to 5.5 L/min.

In addition, a performance comparison was carried out between the jet array waterblock and a commercial waterblock (Danger Den MC-TDX CPU Cooler) for heat loads of 100 W, 150 W and 200 W. The comparison tests were conducted for a nominal inlet temperature of 15℃ to replicate the scenario of data center cooling where the spent flow could be routed to a secondary chilling unit. The jet impingement waterblock demonstrated a considerably better performance than the MC-TDX CPU Cooler because of the lower values of thermal resistance

(60% on average) and the higher values of heat transfer coefficient. However, the proposed CPU cooler experienced pressure drops greater than the MC-TDX CPU Cooler.

Parida *et al.* (2012) proposed an optimized jet impingement heat exchanger, depicted in Figure 2.10, for thermal management of power control units. Power control units are the core component of hybrid systems, such as electric vehicles and hybrid electric vehicles, as they manage the power flow between the electric motor generator, battery and gas engine.

A parametric and optimization study was performed on selected heat exchanger designs. Numerical simulations demonstrated the benefits of adopting special geometrical features such as center walls and angled impingement for better swirl flow and overall heat transfer enhancement. Figure 2.10 presents the heat exchanger geometry that was able to meet the target temperature difference (55℃) between the IGBT device and the coolant as well as the pumping power requirements among several high performance jet impingement designs studied. As shown in this figure, the flow entered the impingement-based cooler from the single inlet, bifurcated into two similar paths and impinged upwardly onto the footprint of the heat sources. Then the flow merged into one single channel and exited the cooler from two outlets.

(a) Flow path

(b) Geometric details
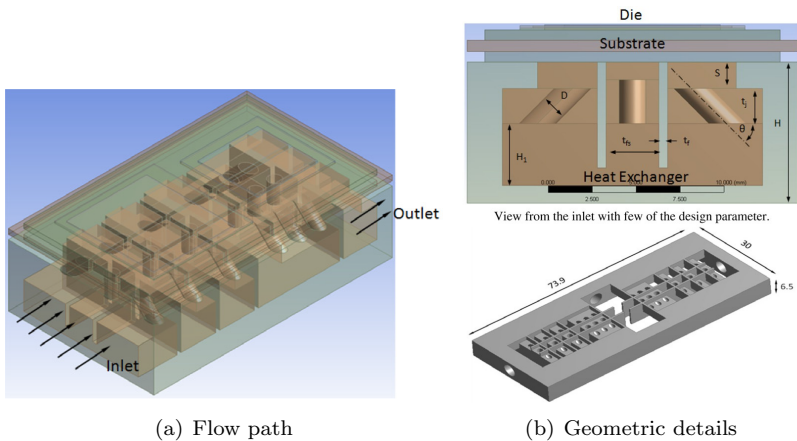
Figure 2.10 – Optimized geometry of the jet impingement heat exchanger proposed by Parida *et al.* (2012). Adapted from Parida *et al.* (2012).

The heat exchanger shown in Figure 2.10 was fabricated and tested under conditions similar to the real application. The cooler was soldered directly to the back side of the single-sided power module and to a bottom cover-plate on the other side. Regulated power was supplied to the heat sources (2 IGBTs and 2 Diodes) to simulate real thermal loads. The experiments were conducted at a various thermal loads ranging from 250 to 650 W. Water at 29℃ with a volumetric flow rate of 1.0 L/min was used as the coolant.

The schematic diagram of the test bed is shown in Figure 2.11. The coolant was heated to the desired temperature in the reservoir. The fluid flow rate and pressure were regulated and monitored before entering the jet impingement cooler. An extra cooler was used to remove the heat added to the coolant by the jet impingement heat exchanger. The temperatures of the coolant, heated surface and other devices as well as the cooler pressure drop were monitored. The proposed cooler was found to perform much better than existing commercial technologies due to lower thermal resistances for the same pressure drop range.
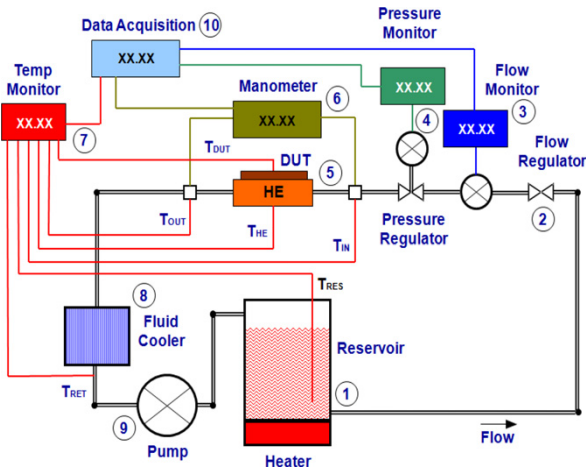
Figure 2.11 – Representation of the experimental setup for cooler performance evaluation. Adapted from Parida *et al.* (2012).

Buchanan and Shedd (2013) studied the thermal behavior of arrays of confined two-phase angled (45°) jets impinging onto a solid square surface. To perform the experimental study, a closed-loop flow facility was built, which is shown in Figure 2.12. The working fluid (R-245fa) was displaced by a gear pump and its mass flow rate was measured with a Coriolis flow meter. A temperature bath equipped

with a temperature controller was used to reject the heat from the system via a heat exchanger inside the refrigerant reservoir.
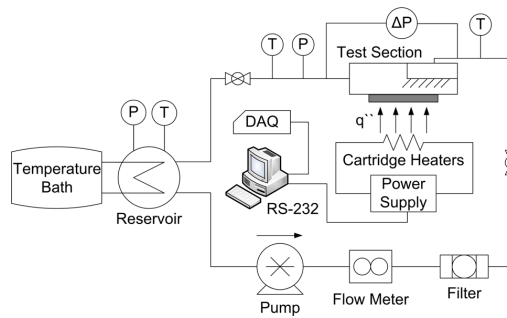
Figure 2.12 – Schematic diagram of the experimental facility studied by Buchanan and Shedd (2013). Adapted from Buchanan and Shedd (2013).
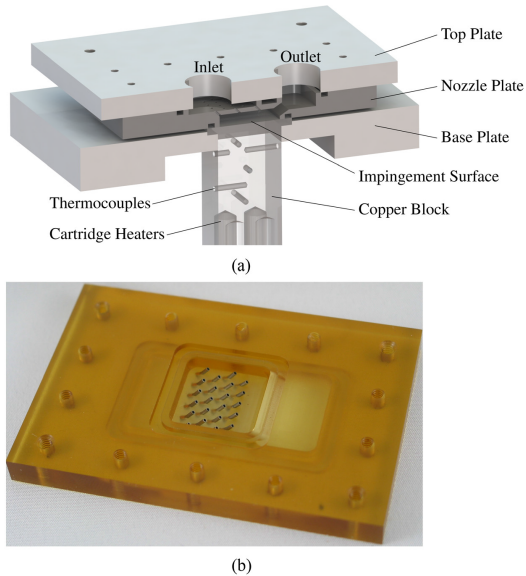
Figure 2.13 – Oblique jet impingement cooler proposed by Buchanan and Shedd (2013): (a) cross-sectional view of the modeled test section and (b) bottom view of a nozzle plate with tubular nozzles installed in a 3 × 3 pattern. Adapted from Buchanan and Shedd (2013).

Figure 2.13 (a) presents a cross-sectional view of the test section composed of a custom nozzle plate clamped on top of the heater between top and base plates. The nozzle plate directed the flow in addition to positioning and supporting the array of 45° oblique jets. The top plate aligned the appropriate inlet and outlet ports, while the base plate supported the heater. Fluid entered from the left side and impinged on the surface of the heater, before exiting to the right. A machined copper block acted as the impingement surface with an area of 3.63 cm^2. Power was provided by a digital DC power supply through four cartridge heaters connected in parallel. Tubular nozzles were cut to length and flared from stainless steel microbore tubing. An example of the nozzle plate with nozzles installed is shown in Figure 2.13 (b).

Four patterns of staggered jet arrays were investigated which were defined by the number of jets (14 to 51) and the spacing between rows and columns (from 2 to 4 mm). The explored values of nozzle length, impingement distance and submerged height ranged from 1.8 to 8.4 mm, 2.3 to 8.9 mm, 3.5 mm and 6.7 mm, respectively. A parametric study was conducted and the relative importance of each parameter changed as the flow transitioned from the single- to two-phase regions.

In the single-phase region, the effects of the jet geometry and the volumetric flux were significant. Increasing the volumetric flux increased the heat transfer performance significantly. Reducing the jet diameter, the number of jets, the impingement distance and the submerged height resulted in a performance increase. In the two-phase region, the inlet fluid temperature and the applied heat flux appeared to govern the heat transfer performance. Overall, the number of nozzles for all four patterns had little influence on the two-phase heat transfer performance.

A heat transfer correlation covering both the single- and two-phase regimes was developed. The model was able to predict the experimental data from the 2848 trials of their study with a mean absolute error of 6.7%. In addition, a new CHF correlation, derived from a pool boiling correlation, was verified to better capture the behavior of the CHF with a mean absolute error of 12%.

Joshi *et al.* (2013a, 2013b), Zhou *et al.* (2014) and Joshi and Dede (2015) carried out an experimental study of a multi-jet two-phase cooler for power electronics aimed at automotive applications. Two jet impingement coolers were evaluated: a multi-device and a single-device. The first one was introduced in the work of Joshi *et al.* (2013a). As depicted in Figure 2.14 (a), the flow entered the test section via an inlet manifold that distributed the coolant to four plenums. Each plenum

ended in a removable jet orifice plate. After passing through the inlet and jet orifices, the coolant impinged on a smooth copper heat spreader and exited the module as a two-phase mixture via four side outlets. An improved version of this multi-device cooler was studied in subsequent works (JOSHI *et al.*, 2013b; ZHOU *et al.*, 2014; JOSHI; DEDE, 2015).

The second cooler, shown in Figure 2.14 (c), consisted of upper, middle, and lower manifold sections in addition to an interchangeable jet orifice plate. Differently from the first version, the inlet and outlet ports of the single-device cooler were located in the upper manifold section. The liquid-vapor mixture resulting from the boiling process was removed via the three-piece outlet manifold, where the sloped and vertical nature of the flow paths took advantage of bubble buoyancy for vapor removal and minimized potential vapor stagnation sites. The experimental facility is shown schematically in Figure 2.14 (d). The coolant (HFE-7100) was first degassed in order to remove non-condensible gases and then it was pumped at a fixed mass flow rate to the inlet of the cooler, where an inline heater was used to set the sub-cooling degree.

Joshi *et al.* (2013a) tested and compared four different types of round jet configurations using the multi-device cooler: a single orifice with 3.75 mm in diameter and three distinct 5×5 jet arrays with orifice diameters of 0.5 mm, 0.6 mm and 0.75 mm - see Figure 2.14 (b) where only three configurations are shown. They reported that the most attractive configuration was the 5×5 array with orifice diameter of 0.75 mm because it showed the same thermal performance and pressure drop as the single jet and also supported higher heat fluxes without reaching the CHF, i.e., 60 W/cm^2 for the single jet configuration.

Based on these results, Joshi *et al.* (2013b), Zhou *et al.* (2014) and Joshi and Dede (2015) investigated the heat transfer performance of the single-device cooler using the 5×5 jet orifice plate. Joshi *et al.* (2013b) tested and compared smooth and finned heat spreaders. Compared to the multi-device cooler, the single-device design reduced the pressure build-up inside the cooler by a factor of 8.43 and promoted an increase of approximately 36% in the effective heat transfer coefficient at 50 W/cm^2 for the smooth heat spreader. As expected, the finned copper heat spreader showed superior single and two-phase heat transfer performance compared to the smooth heat spreader.

Zhou *et al.* (2014) conducted a visualization study of jet impingement boiling under forced convection inside the single-device cooler. An assessment of different regions of the boiling curve via an analysis of the bubble behavior and pressure drop variation at different heat fluxes was carried out.
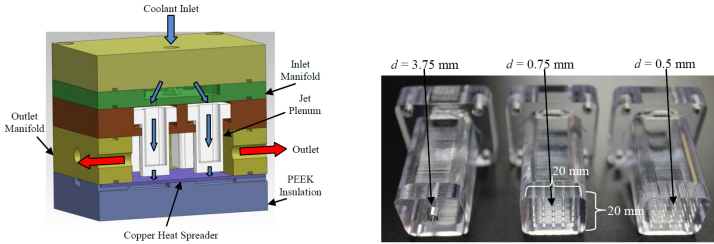
(a) Cross-sectional view of the multi-device jet impingement cooler (half-symmetry model)

(b) Jet orifice plates: single jet (left) and two 5 × 5 jet arrays (center and right)
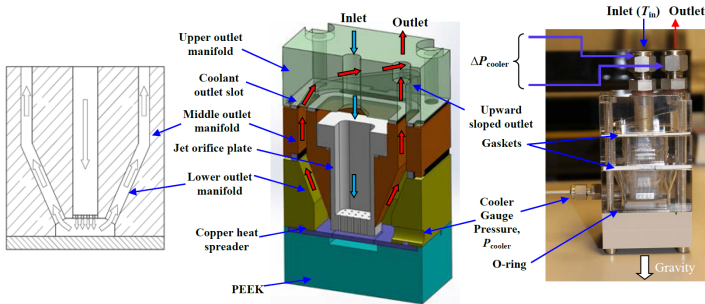
(c) LEFT: Cross-sectional partial view of the sloped vapor outlet flow path; CENTER: Coolant flow path in the single-device cooler; RIGHT: Picture of the single-device cooler
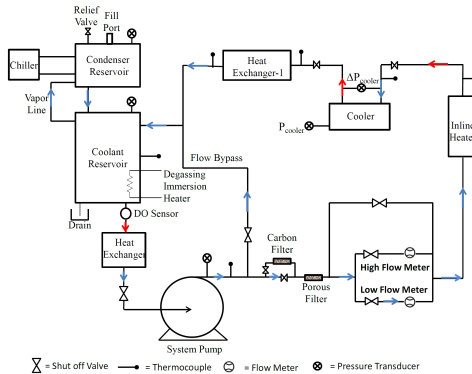
(d) Schematic diagram of the two-phase flow loop

Figure 2.14 – Multi-jet two-phase coolers and test flow loop proposed by Joshi *et al.* (2013a, 2013b). Adapted from Joshi *et al.* (2013a, 2013b).

The cooler heat transfer performance was presented by Joshi and Dede (2015) for the following enhanced target surfaces: (i) smooth pin fins and (ii) three different types of porous coated pin fins, fabricated with varying particle sizes ranging from 10 to 177 μm. The experimental results showed that the cooler performance with the porous coated pin fin surfaces was significantly better as the heat transfer coefficient increased by 79% at a heat flux of 50 W/cm^2 for a surface with a particle size of 75-100 μm. In addition, it was verified that by reducing the inlet sub-cooling from 10 to 5.5 K the two-phase heat transfer performance was further enhanced (by a factor of 1.8). They also reported unique trends in the cooler pressure drop, i.e., a sharp decrease in pressure drop was observed for an increasing heat flux.

Maddox *et al.* (2015) proposed and experimentally evaluated a liquid jet impingement cooling device for thermal management of power electronics, which are present in a variety of vehicles (electric, hybrid-electric and military). The device was developed to be incorporated into the radiator flow loop already present in most vehicles. Thus, the existing infrastructure can be used, which is advantageous from the manufacturing and cost standpoint. Besides, this is also beneficial since the cooling solution is intended to operate under similar flow rate and pressure drop requirements as the other components on the vehicle, using water-based ethylene glycol mixture as the coolant.

The jet impingement cooler, shown in Figure 2.15 (a), had a fixed outer chamber with a smaller inner chamber made of five movable walls. Set screws, located on each of the side walls of the outer chamber, were used to translate the inner chamber to the desired location. Circular jets were produced by a 3 × 3 array of inline, normal-oriented acrylic nozzles with an inside diameter of 3.175 mm and a given extended length from a confining wall, parallel to the impingement surface (copper block). The results presented by Maddox *et al.* (2015) only include jet arrays with a confining wall parallel to the impingement surface. Figure 2.15 (a) shows a jet array with an angled confining wall for better management of the spent fluid.

A schematic diagram of the flow loop is shown in Figure 2.15 (c). The volumetric flow rate of the working fluid (water) was controlled and monitored by a magnetic pump and a turbine flow meter, respectively. A chiller was used to supply chilled water to the heat exchanger and maintain the inlet temperature of the impingement chamber at 30℃. The fluid temperature was measured at the inlet and outlet of the jet impingement cooler.

The temperature readings within the heated block - see Figure

2.15 (b) - were used to calculate the local surface temperature, heat flux, heat transfer coefficient, and Nusselt number as a function of the jet height, nozzle length, and Reynolds number. In addition, experimental 2-D surface maps of temperature, heat flux and heat transfer coefficient were generated by translating the jet array relative to the temperature sensors. The local maximum heat transfer coefficients were observed in the stagnation region for all configurations with secondary peaks occurring halfway between the jets. The authors claimed that by using local measurements of heat flux and surface temperature, the effect of heat losses to the environment on the measured value of heat transfer coefficient was minimized.
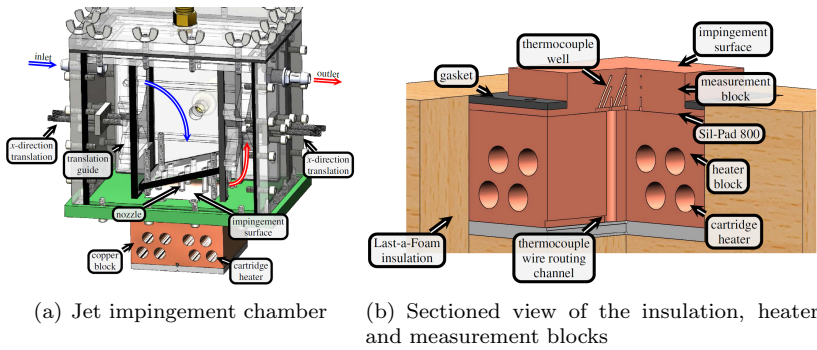
(a) Jet impingement chamber

(b) Sectioned view of the insulation, heater and measurement blocks
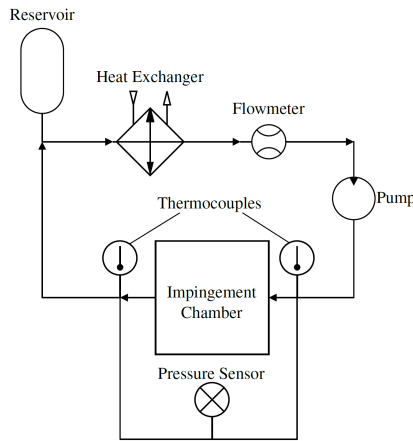
(c) Schematic diagram of the flow loop

Figure 2.15 – Jet impingement cooler and experimental flow loop developed by Maddox *et al.* (2015). Adapted from Maddox *et al.* (2015).

Gould *et al.* (2015) designed, developed and tested a jet impinge-ment-based heat exchanger to cool the base plate of a 600-V/50-A silicon carbide (SiC) power module, whose junction temperature was rated at 175℃. This power module was intended to be used in military hybrid vehicles operating in harsh environments with ambient air at 120℃ and water-ethylene glycol mixture at 100℃ as the only available coolant. The operating parameters were all dictated by real applica-tion requirements. Additionally, the thermal effectiveness of the heat exchanger cooled by jet impingement was compared with conventional cooling techniques, i.e., commercial-off-the-shelf (COTS) heat sink so-lutions such as cold plates and microchannels.

The paper by Gould *et al.* (2015) focused on the optimization of the jet impingement cooling technique by experimentally investigat-ing three different jet arrays and several impingement distances. In order to minimize the cost and complexity of the study and to focus on the thermal problem, experiments were conducted on a test section with resistance heaters mimicking the highest power-dissipating JFET (Junction Field Effect Transistor) components of the module, which dissipated a total of $\approx$ 151 W. A copper heater block coupled with a base plate (8.38 cm^2) was cooled by three devices: (i) COTS cold plate, (ii) COTS microchannel, shown in Figure 2.16 (a), and liquid jet impingement, presented in Figure 2.16 (b).

As depicted in Figure 2.16 (c), the experimental flow loop was driven by a DC gear pump with an adjustable DC power supply. Du-ring each experimental run, the coolant flow rate and the power of the cartridge heaters were set at a desired level. The temperature of the inlet liquid was maintained at 100℃ by setting the preheater at a con-stant input power level and adjusting the flow rate in the secondary cooling loop (water cooling facility into the heat exchanger).

Based on the experimental results of the base plate temperatures, mathematical models were developed to predict the junction tempera-ture of the SiC JFET device. Jet impingement cooling was observed to reduce the thermal resistance by factors of 2.8 and 1.7 compared to COTS cold plate and COTS microchannel, respectively. Among the jet patterns and impingement distances explored, the best cooling performance was obtained for one jet per heat source (SiC JFET and diode devices) impinging at the center of the sources' footprints with an impingement distance equal to the jet diameter, i.e., 200 μm.

Considering the same heat load and coolant flow rate conditions, the optimized jet impingement scheme reduced the device junction tem-perature to 169℃, compared to 290℃ for COTS cold plate cooling and

215℃ for COTS microchannel cooling. Besides, the heat dissipation capability of the module was also increased, i.e., if the device junction temperature was held constant at 175℃, jet impingement cooling enabled the power dissipation to increase to 167 W, which was much higher than 60 W obtained with COTS cold plate and 99 W with COTS microchannel cooler, at a constant volumetric flow rate of 195 cm^3/min.

(a)   COTS
cold plate and
microchannel

(b) Jet impingement cooling module

(c) Experimental flow loop
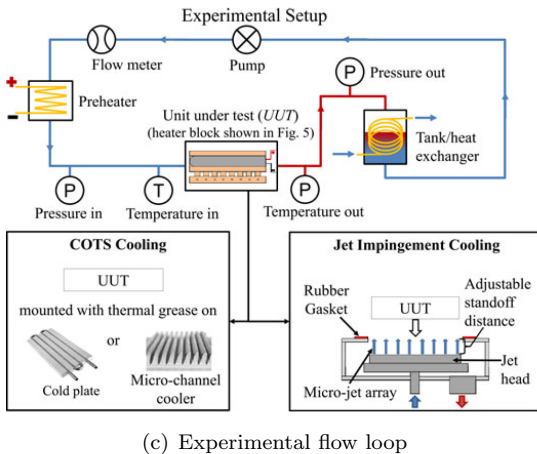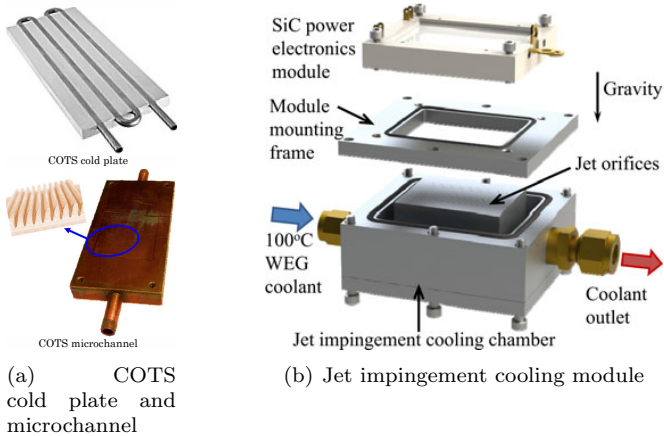
Figure 2.16 – Cooling technologies and experimental flow loop studied by Gould *et al.* (2015). Adapted from Gould *et al.* (2015).

The study of Gould *et al.* (2015) confirmed how poor thermal management is the utmost failure vector for high power electronics.

A number of SiC power modules that were cooled with COTS cold plate failed within 2 to 3 hours of operation during boost mode power conversion. In contrast, the optimized compact jet impingement-based heat sink allowed the power converter to operate for 30 to 50 hours under similar operating conditions. The authors drew attention to the necessity for custom-made cooling solutions for SiC power electronics operating in military hybrid vehicles, since conventional cooling techniques may not be sufficient for such applications.

2.2.2   Hybrid Cooling Devices

Sung and Mudawar (2008a, 2008b) proposed a hybrid cooling scheme for thermal management of high heat fluxes that combined the attributes of two enhanced heat transfer techniques: jet impingement cooling and microchannels. The coolant (liquid HFE-7100) was gradually introduced in the microchannels by slot jets (SUNG; MUDAWAR, 2008a) or circular jets (SUNG; MUDAWAR, 2008b), thus combining the high heat removal capabilities of both cooling techniques while reducing both the axial surface temperature gradient and the high pressure drop of conventional microchannel heat sinks.

Figure 2.17 (a) presents the layered construction and assembly of the test module comprising: a heating block, slot/micro-jet plates, an upper plenum, a lower support plate and 16 cartridge heaters. The slot-jet plate (SUNG; MUDAWAR, 2008a) had five parallel slots of rectangular shape (0.6 mm wide × 1.65 mm deep × 2.94 mm long) whereas the microjet plate (SUNG; MUDAWAR, 2008b), not shown in Figure 2.17 (a), had five parallel rows of fourteen holes (0.39 mm in diameter) drilled equidistantly. In both cases, each row was aligned to impinge fluid along the center line of the microchannels.

Figure 2.17 (b) presents the flow control system used to test the hybrid cooling schemes. The system was composed of a primary circuit for HFE-7100 cooling and a separate low-temperature cooling circuit. The former contained the test module, control throttling valves situated both upstream and downstream of the test module, a reservoir, a centrifugal pump and a Coriolis flow meter. Heat was rejected from the primary coolant to the separate circuit via a heat exchanger in which feedback controls were used to regulate the coolant temperature at the outlet. The coolant was supplied to the test module housing at a controlled volumetric flow rate, pressure and temperature. The thermal performance of the hybrid cooling schemes were tested experimentally for single-phase and two-phase regimes.
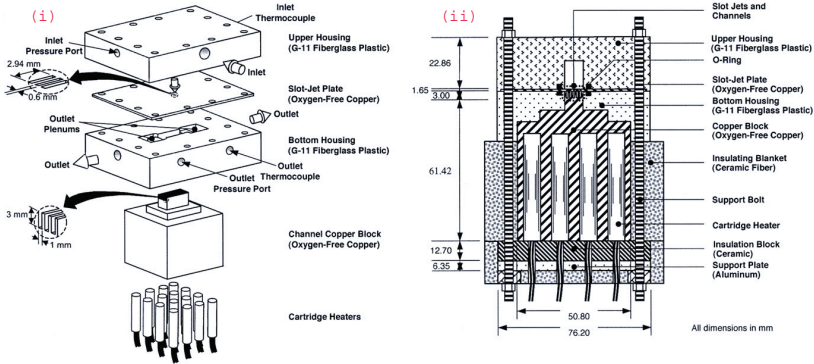
(a) Test module details: (i) construction and assembly, and (ii) cross-sectional view of the assembly
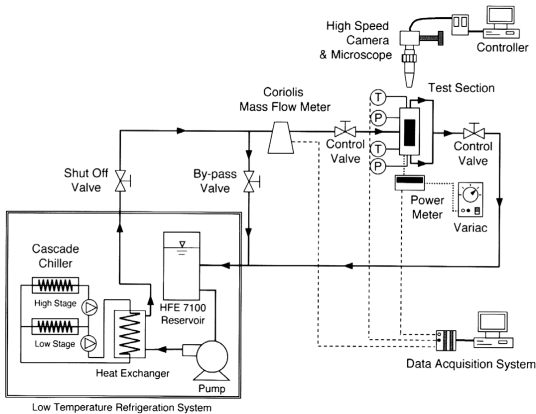
(b) Schematic diagram of the flow loop circuit

Figure 2.17 – Hybrid cooling scheme developed by Sung and Mudawar (2008a, 2008b). Adapted from Sung and Mudawar (2008a).

Using the $k - \epsilon$ turbulence model (VERSTEEG; MALALASEKERA, 1995), a three-dimensional numerical simulation was performed aiming to explore the complex interactions of the single-phase flow inside the cooling module for the reported jet geometries, i.e., rectangular and circular. Sung and Mudawar (2008a, 2008b) verified that jet velocity greatly influences the single-phase cooling performance. At high jet velocities, the cooling performance was dominated by jet impingement and to a much lesser extent by microchannel flow. This happened because high velocity jets more effectively penetrated the axial mi-

crochannel flow and produced strong impingement effect at the wall. Conversely, low velocity jets largely compromised the dominance of jet impingement in the heat transfer process since they were too weak to penetrate the microchannel flow.

In addition, two-phase cooling characteristics were examined regarding to jet velocity and sub-cooling degree and, a correlation for the heat transfer coefficient in the nucleate boiling regime was elaborated, which presented an absolute mean error of 6.1%. The authors reported that the hybrid cooling module was capable of dissipating very high heat fluxes (305.9 W/cm^2 at an inlet temperature-based wall superheat of 110.8℃) even in the single-phase regime. A high degree of surface temperature uniformity was achieved, i.e., the temperature variations were lower than 2℃ for heat fluxes up to 50 W/cm^2 (SUNG; MUDAWAR, 2008a).

This was due to the decrease of the void fraction along the microchannel as the impinging jets contributed to the formation of regions of bubble growth followed by collapse, rather than the continuous bubble growth common to conventional microchannel flow. As already reported by Meyer *et al.* (2006), increasing sub-cooling and/or flow rate delays the onset of nucleate boiling to a higher heat flux and to a higher surface temperature. The critical heat flux was considerably enhanced by the increasing sub-cooling, as the liquid could remove more sensible heat.

In a subsequent investigation, Sung and Mudawar (2009b) evaluated three patterns of microjets using the hybrid cooling scheme previously introduced by Sung and Mudawar (2008b). HFE-7100 was again the working fluid. Each pattern was defined by symmetrical jet-size changes from the center of the microchannel towards the outlet plenum. The examined patterns were: (a) the decreasing-jet-size pattern, (b) the equal-jet-size pattern, and (c) the increasing-jet-size pattern, which are show in Figure 2.18. The performances of the three patterns were compared based on the two-phase heat transfer coefficient, average surface temperature, pressure drop and CHF.

The pressure drop in the two-phase region was the highest for the equal-jet-size pattern and the lowest for the increasing-jet-size pattern. The highest CHF values were achieved with the decreasing-jet-size pattern, as this pattern yielded the highest sub-cooling degree. In addition, a single correlation for phase change heat transfer was proposed considering all the studied jet patterns. In parallel, Sung and Mudawar (2009a) carried out a detailed examination of the CHF behavior of the cooling scheme proposed by Sung and Mudawar (2008b).
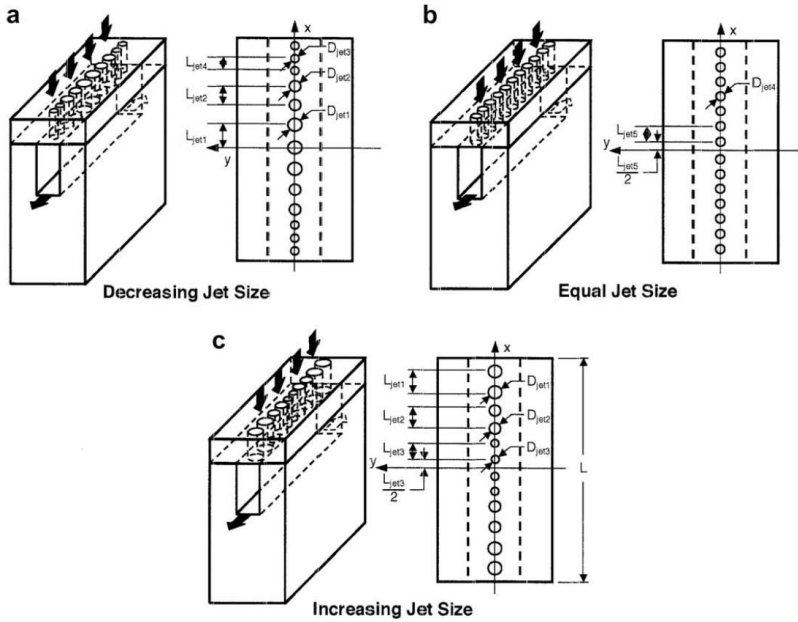
Figure 2.18 – Schematic diagram of an unit cell illustrating the three studied patterns of microjets. Adapted from Sung and Mudawar (2009b).

Barrau *et al.* (2010) experimentally evaluated a hybrid cooling scheme that also involved feeding coolant from a slot jet in a modified microchannel heat sink structure. The design of this cooling module differed from the conventional matrices of impinging jets and also from the hybrid jet impingement/microchannel device proposed by Sung and Mudawar (2008a). Figures 2.19 (a) and (b) present the cooling module and its working principle. The hydraulic circuit used to test the cooling device is shown in Figure 2.19 (c) and provided temperature, pressure and flow rate at the inlet of the cooling module.

In this new design, fluid entered the Plexiglass distributor, located at the top of the heat sink, and was guided by the inlet plenum to the slot located in the symmetry plane of the heat sink (between the two upper plates) and left it through the ends of the channels. Once in the heat sink, the fluid flowed through a series of micro-channels with variable longitudinal distribution. The two outlet plenums collected the liquid leaving the microchannels at the ends of the heat sink.

Although not shown in Figure 2.19, a thermal bath and a heat exchanger may have been used to cool the outlet fluid and maintain the inlet temperature at a desired value. The hybrid cooling scheme was capable to optimize the temperature uniformity of the cooled object, since a global decrease of the temperature of the heat sink in the direction of the fluid flow was verified. The largest heat flux reported was 32 W/cm^2. The single-phase local Nusselt number of this hybrid jet impingement/microchannel cooling scheme (using water as the coolant) was higher than the one reported by Sung and Mudawar (2008a).

(a) Microchannel heat sink

(b) Exploded view of the cooling module

(c) Experimental facility
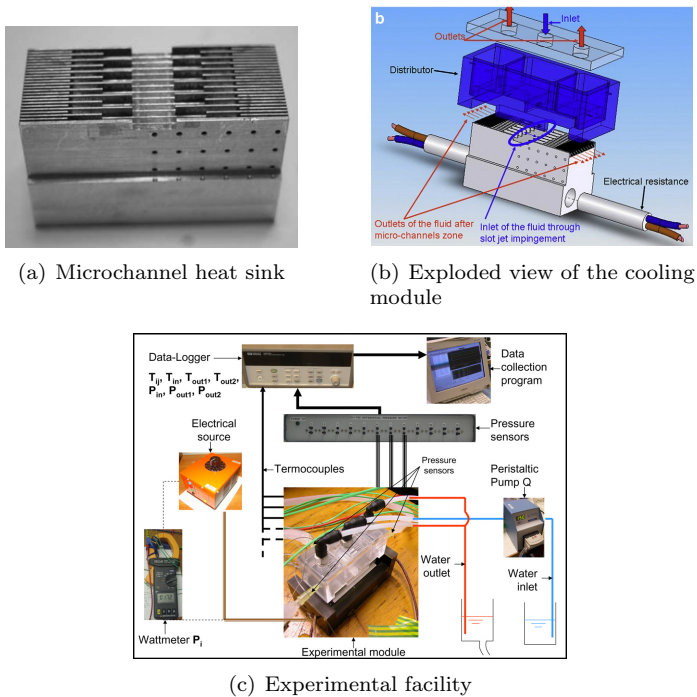
Figure 2.19 – Cooling module and experimental facility developed by Barrau *et al.* (2010). Adapted from Barrau *et al.* (2010, 2012).

Another hybrid microjet/microchannel cooling module was experimentally investigated by Muszynski and Andrzejczyk (2015) - see Figure 2.20 (a). Their study reported the steady-state results for wall temperature and heat flux obtained for single-phase liquid cooling. The nozzles were slots created in a 1-mm thick aluminum plate, which gen-

erate laminar and rectangular microjets of 0.5 mm width covering the
thickness of each channel, as shown in Figure 2.20 (b). The experimen-
tal facility, presented in Figure 2.20 (c), was composed of the cooling
module, fluid supply system, measuring devices and DC power supply.
The pressure was kept constant by a diaphragm tank. Water was fed
by a pulsating gear pump from the supply tank. The fluid flow rate
was controlled with a power inverter and a flow control valve.
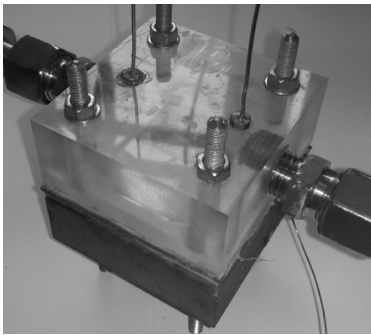
(a) Test module
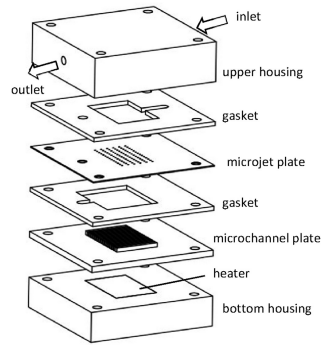
(b) Exploded view of the cool-
ing module
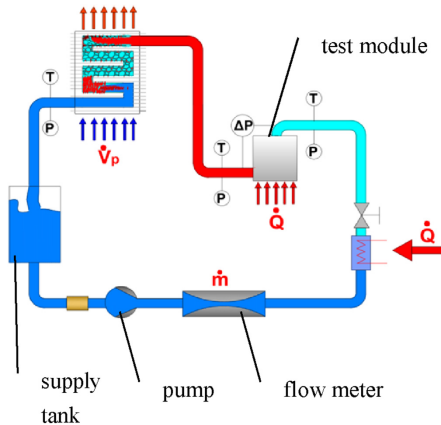
(c) Schematic diagram of the experimental
setup

Figure 2.20 – Cooling module and experimental setup developed by
Muszynski and Andrzejczyk (2015). Adapted from Muszynski and An-
drzejczyk (2015).

The heat transfer coefficient ranged from approximately 2,500 to 2,900 W/(m^{2}K) for heat fluxes (based on the wetted surface area) from around 70 to 180 kW/m^2 and an inlet temperature of 20℃. During the tests, the heater was capable of dissipating up to 240 W. The channel-type confinement enabled the circular jets to be used more effectively by increasing the flow rate over the heater surface, i.e., a 20-mm side brass square. Jet impingement heat transfer was dominant in 90% of the total channel length (20 mm). The performance of the hybrid module was compared with a traditional air cooled heat sink. Although the proposed device performed better since lower temperatures of the heater surface were achieved, unacceptable temperatures (90℃) were reached for heat fluxes (based on the heater area) above 300 kW/m^2.

2.2.3   Spray Cooling Devices

Lin and Ponnappan (2003) investigated the spray cooling of a hot rectangular (1 cm × 2 cm) surface using eight miniature nozzles in a multi-nozzle plate, as depicted in Figure 2.21 (a). Each nozzle had a swirler insert mounted into the multi-nozzle plate. The swirler insert was a hollow disk of 3.18 mm in diameter and 1.0-mm thick with three swirl ports and one central port, both with diameters of 0.2 mm, as shown in Figure 2.21 (b). The liquid jet entered the central port and interacted with the jets coming from the swirl ports generating a swirl flow pattern inside the 60° cone-angled swirl chamber. At the bottom of the swirl chamber, the swirling liquid flowed through the discharge orifice promoting the liquid breakup into fine droplets and the formation of a solid cone with angles larger than 35°. The length and diameter of the discharge orifices were 0.15 mm and 0.25 mm, respectively, and the distance between two adjacent orifices was 5 mm.

The multi-nozzle plate was placed inside a spray chamber (8.8 mm in height × 28.5 mm in length × 17.0 mm in thickness) in an experimental apparatus built to simulate the cooling of high-power laser diodes. The fluid flow was generated by a micro pump. After exiting the spray chamber, the two-phase mixture was sub-cooled in a condenser and pumped again to the liquid chamber according to the flow loop shown in Figure 2.22.

The authors examined the heat transfer characteristics and the effect of non-condensible gases on the performance of the device of Figure 2.22. Visual observations indicated that nucleate boiling was present in all tests, which were conducted using FC-72, FC-87, water and methanol as the working fluids. Results were obtained for several

temperatures, pressure drops (from 0.69 to 3.10 bar) and heat fluxes. The system reached critical heat fluxes up to 90 W/cm^2 for pure FC-87, 490 W/cm^2 for pure methanol and higher than 500 W/cm^2 for pure water. The critical heat flux (CHF) increased with the increase of the volumetric flux or pressure drop. Non-condensible gases had a negative impact on the overall heat transfer of the closed-loop spray cooling system at heat fluxes lower than the CHF due to the higher condensation thermal resistance.

(a) Elements of the orifice plate

(b) Swirler insert (dimensions em milimeters)
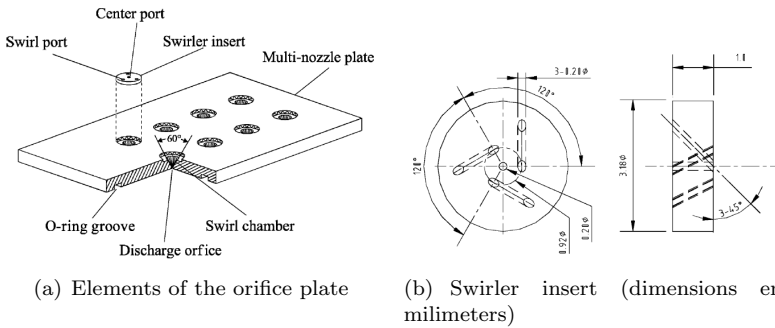
Figure 2.21 – Multi-nozzle plate proposed by Lin and Ponnappan (2003). Adapted from Lin and Ponnappan (2003).
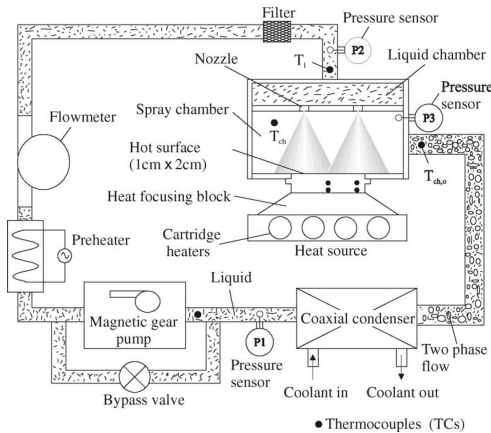
Figure 2.22 – Schematic diagram of the multi-nozzle spray cooler proposed by Lin and Ponnappan (2003). Adapted from Lin and Ponnappan (2003).

Amon *et al.* (2005) developed and tested an integrated evaporative spray cooling device for removing chip heat fluxes over 50 W/cm^2, which was named EDIFICE (Embedded Droplet Impingement For Integrated Cooling of Electronics). The goal was to integrate the chip cooling solution with the chip level packaging using MEMS (Micro Electro-Mechanical Systems) technology, thus offering the possibility of miniaturization and inexpensive batch fabrication. Cooling was performed through the impingement of micron-sized droplets (50 - 100 μm) generated using multiple nozzles manufactured with deep reactive ion etching (DRIE), as shown in Figure 2.23 (a). A schematic of the EDIFICE design is presented in Figure 2.23 (b).

(a) Nozzle geometries

(b) Schematic diagram of EDIFICE and the overall system
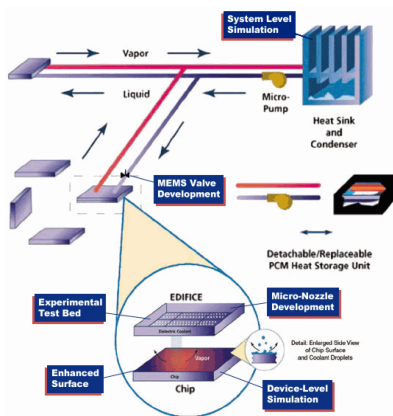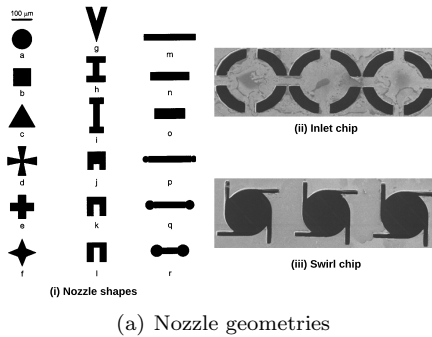
Figure 2.23 – EDIFICE: (a) nozzle geometries and (b) overall system. Adapted from Amon (2003) and Amon *et al.* (2005).

According to the authors, the droplet impingement mechanism avoided temperature overshoot at the onset of nucleate boiling and was efficient in mitigating fluctuations in chip temperature and thermal cycling. The system level arrangement transported the removed heat to a condenser or to a detachable heat storage unit, which contained an organic phase change material. In the case of the condenser arrangement, the vapor generated at the component level was transported through the system to the combined condenser, thereby minimizing thermal resistances offered by multi-material interfaces.

The heat transfer performance of the EDIFICE design was examined with the dielectric coolant HFE-7200 focusing on the influence of the microspray characteristics and surface evaporation. The results included flow visualization of liquid breakup (induced by irregular-shaped micronozzles and swirling) and experiments with microstructured silicon impingement surfaces to enhance fluid spreading and evaporation.

(a) Schematic diagram of the cooling system and swirl silicon nozzle (upper right corner)

(b) Photograph of the EDIFICE test bed
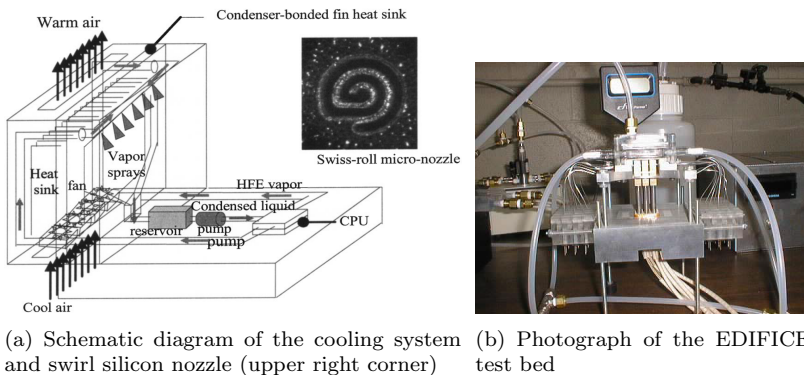
Figure 2.24 – Prototype of an evaporative spray cooling system for notebook PC. Adapted from Amon (2003) and Amon *et al.* (2005).

In addition, a prototype of a notebook PC cooling system was developed, as shown in Figure 2.24 (a). Figure 2.24 (b) depicts the EDIFICE test bed. The spray impingement cooling system was composed of a cooling test bed, a micro diaphragm liquid pump, a coolant reservoir, and a fin-integrated condenser. To provide uniform cooling within the EDIFICE spray chamber, a new swiss-roll nozzle design was proposed, as seen in Figure 2.24 (a). The swiss-roll orifice had a diameter of 460 μm and slot width of 40 μm. A silicon nozzle plate with 737 swiss-roll orifices was fuse bonded with the inlet and swirl chips to provide atomized droplets for the prototype tests. The inlet

sub-cooling of HFE-7200 was about 50℃. The pressure of the cooling chamber was maintained at about 1 atm (saturation temperature of 76℃). At a coolant mass flux of only 33.2 g/(cm^{2}min) an uniform heat flux removal of 45 W/cm^2 was achieved.

Ashwood (2006) and Ashwood and Shedd (2007) presented a comprehensive set of heat transfer data for a spray cooling module operating with single and four-nozzle arrays. The studies focused on five different pure fluids (FC-72, FC-74, FC-40, HFE-7000 and HFE-7100) and their binary mixtures. The experimental facility was provided by Cray Inc. and comprised two integrated sub-systems: the fluid delivery system and the instrumentation system. The former included a chiller, a Coriolis flow meter, a system manifold, a spray cap, a spray plate and a heat exchanger, as illustrated in Figure 2.25 (a). Multiple swirl atomizers for full cone spray generation were custom-designed, manufactured and incorporated into a steel spray plate. Two types of nozzle arrangements were included in the spray plate, as depicted in Figure 2.25 (b): (i) single nozzles located at the corners, and (ii) sets of four nozzle arrays located close to the central region.

The drainage of the upward-oriented spray was gravity assisted. This arrangement was chosen to prevent coolant accumulation (pooling) on the substrate, which is known to significantly decrease the heat transfer performance of impingement cooling in general. The authors found that the heat transfer performance of the mixtures was not poorer than those of the pure substances as is often the case in convective flow boiling. In addition, a dimensional correlation was proposed, which predicted the behavior of the whole database to within 9% mean average error.

Shedd (2007) built and tested a thermal management device based on a new design concept of nozzles for spray cooling. The concept embodied an array of linear sprays directed at the heated surface at approximately 45˚, as shown in Figure 2.26. The nozzles were slots cut at an angle into the wall of a microbore tubing. Small orifices were drilled at the center of the slots to give a controlled, round orifice for spray generation. The atomization process was based on the radial flow of liquid from the slot.

Laboratory tests indicated that these nozzles generated droplets at lower pressure differences than common pressure swirl-atomizers, although the sprays were not as uniform as the commercial ones. Figures 2.27 (a) and (b) illustrate the linear nozzle array cooler and its operation, respectively. Results showed that this new nozzle design reduced the fluid inventory, thus making room for miniaturization.
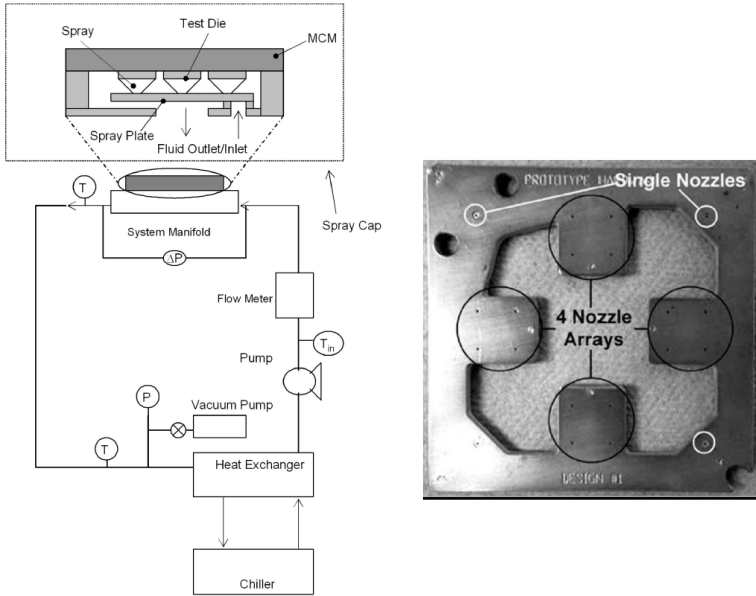
(a) Schematic diagram of the test facil-
ity

(b) Layout of the nozzles on the
spray plate

Figure 2.25 – Experimental facility and cooler details presented by Ash-
wood (2006) and Ashwood and Shedd (2007). Adapted from Ashwood
and Shedd (2007).
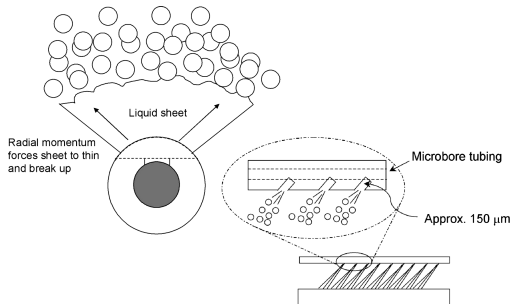
Figure 2.26 – Schematic diagram of the linear nozzle array of sprays
proposed by Shedd (2007). Adapted from Shedd (2007).

(a) Linear nozzle array cooler

(b) Photograph of sprays impinging onto a heated copper block
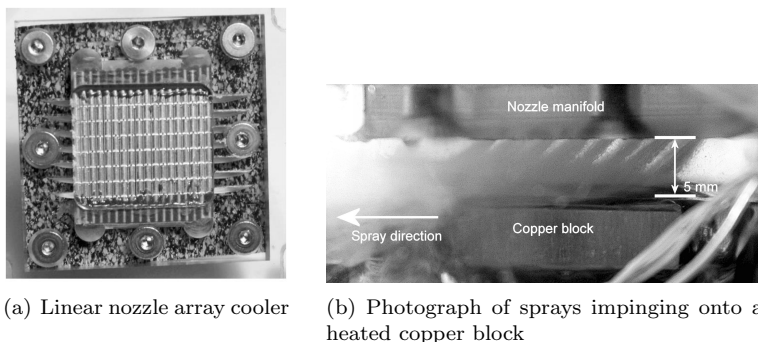
Figure 2.27 – Spray nozzles designed by Shedd (2007). Adapted from Shedd (2007).

2.3   Cooling Devices Integrated with VCRS

Comprehensive reviews of vapor compression refrigeration systems for cooling of electronics and personal cooling have been presented by Barbosa (2011) and Barbosa *et al.* (2012). These works covered a great number of refrigeration system prototypes presenting their components, principal features and main applications, such as computer servers, desktops, notebooks, high-power electronics, etc. R-134a was by far and large the most widely used refrigerant in electronics and personal cooling applications because of its non-flammability, non-toxicity, low cost and compatibility with many products and parts already available in the market.

Regarding the system components, the types of compressor reported in the reviewed studies are: rotary, reciprocating, scroll, linear and diaphragm double-cavity capacitive. For the expansion devices, capillary tubes and orifices were the preferred choice. Air-cooled heat exchangers were the most employed condenser type followed by air-cooled micro-channels and polymeric micro-channels. The most common evaporator/heat sink types were copper cold plates, copper coils, parallel microchannel cold plates, and metallic and polymeric microchannels.

Other recent research papers confirmed the applicability of cold plate evaporators and microchannel heat sinks in electronics and personal cooling, as demonstrated by Jin *et al.* (2011), Wu and Du (2011), Park *et al.* (2011), Park and Yang (2013) and Mancin *et al.* (2013), who developed cold plate evaporators, and Chang *et al.* (2010), Mar-

chinichen *et al.* (2013), Lamaison *et al.* (2014), Sung *et al.* (2014), He *et al.* (2015), Türkakar and Okutucu-Özyurt (2015) and Yuan *et al.* (2015) who made used of microchannel heat sinks.

Several small-scale compression technologies based on different compression mechanisms (rotary, reciprocating, linear, etc.) have been investigated in the open literature. However, a clear-cut decision has not yet been reached as to which working principle is the best for electronics cooling. Special attention has been devoted to the development of linear compressors for miniaturized refrigeration applications (UNGER; NOVOTNY, 2002; BAILEY *et al.*, 2009; WANG; TAI, 2010; BRADSHAW *et al.*, 2011; TAKEMORI; FAGOTTI, 2012; BRADSHAW *et al.*, 2013a, 2013b; LIANG *et al.*, 2014a, 2014b, 2014c). The main advantages of linear driving mechanisms are: (i) reduced frictional losses in comparison to conventional reciprocating compressors (due to the absence of a crank mechanism to drive the piston), (ii) oil-free operation, which improves the thermal performance of the condenser and evaporator, (iii) smaller motors due to operation at a resonant frequency and (iv) gravity-independent operation (BRADSHAW *et al.*, 2011; BARBOSA JR. *et al.*, 2012).

Based on the findings of Barbosa (2011) and Barbosa *et al.* (2012), mechanical vapor-compression refrigeration systems seem to be a viable technology for application in electronics cooling. Nevertheless, there are a number of technical challenges that need to be overcome to make the technology widely available in the market, such as: (i) reliability and high efficiency of the small-scale compressor, (ii) availability at low cost, (iii) moisture condensation management in the heat sink region, (iv) ability to handle varying workloads, power dissipation surges and fast transients, and (v) reduced noise and vibration. Despite the reported advances, more detailed experimental data are needed to allow a comprehensive evaluation of the sources of thermodynamic losses in each component of the system, more notably the heat sink/evaporator and the compressor. As observed by Barbosa *et al.* (2012), only a very limited number of authors have fully characterized the thermal behavior of their systems (through measurements of operating parameters) to a point where a full thermodynamic performance evaluation could be executed.

As far as the direct liquid cooling techniques are concerned, few investigations have focused on their integration with vapor compression refrigeration systems. The existing reported works have employed exclusively spray cooling and come from three research groups in the Far East: (i) Yan *et al.* (2010a, 2010b, 2010c) and Tan *et al.* (2013),

(ii) Chunqiang *et al.* (2012) and Xu *et al.* (2014), and (iii) Hou *et al.* (2015) and Chen *et al.* (2015).

Yan *et al.* (2010a, 2010b, 2010c) investigated a closed-loop spray cooling system for thermal management of high power electronics. The experimental facility was composed of a spray chamber integrated with a modified vapor compression refrigeration system, which used R-134a as the working fluid. The developed VCRS consisted of an oil-free compressor, a condenser, an expansion valve, a liquid-vapor separator and auxiliary devices to control the flow conditions, as illustrated in Figure 2.28 (a).

(a) Schematic diagram of the VCRS

(b) Spray configuration tested by Yan *et al.* (2010a)

(c) Spray configuration tested by Yan *et al.* (2010b)
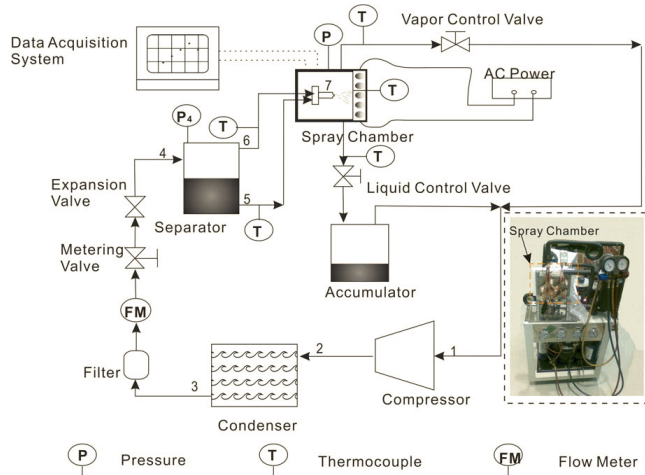
(d) Spray configuration tested by Yan *et al.* (2010c)
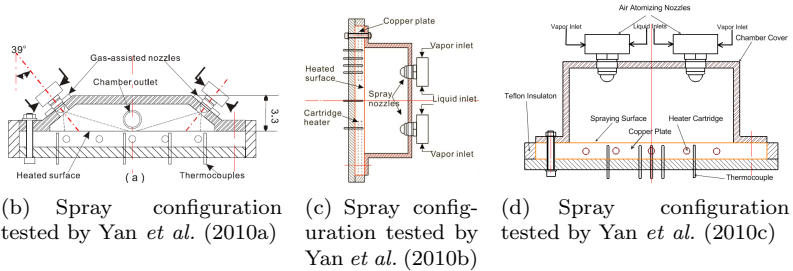
Figure 2.28 – Modified vapor compression refrigeration system and spray configurations tested in the works of Yan *et al.* (2010a, 2010b, 2010c). Adapted from Yan *et al.* (2010a, 2010b, 2010c).

A brief description of the system operation is as follows: at point 1, refrigerant vapor at low pressure entered the compressor from the accumulator and the outlet of the spray chamber. At point 2, superheated vapor exited the compressor and passed through the air-cooled condenser dissipating heat to the surroundings. Saturated or sub-cooled refrigerant exited the condenser at point 3 and partially expanded through a thermostatic expansion valve reaching the phase separator (point 4). The expansion was controlled to guarantee that the pressure in the phase separator was higher than the pressure in the spray chamber. At points 5 and 6, liquid and vapor phases were separated and conducted to the spray nozzles which used the vapor flow to enhance atomization. After absorbing heat from target surface, the vapor was returned to the compressor while the spent liquid was first drained into the accumulator and then cycled back to the compressor (after vaporizing) for the next cycle.

Four vapor atomizing spray nozzles were installed in the spray chamber to cool a 1-kW heated copper plate, which simulated a 6U electronic card (23.3 cm × 16.0 cm) employed in a typical Air Transport Rack chassis (19.4 cm in height × 31.8 cm in length × 25.7 cm in width) under typical working conditions. Two heat transfer areas were tested, i.e., 12.3 cm × 15.5 cm (YAN et al., 2010a) and 13.5 cm × 15.1 cm (YAN et al., 2010b, 2010c). Besides, three spray configurations were explored: (i) sprays angled of 39°; (ii) horizontal sprays impinging on a vertically-oriented heater block; and (iii) vertically downward-oriented sprays, as shown in Figures 2.28 (b), (c) and (d), respectively.

The experimental analysis focused on the effects of mass flow rate, nozzle inlet pressure and spray chamber pressure. It was found that the cooling performance improved with increasing mass flow rate, nozzle inlet pressure and spray chamber pressure, whereas the uniformity of the heated surface temperature could only be improved with higher mass flow rate and nozzle inlet pressure. Increasing the mass flow rate promoted the intensification of forced convection and nucleation site density on the heated surface due to an increase of the spray velocities and the droplet flux, respectively. Besides, increasing the nozzle inlet pressure resulted in better atomization.

The use of inclined sprays enabled the design of a more compact spray chamber since a reasonable coverage area could be obtained with this configuration compared to that required by a normal spray chamber (YAN et al., 2010a). The heated surface was maintained at a stable average temperature below 20℃ (YAN et al., 2010a) and 25℃ (YAN et al., 2010b, 2010c), with a maximum temperature variation of about 2℃

under suitable operating conditions. Heat transfer coefficients up to 5,596 W/(m^{2}K) were achieved for a heat flux of around 5 W/cm^2 (YAN *et al.*, 2010b).

In a subsequent paper, Tan *et al.* (2013) investigated the thermal performance of a new multi-nozzle plate using the same closed-loop spray cooling system developed by Yan *et al.* (2010a, 2010b, 2010c). The nozzle plate (1.9 mm in thick) comprised six miniature jet-swirl nozzles, covering a target area of 1 × 2 cm^2 and was distant 8.8 mm from this area. The input heat flux and the differential pressure across the nozzle plate ranged from 35 to 165 W/cm^2 and from 3.87 to 4.74 bar, respectively. Steady-state temperatures at a particular heat flux were measured over a range of flow rates to analyze the thermal performance of the multi-nozzle plate spray cooling. The highest heat transfer coefficient was 39,000 W/(m^{2}K) at a heat flux of 145 W/cm^2, with a surface temperature of 48℃. The critical heat flux was around 165 W/cm^2. An empirical dimensionless expression was proposed to correlate the relationship between the heat flux in the nucleate boiling regime and the wall superheat degree.

Chunqiang *et al.* (2012) integrated a spray chamber for liquid atomization with a vapor compression refrigeration circuit. The spray chamber comprised a single full-cone pressure nozzle (spray cone angle of 60˚) and a circular copper surface of 1.13 cm^2. The VCRS, portrayed in Figure 2.29, was composed of a variable speed oil-lubricated rotary compressor, a water-cooled condenser, a receiver and other accessories. The throttling device and the evaporator were replaced by the pressure nozzle and the spray chamber. Although the authors claimed that the pressure nozzle was fully responsible for throttling and atomizing, the refrigerant experienced a pre-expansion in expansion valve B - see Figure 2.29. Isobutane was the refrigerant of choice.

The VCRS operated as follows: the high-pressure liquid exiting the condenser entered the receiver and, from there, into the spray chamber through expansion valve B. Full atomization took place in the nozzle. Downstream of the spray chamber, the two-phase mixture entered the gas-liquid separator, before returning to the compressor as superheated vapor. The expansion valve A and the sub-cooler were used to adjust the sub-cooling degree whereas the refrigerant state at the nozzle inlet was regulated by expansion valve B.

The heat transfer performance of the system was investigated by adjusting the nozzle inlet pressure, the evaporation pressure and the sub-cooling degree at nozzle inlet. The results revealed that for a heat flux of 60 W/cm^2, the heat transfer coefficient was higher than

30,000 W/(m^{2}K). The surface temperature was 31.5℃ at the CHF, i.e., 110 W/cm^2, which corresponded to a cooling capacity of 124.5 W. For a combination of fixed nozzle inlet pressure (3.9 bar), evaporating pressure (1.8 bar) and heat flux (72 W/cm^2), the experimental results showed that the optimal sub-cooling degree was 5.8℃.
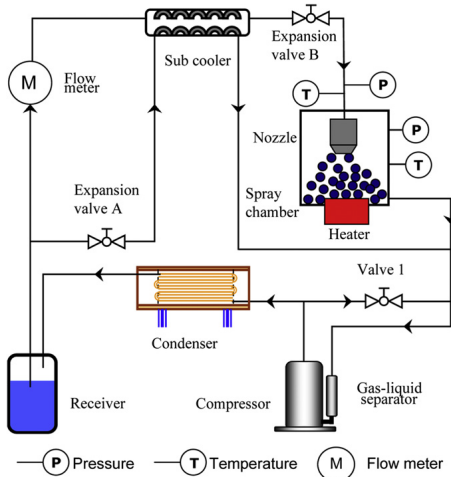
Figure 2.29 – Spray-integrated vapor compression refrigeration system proposed by Chunqiang *et al.* (2012). Adapted from Chunqiang *et al.* (2012).

More recently, Xu *et al.* (2014) modified the vapor compression refrigeration system of Chunqiang *et al.* (2012). In addition to the parametric study conducted by Chunqiang *et al.* (2012), the influence of other parameters (mass flow rate and heat flux) on the system heat transfer performance was explored. For a refrigerant mass flow rate of approximately 6.9 kg/h, the surface temperature was kept at 57.3℃ with a heat flux of 145 W/cm^2. Heat transfer coefficients up to 35,000 W/(m^{2}K) were achieved for specific conditions. The surface temperature uniformity was influenced mainly by the mass flow rate, heat flux and nozzle inlet pressure; its standard deviation was less than 4.0℃.

Hou *et al.* (2015) developed a R-134a closed-loop spray refrigeration system. As shown in Figure 2.30, the refrigerant flow loop was composed of a rotary compressor, a reservoir, a water-cooled condenser, a water-cooled evaporator and the spray chamber. After compression (11-1) and condensation (1-2), the refrigerant temperature at the nozzle inlet (first liquid stream) was controlled by the sub-cooling system and

by the electric heater (3-4-5). The second stream through the bypass (3-8-9) was used to change the system flow rate measured at the flow meter (5-6). After impinging on the target surface (with ≈ 2.0 cm^2), the first R-134a stream was mixed with the second stream at the evaporator (9-10) inlet. A reservoir (10-11) was used for phase separation before the refrigerant returns to the compressor. A secondary vapor-compression refrigeration unit was employed as a sub-cooling system to condition the refrigerant at the inlet of the test section.
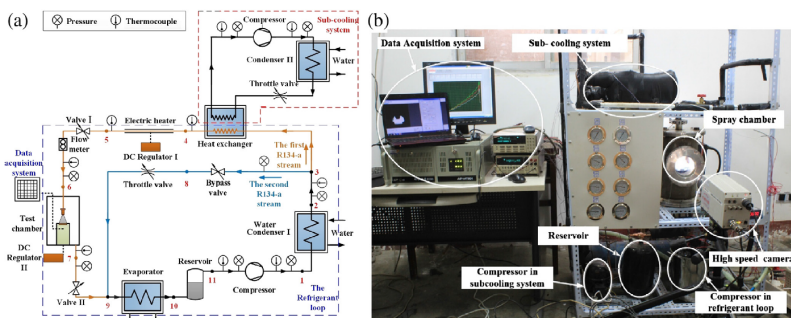
Figure 2.30 – R-134a spray cooling refrigeration system developed by Hou *et al.* (2015): (a) schematic diagram and (b) photograph. Adapted from Hou *et al.* (2015).

The experiments focused on the influence of the volumetric flow rate on the spray cooling characteristics. The boiling curve and the heat transfer coefficient were evaluated for different flow rates. The results showed that a larger volumetric flow rate enhanced the heat transfer performance for a given wall superheat as well as prevented dry-out at high heat fluxes. The CHF increased linearly with the flow rate. Its maximum value was 117.2 W/cm^2 with a target surface temperature of 46℃ for a volumetric flow rate of 0.356 L/min. The efficiency of the spray cooling increased with the wall superheat and decreased with the volumetric flow rate, indicating that simply increasing the flow rate was not a strategic way to improve the heat transfer performance.

Chen *et al.* (2015) compared the thermal performances of R-22 and R-134a using two closed-loop spray cooling test rigs (VCRS). Regarding the R-134a system, the same experimental facility reported by Hou *et al.* (2015) was used. The experimental setup for R-22 is presented in Figure 2.31. It operated similarly to the R-134a system, except for some differences regarding the sizes of some components, control elements and metering equipment.
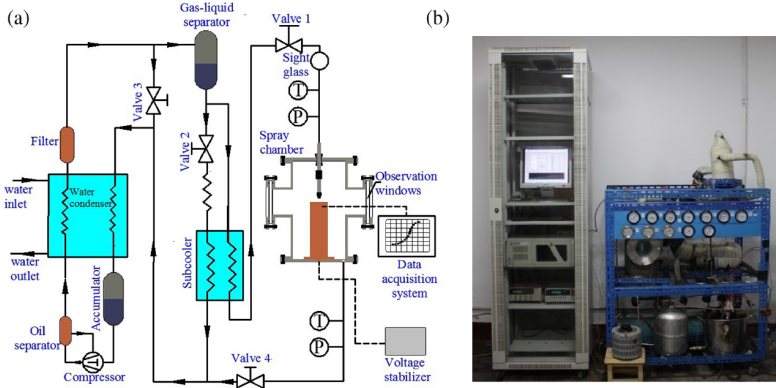
Figure 2.31 – R-22 spray cooling refrigeration system studied by Chen *et al.* (2015): (a) schematic diagram and (b) photograph. Adapted from Chen *et al.* (2015).

Parameters such as critical heat flux, heat transfer coefficient and target surface temperature were compared for the same spray nozzle (commercial full cone nozzle with 0.46 mm in diameter) under similar operating conditions. In order to operate with the target surface totally covered by the spray, the spray height was set as 13 mm and 22 mm for the R-134a and R-22 systems, respectively. The CHF of R-134a spray was lower due to the lower latent heat. The heat transfer coefficient of R-22 spray was higher than that of R-134a spray for the same spray chamber pressure. However, the authors claimed that R-134a spray cooling is still expected to replace R-22 spray cooling in the phase change region when the heat flux requirements are less than 80 W/cm^2.

2.4   Summary and Contributions

Based on the present state-of-the-art review, it is possible to perceive that the majority of the existing direct liquid cooling-based devices did not operate integrated with mechanical vapor compression refrigeration systems. The few exceptions introduced in the previous section made use only of spray cooling as the heat transfer technique and did not devote specific attention to the miniaturization aspect of the application, either by using a small-scale compressor or by designing a truly compact cooler unit. Except for the researches carried out by Yan *et al.* (2010a, 2010b, 2010c) and Tan *et al.* (2013), the other

reported refrigeration systems used oil-lubricated compressors with R-600a, R-134a and R-22 as refrigerants. Besides, ancillary expansion valves (YAN *et al.*, 2010a, 2010b, 2010c; TAN *et al.*, 2013; CHUNQIANG *et al.*, 2012; XU *et al.*, 2014) and evaporators/wounded tubes (HOU *et al.*, 2015; CHEN *et al.*, 2015) were needed to properly operate the active cooling system.

As far as the present author is aware, an active cooling system that integrates two-phase impinging jets and mechanical vapor compression refrigeration has not yet been reported in the literature. As a heat transfer strategy, two-phase impinging jets offer the advantage of combining micro-orifices as the expansion device and the evaporator/heat sink into a single unit. The full potential size reduction is illustrated by the usage of a small-scale oil-free compressor.

The review also revealed that the papers which presented direct liquid cooling solutions integrated with vapor compression refrigeration did not quantify the thermodynamic performance of their systems. Thus, it has not been possible to quantify, from a thermal systems engineering perspective, the advantages of using the proposed active cooling systems in comparison with simpler approaches, i.e., passive techniques or simply liquid circulation.

With the above points in mind, the three main contributions of the present thesis to the state of the art can be listed as follows:

1. The design, development and experimental characterization of an innovative thermal management solution, i.e., a two-phase jet heat sink capable of dissipating high heat loads and of providing full expansion required by the refrigerant;

2. The design and development of a small-scale vapor compression refrigeration system in which the novel jet heat sink can be integrated;

3. The presentation of a detailed thermodynamic performance evaluation for the proposed active cooling system.

3   *Experimental Apparatus*

This chapter addresses the design of the experimental apparatus built for testing the two-phase jet heat sink. Because of the complexity of the fluid flow and heat transfer phenomena occurring inside the jet cooler and their connection with some operating parameters of the refrigeration system, experiments are the most straightforward and reliable way to evaluate the performance of the proposed electronics cooling device. First, the design principles are presented, followed by a detailed description of the experimental facility and its sub-systems. Particular attention is dedicated to the presentation of the concept and design details of the two-phase jet heat sink, i.e., the test section and the small-scale compressor calorimeter. At last, additional aspects such as thermal insulation, leakage tests and the procedure for the experimental runs are reported as well.

3.1   Design Guidelines

The experimental apparatus and the test section in particular were designed according to the following guidelines:

- Simplicity, to facilitate the manufacturing, assembling and disassembling of the two-phase jet cooler. Besides, regarding the refrigeration system, the effectiveness of setting and varying its operating parameters is directly related to a simple design concept and layout;

- Modularity, to make it easy to assemble, disassemble, repair and make changes in a particular sector of the experimental facility without having to interfere with the remaining sectors (modules);

- Versatility, to enable the application of different types of compressors as well as commercial and laboratory-scale solutions for

electronics cooling using the same active cooling system. This also allows performing comparative experimental investigations between different competing technologies under the same operating conditions;

- Compactness, resulting in an active cooling system as small as possible. However, there must be enough space for access to tubing, connections and equipment. Moreover, since the proposed refrigeration system is still a laboratory-scale research device, the existing valves, hydraulic connections and instrumentation add a significant volume to the system, which would not be the case in a prototype or in a commercial application;

- Robustness, particularly with respect to the instrumentation, as temperature, pressure, flow rate and power transducers have been installed to perform a complete characterization of the refrigeration system. In addition, robustness concerning variable control strategies was also pursued during the design stages.

3.2   Description

The experimental apparatus built for testing the performance of the two-phase jet heat sink is an active cooling system which employs mechanical vapor compression refrigeration. It was designed to investigate the cooling performance of two different electronics thermal management solutions operating independently (but not simultaneously) under a variety of experimental conditions. The apparatus is composed of four sub-systems as follows:

- Sub-system 1: the primary cooling circuit;

- Sub-system 2: the secondary cooling circuit or the chiller circuit;

- Sub-system 3: the electrical and electronic circuit;

- Sub-system 4: the instrumentation, data acquisition and control devices.

Each sub-system is presented in detail in the following subsections.

3.2.1 Sub-systems 1 and 2: Primary and Secondary Cooling Circuits

A schematic diagram of the experimental apparatus is presented in Figure 3.1. The primary cooling circuit is the main sub-system of the test facility, i.e., the vapor compression refrigeration system that operates with pure refrigerant R-134a (Sub-system 1). It is composed of two small-scale compressors, a compact condenser, two separate evaporation circuits, and a purpose-built calorimeter for the miniature compressors. AISI 316 stainless steel tubes (6.35-mm outer diameter), hydraulic connections, two- and three-way ball valves and filters are used to connect the aforementioned components.
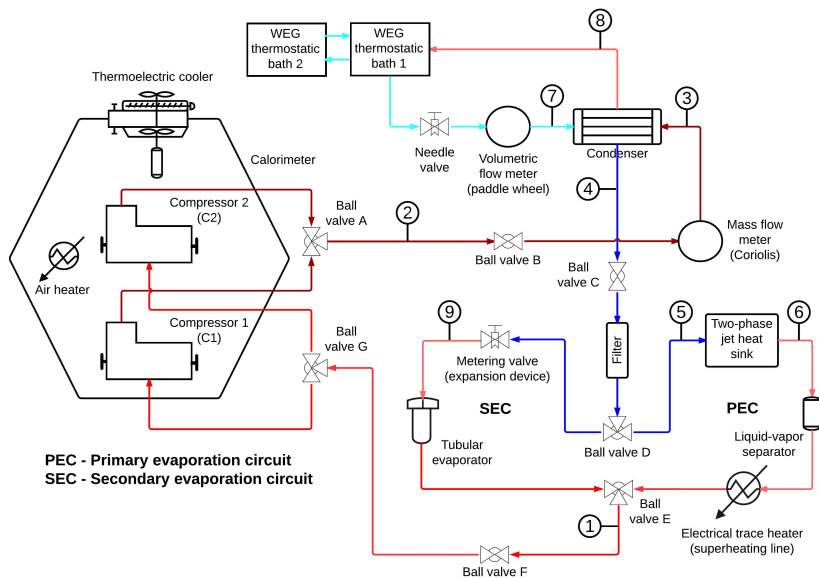
Figure 3.1 – Schematic representation of the experimental apparatus.

A theoretical representation of the test facility refrigeration cycle is shown in the P-h diagram portrayed in Figure 3.2. For illustration purposes, an isentropic compression process is supposed between points 1 and 2. In addition, an isenthalpic expansion is assumed between points 4 and 9 and an adiabatic flash is considered inside the two-phase jet heat sink, i.e., between points 5 and 5' (which corresponds to the orifice exit). Processes 2 – 3 and 4 – 5 are the pressure drops at the Coriolis mass flow meter and at the filter, respectively.
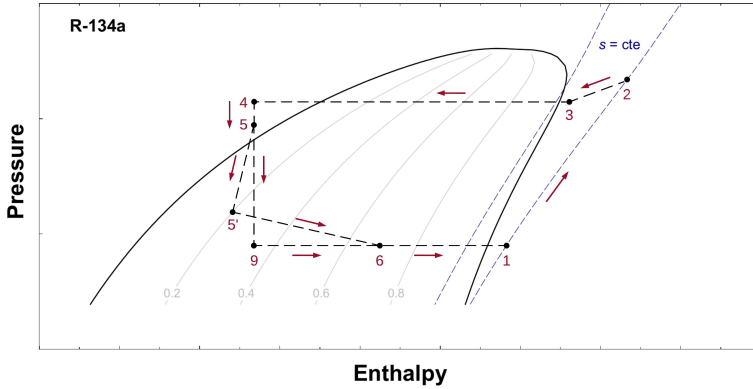
Figure 3.2 – *P-h* diagram of the test facility (schematic representation).

A small-scale oil-free linear motor compressor is used (0.27 cm^3 maximum volumetric displacement, 340 Hz operating frequency, 1.3 kg total weight). The linear motor is an electromagnetic actuator operated via an electronic control unit (frequency inverter) that allows the motor to control the volumetric displacement, i.e., the piston stroke. It was developed by Embraco and designed to operate with R-134a at high back-pressure (HBP) and medium back-pressure (MBP) applications. Figure 3.3 presents the compressor and its basic dimensions.
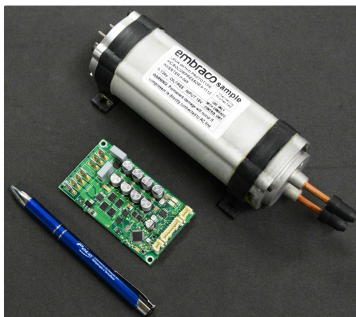
(a) Compressor and electronic control unit
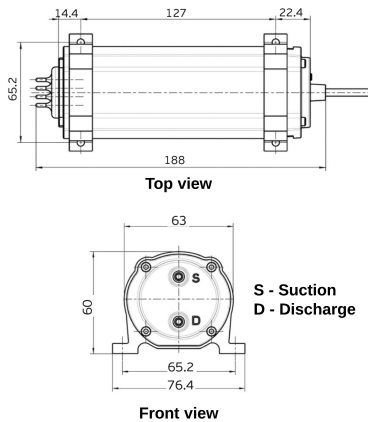
(b) Basic dimensions (in milimeters)

Figure 3.3 – Small-scale linear compressor: (a) photograph and (b) basic dimensions. Note: dimensions are reported by the manufacturer.

Two compressors are installed in the experimental facility to broaden the ranges of the refrigerant mass flow rate and cooling capacity in the tests. Besides, a spare compressor is particularly useful in case of failure, as the tests can be readily continued without having to evacuate the entire refrigeration loop for the damaged compressor to be replaced.

The experimental apparatus was designed to operate with a single compressor or with the two compressors simultaneously. However, in the present thesis, all experimental tests were run using a single compressor. The compressors are positioned inside a purpose-built calorimeter to determine the heat dissipation rate through the compressor shell.

A brazed plate counter-flow heat exchanger is used as the condenser due to its special features such as high effectiveness, compactness, flexibility for the desired heat load and low pressure drop. The thermal design method proposed by Lee (2010) and the optimization routines of EES (KLEIN, 2004) were used to select a condenser as compact as possible capable of fulfilling the mass flow and heat transfer rates requirements and constrains. The selected condenser external dimensions are 154 mm in length × 74 mm in width × 32 mm in height (GEA Heat Exchangers - Model M12-10L2G2).

Although air-cooled condensers might be a more suitable choice in real applications, a liquid-cooled condenser was used in the present test apparatus to facilitate the evaluation of the system performance under different operating conditions, particularly the hot reservoir (ambient) temperature, without having to alter the room temperature, which would be disadvantageous for the calorimeter operation.

After the condenser, the refrigerant passes through a porous filter (15 micron pore size) before reaching the three-way ball valve D, shown in Figure 3.1. This prevents clogging of the nozzles inside the test section. Ball valve D directs the refrigerant to either the primary or the secondary evaporation circuits.

Figure 3.4 presents the primary and secondary evaporation circuits. The former comprises the two-phase jet cooler (the test section), the liquid-vapor separator (suction-line accumulator) and the superheating line, as shown in Figure 3.5. The high-pressure liquid from the condenser flows through the jet cooler, expanding in the nozzle(s) and impinging vertically at the center of the top surface of a heated cylindrical copper block. Thereafter, the two-phase mixture exiting the jet cooler is directed to the liquid-vapor separator, i.e., a 150-ml AISI 316 stainless steel cylinder positioned below the test section.
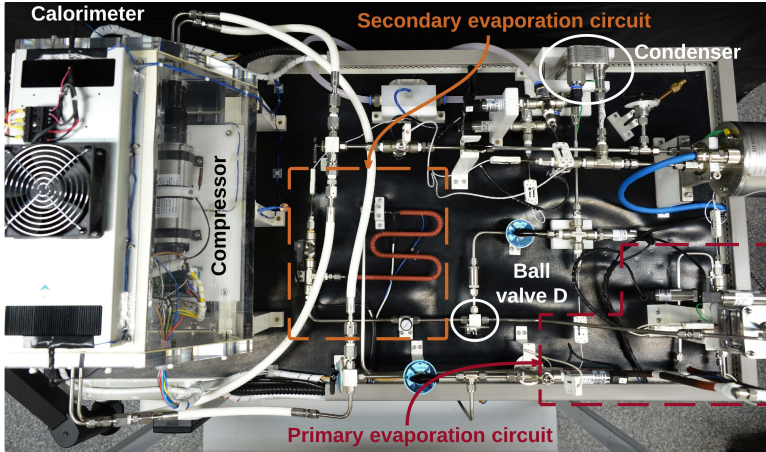
Figure 3.4 – Top view of the experimental apparatus focusing on the primary and secondary evaporation circuits.
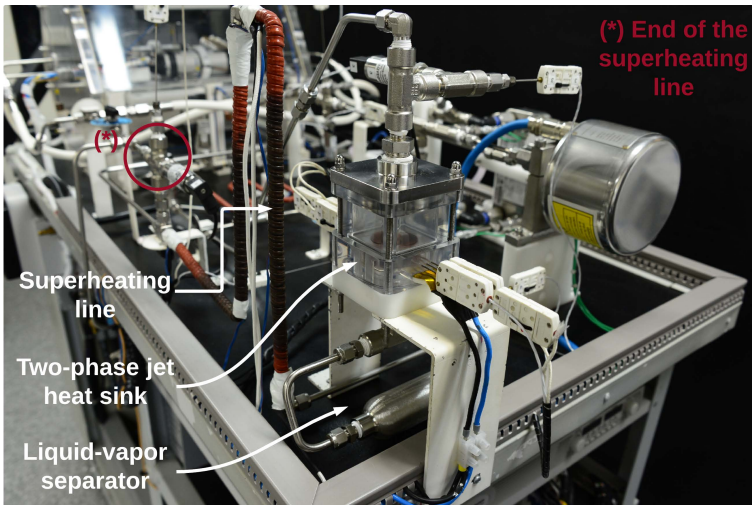
Figure 3.5 – Components of the primary evaporation circuit.

The superheating line downstream of the jet cooler is composed of an electrical trace heater wrapped around copper tubes (6.35-mm outer diameter) as shown in Figure 3.5. The major extent of the superheating line is vertically oriented in order to impose the refrigerant to flow upwards. In addition to the liquid-vapor separator, this enhances

phase separation to superheat the saturated vapor guaranteeing that no liquid will flow back to the compressor. Finally, the superheated vapor returns to the compressor, closing the refrigeration circuit.

Figure 3.6 illustrates the second evaporation circuit. It is composed of a metering valve, which functions as the expansion device, and a dry tubular evaporator, i.e., an electrical trace heater wrapped around a stainless steel tube (6.35-mm outer diameter). Applying the models for flow boiling in horizontal tubes proposed by Kattan *et al.* (1998a, 1998b) and Wojtan *et al.* (2005), an in-house EES (KLEIN, 2004) code was developed to determine the tube length (≈ 60 cm) necessary to dissipate a heat load of up to 200 W that guarantee superheated vapor refrigerant at the outlet of the dry evaporator without too high tube wall temperatures.
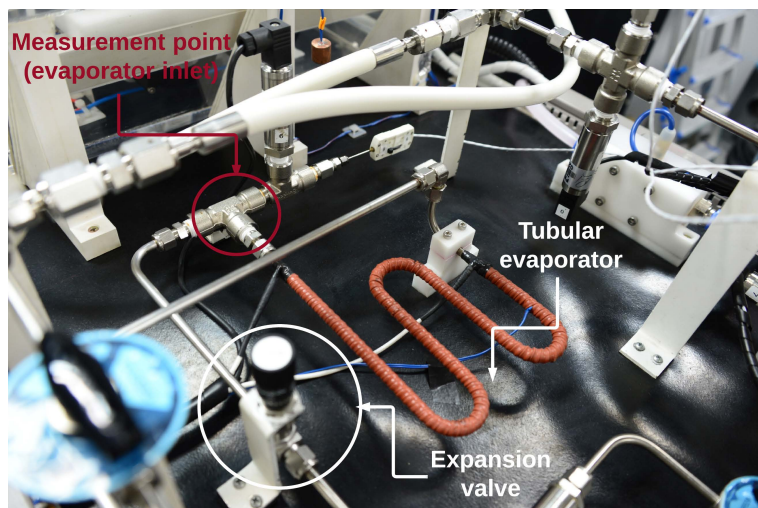
Figure 3.6 – Components of the secondary evaporation circuit.

Two reasons justify the design and incorporation of a secondary evaporation circuit in the present active cooling system: (i) to preliminarily verify the behavior of a particular compressor operating in a classical refrigeration system and to gain insight about the parametric response of the refrigeration system, and (ii) to make room for thermal performance tests using other high heat flux removal devices, such as microchannels and cold plate evaporators. By using the same refrigeration system under the same operating conditions, a fair and robust basis for comparative analyses can be established.

Ball valves are installed upstream and downstream of the compressor, condenser, two-phase jet cooler and tubular evaporator to allow quick setup changes without having to evacuate the entire refrigeration loop, as schematically represented in Figure 3.1. Vacuum and refrigerant charge lines are positioned behind the Sub-system 1 and are both connected to the suction line. In the vacuum line, a check valve is used to avoid the flow of oil from the vacuum pump to the experimental facility. Three inline filters of decreasing pore size values, i.e., 15 micron, 2 micron and 0.5 micron, are installed in the refrigerant charge line to retain impurities.

The secondary cooling circuit operates with a 90%/10% vol. mixture of distilled water and ethylene glycol (WEG). Its main function is to establish the conditions of the hot end reservoir. The WEG solution flow rate and temperature at the condenser inlet are measured and controlled. Figure 3.7 depicts the secondary cooling circuit components, i.e., two cascade thermal baths, a needle valve for flow control and a volumetric flow meter.
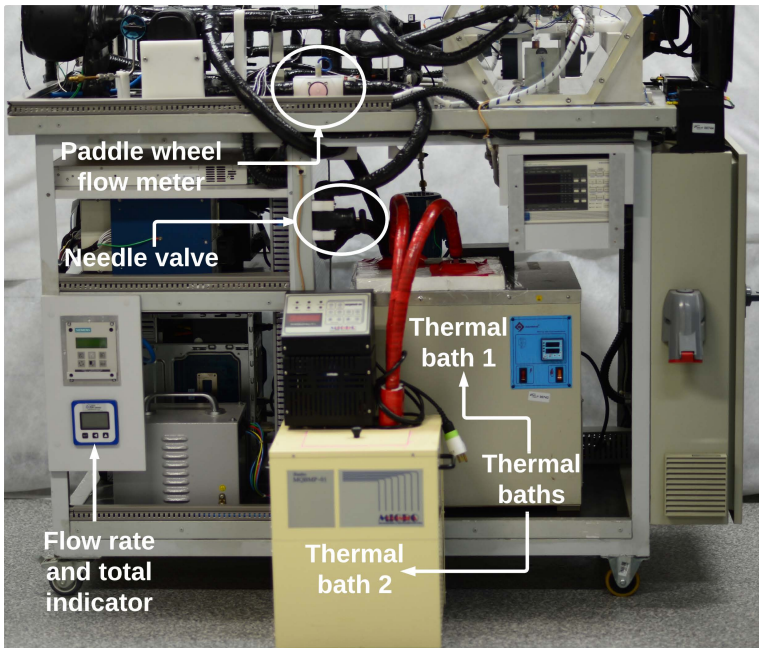
Figure 3.7 – Side view of the experimental apparatus focusing on the secondary cooling circuit.

The usage of two thermal baths was necessary for chiller circuit to be capable of dissipating high heat transfer rates while controlling the temperature of the WEG mixture at the inlet of the condenser.

3.2.2   Sub-system 3: Electrical and Electronic Circuit

The electrical and electronic circuit, i.e., Sub-system 3, comprises a series of power sources, solid-state relays, contactors, fuses, breakers and other components installed inside the electrical panel presented in Figure 3.8. Sub-system 3 provides support for a proper operation of the experimental apparatus, particularly the instrumentation, data acquisition and parameter control devices.
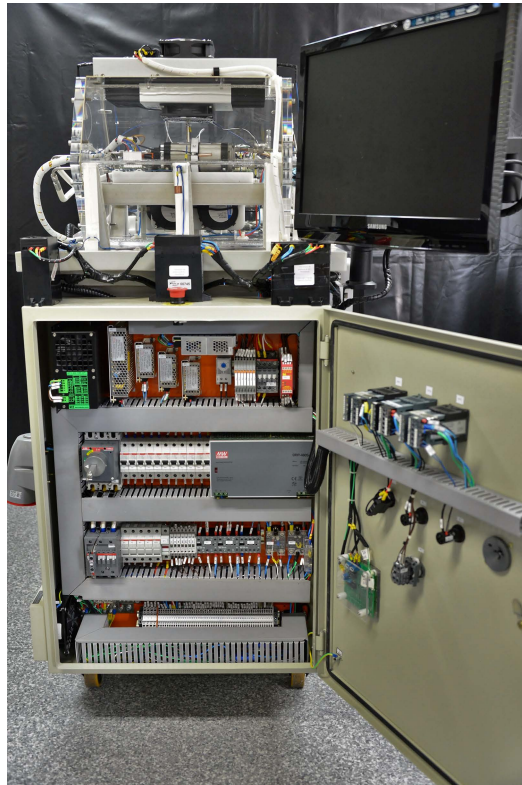
Figure 3.8 – Front view of the experimental apparatus focusing on the electrical and electronic circuit (Sub-system 3).

3.2.3 Sub-system 4: Instrumentation, Data Acquisition and Control Devices

The experimental facility is equipped with different transducers to measure pressure, temperature, flow rate and power. Absolute pressure transducers and resistance temperature detectors (RTD) are used to measure the local values of pressure and temperature in the following positions according to the numbers indicated in Figure 3.1: (1) Compressor inlet (suction); (2) Compressor outlet (discharge); (3) Condenser inlet (refrigerant side); (4) Condenser outlet (refrigerant side); (5) Jet cooler inlet; (6) Jet cooler outlet; (7) Condenser inlet (WEG side); (8) Condenser outlet (WEG side); (9) Tubular evaporator inlet. Pressure and temperature are measure at the same point, i.e., the center region of the metallic union crosses shown in Figure 3.9.
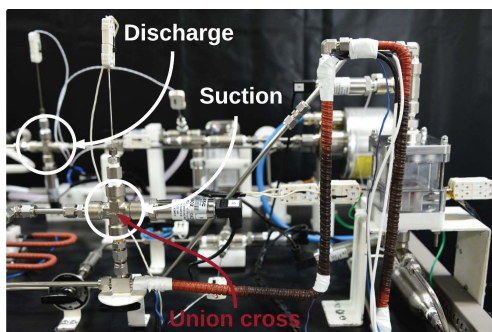
(a) Compressor measurements points
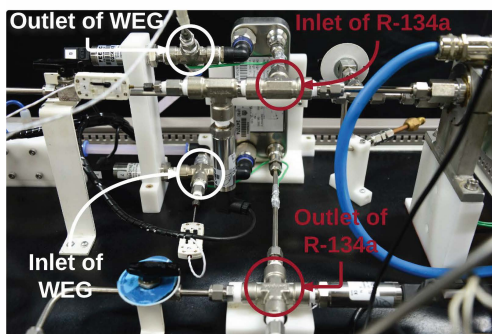
(b) Condenser measurements points

Figure 3.9 – Measurement points at different regions of the experimental apparatus: (a) suction and discharge lines and (b) condenser.

In Sub-system 1, downstream of the discharge line, a Coriolis mass flow meter is placed to measure the refrigerant mass flow rate. This position was chosen to avoid two-phase flow in the transducer. In Sub-system 2, the volumetric flow rate of the WEG mixture is measured by a paddle wheel flow meter, which has a microcontroller-based indicator/transmitter (Seametrics FT420-P) that displays the volumetric flow rate and the total flow volume.

A digital power meter is employed to measure the electrical power consumption of the compressor. The measurement point is positioned between the compressor and the compressor control unit. The thermal power provided by the electrical trace heater in the superheating line and in the tubular evaporator are measured by power line transducers with ranges of 0 - 200 W and 0 - 400 W, respectively.

Regarding the calorimeter, the internal temperature, i.e., the temperature inside the enclosure, is controlled by an air heater (electrical resistance) and a thermoelectric cooler. A power line transducer (range of 0 - 200 W) is also used to measure the thermal energy dissipated by the air heater inside the calorimeter. T-type thermocouples are used to measure the internal temperature. Analogously, the room temperature is measured by T-type thermocouples welded to a copper block, placed adjacent to the outside of the calorimeter walls.

In-house calibration procedures were performed for the thermocouples, RTDs, pressure transducers, flow meters and power line transducers. Thermocouples and RTDs were calibrated using a standard thermometer with an uncertainty of 0.10℃. The sensors and the standard thermometer were positioned inside a thermostatic bath (Thermo Scientific Model SC150-A40) covering a variable temperature range. For every temperature set point, after stabilization, the readings were averaged over 2 minutes. Two types of pressure transducers are used for the high- and low-pressure sides of the refrigeration circuit. These pressure transducers were calibrated using a DH Bundenberg 580-series dead-weight tester. Small experimental setups were specially designed and constructed to calibrate the flow meters and the power line transducers. The power transducers were calibrated using the Agilent AC power source/analyzer (model 6812B) as the reference instrument.

The description of the instrumentation used for the thermal performance characterization of the two-phase jet cooler and the refrigeration system is given in Table 3.1. The overall uncertainties of the measured parameters resulting from the in-house calibration procedures are presented in Table 3.2. Further details regarding the uncertainty computation of the measured parameters can be found in Appendix A.

Table 3.1 – Summary of the instrumentation specifications.

Sensor	Manufacturer	Model/Part Number
Thermocouple	Omega	Type T
Temperature probe	Omega	PT-100 1/16" RTD
Pressure transducer (0 - 30 bar)	Omegadyne	MMA500C1B2 C6T4A6CE
Pressure transducer (0 - 10 bar)	Omegadyne	MMA150C1B2 C6T4A6CE
Mass flow meter	Siemens	SITRANS F C MASS 2100 DI 1.5
Volumetric flow meter	Seametrics	SPX-038
Digital power meter	Yokogawa	WT230
Power line transducer (0 - 200 W)	Yokogawa	2375A10
Power line transducer (0 - 400 W)	Yokogawa	2285A-0Z3/W26/AE

Table 3.2 – Expanded (overall) uncertainty of the measured parameters.

Instrument/sensor	Expanded uncertainty
Thermocouples	0.22°C [†]
Temperature probes (RTDs)	0.20°C [†]
High-pressure side transducers	0.05 bar [†]
Low-pressure side transducers	0.03 bar [†]
Mass flow meter	0.05 kg/h
Volumetric flow meter	0.07 L/min
Power line transducer (superheating line)	0.58 W
Power line transducer (calorimeter air heater)	0.65 W
Power line transducer (tubular evaporator)	2.72 W

[†]Maximum value.

The reading, logging and storage of data are performed with a National Instruments data acquisition system connected to a computer equipped with LabVIEW 2009. Additional information about the main

components of the data acquisition system are presented in Table 3.3.

Table 3.3 – Main components of the National Instruments data acquisition system.

Component	Model
Chassis	SCXI-1000 - 4 slots
Board	NI PCI-6259 - 16-bits
Relay Module	SCXI-1161 - 8ch
RTD Module	SCXI-1503 - 16ch
Voltage module	SCXI-1102 - 32ch
Terminal block	SCXI-1303 - 32ch

Regarding the variable control strategies, thermal baths 1 and 2 are responsible for maintaining a fixed temperature of the WEG mixture at the condenser inlet. The cooling load imposed on the refrigeration system (evaporation circuit 1) is provided and finely controlled by a DC digital power supply. During the experimental runs, the cooling load was increased by increasing the voltage or the current provided by the power supply. The temperature of point 1 (compressor inlet) and the internal temperature of the calorimeter are accurately controlled using a built-in LabVIEW PID controller code, which operates coupled with a specially designed voltage-to-current converter electronic board. Therefore, at steady state, it was possible to maintain a fixed refrigerant superheating degree at the compressor inlet. Concerning the calorimeter, a thermoelectric cooler controls the enclosure internal temperature whereas a split air conditioner controls the room temperature. Table 3.4 outlines the specifications of some control strategies.

Table 3.4 – Control strategies specifications.

Component	Manufacturer	Model
DC digital power supply	Agilent	N5770A
Thermoelectric cooler	CALIENTÉ	Frio Air 210-48
Thermal bath 1	Quimis	Q214M2 ($\approx$ 240 W)
Thermal bath 2	Microquímica	MQBMP-01 (225 W)
Air conditioner	LG	Inverter V AS-Q242C4A0

3.3   Jet Heat Sink Design

The jet heat sink combines the expansion device and the evaporator into a single unit as a means to reduce the size of the refrigeration system. The cooler design details regarding the concept, components, assembly and thermal losses are presented next.

3.3.1   Concept, Components and Assembly

The core idea of the two-phase jet cooler is to remove high heat loads from a small surface by producing a highly effective two-phase jet impingement cooling on the heated surface. The two-phase jet cooler is presented in Figure 3.10 together with some ancillary components. The heat sink is composed of a metallic cap, a jet impingement chamber, an internal orifice plenum, a polymeric unit that serves for thermal insulation and fluid drainage, a reservoir to collect the spent two-phase mixture, a film heater and a copper block that emulates the electronic component. Figure 3.10 shows two versions of the jet cooler which differ with respect to the jet chamber height. For both versions, the external dimensions are 80 mm in width × 80 mm in depth and the heights are 112.5 mm and 93.5 mm for Figures 3.10 (a) and (b), respectively.

(a) Jet cooler with the high chamber   (b) Jet cooler with the low chamber
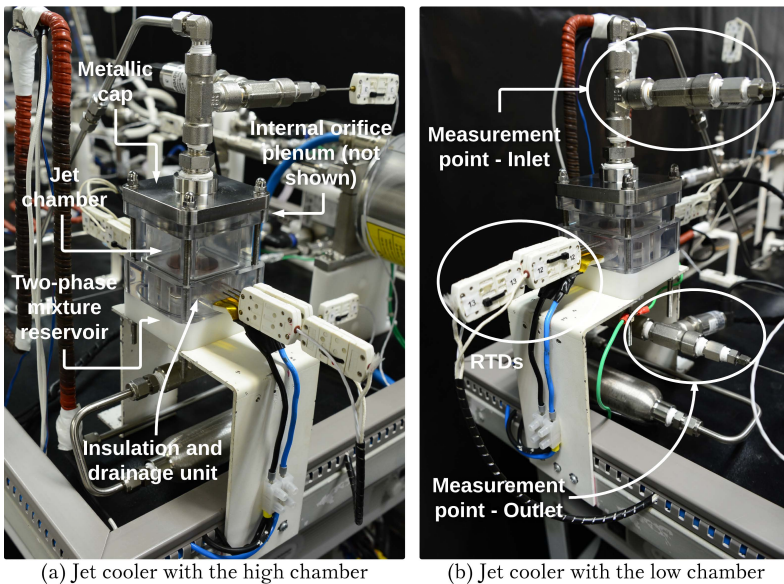
Figure 3.10 – Two-phase jet coolers: assembly and main components.

The high-pressure sub-cooled liquid from the condenser flows through the top of the test section, i.e., the metallic cap, directly into the orifice plenum. The plenum, depicted in Figure 3.11, comprises a metallic outer orifice plate, a polyacetal resin (POM) inner orifice plate and the expansion device, which is an array of POM threaded screws with the actual orifices drilled along their centerlines. The screws are responsible for fixing the assembly of the orifice plates in order to form the orifice plenum. The plenum can accommodate up to 13 orifices in a staggered array, covering a square area with a 20-mm side. The center-to-center spacing between orifices on the same row and column is 6.67 mm.

(a) Orifice plenum (assembly)

(b) Base plates (disassembly)
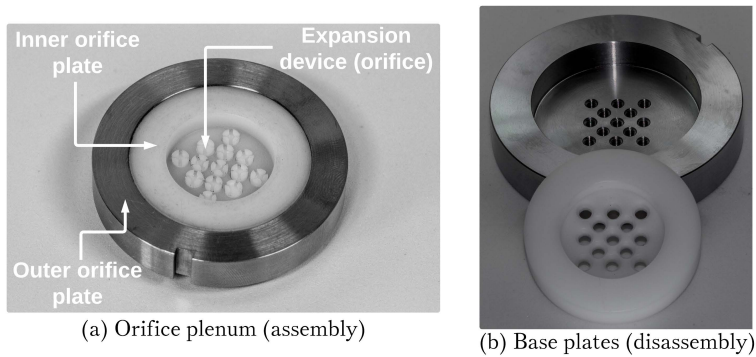
Figure 3.11 – Orifice plenum: (a) assembled components and (b) outer and inner orifice plates.

The metallic base plate provides support to the assembly preventing the polymeric components from bending because of continuous pressure solicitations. The metallic parts are made of AISI 316 stainless steel. The thermoplastic POM was used due to its high stiffness, excellent dimensional stability, chemical compatibility with the working fluid and, most importantly, low thermal conductivity (between 0.20 and 0.3 W m^{-1} K^{-1}). The latter feature is important to reduce thermal losses from the refrigerant to the surroundings (inner orifice plate and screws) before the expansion.

The use of hollow threaded screws as expansion devices is one of the main features of the novel jet heat sink. Considering (i) the ease for material (POM) machining, (ii) the range of orifice diameters that can be drilled along their centerlines, and (iii) the flexibility in terms of number of screws and their positions, several jet array configurations can be tested with the same orifice plenum.

   Tests with single and multiple jets were performed in the present
thesis. For the single-jet experiments, the orifice screw was positioned
at the center of the orifice plate assembly and dummy screws occupied
the remaining positions. Dummy screws were also used in the multiple-
jet experiments, for which three configurations of a five-jet-array were
tested. The orifices are 10-mm long and were machined in a range of
diameters, as illustrated in Figure 3.12.
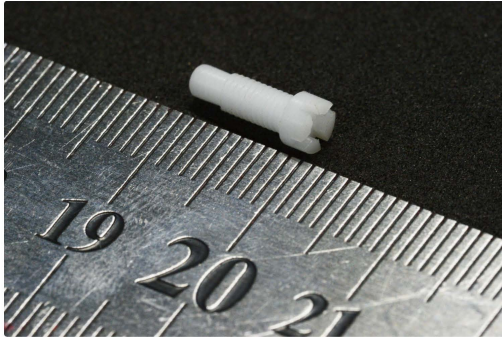
(a) Size of the threaded screw (nozzle)
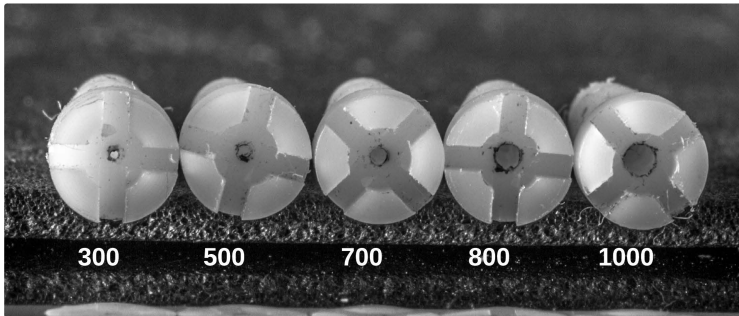
(b) Several orifice diameters (dimensions in micrometers)

Figure 3.12 – Dimensions of the threaded screw (nozzle): (a) size and
(b) orifice diameters.

   As the liquid passes through the nozzle, or nozzle array, it ex-
pands generating a downward-oriented normal jet inside the jet cham-
ber. As shown in Figure 3.13 (a), two jet chambers were constructed
for the experimental tests which differ in height, H, i.e., $H = 28.84$
mm and $H = 9.75$ mm. The jet length, i.e., the height of the chamber,
is the vertical distance from the outlet of the orifice to the base of the

chamber that is at the same level of the impingement surface. Figure
3.13 (b) shows the outlet of the single-orifice configuration inside the
chamber.
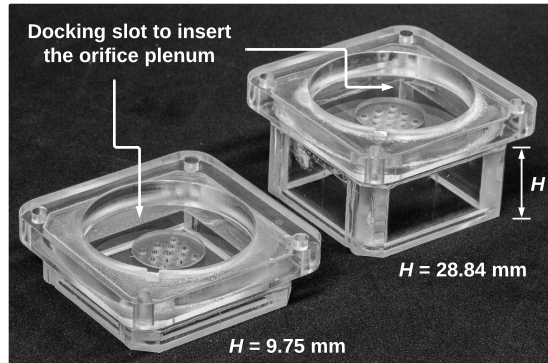
(a) Jet chambers
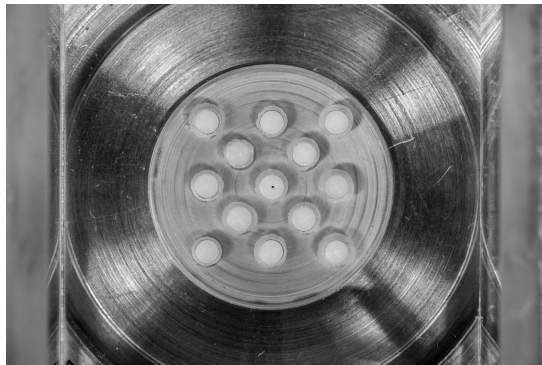
(b) View of the bottom side of the orifice plenum as-
sembled to the jet chamber

Figure 3.13 – Jet chamber: (a) heights and (b) inside view.

As the jet expands in the jet chamber, it impinges vertically at
the top surface of a heated cylindrical copper block. The copper block
is mounted vertically in a plastic bottom piece designed to thermally
insulate the sides and the bottom of the block and to facilitate the
drainage of the two-phase mixture from the jet chamber into the reser-
voir and liquid-vapor separator positioned below the jet cooler - see
Figures and 3.10 and 3.5, respectively. The heat source is a skin (film)
heater placed below the copper block. A Teflon base plate is used as an

insert tool to guide and properly place the skin heater inside the insula-
tion and drainage unit and to press the heater against the bottom side
of the copper block. In addition, a thin layer of thermal grease (Artic
Silver 5) is used to enhance the contact between the heater and the
copper block. Figure 3.14 presents each aforementioned component.
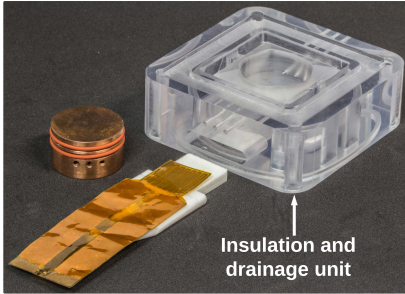
(a) Copper block, heater, Teflon base plate,
insulation and drainage unit
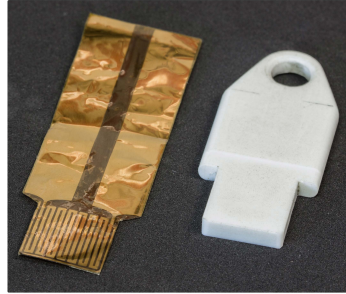
(b) Film heater and Teflon base plate
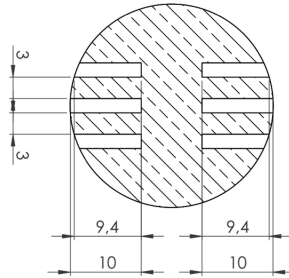
(c) Copper block

(d) Cross-sectional view of the copper
block (RTDs' plane)

Figure 3.14 – Presentation of the following components: (a) insulation
and drainage unit, (b) skin heater and Teflon base plate, (c) copper
block and (d) design details concerning the instrumentation of the cop-
per block (dimensions in millimeters).

As can be seen in Figure 3.14 (d), the copper block has six RTD
wells. Five RTDs are used to measure the temperature and allow for an
estimate of the surface temperature to be made using Fourier's law. The
remaining one is connected to a commercial PID controller (Autonics
- Model 4KS) which functions as a safety system cutting the heating
power supply in the event of a temperature runaway associated with
the critical heat flux. The area of the circular target surface is 6.36 cm^2
($D = 28.54$ mm) and the distance from the plane of the RTDs to the

impingement surface is 10.03 mm. Figure 3.15 illustrates the assembly procedure to fit the skin heater (with the Teflon bed) and the copper block in the insulation and drainage unit.

(i)

(ii)

(iii)

(iv)
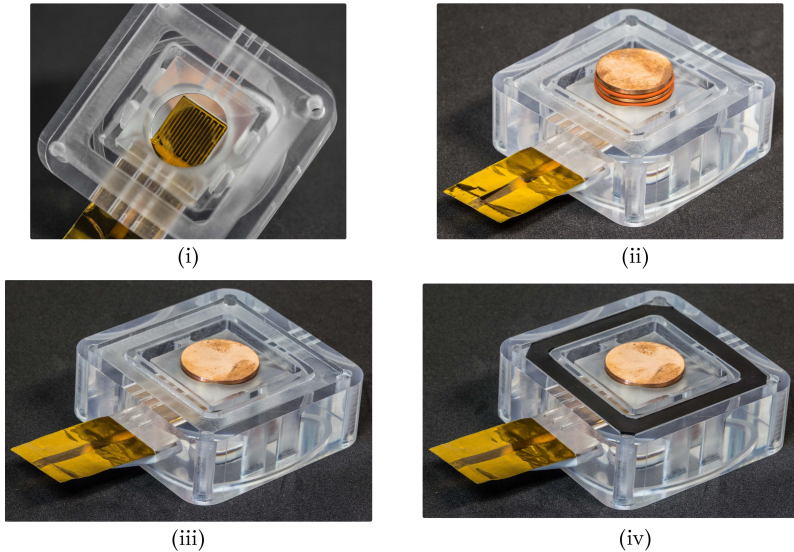
Figure 3.15 – Assembly of the following components: insulation and drainage unit, skin heater (with the Teflon bed) and copper block.

Figure 3.16 presents the design details of the insulation and drainage block, including the holes for placing the RTD probes for temperature measurement, drainage channels and sealing characteristics. Like the jet chambers, the unit is made of polycarbonate, which was chosen because of its notably high toughness, good heat resistance, low thermal conductivity and chemical compatibility with the refrigerant.

Particularly for the jet chambers, another feature of interest is the high optical transparency, which is crucial for visual observations of the impinging jets. Inclined surfaces were specially designed to promote drainage of the fluid coming from the impingement surface. They are present in the drainage channels shown in Figure 3.16 (b) (i.e., surfaces angled of 30°), and also in the pyramidal-shaped drainage surfaces (angled of 17°) immediately adjacent to the impingement surface, as depicted in Figure 3.16 (a) and (c). Regarding the sealing aspects, O-rings and a gasket seal are used to prevent refrigerant leakage from the inside of the jet cooler, as portrayed in Figure 3.17.

(a) Isometric view

(b) Side view

(c) Top view

(d) Bottom view
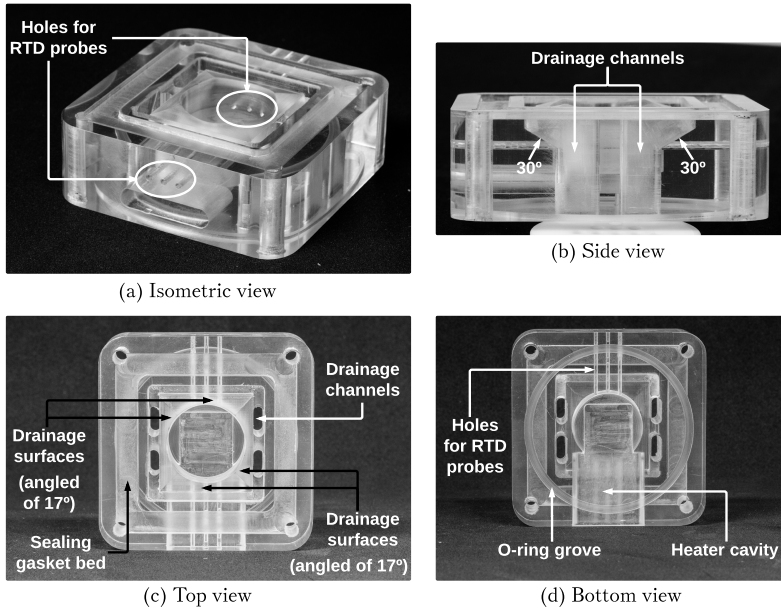
Figure 3.16 – Insulation and drainage unit: views presenting different design details.
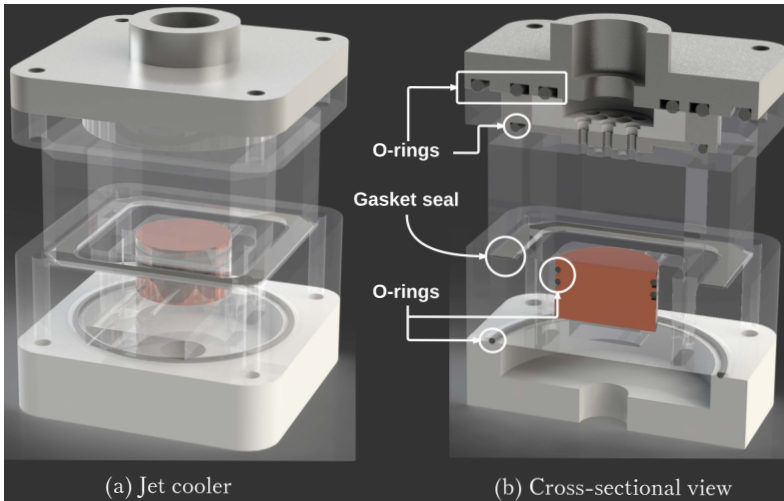
Figure 3.17 – CAD renderings of the two-phase jet cooler: (a) final assembly and (b) cross-sectional view showing the sealing design details.

Figure 3.17 shows three concentric O-rings are positioned in the contact points of the bottom side of the metallic cap and the inner orifice plate, the outer orifice plate and the jet chamber. On the bottom of the metallic outer orifice plate, an extra O-ring prevents refrigerant leakage from the screw(s) mounting in the internal plenum. A sealing gasket is used between the base of the jet chamber and the top of the insulation and drainage unit.

The contact between the copper block and the circular polycarbonate wall inside the insulation and drainage unit is sealed by two radial O-rings that prevent the flow of refrigerant to the cavity where the skin heater is placed. This cavity is in direct contact with the external ambient. Finally, the assembly between the insulation and drainage unit and the two-phase mixture reservoir is sealed by another O-ring. Except for the radial O-rings in the copper block, which are made of silicone to resist the high temperatures, the remaining ones are made of Buna N. Both elastomers are chemically inert in contact with R-134a.

3.3.2 Thermal Losses

A numerical study was performed to estimate the thermal losses in the insulation and drainage unit when the film heater is providing the heat load to the refrigeration system, $\dot{W}_h$. The aim of this investigation was to determine the fraction of the input thermal load that actually reaches the top surface of the copper block, i.e., the jet impinging surface. Accounting for the thermal losses help to correct the surface temperature and the jet impingement heat transfer coefficient. Thus, the correction factor for the input thermal load, κ, is defined as,

$$\kappa = \left| \frac{\dot{Q}_c^* - \dot{W}_h}{\dot{W}_h} \right| \times 100\% \tag{3.1}$$

where $\dot{Q}_c^*$ is the heat transfer rate effectively dissipated at the impingement surface and the input thermal load, $\dot{W}_h$, is given by the product of the voltage, V, and the current, i, provided by the DC power supply.

The CAD geometry shown in Figure 3.18 was used in the simulations and comprises the insulation and drainage unit, the copper block, the radial O-rings and the thermal interface material (TIM) layer, which is in contact with the bottom side of the copper block and has the same dimensions of the useful heater area (20 mm × 20 mm). The three-dimensional geometry was modeled as a conduction heat transfer problem with convective boundary conditions according to the following simplifying assumptions: (i) steady state; (ii) homoge-

neous and isotropic materials, (iii) constant thermophysical properties, and (iv) no heat generation.
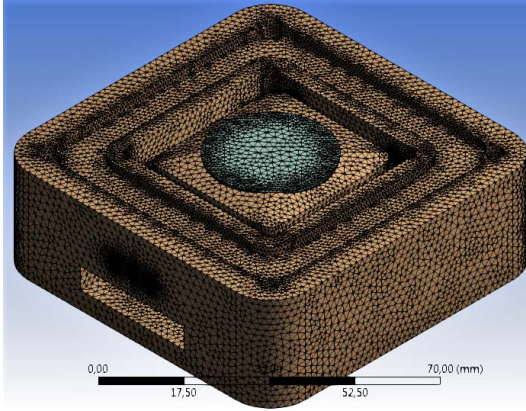
Figure 3.18 – Meshed CAD geometry used in the numerical study on the thermal losses of the test section.

Based on the adopted assumptions, the heat conduction equation is (POULIKAKOS, 1994),

$$\vec{\nabla} \cdot \left(k_\varphi \vec{\nabla} T_\varphi\right) = 0 \tag{3.2}$$

where T_φ and k_φ are the temperature and thermal conductivity of a particular component (material) φ of the CAD model, respectively.

Regarding the boundary conditions, the thermal coupling between two adjacent solid surfaces is such that a continuity of temperatures and heat fluxes is applied. In the experimental tests, the jet cooler was completely covered by a thick layer of thermal insulation. Therefore, the external lateral surfaces were considered adiabatic,

$$q_{\varphi,\text{ex}}'' = -k_\varphi \vec{\nabla} T_\varphi = 0 \tag{3.3}$$

where $q_{\varphi,\text{ex}}''$ is the heat flux through the external lateral surfaces.

The input heat load (film heater) is introduced as a constant prescribed heat flux at the bottom surface of the TIM layer, $q_{\varphi,\text{TIM}}''$. Thus, one has,

$$q_{\varphi,\text{TIM}}'' = \frac{\dot{W}_h}{A_h} \tag{3.4}$$

where A_h is the skin heater area (4 cm^2).

Figure 3.19 illustrates the aforementioned boundary conditions, respectively,

(a) Adiabatic surfaces

(b) Prescribed heat flux
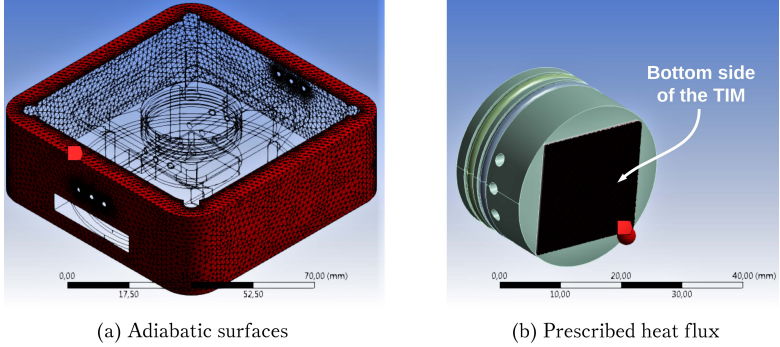
Figure 3.19 – Adiabatic (a) and prescribed heat flux (b) boundary conditions.

The heat transfer to regions in contact with the liquid film is incorporated into the numerical model via convective boundary conditions as follows,

$$-k_\varphi \vec{\nabla} T_\varphi = \hbar_\varphi \left(T_\varphi - T_f \right) \tag{3.5}$$

where $\hbar_\varphi$ is the heat transfer coefficient at the surface of a particular component φ and T_f is the temperature of the liquid film, which is equal to the evaporating temperature, T_{evap}, inside the jet chamber as the liquid film is in contact with the saturated vapor.

For the simulations performed, the input data for the convective boundary condition are the heat transfer coefficient and the liquid film temperature. It is important to mention that, at the impingement surface, the heat transfer coefficient and the surface temperature, $\hbar_\varphi = \hbar_s$ and T_s, were calculated directly from experimental data using equations to be defined in Chapter 4, i.e., Eq. (4.7) and (4.8), respectively. For the remaining surfaces, where liquid film flow occurs, the heat transfer coefficient was computed according to the model proposed by Labuntsov (1957) for turbulent film heat transfer,

$$\hbar_\varphi = k_f \left(\frac{\mu_f^2}{\rho_f^2 g} \right)^{-\frac{1}{3}} \left[\frac{Re_f}{8750 + 58 Pr_f^{-\frac{1}{2}} \left(Re_f^{0.75} - 253 \right)} \right] \tag{3.6}$$

where the thermal conductivity, k_f, dynamic viscosity, μ_f, density, ρ_f, and the Prandtl number, Pr_f, were evaluated at saturated liquid film conditions. For inclined surfaces, the gravity acceleration, g, was substituted by $g \sin \theta$, where θ is the inclination angle of the surface.

The Reynolds number of the liquid film, Re_f, is defined as,

$$Re_f = \frac{4\Gamma}{\mu_f} = \frac{4\dot{m}_r}{\mu_f W_s} \tag{3.7}$$

where Γ is the refrigerant mass flow rate, $\dot{m}_r$, per unit surface width, W_s. If the surface is circular (e.g., a cylindrical cavity), then W_s is the diameter. Figure 3.20 presents the surfaces where convective boundary conditions were applied.

(a) Impingement surface   (b) Horizontal surfaces

(c) Vertical surfaces   (d) Inclined surfaces

(e) Bottom side surface
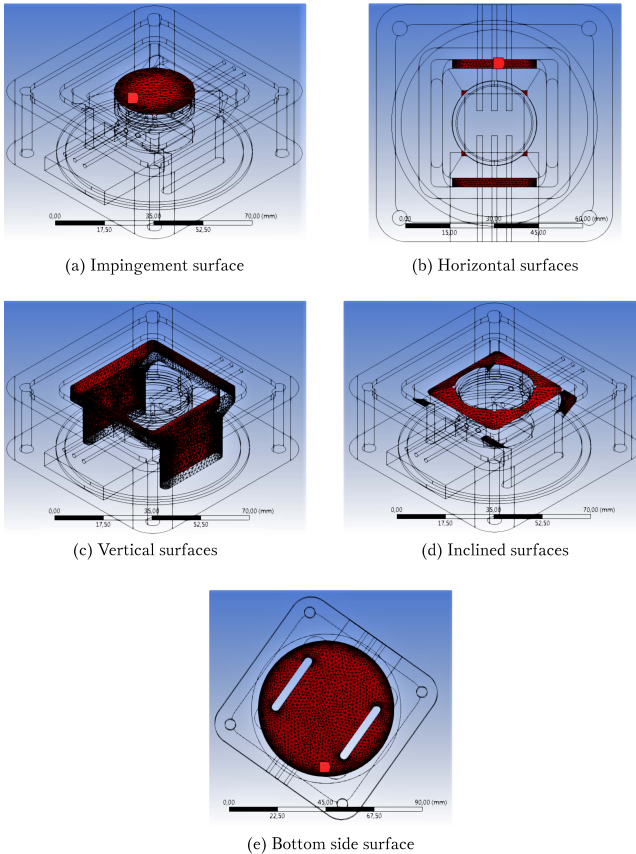
Figure 3.20 – Positions of the convective boundary conditions.

The numerical model was solved with the Element-based Finite Volume Method (MALISKA, 2004) using the commercial CFD code ANSYS Fluent 15. As can be seen in Figure 3.18, a fine mesh (more than 2 million elements) was used with an average orthogonal quality of 0.86. The correction factor that accounts for the thermal losses, κ, varies for each experimental test because it depends on the experimental conditions and parameters of the test, namely the input thermal load, evaporating temperature, heat transfer coefficient and surface temperature. The simulations showed that the heat transfer rate effectively dissipated at the impingement surface, $\dot{Q}_c^*$, was quite close to the input thermal load, $\dot{W}_h$. The relative difference between $\dot{W}_h$ and $\dot{Q}_c^*$ was lower than 5%. Therefore, in the real device, the thermal losses in the insulation and drainage unit are considered to be 5% of the input heat load ($\kappa = 5\%$).

3.4 Calorimeter Design

A calorimeter was designed and built as a tool to indirectly measure the heat dissipation rate through the shell of the small-scale compressor and close the system first-law energy balance. This section describes the calorimeter components in detail, the working principle and the calibration procedure.

3.4.1 Main Components

The calorimeter is composed of a hexagonal enclosure with a thermoelectric cooler embedded on its top, as presented by Figure 3.21. The dimensions of the calorimeter are 460 mm in length × 420 mm in width × 453 mm in height. The enclosure was carefully manufactured from thick acrylic plates (20 mm) in order to minimize the thermal losses to the surroundings by taking advantage of the thermoplastic low thermal conductivity (between 0.17 and 0.25 W m^{-1} K^{-1}). Besides, acrylic was chosen because of its high level of transparency, which facilitates the assembly and disassembly of the internal components in comparison to opaque materials.

Figure 3.22 displays the internal components of the calorimeter, namely a purpose-built base plate, two miniature compressors with their respective inverters, four centrifugal fans and a tubular-finned air heater. Outside and inside the calorimeter, T-type thermocouples are responsible for the temperature measurements as shown in Figures 3.21 and 3.22, respectively.
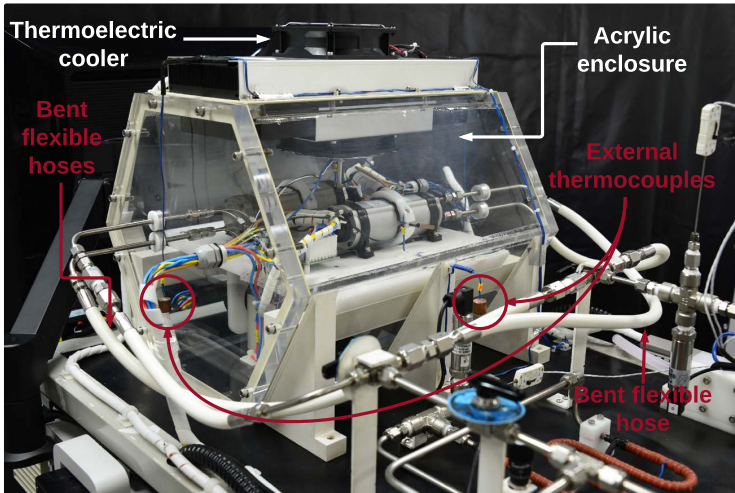
Figure 3.21 – External view of the calorimeter.
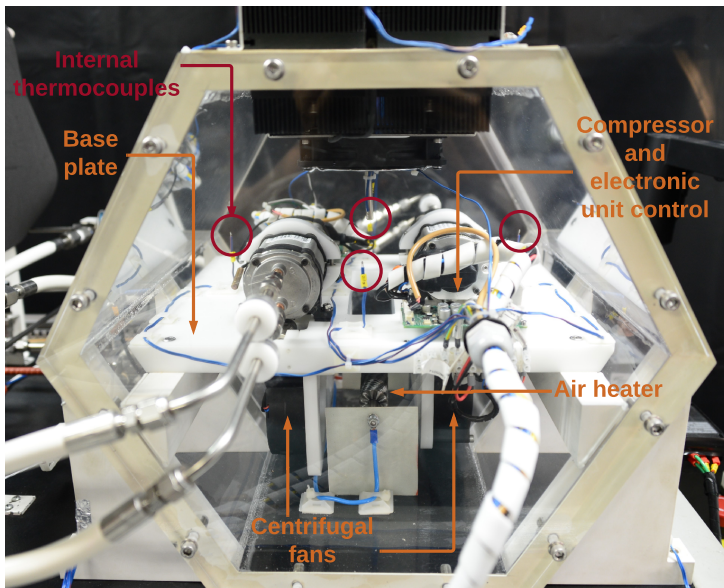
Figure 3.22 – View of internal components of the calorimeter.

Figure 3.21 also shows two of the four external copper block-welded thermocouples positioned on each side of the enclosure. They are used to measure the room temperature, T_{room}, at the surroundings of the calorimeter. Analogously, five T-type thermocouples are used to determine the internal temperature of the enclosure, i.e., the calorimeter temperature, T_{cal}. As shown in Figure 3.22, four thermocouples are cross-distributed at the top of the base plate in order to capture the temperature field in the region near the compressors. The remaining thermocouples are positioned above the others in a vertical alignment with the air heater to measure the temperature of the hot air stream, as shown in Figure 3.22.

The purpose-built base plate is made of polyacetal and was specially designed to allocate the compressors, inverters and the centrifugal fans. As shown in Figure 3.23 (a), the base plate has several venting ports for air circulation. The circular ports in the vertical supports enable the axial intake of air by the fans. Each fan cooler is vertically mounted on a frame, which is also the centrifugal air exhaust port, as depicted in Figure 3.23 (b). These ports are located immediately behind the compressors. The fans are positioned in such a way that the cooling air is blown perpendicularly to the compressor cylindrical shell. This is done to keep the temperature of the compressor shell under the maximum temperature limit (85℃) specified by the manufacturer. In addition to the exhaust ports of the fans, the central ventilation port promotes better circulation of the hot air stream.
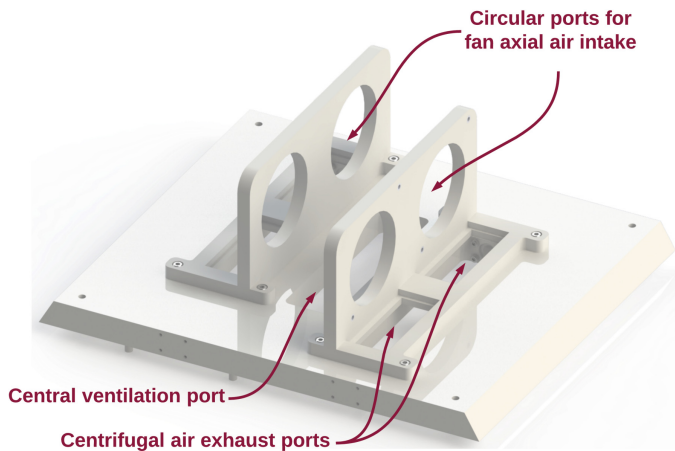
(a) Design and ports for air flow
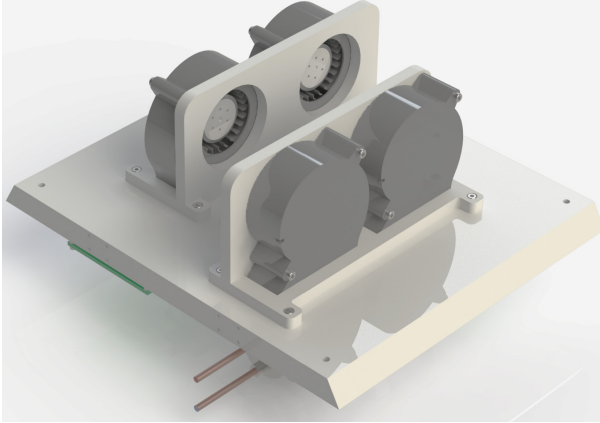
(b) Assembly of the centrifugal fans in the base plate

Figure 3.23 – Base plate: (a) design and ports for air flow and (b) assembly of the compressor cooler fans and the base plate.

3.4.2   Ancillary Components

The compressor is fixed to the surface of the base plate by using rubber dampers attached to its shell, as presented in Figure 3.24 (a). During the operation of the linear motor, a high level of operation-induced mechanical vibration can be transmitted to the other components of the refrigeration system. Preliminary tests have shown that the rubber dampers were not sufficient to provide attenuation of the mechanical vibrations. Several detrimental effects can result from this, particularly in regard to the jet(s) formation inside the jet heat sink.

With the aim to avoid vibration transmission, a custom-designed support was built to hold the compressor. The acetal-made support is attached to a threaded rod with two compression springs at each end, as shown in Figure 3.24 (a). The springs are free to move along the longitudinal axis of the threaded rod. Figure 3.24 (b) exhibits the fixing of the compressor support to the base plate. Although the vibration motion is three-dimensional, its principal component is along the axial direction of the compressor, i.e., the orientation of the piston displacement. The plastic support is attached to the compressor and is free to move axially as it is not in contact with any surface of the base plate.

Rubber damper

**Electronic control
unit (inverter)**

Compressor support

(a) Compressor assembly

**Compressor
support**

Springs
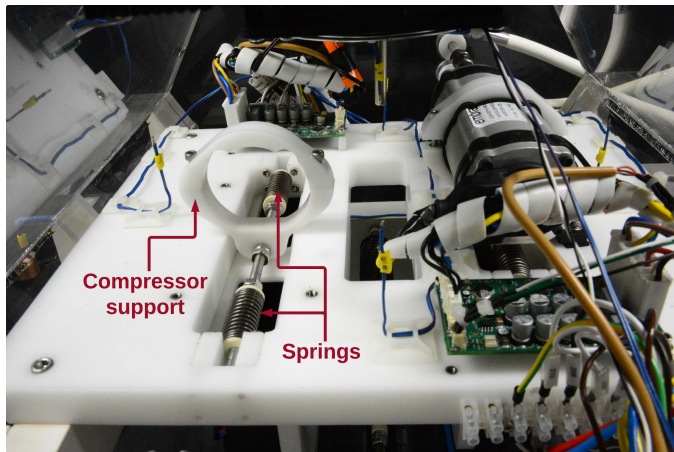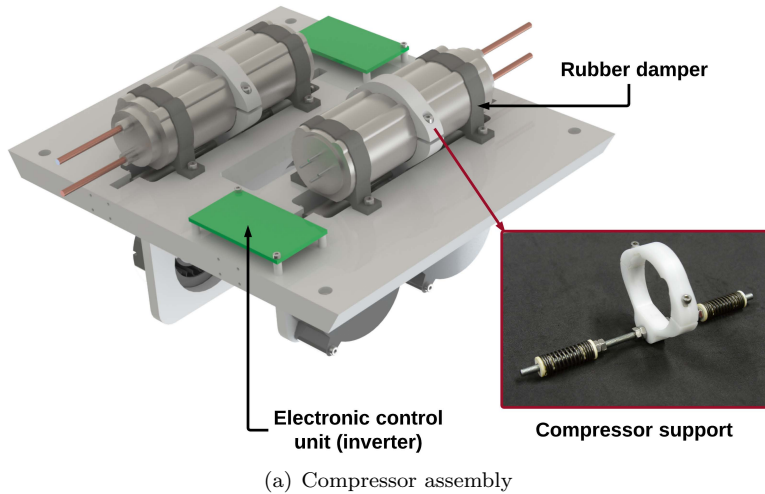
(b) Compressor support and vibration control system

Figure 3.24 – Compressor support, vibration control system and assembly.

The flexible hoses presented in Figure 3.21, which are part of the discharge and suction lines, also contribute to reducing the vibration transmission generated by the compressor. It was empirically verified that installing the hoses in a way that accommodates a bend, as can be seen in Figure 3.21, was determinant to mitigate the vibration transmission. It is believed that the combined action of both the vibration

isolation system (springs) and the flexible hoses successfully minimized the mechanical vibration transmission, making the vibrations near and at the test section almost imperceptible.

3.4.3   Working Principle

The aim of the calorimeter is to determine the heat dissipation rate through the compressor shell via an energy balance. For that, the calorimeter needs to operate in a temperature-controlled environment and the temperature inside the calorimeter enclosure must be kept at a pre-determined value. All input and output energy rates are measured.

The internal temperature is finely controlled by the combined action of a heat source, i.e., a 150-W tubular-finned air heater resistance, and a cooling device, i.e., an air-based-assembly thermoelectric cooler (TEC). The heat transfer rate dissipated by the air heater is controlled by a PID controller LabVIEW code in order to achieve a specified target temperature. A surface mount temperature controller (FRIO TC 12-24 with a PTC sensor $\pm$ 2℃) controls the target temperature set for the thermoelectric cooler.

According to the control volume presented in Figure 3.25, several heat transfer and work rates are present in the operation of the calorimeter. The input energy transfer rates are the following: (i) the thermal power provided by the tubular-finned air heater, $\dot{W}_{ah}$, the electrical power consumption of the compressor, $\dot{W}_{comp}$ and the electrical power consumption of all fans inside the enclosure, $\dot{W}_{fans}$. The latter takes into consideration the four centrifugal fans assembled in the base plate, shown in Figure 3.23 (b), and the internal fan of the thermoelectric cooler. It should be clear that the four centrifugal fans were used to homogenize the temperature inside the calorimeter. As far as the compressor is concerned, the volumetric air flow rate provided by only one centrifugal fan is sufficient to maintain the temperature of the compressor shell below the manufacturer-specified safety limit. Therefore, in the calculation of the system performance metrics, such as the coefficient of performance, only the electrical power consumption of a single centrifugal fan is considered, as will be introduced in Chapter 4.

The output energy transfer rates are: (i) the cooling capacity removed by the thermoelectric cooler, $\dot{Q}_{TEC}$, (ii) the indicated power or compression power, $\dot{W}_{ind}$, and (iii) the heat transfer rate lost to the surrounds through the walls of the calorimeter enclosure, $\dot{Q}_{enc}$. It should be mentioned that $\dot{W}_{ind}$, to be defined in Chapter 4, refers to the product of the refrigerant mass flow rate by the difference between

the specific enthalpies at the discharge and suction lines, points 2 and 1 of Figure 3.1, respectively. The cooling capacity of the thermoelectric cooler can be directly obtained from a linear relationship between $\dot{Q}_{TEC}$ and the temperature difference between the outside and inside regions of the calorimeter, i.e., $\Delta T_{cal} = |T_{room} - T_{cal}|$ (LEE, 2010). It is advantageous to operate the thermoelectric cooler at the maximum cooling capacity, for which the corresponding calorimeter temperature difference is $\Delta T_{cal} = 0$. Considering a near-zero temperature difference between the outside and inside of a very low thermal conductivity thickwall, it is fairly reasonable to neglect the heat transfer rate dissipated at the walls, i.e., $\dot{Q}_{enc} = 0$.

During all the experimental tests, the room and calorimeter temperatures were set at the same value and controlled with the aforementioned temperature control strategies. According to the manufacturer, the maximum cooling capacity of the Frio Air 210-48 thermoelectric cooler occurs for operating the system at an ambient temperature of 25℃.
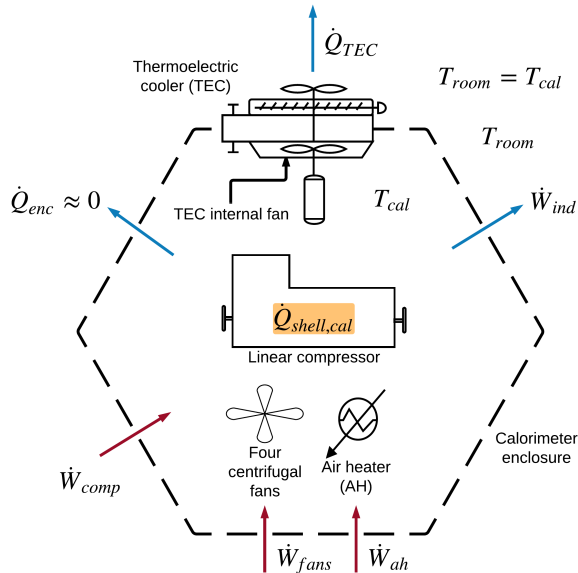
Figure 3.25 – Heat balance on the calorimeter: input and output heat transfer and work rates.

Based on Figure 3.25, the energy balance on the calorimeter is given by the following equation,

$$\dot{Q}_{TEC} + \dot{W}_{ind} + \dot{Q}_{enc} = \dot{W}_{comp} + \dot{W}_{ah} + \dot{W}_{fans} \qquad (3.8)$$

Neglecting the heat loss through the calorimeter walls since $\Delta T_{cal} = 0$, and considering the energy transfer in the compressor only, the previous equation becomes,

$$\dot{Q}_{TEC} = \dot{W}_{ah} + \dot{W}_{fans} + \underbrace{(\dot{W}_{comp} - \dot{W}_{ind})}_{\dot{Q}_{shell,eb}} \qquad (3.9)$$

where $\dot{Q}_{shell,eb}$ is the heat dissipation rate through the compressor shell computed via an energy balance on the compressor itself.

It should be remembered that the aim of the calorimeter is to determine $\dot{Q}_{shell,eb}$ indirectly, i.e., not through measurements of the compressor electrical power consumption and indicated power. Therefore, $\dot{Q}_{shell,eb}$ is substituted by $\dot{Q}_{shell,cal}$ in Eq. (3.9). Hence, one has,

$$\dot{Q}_{TEC} = \dot{W}_{ah} + \dot{W}_{fans} + \dot{Q}_{shell,cal} \qquad (3.10)$$

Thus the heat dissipation rate through the compressor shell calculated via the calorimeter energy balance, $\dot{Q}_{shell,cal}$, is given by,

$$\dot{Q}_{shell,cal} = \dot{Q}_{TEC} - \dot{W}_{ah} - \dot{W}_{fans} \qquad (3.11)$$

3.4.4 Calibration

A calibration procedure was performed with the aim of determining the cooling capacity of the thermoelectric cooler for $\Delta T_{cal} = 0$ at $T_{room} = 25°C$. The procedure consisted of ten-repeated tests for which the calorimeter was operated with the compressor off. Therefore, Eq. (3.10) becomes,

$$\dot{Q}_{TEC} = \dot{W}_{ah} + \dot{W}_{fans} \qquad (3.12)$$

By knowing the work rates on the right-hand side of Eq. (3.12), the cooling capacity of the thermoelectric cooler, $\dot{Q}_{TEC}$, at $\Delta T_{cal} = 0$ can be determined straightforwardly. The electrical power consumption of the fans, $\dot{W}_{fans}$, was obtained from a series of power measurements with each centrifugal fan and the internal cooler fan of the TEC. Measurements of voltage and current were carried out using two digital multimeters (Minipa - Model ET-2517A). The measurements were repeated five times for each fan. The averaged total electrical

power consumption of the five fan coolers (including the TEC) was $\dot{W}_{fans} = 57.33 \pm 3.10$ W. From the experiments with the four compressor fan coolers, the average power consumption of one single fan was $\dot{W}_{fan} = 12.44 \pm 0.77$ W. The procedure to calculate the uncertainty of $\dot{W}_{fan}$ and $\dot{W}_{fans}$ can be found in Appendix A.

The calibration procedure starts by adjusting the room temperature to the desired value of 25℃. Then, the centrifugal fans were turned on to promote air mixing inside the calorimeter. Afterwards, the thermoelectric cooler and the air heater were switched on so that the internal temperature of the calorimeter reaches and stays at 25℃. After the steady state was reached, the calorimeter was operated for 2 hours. During this time interval, the time series of the temperatures, T_{room} and T_{cal}, and the input thermal power dissipated by the air heater, $\dot{W}_{ah}$, were saved for data analysis. Figure 3.26 presents a typical time-dependent behavior of T_{room}, T_{cal} and $\dot{W}_{ah}$, demonstrating the effectiveness of the control strategies.

Table 3.5 outlines the results of the calibration procedure. The mean of the ten-measurement averaged values is reported for the input thermal power, $\dot{W}_{ah}$, and calorimeter temperature difference, ΔT_{cal}. The standard deviation of the averaged values is also presented.

Table 3.5 – Results for the calibration procedure of the calorimeter.

Parameter	Mean	Standard Deviation
$\dot{W}_{ah}$	86.10 W	0.62 W
ΔT_{cal}	0.18℃	0.06℃

During the calibration tests, it was observed that the maximum data scatter, i.e., the maximum standard deviation of the instantaneous values for each test, regarding $\dot{W}_{ah}$ and ΔT_{cal} was 4.45 W and 0.17℃, respectively. Using the mean values for $\dot{W}_{ah}$ and $\dot{W}_{fans}$, Eq. (3.12) gives the cooling capacity of the thermoelectric cooler, i.e., $\dot{Q}_{TEC} = 143.42 \pm 4.23$ W. Again, the mathematical procedure to determine the uncertainty of the calculated parameter $\dot{Q}_{TEC}$ is described in detail in Appendix A.
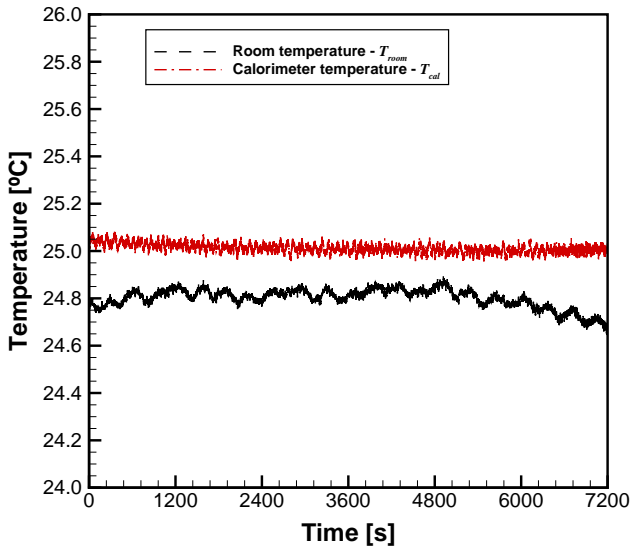
(a) Room and calorimeter temperatures
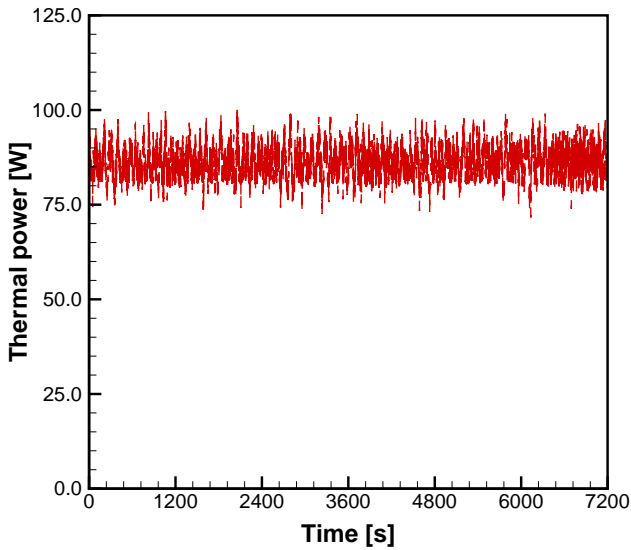
(b) Thermal power dissipated by the air heater

Figure 3.26 – Time-dependent behavior of calorimeter variables during the calibration procedure: (a) temperatures and (b) thermal power.

3.5   Thermal Insulation and Leakage Tests

In order to perform the experimental tests, the experimental apparatus was thermally insulated with elastomeric foam pipes, as shown in Figure 3.27. Some components of the test facility were wrapped in a thick layer of thermal insulation such as the condenser, the mass flow meter and, particularly, the two-phase jet cooler.
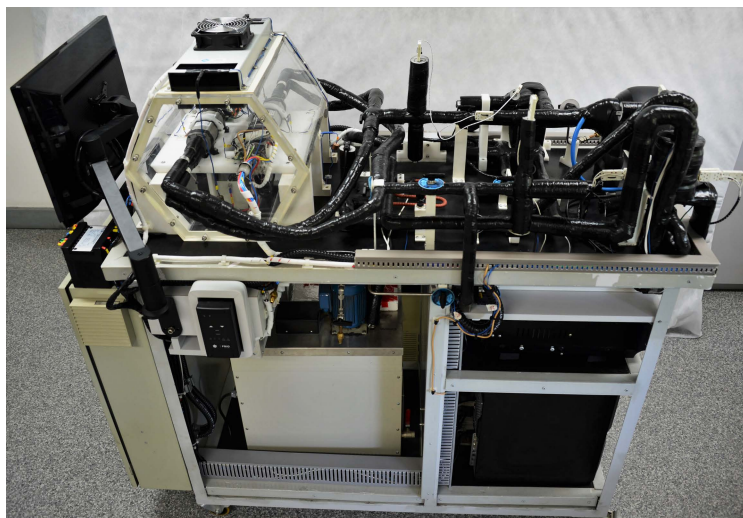
Figure 3.27 – Thermally insulated experimental apparatus.

When one is dealing with a closed-loop vapor compression refrigeration system, a fundamental operating concern is to guarantee the continuity of the refrigerant mass (charge) inside the system. Therefore, leakage tests were performed according to two fronts: (i) tests focusing on the refrigeration circuit, particularly the discharge and suction lines as well as the secondary evaporation circuit (see Figure 3.4), and (ii) tests focusing exclusively on the two-phase jet cooler. Previously to the leakage tests, the experimental facility was carefully inspected in order to find and fix leakage points. Appendix B describes the procedure adopted to perform the leakage tests. The results of the two-front tests evinced that the assembly of the proposed active cooling system provides proper sealing to perform the experimental investigation.

3.6   Experimental Procedure

To perform the proposed experimental investigation, an in-house LabVIEW code was developed to automate the operation of the experimental apparatus, control important variables and record selected data. Once the experimental facility was evacuated and filled with a charge of R-134a, the following steps were executed in order to properly operate the active cooling system and coordinate the experimental tests:

1. The room temperature was set;

2. The electrical panel was switched on;

3. The data acquisition system, desktop computer, and power meter were turned on;

4. After the LabVIEW code was initialized, the operation of the calorimeter was started, i.e., turn on the centrifugal fans, the thermoelectric cooler and the air heater. For the latter, the calorimeter temperature was set in the PID controller subroutine (subVI) that modulates the dissipated thermal power;

5. In the LabVIEW code, the operation of the secondary cooling circuit was started. Afterwards, the temperature of the WEG mixture was set at both thermostatic baths and its mass flow rate was adjusted manually with the needle valve;

6. As the prescribed temperatures for the room, calorimeter and WEG mixture (at the condenser inlet) were reached, the operation of the compressor was started. The stabilization of the temperatures took from 15 to 20 minutes;

7. The compressor piston displacement was set;

8. Refrigerant was allowed to circulate through the refrigeration loop. Once there is refrigerant flow inside the jet heat sink, the DC power supply was turned on at a low cooling capacity (25 W);

9. At the superheating line, the electrical trace heater was turned on via the LabVIEW code. The temperature of the refrigerant at the suction line was set in the PID controller subroutine (subVI) that controls the Joule heating. By monitoring the evaporation temperature and by adjusting the set point of the suction temperature, the superheating degree at the compressor inlet was set;

10. The mass flow rate was adjusted to the desired value;

11. As the refrigeration system reached steady state, whose criteria is to be defined in Chapter 4, data was recorded.

4 Experimental Analysis of the Cooling System

This chapter discusses the experimental evaluation of the proposed refrigeration system. It starts with the presentation of the test matrices and the experimental plan. Next, performance metrics, steady-state heat transfer parameters and the expansion device thermodynamic model are introduced. Then, the measurement uncertainties and the repeatability of the experimental results are discussed. The effects of orifice diameter, compressor stroke, hot reservoir temperature, orifice-to-heater distance and orifice array geometry are quantified and evaluated from the system thermodynamic performance standpoint.

4.1 Experimental Plan

The experimental tests were conducted according to the conditions presented in the following tables. Tables 4.1 and 4.2 show the tests carried out to study the effect of the (single) orifice diameter, d_o, i.e., Matrices 1 and 2, respectively. Likewise, Matrices 1 and 3, the latter given in Table 4.3, are concerned with the influence of the jet length, H, i.e., the height of the jet chamber. Each matrix is divided in two groups, which are related to different temperatures of the hot-side reservoir, i.e., the temperature of the thermal bath.

For a given piston displacement of the compressor piston stroke, α, the cooling load was increased until the critical heat flux was reached. This explains the different number of tests per row in each one of the matrices. This procedure was adopted to guarantee the integrity of the test section. It is important to point out that some tests in Matrix 2 (t#6 and t#7 in Group B) could not be completed due to experimental problems, i.e., continuous pressure solicitations generated leakage points in the jet chamber.

Table 4.1 – Input variables for the experimental tests (t) of Matrix 1.

Matrix 1 (M1) - Jet cooler geometric parameters: single orifice with $d_o = 300\ \mu$m and $H = 28.84$ mm								
Group	α	Test cooling load [W]						
($T_{w,i}$ [°C])	[%]	t#1	t#2	t#3	t#4	t#5	t#6	t#7
	50	25	50	75	–	–	–	–
A (15)	75	25	50	75	100	120	–	–
	100	25	50	75	100	125	150	
B (25)	100	25	50	75	100	125	150	160

Table 4.2 – Input variables for the experimental tests (t) of Matrix 2.

Matrix 2 (M2) - Jet cooler geometric parameters: single orifice with $d_o = 500\ \mu$m and $H = 28.84$ mm								
Group	α	Test cooling load [W]						
($T_{w,i}$ [°C])	[%]	t#1	t#2	t#3	t#4	t#5	t#6	t#7
	50	25	50	75	85	–	–	–
A (15)	75	25	50	75	100	120	–	–
	100	25	50	75	100	125	150	160
B (25)	100	25	50	75	100	125	n.a.d.	n.a.d.

n.a.d. - no available data (experimental setup malfunction).

Table 4.3 – Input variables for the experimental tests (t) of Matrix 3.

Matrix 3 (M3) - Jet cooler geometric parameters: single orifice with $d_o = 300\ \mu$m and $H = 9.75$ mm						
Group	α	Test cooling load [W]				
($T_{w,i}$ [°C])	[%]	t#1	t#2	t#3	t#4	t#5
	50	25	50	75	–	–
A (15)	75	25	50	75	85.0	–
	100	25	50	75	82.5	–
B (25)	100	25	50	75	100	107.5

Whereas Matrices 1 to 3 are concerned with single-jet impingement cooling, Matrix 4 deals with the investigation of the refrigeration system behavior when multiple jet impingement configurations are adopted. Table 4.4 displays the conducted tests according to three jet arrays portrayed in Figure 4.1.

Table 4.4 – Input variables for the experimental tests (t) of Matrix 4.

Matrix 4 (M4) - Jet cooler geometric parameters: multiple orifices with $d_o = 300$ μm and $H = 28.84$ mm							
$T_{w,i}$ α	Multiple jet array	Test cooling load [W]					
		t#1	t#2	t#3	t#4	t#5	t#6
25℃ 100%	#1	75	100	125	150	175	200
	#2	75	100	125	150	175	200
	#3	75	100	125	150	175	200

(a) Multiple jet array #1   (b) Multiple jet array #2

(c) Multiple jet array #3
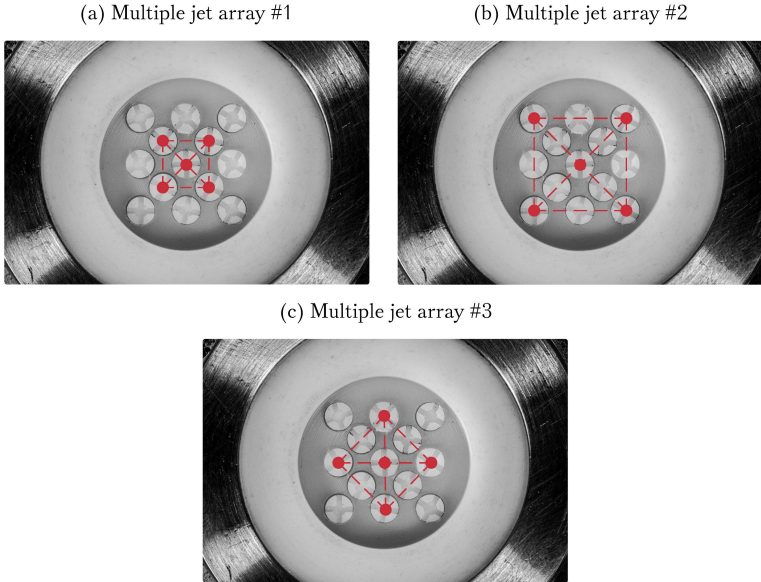
Figure 4.1 – Multiple jet arrays explored in Matrix 4.

Differently from the previous three matrices, all tests of Matrix 4 were run for fixed conditions of hot-side reservoir temperature and

compressor piston stroke. Besides, only moderate and high cooling capacities were considered. The reasons behind this choice will be presented along the text. The star-shaped jet arrays explored in Matrix 4 are different combinations of a five-orifice configuration, as illustrated in Figure 4.1. The same orifice diameter and jet impingement length were adopted in all tests of Matrix 4.

The operating conditions under which the experimental tests were run are presented in Table 4.5, where $\dot{m}_w$ represents the mass flow rate of the water-ethylene glycol mixture and $T_{w,i}$ its temperature at the condenser inlet. Variables T_{room}, T_{cal} and ΔT_{cal} denote the temperatures of the room, calorimeter and their absolute difference, i.e., $\Delta T_{cal} = |T_{room} - T_{cal}|$. ΔT_{sup} is the superheating degree at the compressor inlet, i.e., $\Delta T_{sup} = T_{comp,i} - T_{evap}$.

Table 4.5 – Operating conditions for the experimental tests in matrices 1 to 4.

Variable	Value
$\dot{m}_w$ [kg/h]	180
$T_{w,i}$ [°C]	15 and 25
T_{room} [°C]	25
T_{cal} [°C]	25
ΔT_{cal} [°C]	0
ΔT_{sup} [°C]	10

The output (dependent) variables of the experimental apparatus are the refrigerant mass flow rate, pressures, temperatures, refrigerant sub-cooling degree at the outlet of the condenser, vapor mass quality at the outlet of the two-phase jet cooler, heat transfer rates and compressor power. Based on the output variables, the jet impingement heat transfer coefficient and the system performance metrics can be calculated. These will be introduced in following sections.

All output data were recorded during a 15-minute time interval, $\Delta \tau$, after guaranteeing that the following steady-state criteria were simultaneously satisfied,

$$s(X)|_{\Delta \tau} \leq U(X) \tag{4.1}$$

$$\left(\max \frac{\partial X}{\partial \tau} \right) \Bigg|_{\Delta \tau} \Delta \tau \leq j \, s(X) \tag{4.2}$$

where $s(X)$ is the standard deviation of a generic output variable X and U expresses its corresponding overall experimental uncertainty. j is an integer corresponding to each one of the three divisions of the Gaussian probability distribution, i.e., $j = 1, 2$ or 3. The left-hand side of Eq. (4.2) was approximated by finite differences of the sampled variable using a second-order central scheme.

Before recording the data, Eqs. (4.1) and (4.2) were verified during three consecutive time intervals, $\Delta\tau$, to ascertain that the steady state was actually reached. The output data were recorded only when the left-hand side of Eq. (4.2) was lower than $2\,s(X)$.

It is important to mention that the same refrigerant mass flow rate was enforced on the first elements of Matrices 1 to 3, i.e., test t#1 for a piston stroke of 50%, as well as on test t#1 for each multiple jet array in Matrix 4. This was achieved by adjusting the refrigerant mass in the system through the ball valves in the charge line. Considering that each matrix actually corresponds to a distinct cooling system due to the different configurations of the jet cooler module, this procedure establishes a fair basis for comparing results for different matrices.

4.2 Dependent Variables

Energy balances between the inlet and outlet of the condenser and superheating line can be written as follows:

$$\dot{Q}_{cond} = \dot{m}_r(h_{cond,i} - h_{cond,o}) \tag{4.3}$$

$$\dot{Q}_{sh} = \dot{m}_r(h_{comp,i} - h_{jc,o}) \tag{4.4}$$

where $\dot{m}_r$ is the refrigerant mass flow rate. The refrigerant enthalpy at the compressor inlet, $h_{comp,i}$, condenser inlet, $h_{cond,i}$, and condenser outlet, $h_{cond,o}$, were computed via REFPROP 8.0 (LEMMON *et al.*, 2007) using the local experimental values of pressure and temperature.

The refrigerant enthalpy at the outlet of the two-phase jet cooler, $h_{jc,o}$, was calculated from the energy balance on the cooler, neglecting the kinetic and potential energy contributions. Thus:

$$h_{jc,o} = h_{jc,i} + \frac{\dot{Q}_c}{\dot{m}_r} \tag{4.5}$$

where $\dot{Q}_c$ is the cooling capacity and the refrigerant specific enthalpy at the inlet of the jet cooler, $h_{jc,i}$, was determined from local measure-

ments of pressure and temperature.

The vapor mass quality at the exit of the jet cooler, $x_{jc,o}$, was determined using $h_{jc,o}$ and the measured outlet pressure, $P_{jc,o}$. The saturation pressures were calculated directly from the experimental data, i.e., $P_{evap} = P_{jc,o}$ and $P_{cond} = P_{cond,o}$, both taken at the outlets of the jet heat sink and condenser, respectively.

The indicated power, i.e., the useful work performed on the refrigerant by the compressor per unit time, can be determined by the following equation,

$$\dot{W}_{ind} = \dot{m}_r(h_{comp,o} - h_{comp,i}) \tag{4.6}$$

where $h_{comp,o}$ is the enthalpy at the compressor outlet computed using the local experimental values of pressure and temperature. As will be seen, an energy balance on the compressor will give the energy rate dissipated as heat through the shell, $\dot{Q}_{shell}$, as the difference between the electrical power consumption, $\dot{W}$, and the indicated power, $\dot{W}_{ind}$.

The jet impingement (surface) heat transfer coefficient, $\hbar_s$, is a key parameter in the design of the two-phase jet cooler. It is defined by:

$$\hbar_s = \frac{\dot{Q}_c^*}{A_s \Delta T_s} \tag{4.7}$$

where $\Delta T_s = T_s - T_{evap}$ is the wall superheat of the impingement surface and $\dot{Q}_c^*$ is the corrected cooling capacity, i.e., the useful fraction of the input thermal (cooling) load, $\dot{W}_h$, that actually reaches the impingement surface, as previously discussed in Chapter 3. It was assumed that $\dot{W}_h = \dot{Q}_c$ for steady-state conditions and considering negligible thermal losses through the thermal insulation that covers the cooling system.

The temperature of the top (impingement) surface of the copper block, T_s, was determined through a linear extrapolation of Fourier's Law (POULIKAKOS, 1994) considering an one-dimensional heat conduction in the axial direction,

$$T_s = \overline{T}_{RTD} - \frac{L_s \dot{Q}_c^*}{A_s k_s} \tag{4.8}$$

where L_s is the distance between the copper block surface and the plane of the RTDs, $A_s = (\pi D^2)/4$ is the surface impingement area, D is the copper block surface diameter and k_s is the copper thermal conductivity evaluated at $\overline{T}_{RTD}$, which is the arithmetic mean of the five RTDs used to measure the copper block temperature.

4.3 Expansion Device (Nozzle) Model

The pressure drop experienced by the refrigerant as it flows through the jet cooler, ΔP_{jc}, was obtained directly from the difference between the absolute pressures measured at the cooler inlet, $P_{jc,i}$, and outlet, $P_{jc,o}$. Thus,

$$\Delta P_{jc} = P_{jc,i} - P_{jc,o} \tag{4.9}$$

The mixture velocity at the nozzle exit, V_o, and the vapor mass quality at the nozzle exit, x_o, were estimated using the expansion device model proposed by Oliveira and Barbosa (2015). This model is based on the assumption of homogeneous equilibrium two-phase flow (GHIAASIAAN, 2008), which is known to give reasonably accurate results (relative errors smaller than 15%) for adiabatic flows in capillary tubes (HERMES *et al.*, 2010).

The homogeneous model disregards the two-phase flow patterns and treats the liquid-vapor mixture as a pseudo fluid with average properties. The flow in the orifice was assumed to be one-dimensional, compressible and adiabatic. By neglecting the kinetic energy at the orifice inlet and the potential energy variation along the orifice length (justified by the small diameter and short orifice lengths, respectively), the energy conservation equation between the orifice inlet and the outlet gives,

$$h_{jc,i} = \bar{h}_o + \frac{V_o^2}{2} + \Delta h_f \tag{4.10}$$

The discharge velocity, V_o, is defined as,

$$V_o = \frac{\dot{m}_r}{\bar{\rho}_o A_o} \tag{4.11}$$

where $A_o = (\pi d_o^2)/4$ is the cross-sectional area of the orifice.

As the change in vapor mass quality along the orifice is expected to be small, the specific energy loss due to fluid friction, Δh_f, was calculated assuming a linear variation the vapor quality along the orifice length, L_o (OLIVEIRA; BARBOSA, 2015). Thus,

$$\Delta h_f = 2 C_f V_o^2 \left(\frac{L_o}{d_o} \right) \left(\frac{\bar{\rho}_o}{\rho_{l,o}} \right) \left[1 + \frac{x_o}{2} \left(\frac{\rho_{l,o}}{\rho_{v,o}} - 1 \right) \right] \tag{4.12}$$

The average two-phase enthalpy and density, evaluated at the orifice exit conditions, are defined by,

$$\bar{h}_o = x_o h_{v,o} + (1 - x_o) h_{l,o} \tag{4.13}$$

$$\bar{\rho}_o = \left[\frac{x_o}{\rho_{v,o}} + \frac{(1 - x_o)}{\rho_{l,o}} \right]^{-1} \tag{4.14}$$

The two-phase friction coefficient, C_f, was determined via the Blasius correlation for turbulent flow in smooth tubes,

$$C_f = \frac{0.079}{Re_o^{0.25}}, \tag{4.15}$$

where Re_o is the two-phase Reynolds number given by,

$$Re_o = \frac{\bar{\rho}_o V_o d_o}{\bar{\mu}_o} \tag{4.16}$$

and $\bar{\mu}_o$ is the two-phase dynamic viscosity at the orifice exit.

The average two-phase viscosity was calculated using the mean Maxwell-Eucken effective viscosity model (model #6) of Awad and Muzychka (2008) for it provided satisfactory agreement with experimental data for liquid-gas mixtures with large density ratios. Thus,

$$
\begin{aligned}
\bar{\mu}_o = \frac{1}{2} \Bigg[&\mu_{l,o} \frac{2\mu_{l,o} + \mu_{v,o} - 2(\mu_{l,o} - \mu_{v,o})x_o}{2\mu_{l,o} + \mu_{v,o} + (\mu_{l,o} - \mu_{v,o})x_o} + \\
&\mu_{v,o} \frac{2\mu_{v,o} + \mu_{l,o} - 2(\mu_{v,o} - \mu_{l,o})(1 - x_o)}{2\mu_{v,o} + \mu_{l,o} + (\mu_{v,o} - \mu_{l,o})(1 - x_o)} \Bigg]
\end{aligned}
\tag{4.17}
$$

In the solution of the above equations, the orifice outlet pressure was assumed equal to the jet chamber pressure, i.e., $P_o \approx P_{jc,o} = P_{evap}$. Therefore, the model equations presented above were solved numerically for the vapor mass quality that satisfies the energy balance. An in-house EES program (KLEIN, 2004) was developed specifically for this calculation.

The mixture velocity calculated according to Eq. (4.11) was compared with the sonic (or critical) velocity of the two-phase mixture defined as,

$$V_{o,cr} = \sqrt{\left. \frac{\partial P_o}{\partial \bar{\rho}_o} \right|_{s_{up}}} \tag{4.18}$$

which requires an isentropic flash calculation from the upstream conditions ($s_{up} = s_{jc,i}$) to the orifice exit pressure P_o. Homogeneous equilibrium two-phase flow was assumed in the sonic velocity calculation. The partial derivative in the previous equation was discretized via a second-order finite difference scheme (FERZIGER; PERIĆ, 2002). If the mixture velocity calculated from Eq. (4.11) is higher than the sonic velocity, then it can be assumed that choked flow exists at the orifice outlet and the mixture velocity is then equal to the sonic velocity.

4.4 Performance Metrics

The performance metrics of the present refrigeration system are defined based on the cooling capacity, energy transfer rates imposed on the system and the associated thermal resistances. Figure 4.2 depicts a schematic diagram of the main variables of an active cooling system for electronic devices.
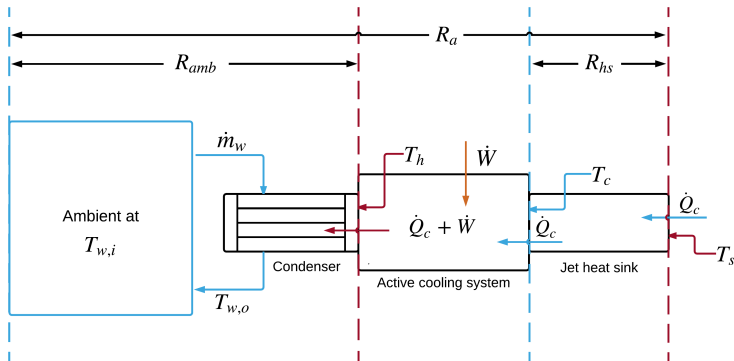
Figure 4.2 – Active cooling system for thermal management of electronic devices. Adapted from Miner and Ghoshal (2006).

Energy is drawn from the hot surface of the electronic equipment at a temperature T_s and a rate $\dot{Q}_c$ through a heat sink with thermal resistance R_{hs}. The active cooler consumes energy at a rate $\dot{W}$, i.e., the input work, and rejects both $\dot{Q}_c$ and $\dot{W}$ to an ambient at a constant temperature $T_{w,i}$ through a thermal resistance R_{amb}. The system operates between cold and hot side temperatures, T_c and T_h, respectively. In the present system, T_c and T_h correspond to the evaporating and condensing temperatures, i.e., T_{evap} and T_{cond}, respectively.

Three performance metrics are introduced to support the present analysis. The first one is the coefficient of performance considering the overall power consumption of the refrigeration system, COP_{os}, calculated by,

$$COP_{os} = \frac{\dot{Q}_c}{\dot{W}} \qquad (4.19)$$

where $\dot{W}$ is the total input work, which is made up of three parts,

$$\dot{W} = \dot{W}_{comp} + \dot{W}_{fan} + \dot{W}_{sh} \qquad (4.20)$$

where $\dot{W}_{comp}$ is the electrical power consumption of the compressor, $\dot{W}_{fan}$ is the electrical power consumption of a single cooler fan and $\dot{W}_{sh}$ is the input superheating thermal power provided by an electrical (trace) heater wrapped around the compressor suction line.

It should be noted that $\dot{W}_{sh}$ is responsible for providing the refrigerant superheating heat transfer rate in Eq. (4.4). It is actually slightly higher than $\dot{Q}_{sh}$ because of thermal losses from the trace heater to the ambient.

$\dot{W}_{sh}$ (and $\dot{Q}_{sh}$) are necessary to guarantee the superheating degree at the compressor inlet required for a safe operation of the compressor. Moreover, as in other high-thermal performance heat sinks, such as microchannel heat exchangers (MARCHINICHEN *et al.*, 2013), the heat sink overall thermal conductance decreases significantly as the outlet vapor quality increases. This means that, to generate the high heat transfer coefficients required to remove the high heat fluxes and maintain a low surface temperature, there must be a significant liquid fraction at the outlet of the heat sink. In a laboratory test device such as the present facility, Joule heating is the preferred mode of supply of $\dot{W}_{sh}$ due to its low cost and simple control. However, in a real application, the superheating thermal energy may come from another heat transfer process (HOU *et al.*, 2015) or from an internal heat exchanger (BARBOSA; HERMES, 2006), not necessarily adding to the electrical supply to the system.

Hence, a modified version of the coefficient of performance can be introduced as in Eq. (4.19). This coefficient of performance accounts for the energy consumption strictly necessary to remove the imposed heat load upon the jet cooler, COP_{jc}, and is given by,

$$COP_{jc} = \frac{\dot{Q}_c}{\dot{W}_{comp} + \dot{W}_{fan}} \qquad (4.21)$$

The second performance metric is the second-law efficiency, η. This parameter can help to quantify the external irreversibilities in the system, i.e., those linked to the heat transfer with finite temperature differences in the heat exchangers. It is defined as the ratio of the coefficient of performance of the real refrigeration system to that obtained assuming an ideal cooling device operating with real heat exchangers (BARBOSA *et al.*, 2012; HERMES; BARBOSA, 2012). Based on the previous COP definitions, two second-law efficiencies can be defined,

$$\eta_{os} = \frac{COP_{os}}{COP_{id}} \tag{4.22}$$

$$\eta_{jc} = \frac{COP_{jc}}{COP_{id}} \tag{4.23}$$

where COP_{id} is the ideal (Carnot) coefficient of performance based on saturation temperatures of the refrigerant in the condenser and evaporator (jet heat sink) (BARBOSA, 2011; BARBOSA *et al.*, 2012),

$$COP_{id} = \frac{T_{evap}}{T_{cond} - T_{evap}} \tag{4.24}$$

The third performance metric accounts for the internal and external irreversibilities in the refrigeration system. Different from the thermodynamic approach of Barbosa *et al.* (2012) and Hermes and Barbosa (2012), Miner and Ghoshal (2006) proposed an alternative figure of merit to evaluate the overall performance of the active cooling system, which incorporates more directly the thermal resistances associated with the heat transfer rates in the heat exchangers.

Miner and Ghoshal (2006) pointed out the inability of the second-law efficiency alone to capture the effects of performance degradation that arise from the resistances to heat flow into the active cooler near the source of heat, R_{hs}, and out of it near the hot-side reservoir, R_{amb}. Based on the thermal analysis of a passive cooling system, and using the concept of thermal resistance, they proposed a temperature rise per watt of cooling power (a quasi-thermal or apparent resistance) as a performance variable for active cooling systems.

The *apparent* thermal resistance of the active cooler, R_a, is defined as,

$$R_a = \frac{T_s - T_{w,i}}{\dot{Q}_c} \tag{4.25}$$

Similarly, the combined thermal resistance of the hot and cold

ends, R_c, is expressed by,

$$R_c = R_{amb} + R_{hs} \tag{4.26}$$

where R_{hs} and R_{amb} are, respectively, given by,

$$R_{hs} = \frac{T_s - T_{evap}}{\dot{Q}_c} \tag{4.27}$$

$$R_{amb} = \frac{T_{cond} - T_{w,i}}{\dot{Q}_c + \dot{W}} \tag{4.28}$$

Using the definitions of COP and η, introduced in Eqs. (4.19) to (4.24), and after some algebraic manipulation, Eq. (4.25) can be re-written as,

$$R_a = \frac{2\Delta T_a R_c}{\Delta T_a - \gamma + \sqrt{4R_c T_s \dot{W}\eta + (\gamma - \Delta T_a)^2}} \tag{4.29}$$

where ΔT_a and γ are given by,

$$\Delta T_a = T_s - T_{w,i} \tag{4.30}$$

$$\gamma = \dot{W}(R_{amb} + \eta R_{hs}) \tag{4.31}$$

According to Miner and Ghoshal (2006), the apparent thermal resistance, R_a, should be lower than the combined thermal resistance of the system reservoirs, R_c, in order to justify the benefit of implementing an active cooling solution for electronics thermal management.

Miner and Ghoshal (2006) also propounded a minimum second-law efficiency, η_{min}, that a system with an active component must exhibit to perform equally as the *identical system without active cooling*. Equating the thermal resistances defined by Eqs. (4.26) and (4.29) and solving for the efficiency that satisfies this relation, one obtains,

$$\eta_{min} = \frac{T_s - T_{w,i}}{\left(\dfrac{R_{hs}}{R_{amb}}\right)T_{w,i} + T_s} \tag{4.32}$$

It should be clear that the apparent resistance R_a can be calculated using both Eqs. (4.25) or (4.29), however Eq. (4.29) is necessary to derive Eq. (4.32). A second-law ratio, η^*, can be introduced to evaluate how efficient the active cooling system is in comparison with its *passive* counterpart. Therefore, the third metric is defined as,

$$\eta^* = \frac{\eta}{\eta_{min}} \tag{4.33}$$

The above relation, Eq. (4.33), allows one to to better evaluate the merits of moving from *simple passive cooling* to an active cooling solution. The mathematical derivation of Eqs. (4.29) and (4.32) is presented in Appendix C.

4.5   Experimental Uncertainty Analysis

The experimental uncertainties were evaluated according to the procedure presented in Coleman and Steele (2009) and INMETRO (2012). The dependent variables and performance metrics were calculated based on experimental measurements of independent variables, X, such as temperature, pressure and mass flow rate. The combined standard uncertainty of a dependent variable $\xi = f(X_1, X_2, ..., X_m)$, denoted by $u(\xi)$, can be expressed by,

$$u(\xi) = \sqrt{\left[\frac{\partial \xi}{\partial X_1} u(X_1) \right]^2 + \left[\frac{\partial \xi}{\partial X_2} u(X_2) \right]^2 + ... + \left[\frac{\partial \xi}{\partial X_m} u(X_m) \right]^2}$$
$$\tag{4.34}$$

where $u(X_j)$ with $j = 1, 2, ..., m$ are the standard uncertainties from each possible source.

The expanded uncertainty of ξ, $U(\xi)$, is calculated as,

$$U(\xi) = k_{95} u(\xi) \tag{4.35}$$

where k_{95} is the Student's t-distribution factor calculated based on the effective number of degrees of freedom and on the confidence level.

Table 4.6 presents the expanded uncertainty for the calculated parameters explored in the present analysis. It should be understood that $U(\xi)$ varies according to each experimental run. Therefore, the maximum values are reported for each parameter and for each matrix. In addition to the uncertainty calculation procedure for the measured parameters, Appendix A describes the uncertainty propagation analysis in more detail and presents the mathematical expressions associated with the uncertainty computation of each calculated parameter.

For some calculated parameters, the expanded uncertainty does not vary between the experimental tests. Their $U(\xi)$ values are summarized below:

- $U(T_{room}) = 0.09°C$;

- $U(T_{cal}) = 0.05°C$;

- $U(\Delta T_{cal}) = 0.10°C$;

- $U(\Delta P_{jc}) = 0.03$ bar;

- $U(\dot{Q}_{shell,cal}) = 5.29$ W.

Table 4.6 – Expanded uncertainties (maximum values) of the experimental parameters for each matrix.

Expanded uncertainties - $U(\xi)$				
Parameter (ξ)	Matrix 1	Matrix 2	Matrix 3	Matrix 4
Heat transfer rates				
$\dot{Q}_c$ [W]	1.77	1.77	1.42	2.01
$\dot{Q}_{sh}$ [W]	2.73	2.76	2.58	2.93
$\dot{Q}_{cond}$ [W]	3.07	3.09	3.08	2.88
$\dot{Q}_{shell,eb}$ [W]	6.87	5.13	5.22	5.10
Work rates				
$\dot{W}_{ind}$ [W]	0.42	0.41	0.40	0.42
$\dot{W}_{comp}$ [W]	4.53	4.43	4.51	4.43
Coefficients of performance				
COP_{os} [-]	0.03	0.03	0.02	0.05
COP_{jc} [-]	0.49	0.61	0.44	0.23
Temperatures				
T_s [°C]	0.10	0.10	0.09	0.11
T_{evap} [°C]	0.26	0.26	0.24	0.22
T_{cond} [°C]	0.09	0.10	0.10	0.09
ΔT_s [°C]	0.27	0.27	0.26	0.24
ΔT_{sup} [°C]	0.31	0.31	0.30	0.28
ΔT_{sub} [°C]	0.17	0.18	0.18	0.17
Other parameters				
$x_{jc,o}$ [-]	0.013	0.011	0.012	0.009
$\hbar_s$ [W/(m^{2}K)]	433	1056	277	285

4.6 Repeatability of the Results

The first performance evaluation of the cooling apparatus focused on demonstrating the repeatability of the experimental results. For each piston stroke, two tests from Group A of Matrix 1 (Table 4.1) were selected for the evaluation, which consisted of the following procedure:

- The experimental setup was evacuated and filled with a charge of R-134a;

- The desired mass flow rate was set for the first element of Matrix 1 (Group A), i.e., test t#1, for a compressor piston displacement of 50%;

- The selected experimental tests were executed two times by running the refrigeration system on different days.

Table 4.7 reports the relative difference, Θ, between each pair of repeatability tests ($t_r\#1$ and $t_r\#2$) for the independent (raw data) variables and two dependent parameters. The raw data consist of the refrigerant mass flow rate as well as pressures and temperatures measured at several points of the experimental apparatus (inlet and outlet of the compressor, condenser, thermal bath, jet heat sink and copper block). The dependent variables are the condenser heat transfer rate and the surface (jet impingement) heat transfer coefficient. The following equation shows how Θ was computed,

$$\Theta_X = \left| \frac{X_{t_r\#1} - X_{t_r\#2}}{X_{t_r\#1}} \right| \times 100\% \qquad (4.36)$$

where X is a dummy variable/subscript that stands for P, T, $\dot{m}_r$, $\dot{Q}_{cond}$ and $\hbar$.

In Table 4.7, the values of Θ_P and Θ_T are reported in terms of the average and maximum values. A very good repeatability of the experimental results can be inferred, as the relative difference is lower than 10% for all averaged values of P and T. The same holds for $\dot{m}_r$, $\dot{Q}_{cond}$ and $\hbar$. Special attention should be paid to $\dot{m}_r$ and $\dot{Q}_{cond}$, for which the averaged values are lower than 6%. As regards Θ_P and Θ_T, except for two values around 10%, the majority of the maximum relative differences are also lower than 10%.

It should be emphasized that the good results presented in Table 4.7 are directly related to the robust instrumentation and advanced

control strategies adopted in this experimental apparatus. In order to express the quality of the variable control strategies, Appendix D introduces several tables with the measured values of the operating parameters shown in Table 4.5 during each test. The results presented in Appendix D indicate that the parameters were successfully controlled and kept fairly constant with small variations that were lower than their corresponding experimental uncertainties.

Table 4.7 – Values of Θ_X in the repeatability tests.

Matrix 1 - Group A								
α	$\dot{Q}_c{}^\dagger$	P [%]		T [%]		$\dot{m}_r$	$\dot{Q}_{cond}$	$\hbar_s$
[%]	[W]	avg.	max.	avg.	max.	[%]	[%]	[%]
50	25	6.1	9.5	3.1	8.3	5.9	5.5	2.2
	75	1.9	2.7	1.2	4.6	0.6	0.8	9.3
75	25	3.7	6.0	1.4	4.0	0.5	0.1	2.4
	50	6.4	10.8	1.8	5.6	0.8	1.4	7.7
100	25	1.8	2.7	3.4	6.0	3.2	4.0	0.1
	150	2.5	3.2	1.4	4.0	0.5	0.8	6.3

†Nominal cooling capacities.

It is important to introduce information on the energy balances performed on the experimental setup. The first-law (heat balance) residue, δ_{1st}, is defined as the difference between the heat transfer rates out of and into the refrigeration system,

$$\delta_{1st} = |\dot{Q}_{cond} - (\dot{Q}_c + \dot{Q}_{sh} + \dot{W}_{ind})| \qquad (4.37)$$

which can also be expressed in relative terms,

$$\delta_{1st,\%} = \frac{\delta_{1st}}{\dot{Q}_c + \dot{Q}_{sh} + \dot{W}_{ind}} \times 100\% \qquad (4.38)$$

Furthermore, an indirect approach to verify whether the first-law balance is satisfied is to compute the calorimeter heat balance residue, δ_{cal}, defined as,

$$\delta_{cal} = |\dot{Q}_{shell,cal} - \dot{Q}_{shell,eb}| \qquad (4.39)$$

where $\dot{Q}_{shell,cal}$ is the heat transfer rate through the compressor shell estimated using the calorimeter heat balance introduced in Chapter 3,

Eq. (3.4), and $\dot{Q}_{shell,eb}$ represents its corresponding value calculated directly from the following difference,

$$\dot{Q}_{shell,eb} = \dot{W}_{comp} - \dot{W}_{ind} \qquad (4.40)$$

Likewise, the calorimeter heat balance residue can also be expressed in relative terms,

$$\delta_{cal,\%} = \frac{\delta_{cal}}{\dot{Q}_{shell,eb}} \times 100\% \qquad (4.41)$$

Table 4.8 reports the average and maximum values of δ_{1st} and δ_{cal} for each test matrix. They are expressed in absolute (abs.) terms, Eqs. (4.37) and (4.39), and relative (rel.) terms, Eqs. (4.38) and (4.41), respectively.

Table 4.8 – Heat balance residues.

Matrix	Type of value	δ_{1st}		δ_{cal}	
	abs. [W] and rel. [%]	avg.	max.	avg.	max.
1	abs. [W]	2.2	5.7	4.4	8.2
	rel. [%]	0.9	2.1	9.7	14.8
2	abs. [W]	1.7	3.7	1.8	3.8
	rel. [%]	0.7	1.5	6.8	20.6
3	abs. [W]	2.1	5.0	3.1	6.7
	rel. [%]	0.9	1.8	8.6	14.7
4	abs. [W]	3.6	4.1	1.7	3.6
	rel. [%]	1.3	1.5	4.5	9.0

According to the results presented in Table 4.8, the very small values of $\delta_{1st,\%}$, which are lower than 2.5%, confirm that the first-law heat balance is fully satisfied. Besides, the calorimeter heat balance average residue also exhibits fairly low values ($< 10\%$) indicating that the heat leaks that may affect the computation of $\dot{Q}_{shell,eb}$ can be considered negligible for practical purposes. This can be understood as a very good result considering the significant challenges encountered in measuring accurately the heat dissipation rate through the compressor shell using the calorimeter.

4.7   Results for Matrix 1

This analysis is divided into two subsections concerned with the parameters and metrics that characterize the performances of the refrigeration system as a whole as well as the two-phase jet heat sink, respectively.

4.7.1   Cooling System Parameters

Figure 4.3 presents the values of the system mass flow rate. As expected, for a given cooling capacity, increasing the piston stroke yields higher mass flow rates, which results also in a gradual increase of the pressure lift, i.e., the difference between the condensing and evaporating pressures, as seen in Figure 4.4.
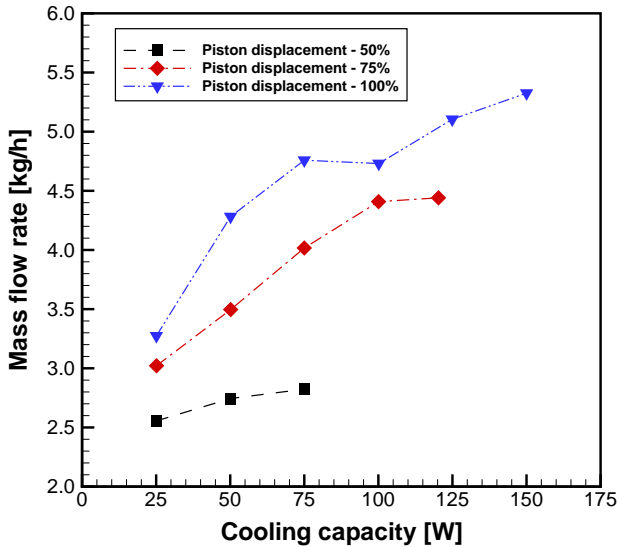
Figure 4.3 – Refrigerant mass flow rate as a function of the cooling load (results for Matrix 1 - Group A).

For a fixed piston stroke, higher cooling loads impose a continuous increase of the condenser heat transfer rate in order to satisfy the first-law balance, as shown in Figure 4.5. Therefore, higher flow rates resulting from the increase in refrigerant density at the compressor inlet (increasing evaporating pressures) are observed.
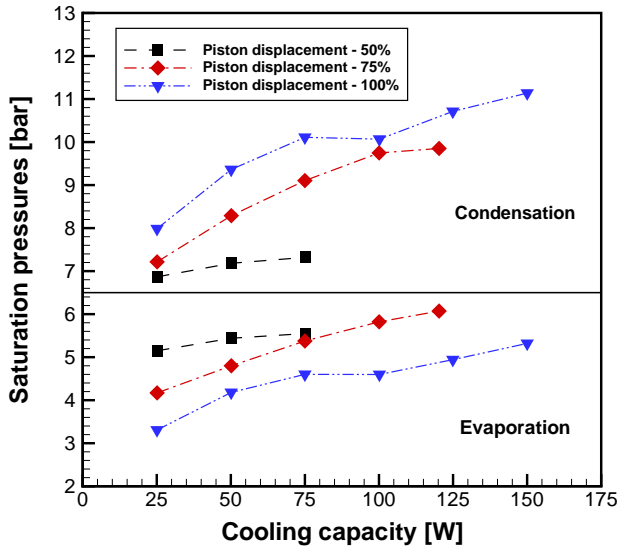
Figure 4.4 – Saturation pressures as a function of the cooling load (results for Matrix 1 - Group A).
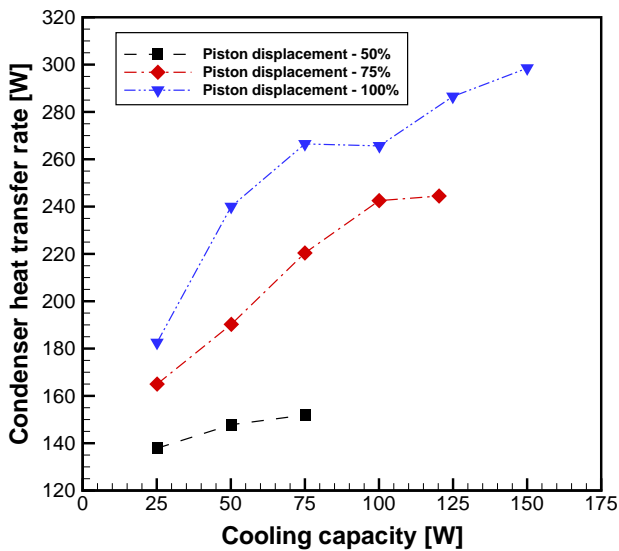
Figure 4.5 – Condenser heat transfer rate as a function of the cooling load (results for Matrix 1 - Group A).

In Figure 4.3, an uncommon behavior can be noticed, i.e., as the cooling load is increased from 75 W to 100 W, the mass flow rate decreases slightly. A possible explanation for that may be attributed to some compressor malfunction at the maximum piston stroke operation.

Figure 4.6 depicts the behavior of the superheating heat transfer rate, $\dot{Q}_{sh}$, required to maintain the superheating degree at 10℃. Despite the continuous downward trend shown by the curve for 50% piston stroke, the two remaining curves (75% and 100% piston stroke) initially increase and then go through a maximum at moderate values of cooling capacity.
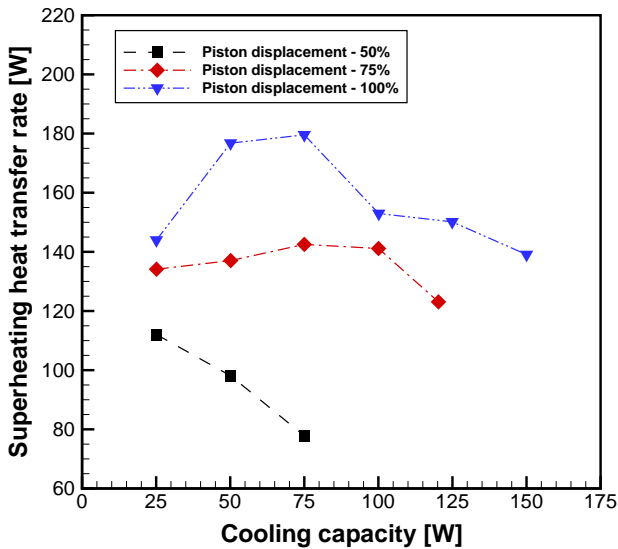
Figure 4.6 – Superheating heat transfer rate as a function of the cooling load (results for Matrix 1 - Group A).

The explanation for the observed trends lies in the behavior of the mass flow rate of the liquid phase at the outlet of the two-phase jet cooler, calculated as $\dot{m}_r(1 - x_{jc,o})$. As shown in Figure 4.7, the superheating heat transfer rate, $\dot{Q}_{sh}$, increases linearly with the liquid flow rate. Also, the input thermal power, $\dot{W}_{sh}$, is slightly higher than $\dot{Q}_{sh}$, reflecting the small heat losses to the ambient.

In Figure 4.6, $\dot{Q}_{sh}$ goes through a maximum for piston strokes of 75% and 100% because at low cooling capacities $\dot{m}_r$ is low, but $(1 - x_{jc,o})$ is high. As $\dot{Q}_c$ increases, the total mass flow rate increases, but the liquid mass fraction at the outlet of the test section is reduced.
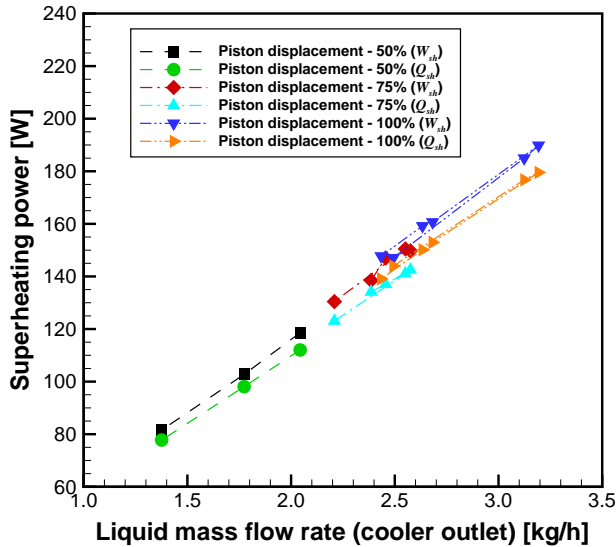
Figure 4.7 – Superheating power, $\dot{W}_{sh}$ and $\dot{Q}_{sh}$, as a function of the liquid-phase mass flow rate (results for Matrix 1 - Group A).

The behavior of the overall coefficient of performance of the refrigeration system is depicted in Figure 4.8. COP_{os} increases in a quasi-linear fashion with the cooling capacity. The sharpest increase is observed for $\alpha = 50\%$, for which the compressor electrical power consumption is virtually constant and is the lowest considering the entire range of piston displacements, as seen in Figure 4.9. In addition, the superheating heat transfer rate always decreases for this particular value of piston stroke, as previously shown in Figure 4.6. On the other hand, for a given thermal load, COP_{os} always decreases as the compressor electrical power consumption increases for greater values of piston displacement. Moreover, the resulting higher mass flow rate increases the superheating heat transfer rate, which contributes to lowering COP_{os}, as can also be observed in Figure 4.6.

Figure 4.8 demonstrates that the present compact cooling system reaches reasonable overall performances only at very high cooling capacities. According to the results presented for 75% and 100% piston strokes, for which the highest cooling capacities were attained, it is not beneficial to operate the system at $\dot{Q}_c < 75$ W because the Joule heating power required to superheat the refrigerant is at least twice as high as the imposed heat load, only decreasing for higher values of $\dot{Q}_c$.
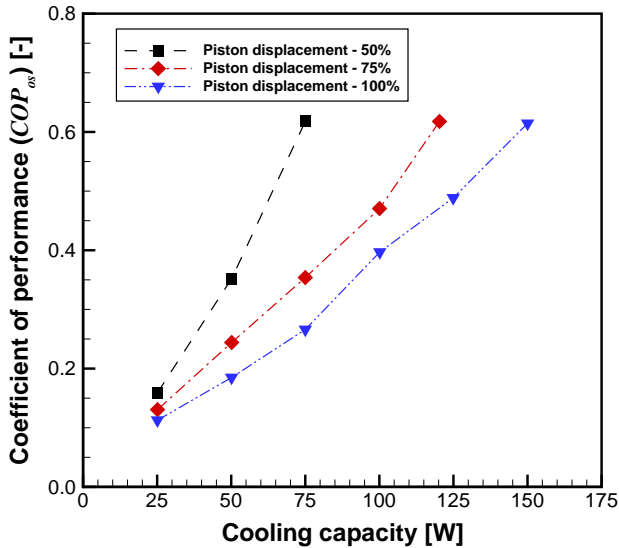
Figure 4.8 – Overall system *COP* as a function of the cooling load (results for Matrix 1 - Group A).
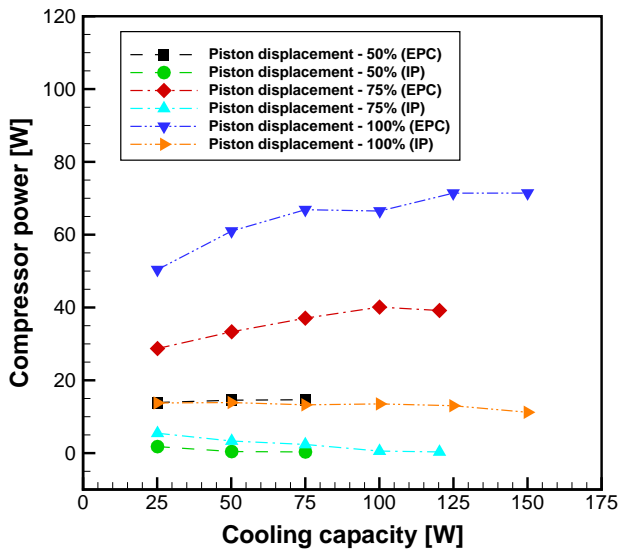
Figure 4.9 – Compressor power as a function of the cooling load (results for Matrix 1 - Group A). Abbreviations: Electrical Power Consumption (EPC) and Indicated Power (IP).

However, if the system could be combined with a heat source other than Joule heating for achieving the required superheating degree at the compressor inlet, the thermodynamic performance of the system could be significantly increased, as can be seen by the values of the modified (jet-cooler) coefficient of performance (COP_{jc}) shown in Figure 4.10.
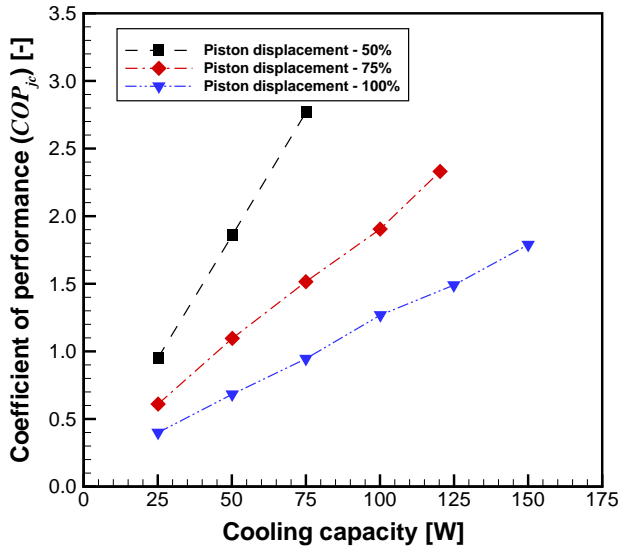
Figure 4.10 – Modified (jet-cooler) coefficient of performance (COP_{jc}) as a function of the cooling load (results for Matrix 1 - Group A).

Figure 4.9 also shows that only a small amount of the energy rate transferred to the compressor is actually used to raise the fluid pressure (indicated power). Thus the heat dissipated through the shell is quite high for all the three piston strokes investigated. The curves for $\alpha = 50\%$ and 75% exhibit values of indicated power of the order of a few watts. To some extent, this can be explained by the fact that the compressor is functioning outside (below) the operating envelope recommended by its manufacturer, as portrayed in Figure 4.11. It is important to point out that the values of indicated power close to zero were obtained via the calorimeter heat balance, computing the difference between $\dot{W}_{comp}$ and $\dot{Q}_{shell,cal}$, the latter given by Eq. (3.11). This was done to avoid large errors, as the computation of the work rate $\dot{W}_{ind}$ by means of Eq. (4.6) resulted in values of the order of magnitude of the expanded uncertainty ($\pm$ 0.42 W).
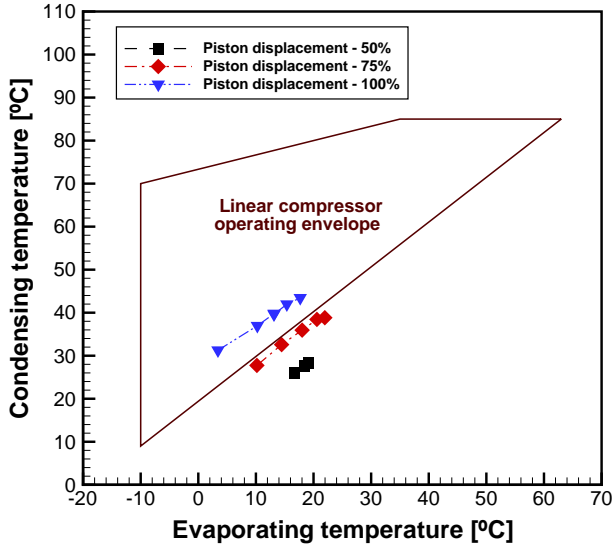
Figure 4.11 – Linear small-scale compressor operating envelope (results for Matrix 1 - Group A).

According to the definitions introduced in Section 4.4, the higher the value of η^* the more efficient the active cooling system is in comparison with its passive counterpart. Therefore, η^* should be always higher than unity for the active cooling system to offer a thermal advantage over passive cooling. Table 4.9 shows the values of the associated thermal resistances, second-law efficiencies and η^*. The graphical behavior of η^* is portrayed in Figure 4.12. Since this metric was negative for the first test at 100% of piston displacement, because $T_s < T_{w,i}$, it does not make sense to report these results in Figure 4.12.

Clearly, there is no benefit in operating the cooling system at the smallest piston stroke, particularly for cooling capacities of 25 W and 50 W. At these conditions, η^* is very close to unity. Therefore, a passive cooling solution may be more attractive, especially from the cost point of view. On the other hand, for the other piston strokes, the use of an active cooling solution is fully justified, since η^* is much greater than unity, more notably for $\alpha = 100\%$ (see Table 4.9).

As the cooling capacity is increased, η^* tends to unity, particularly for $\alpha = 75\%$. This behavior implies that for higher cooling loads, a better refrigeration system is necessary to achieve higher η^* values.

Table 4.9 – Performance metrics for Matrix 1 (overall system).

α [%]	$\dot{Q}_c$ [W]	R_c [K/W]	R_a [K/W]	η_{os} [%]	η_{min} [%]	$\eta*$ [-]
			Results for Group A			
	25.12	0.34	0.35	0.56	0.59	0.96
50	50.16	0.27	0.27	1.22	1.22	1.00
	75.05	0.25	0.24	2.17	1.75	1.24
	25.12	0.34	0.09	0.87	0.15	5.84
	50.16	0.27	0.19	1.64	0.88	1.87
75	75.00	0.23	0.20	2.32	1.69	1.37
	100.06	0.20	0.18	3.04	2.38	1.28
	120.29	0.19	0.17	3.78	2.92	1.30
	25.09	0.29	-0.23†	1.20	-0.48†	-2.50†
	50.11	0.27	0.11	1.83	0.51	3.61
100	75.00	0.23	0.14	2.59	1.10	2.35
	100.14	0.20	0.11	3.87	1.41	2.75
	124.92	0.19	0.12	4.74	1.99	2.38
	150.02	0.19	0.13	5.74	2.67	2.15

†Test for which $T_s < T_{w,i}$.
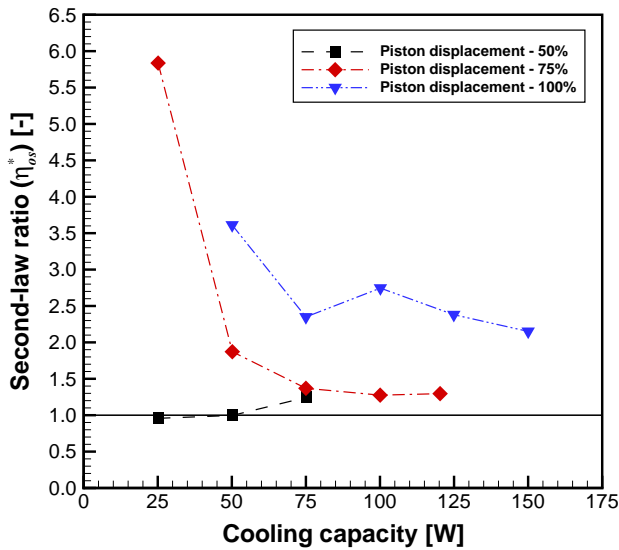
Figure 4.12 – Overall system second-law ratio, η_{os}^*, as a function of the cooling load (Results for Matrix 1 - Group A).

This could be done by adopting different design strategies concerning the two-phase jet heat sink, such as multiple jet arrays, different atomization techniques, or simply by using a more efficient linear compressor.

Based on the discussions in Section 4.4, the elimination of Joule heating to achieve the desired compressor inlet superheat substantially increases η^*, as depicted in Figure 4.13. The parameters presented in Table 4.9 were recalculated considering the modified (jet-cooler) coefficient of performance, COP_{jc}, and the updated values are given in Table 4.10.

As expected, the second-law efficiency η_{jc} can be significantly improved compared to η_{os}. It becomes evident that to remove higher heat loads it is necessary to operate the compressor at the full piston stroke to justify its application in an active cooling solution for the removal of high heat fluxes. This is confirmed by the second-law efficiency ratio, which indicates that the highest performance amongst all investigated conditions was achieved for $\alpha = 100\%$.

Table 4.10 – Performance metrics for Matrix 1 (jet cooler).

Results for Group A						
α [%]	$\dot{Q}_c$ [W]	R_c [K/W]	R_a [K/W]	η_{jc} [%]	η_{min} [%]	$\eta*$ [-]
50	25.12	0.50	0.35	3.09	1.33	2.32
	50.16	0.37	0.27	5.86	2.10	2.80
	75.05	0.31	0.24	8.72	2.54	3.44
75	25.12	0.48	0.09	3.79	0.33	11.40
	50.16	0.38	0.19	6.90	1.56	4.42
	75.00	0.32	0.20	9.33	2.62	3.55
	100.06	0.28	0.18	11.57	3.39	3.41
	120.29	0.25	0.17	13.33	3.85	3.46
100	25.09	0.41	-0.23[†]	4.02	-0.92[†]	-4.36[†]
	50.11	0.38	0.11	6.43	0.90	7.13
	75.00	0.32	0.14	8.80	1.76	5.00
	100.14	0.27	0.11	11.75	2.01	5.84
	124.92	0.25	0.12	13.73	2.69	5.11
	150.02	0.24	0.13	15.84	3.46	4.58

[†]Test for which $T_s < T_{w,i}$.
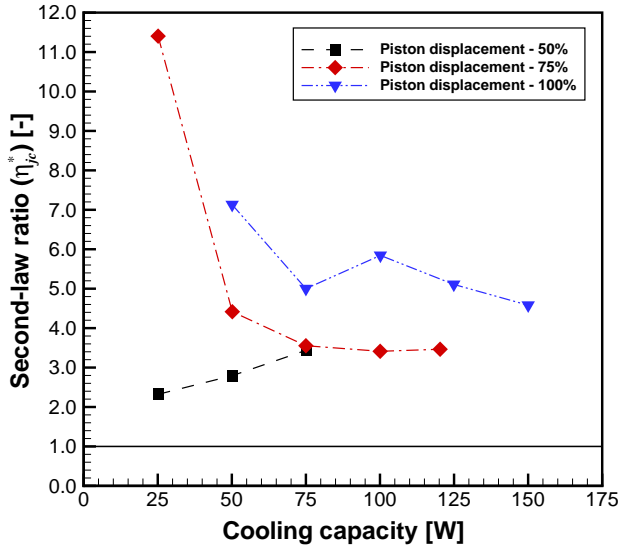
Figure 4.13 – Modified (jet-cooler) second-law ratio, η_{jc}^*, as a function of the cooling load (Results for Matrix 1 - Group A).
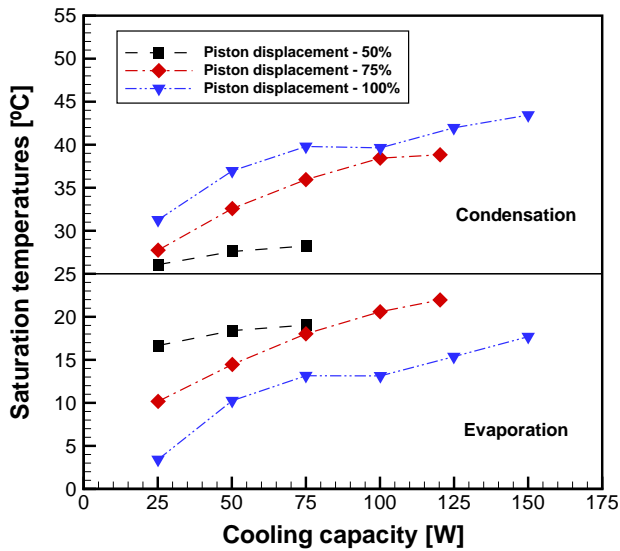
Figure 4.14 – Saturation temperatures as a function of the cooling load (results for Matrix 1 - Group A).

The second-law ratio, η^*, exhibits a general decreasing trend as a function of the increasing thermal load, as η_{min} is more sensitive to this variable than is η_{os} (or η_{jc}), as shown in Tables 4.9 and 4.10. Taking the overall system performance as an example, the increase of η_{os} can be explained by the combined effect of two factors: (i) the increase of COP_{os}, as demonstrated in Figure 4.8, and (ii) the very small influence of the cooling capacity on $\Delta T_{sat} = T_{cond} - T_{evap}$, for a fixed piston displacement, as can be seen in Figure 4.14. As a result, the ideal coefficient of performance, COP_{id}, changes very little.

4.7.2   Jet Cooler Parameters

Figure 4.15 presents the surface temperature for the tests in Group A, calculated using Eq. (4.8). For a constant cooling capacity, the surface temperature decreases significantly as a result of the increase in compressor piston stroke.
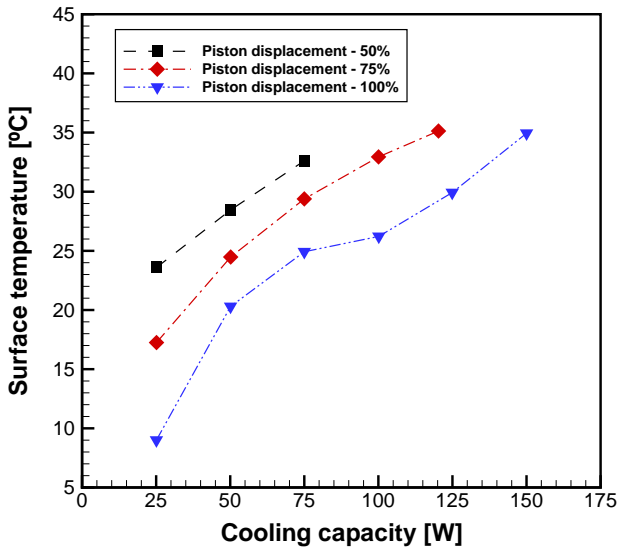
Figure 4.15 – Surface temperature as a function of the cooling load (results for Matrix 1 - Group A).

A major factor contributing to the lowering of the surface temperature is the reduction of the evaporating temperature inside the jet cooler chamber. As previously shown in Figure 4.14, the evaporating temperature is reduced for larger compressor piston strokes at a fixed

heat load. This is an immediate consequence of the higher mass flow rates delivered by the compressor, which help to build up a greater pressure difference between the condenser and the jet cooler chamber. The influence of the refrigerant mass flow rate on the behavior of the pressure drop across the jet heat sink is shown in Figure 4.16. Very distinct ranges of values are identified for the three compressor piston displacements.

The jet impingement heat transfer coefficient increases almost linearly with respect to the thermal load, as depicted in Figure 4.17. In principle, in addition to the wall heat flux (nucleate boiling component), the heat transfer coefficient is influenced by the refrigerant mass flow rate. However, it is not possible to completely separate the two effects, since the mass flow rate increases with the heat transfer rate. Taking the effect of the piston stroke alone, for a fixed cooling capacity, it is fair to say that the heat transfer coefficient is very mildly affected by the mass flow rate. As a matter of fact, the heat transfer coefficient is slightly lower for the 100% piston stroke.

A possible explanation for this lies in the increase of the liquid splattered fraction, which is shown to be directly proportional to the jet velocity (LIENHARD V, 2006). Strong splattering may result in significant atomization of the liquid jet. Since the airborne droplets do not contribute to the cooling of the wall, the heat transfer coefficient can be severely degraded (LIENHARD V, 2006). In the present experiments, visual observations revealed that the splattering rate is more significant at the highest flow rates. Nucleate boiling at the heater surface was observed to increase significantly with the thermal load. Heat transfer coefficients of the same order of magnitude of those reported by Ulson de Souza and Barbosa (2012, 2013) have been found for similar values of heat flux and mass flow rate.

As can be seen in Figure 4.18, the vapor quality at the outlet of the jet cooler increases also approximately linearly with the thermal load. The outlet vapor quality can be interpreted as an evaporation efficiency (XIE *et al.*, 2014), as the liquid that leaves the test section does not produce a cooling effect. Therefore, evaporation efficiencies higher than 50% are observed for all piston strokes, showing that the designed heat sink was capable of converting around 50% of the impinging liquid jet into vapor, which is the main physical mechanism responsible for the heat removal from the test surface.

Table 4.11 presents the values of the wall superheating degree, ΔT_s, for each piston stroke. They represent, in effect, the reciprocal of the behavior of the heat transfer coefficient shown in Figure 4.17.
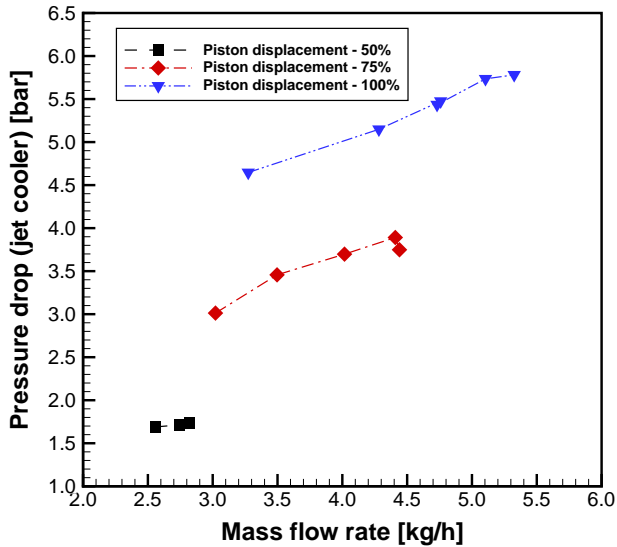
Figure 4.16 – Behavior of the pressure drop across the jet heat sink: influence of the refrigerant mass flow rate dependance (results for Matrix 1 - Group A).
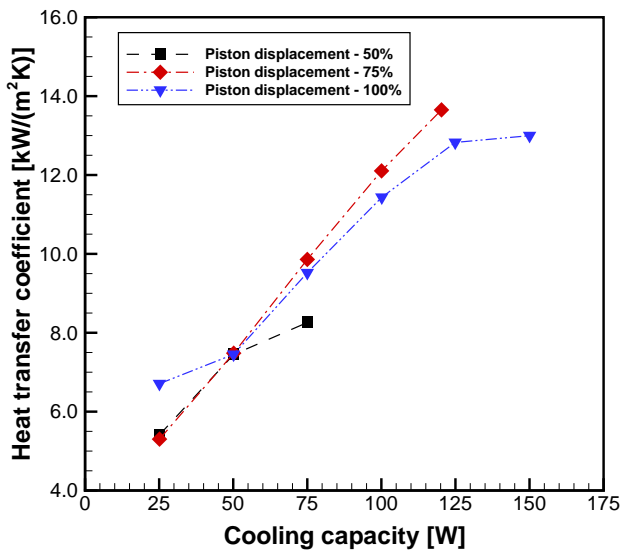
Figure 4.17 – Jet impingement heat transfer coefficient as a function of the cooling load (results for Matrix 1 - Group A).
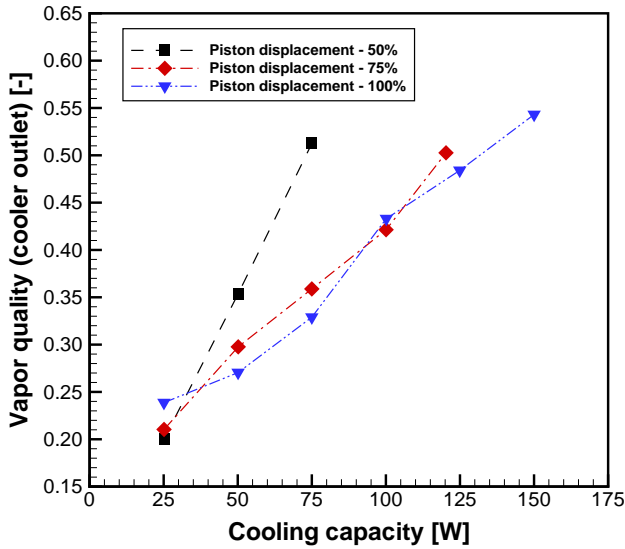
Figure 4.18 – Vapor mass quality at the outlet of the jet cooler as a function of the cooling load (results for Matrix 1 - Group A).

Table 4.11 – Values of the wall superheating degree.

Results for Group A		
α [%]	$\dot{Q}_c$ [W]	ΔT_s [℃]
50	25.12	6.94
	50.16	10.06
	75.05	13.58
75	25.12	7.08
	50.16	10.02
	75.00	11.37
	100.06	12.35
	120.29	13.17
100	25.09	5.59
	50.11	10.05
	75.00	11.77
	100.14	13.09
	124.92	14.56
	150.02	17.25

The ultimate limit to the increase of the evaporation efficiency is the critical heat flux. At this point, the liquid no longer touches the heated surface, which is covered by a vapor film. As a result, a sudden and sharp rise of the surface temperature is observed. As mentioned previously, the experimental tests were stopped just before the critical heat flux.

4.8   Results for Matrices 1 and 2

The previous section presented a detailed characterization of the refrigeration system behavior. Now, the effect of increasing the nozzle diameter is explored and a comparison between the results for Matrices 1 and 2 is performed. Firstly, the analysis is focused on the results for Groups A. Then, the results for Groups B are reported. Differently from the previous section, some parameters related to the jet cooler performance, such as pressure drop and outlet vapor quality, are examined together with the overall cooling system parameters to emphasize the connection between some variables.

At this point, it is worth remembering that the reference point between the two matrices is an equal mass flow rate for the first experimental run (test t#1). The refrigerant mass in the system (charge) was not measured and, most probably, it is not the same for matrices A and B; however, the two values may be close to each other. Considering each matrix independently, the mass of refrigerant is constant during all tests. This is guaranteed by the leakage tests described in the previous chapter.

4.8.1   Cooling System Parameters

Changing the orifice diameter of the orifice from 300 to 500 μm affects the saturation pressures in the way portrayed in Figure 4.19. The compressor discharge and suction pressures follow the same behavior of the saturation pressures. The orifice represents a restriction to refrigerant flow from the high-pressure side to the low-pressure side of the system. An orifice with a smaller diameter imposes a greater resistance to the flow of fluid so that a larger refrigerant mass is accumulated in the high-pressure components (condenser, Coriolis flow meter, pipes and hydraulic connections), which elevates the pressure upstream of the orifice. The larger pressure drop through the orifice reduces the pressure downstream.
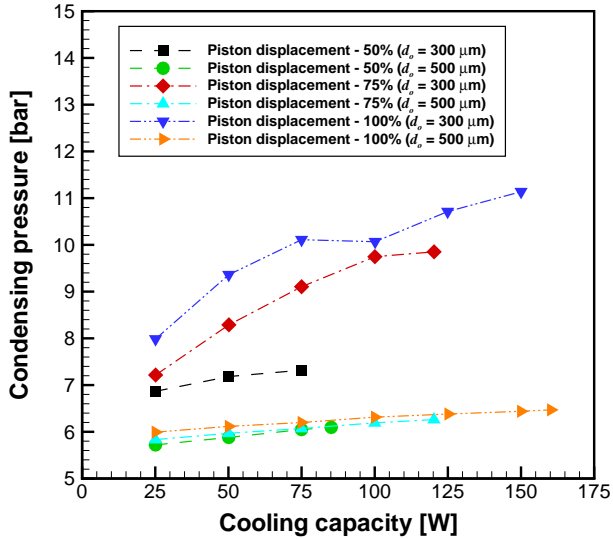
(a) Condensation
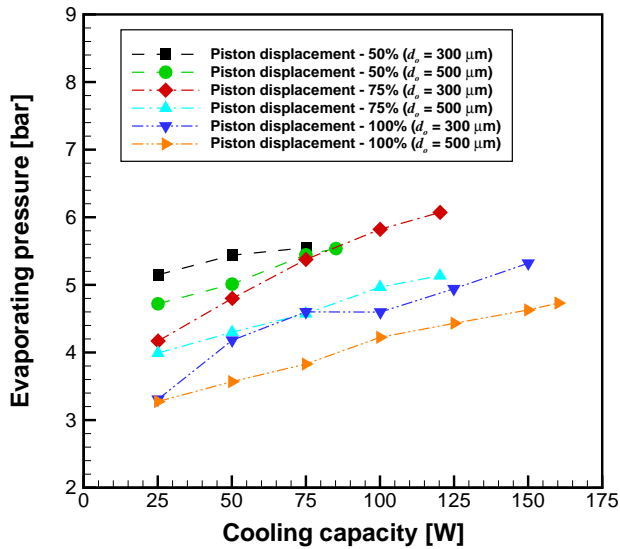
(b) Evaporation

Figure 4.19 – Saturation pressures as a function of the cooling load (comparison between Matrices 1 and 2 - Groups A).

An orifice with a larger diameter imposes a lower restriction, which reduces the condensing pressure as can be seen in Figure 4.19 (a). Besides, for a given cooling load, the separation between the curves for $d_o = 300$ μm is far greater than for $d_o = 500$ μm, for which condensing pressure also rises, but very slightly.

A somewhat unexpected behavior is observed in Figure 4.19 (b), as the evaporating pressures were higher for the 300-μm orifice for each value of piston displacement. A possible cause may be attributed to different refrigerant mass charges in the system regarding the different orifices investigated (the system is evacuated when a new orifice configuration is installed). As the internal volume of the system is small, little variations in the refrigerant mass can result in greater changes in pressure.

The *P-h* diagram portrayed in Figure 4.20 helps to understand the system response to the orifice diameter change, especially the evaporating pressure behavior, depicted in Figure 4.19 (b). Two refrigeration cycles are presented for tests with same piston stroke (100%) and cooling load (150 W). Moreover, the mass flow rates in these two tests are quite close, with a difference of 3.2%. It is important to mention that, differently from the schematic representation shown in Figure 3.2, only points with measured properties are reported in the *P-h* diagram of Figure 4.20, which are listed below,

- Point 1 - compressor inlet (suction);

- Point 2 - compressor outlet (discharge);

- Point 3 - condenser inlet;

- Point 4 - condenser outlet;

- Point 5 - jet cooler inlet;

- Point 6 - jet cooler outlet;

It should be clear that process $5 - 6$ in Figure 4.20 incorporates the refrigerant expansion in the orifice and the phase change resulting from the thermal load transferred to the two-phase mixture. The pressure drop between points 2 and 3 is caused by the Coriolis mass flow meter. Likewise, the pressure drop between points 4 and 5 is related to the fluid flow across the porous filter and the angled tubing that connects the filter outlet and the inlet of the jet cooler.

Based on System 1 it is clear that there is heat transfer from the vapor during compression because point 2 lies to the left of the isentropic curve from point 1. According to Gosney (1982), this characterizes a non-adiabatic compression process. If the actual process were adiabatic, point 2 would be on the right of the isentropic curve. Also, three aspects should be kept in mind: (i) the cooling capacity is fixed, which results in approximately the same enthalpy difference between points 5 and 6; (ii) points 4 and 5 lie on the 15℃ isotherm, as this is the hot reservoir temperature; and (iii) the superheating degree is fixed at 10℃.
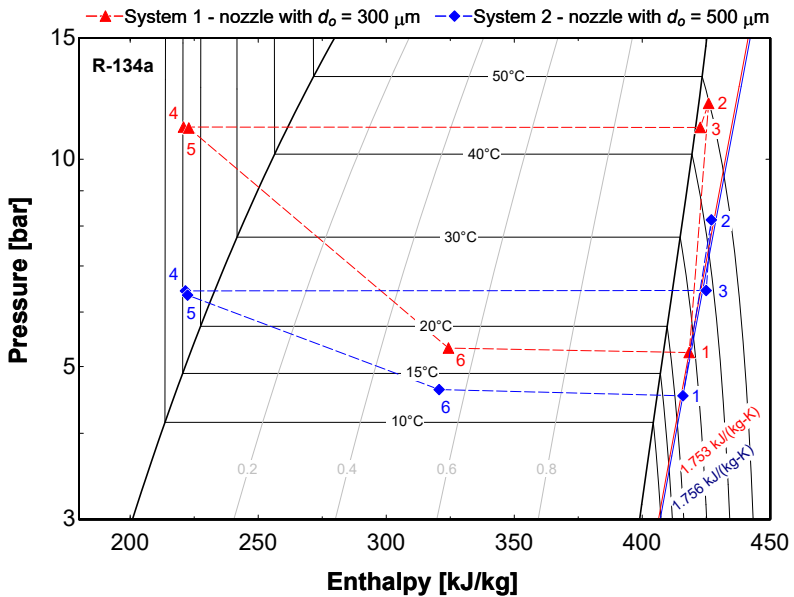
Figure 4.20 – *P-h* diagram: comparison between Matrices 1 and 2 for tests with same piston stroke (100%) and cooling load (150 W).

Regarding System 2, although the enthalpy of point 2 is very close to the discharge enthalpy corresponding to an isentropic compression, this does not mean that this process is reversible. It simply means that the irreversibilities during compression have been partially compensated by the heat transfer from the vapor (GOSNEY, 1982).

Figure 4.19 shows that, for both orifice diameters at a fixed piston displacement, the saturation pressures increase with the cooling capacity. Nevertheless, the rates are different for the two systems. While

the condensing pressure rises rapidly for $d_o = 300$ μm, it increases only slightly for $d_o = 500$ μm. This helps to explain the opposing behaviors presented in Figure 4.21, which shows the jet cooler pressure drop increasing for $d_o = 300$ μm and decreasing for $d_o = 500$ μm, as the cooling load is raised for each piston stroke.
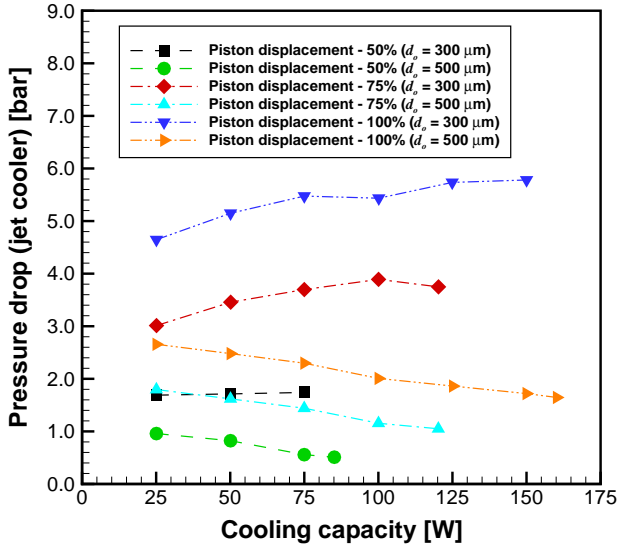
Figure 4.21 – Jet cooler pressure drop as a function of the cooling load (comparison between Matrices 1 and 2 - Groups A).

Figure 4.22 presents, for each matrix, the thermodynamic cycles for two distinct cooling loads (100 W and 150 W) for a given piston stroke (100%). The effect of the orifice diameter on the enthalpy change in each component, on the evaporating and condensing pressures, on the pressure drop through the mass flow meter (points 2 – 3) and on the sub-cooling degree at the condenser outlet can be clearly observed.
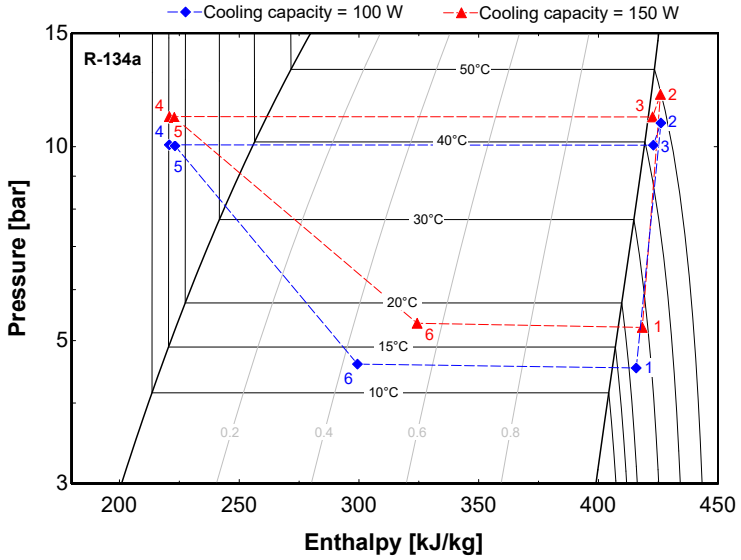
(a) Matrix 1 - $d_o = 300$ μm and $H = 28.84$ mm
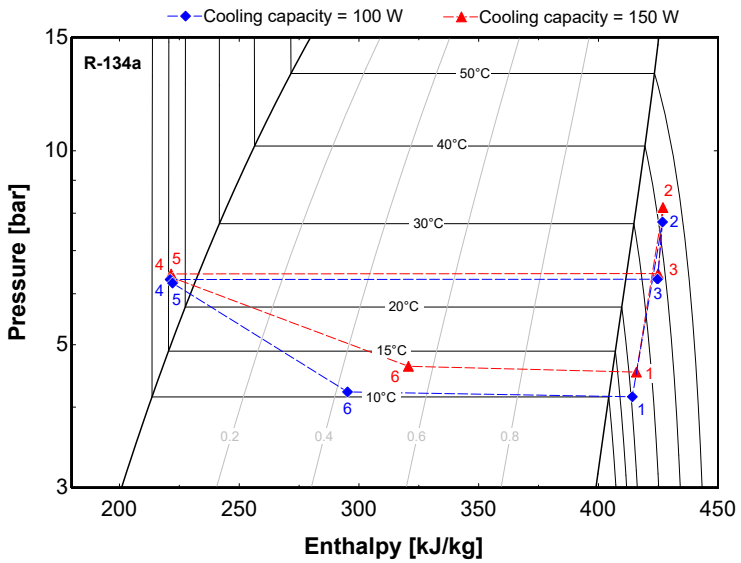
(b) Matrix 2 - $d_o = 500$ μm and $H = 28.84$ mm

Figure 4.22 – *P-h* diagram: comparison for tests with same piston displacement (100%) and matrices.

As the condensing pressure is significantly reduced by increasing the orifice diameter, the sub-cooling degree at the condenser outlet is greatly reduced. Figure 4.23 presents the behavior of the condenser sub-cooling and the small sensitivity of this parameter with respect to the piston stroke for Matrix 2.

Figure 4.23 – Sub-cooling degree as a function of the cooling load (comparison between Matrices 1 and 2 - Groups A).

Figures 4.24 and 4.25 show the relation between the refrigerant mass flow rate and the superheating heat transfer rate with respect to the cooling capacity and piston stroke, respectively. As already discussed in the previous section, the mass flow rate increases with both the cooling capacity and the piston stroke (see Figure 4.3). As seen in Figure 4.24, the change in orifice diameter does not seem to affect considerably the mass flow rate (except for the largest cooling capacity of the 50% piston stroke). There is a clear coupling between the superheating heat transfer rate and the refrigerant flow rate. Comparing the curves for different orifice diameters, it is clear that the superheating heat transfer rate becomes smaller as the mass flow rate decreases. Although the curves for 75% and 100% piston stroke for $d_o = 500$ μm do not exhibit clear maxima as the curves for Matrix 1, $\dot{Q}_{sh}$ was observed to follow the same linear behavior with respect to the liquid mass flow rate at the outlet of the test section described in Figure 4.7.
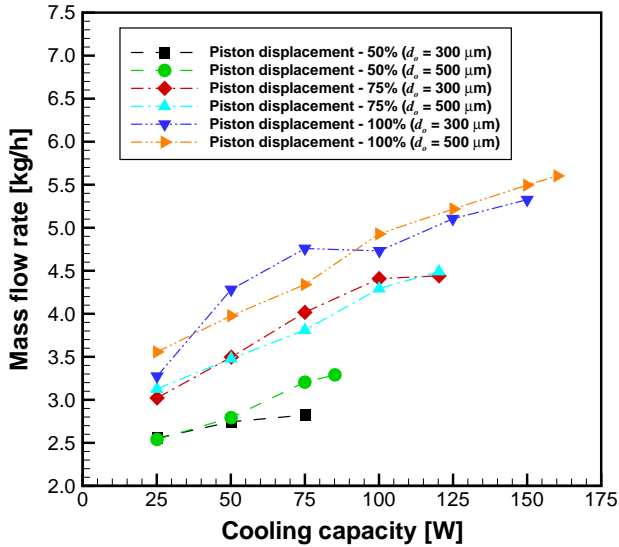
Figure 4.24 – Mass flow rate as a function of the cooling load (comparison between Matrices 1 and 2 - Groups A).
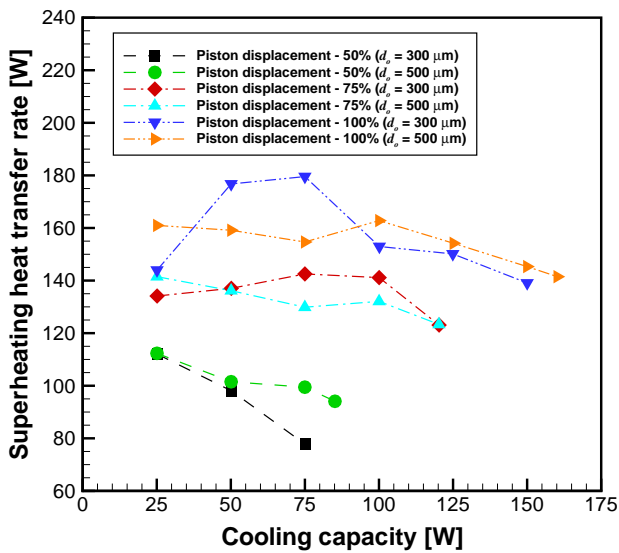
Figure 4.25 – Superheating heat transfer rate as a function of the cooling load (comparison between Matrices 1 and 2 - Groups A).

The vapor quality of the two-phase mixture at the inlet of the superheating line (outlet of the jet cooler) is shown in Figure 4.26. In general, the vapor quality is higher for $d_o = 500$ μm, especially for the piston displacements of 75% and 100%. For tests in which vapor quality was higher, the thermal power required to maintain the superheating degree was smaller, as shown in Figure 4.25.
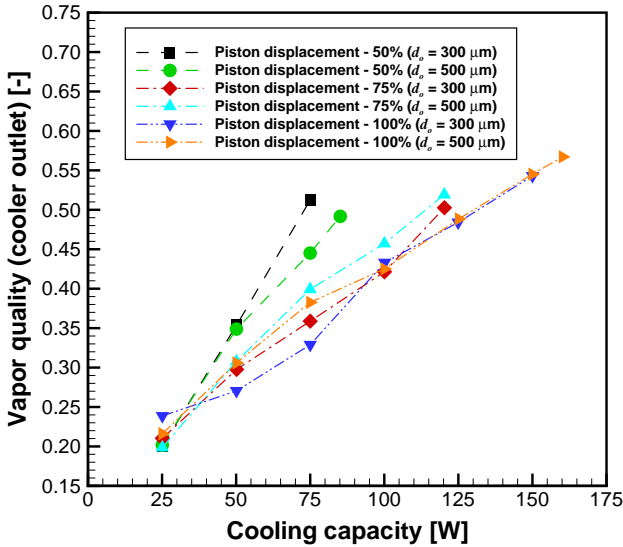
Figure 4.26 – Vapor mass quality at the outlet of the jet cooler as a function of the cooling load (comparison between Matrices 1 and 2 - Groups A).

A comparison between the coefficients of performance of the two refrigeration systems is presented in Figure 4.27. For most cases, the refrigeration system performs better with the larger orifice. The coefficient of performance for the overall system, shown in Figure 4.27 (a), reaches higher values for $d_o = 500$ μm due to two combined effects. Firstly, as the pressure lift decreases, the electrical power consumption of the compressor is reduced, as can be seen in Figure 4.28. The reduction is stronger for the piston strokes of 75% and 100%. The compressor operation envelope as provided by the compressor manufacturer is presented in Figure 4.29 for completeness. Secondly, but not as significant, the superheating heat transfer rate is generally lower for $d_o = 500$ μm.
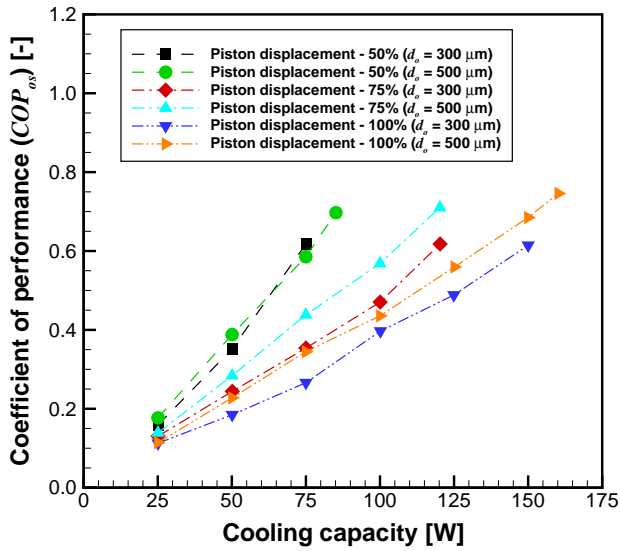
(a) Overall refrigeration system
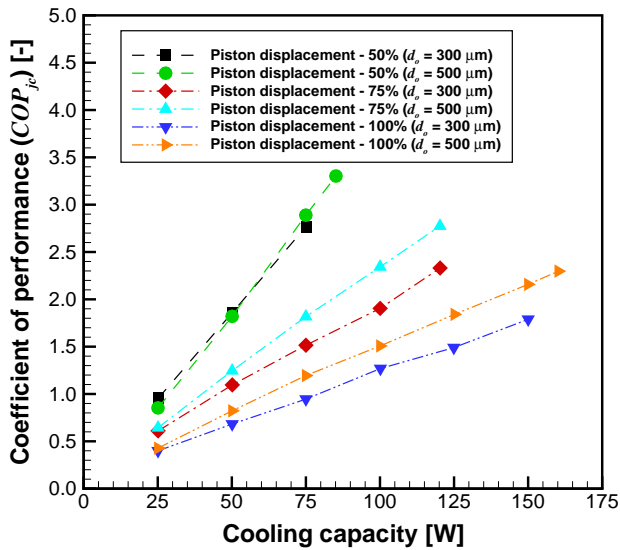
(b) Two-phase jet cooler

Figure 4.27 – Coefficients of performance as a function of cooling load (comparison between Matrices 1 and 2 - Groups A).
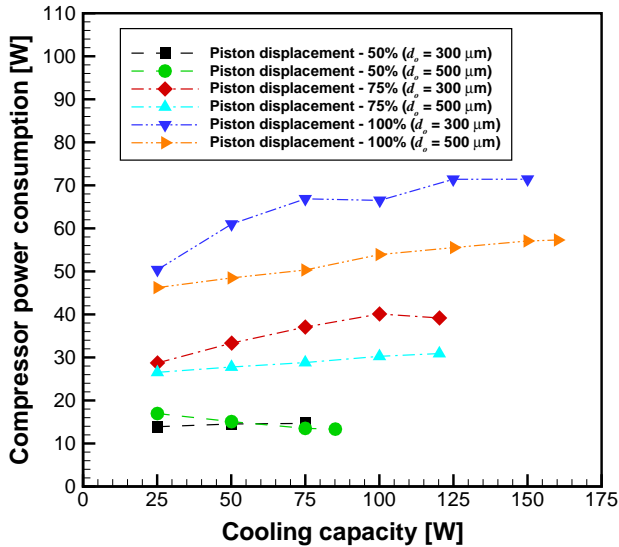
Figure 4.28 – Compressor (electrical) power consumption as a function of the cooling load (comparison between Matrices 1 and 2 - Groups A).
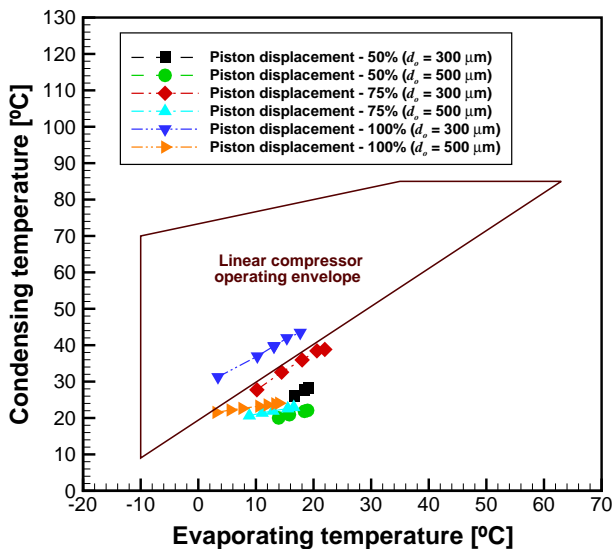
Figure 4.29 – Compressor operating envelope (comparison between Matrices 1 and 2 - Groups A).
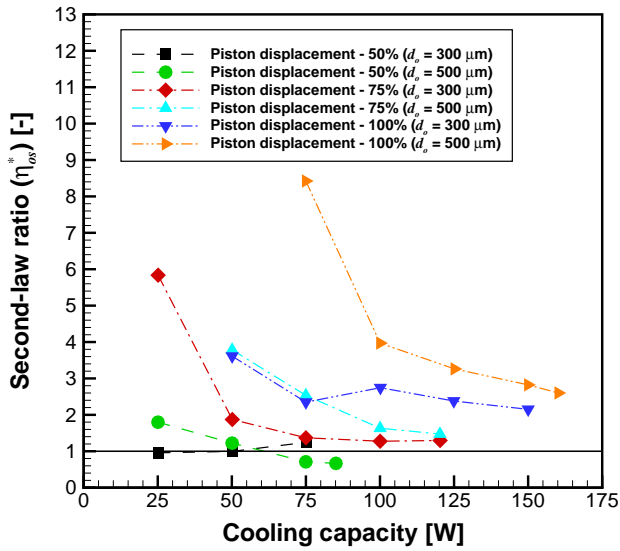
(a) Overall refrigeration system
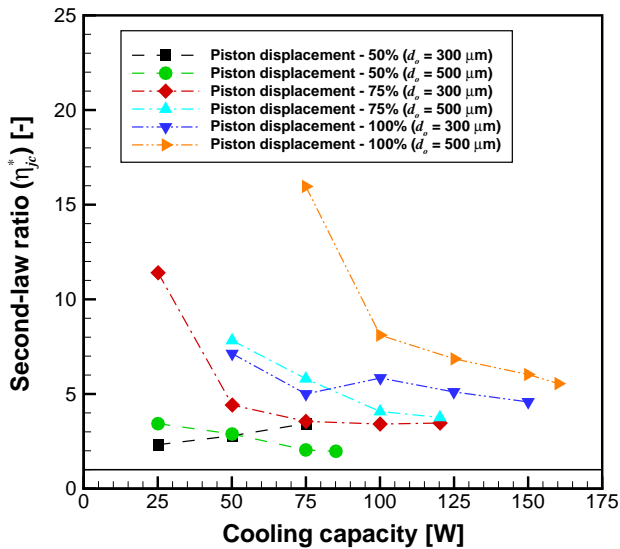
(b) Two-phase jet cooler

Figure 4.30 – Second-law ratio, η^*, as a function of the cooling load (comparison between Matrices 1 and 2 - Groups A).

Still regarding the COP, Figure 4.27 (b) shows a considerable potential increase of the coefficient of performance if Joule heating is substituted by another source for the superheating thermal input. As previously discussed and considering the trends of the curves in Figure 4.27, the performance of the system is expected to increase at higher cooling capacities, indicating that a hybrid system can be a suitable design for high heat flux removal.

Figure 4.30 illustrates how the orifice diameter affects the second-law ratio, considering the overall system and the jet cooler individually. Like the coefficient of performance, a larger orifice diameter is beneficial for the refrigeration system since higher values of η^* are achieved. Again, this metric indicates that operation at a compressor volumetric displacement of 50% is discouraged.

Regarding the system thermal resistances, the orifice diameter increase caused a reduction of both R_c and R_a. The main contribution to the reduction of the combined resistance of the cold and the hot ends, R_c, came from the thermal resistance of the ambient, R_{amb}, which decreased by more than 50%. According to Eq. (4.28), this resulted from the decrease of the compressor power and the reduction of the condensing temperature, particularly the latter. The heat sink thermal resistance, R_{hs}, decreased by as much as 33%. The reduction of the active cooler apparent resistance, R_a, ranged from 4% to 56%.

4.8.2   Jet Cooler Parameters

Figure 4.31 presents the behavior of the surface temperature as the orifice diameter is enlarged. It is clear that this change has a positive effect since the surface temperature decreases, particularly for the curves for piston strokes of 75% and 100%.

The surface temperature decreases mainly as a result of the evaporating temperature behavior inside the jet chamber, which is presented in Figure 4.32. As discussed previously, using an orifice with a larger diameter reduces the pressure lift by lowering the saturation pressures and, therefore, the saturation temperatures. Again, a minor role is played by the heat transfer coefficient. The results shown in Figure 4.33 indicate that heat transfer coefficient increase almost linearly with the cooling capacity and is mildly affected by the refrigerant mass flow rate. For 100% piston stroke, $\hbar_s$ is higher for $d_o = 500$ μm, with the difference with respect to $d_o = 300$ μm increasing as the critical heat flux is approached.
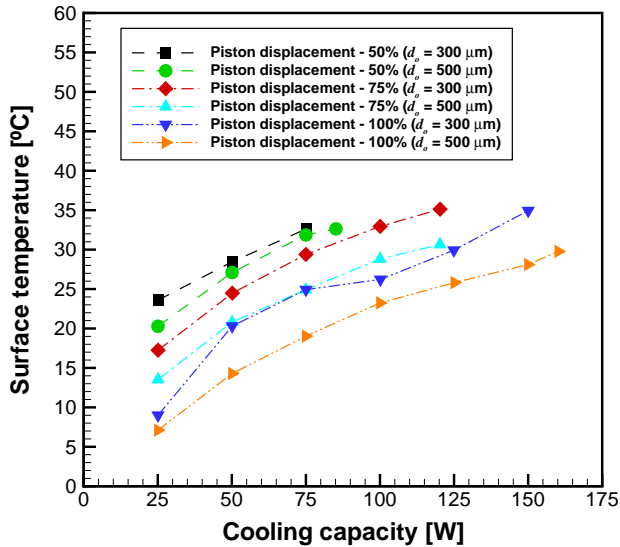
Figure 4.31 – Surface temperature as a function of the cooling load (comparison between Matrices 1 and 2 - Groups A).
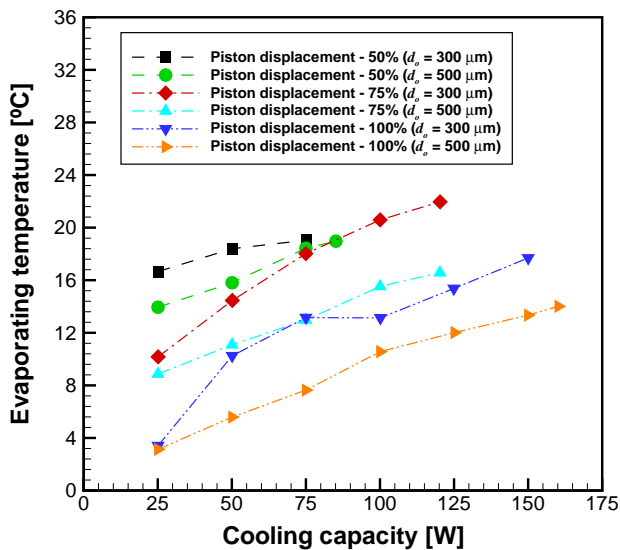
Figure 4.32 – Evaporating temperature as a function of the cooling load (comparison between Matrices 1 and 2 - Groups A).
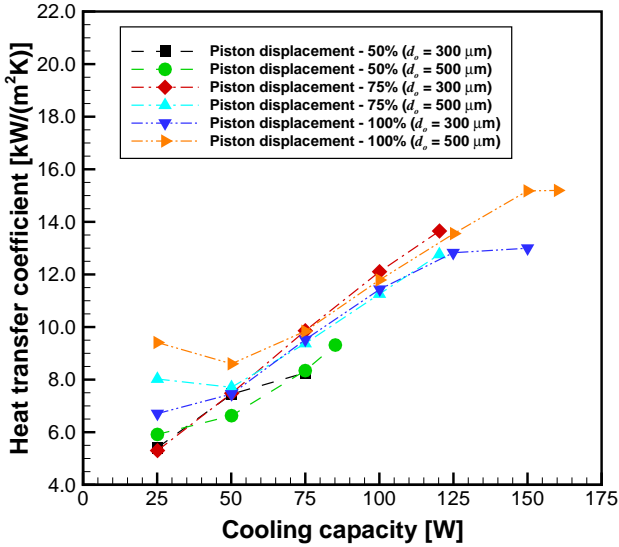
Figure 4.33 – Jet impingement heat transfer coefficient as a function of the cooling load (comparison between Matrices 1 and 2 - Groups A).

4.8.3   Influence of The Hot End Temperature

This section is dedicated to the analysis of the effect of the hot ambient (secondary fluid) temperature, $T_{w,i}$. Thus, the results for Groups B of Matrices 1 and 2 will be presented. Differently from Group A, the experimental tests for Group B were run only at 100% compressor stroke. This was based on the previous results for the second-law efficiency ratio, which showed that it is more advantageous to operate the active cooling system at such conditions. The temperature of the water-ethylene glycol mixture for Groups A and B was 15℃ and 25℃, respectively. It is worth mentioning that the tests for Groups B are also based on the same reference point, i.e., a fixed mass flow rate for test t#1. However, it should be clear that this value differs from that for test t#1 ($\alpha = 50\%$) in Groups A.

Operating the system at a higher hot end temperature increases the condensing temperature compared to the cases for which $T_{w,i} = 15℃$, as portrayed in Figure 4.34. In addition, a higher hot end temperature necessarily increases the refrigerant temperature at the condenser outlet, $T_{cond,o}$. As the rise in $T_{w,i}$ is significantly higher than the increase in $T_{cond,o}$ for Groups A and Group B, the sub-cooling degree

decreases as exhibited in Figure 4.35. Therefore, the coolant reaches the jet heat sink at higher temperatures. The temperature after expansion, i.e., the evaporating temperature, is also higher compared to the test conducted with the lower $T_{w,i}$, for the same cooling capacity. The evaporating temperature behavior is presented in Figure 4.36.

The increase of the saturation temperatures generates a higher pressure lift, which is confirmed by the noticeable increase of the electrical power consumption, as depicted in Figure 4.37. For the same orifice diameter, Figure 4.38 shows that the surface temperature changes very little with $T_{w,i}$. As the evaporating temperature is observed to increase with an increase in $T_{w,i}$, the wall superheat becomes lower, which is, essentially, a manifestation of the higher heat transfer coefficient shown in Figure 4.39. The increase in $\hbar_s$ is a function of the mass flow rate increase with the cooling capacity, as shown in Figures 4.40 and 4.41.

For a given orifice diameter, minute variations (from 1% to 6%) in the condenser heat transfer rate, $\dot{Q}_{cond}$, are observed as the secondary fluid temperature is increased. This can be attributed to the small increase in the condenser overall heat transfer coefficient, $\hbar_{cond}$, shown in Table 4.12. Appendix E presents the mathematical model used to calculate $\hbar_{cond}$ for a brazed plate heat exchanger. The correlations proposed by Longo (2008) and Bogaert and Bölcs (1995) were used to compute the heat transfer coefficients on the refrigerant and WEG sides. As reported by Longo (2008), the heat transfer coefficient for R-134a condensation inside a small brazed plate heat exchanger shows a weak sensitivity to condensing temperature. Besides, as the refrigerant mass flux is lower than 20 kg/(m^{2}s), there is no relevant vapor shear effect and the condensation is governed by gravity.

Table 4.12 – Condenser overall heat transfer coefficient, $\hbar_{cond}$ [W/(m^{2}K)], for Matrices 1 and 2.

	Matrices 1 and 2 - Groups A and B			
$\dot{Q}_c$[†] [W]	Matrix 1		Matrix 2	
	Group A	Group B	Group A	Group B
25	1245.30	1267.21	1436.61	1531.80
50	1179.56	1240.34	1420.34	1513.78
75	1151.43	1195.52	1410.65	1501.23
100	1151.68	1182.70	1398.06	1489.46
125	1131.35	1169.94	1393.10	1481.64

[†]Nominal cooling capacities.
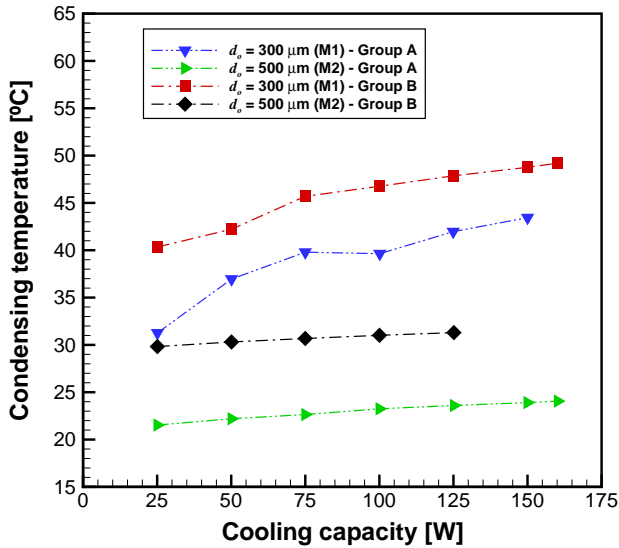
Figure 4.34 – Condensing temperature as a function of the cooling load (comparison between Matrices 1 and 2 - Groups A and B - $\alpha = 100\%$).
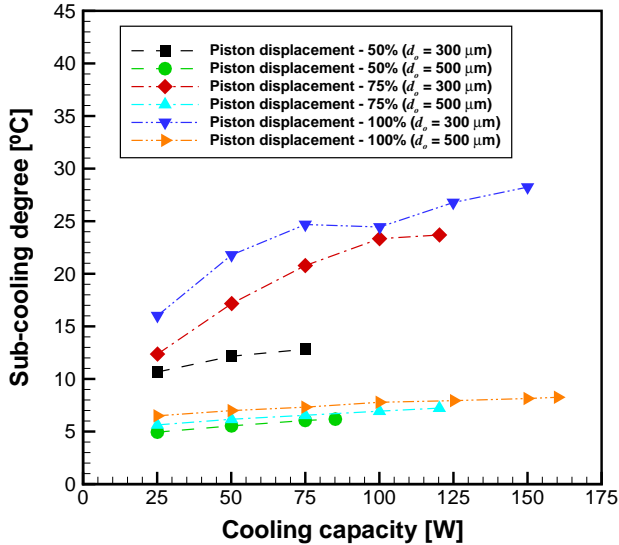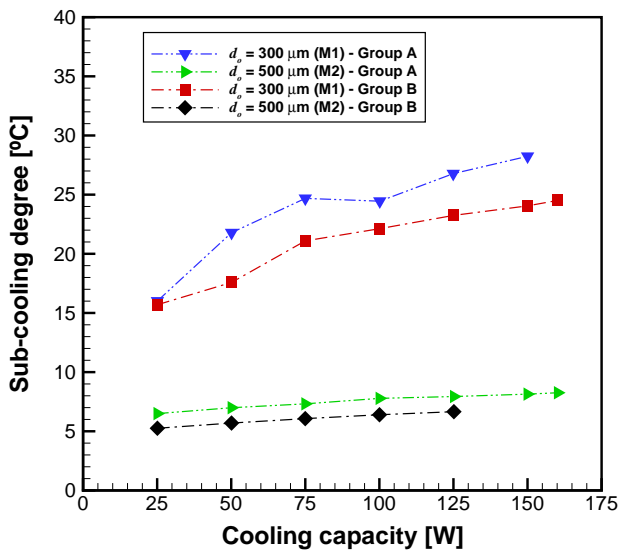

Figure 4.35 – Sub-cooling degree as a function of the cooling load (comparison between Matrices 1 and 2 - Groups A and B - $\alpha = 100\%$).
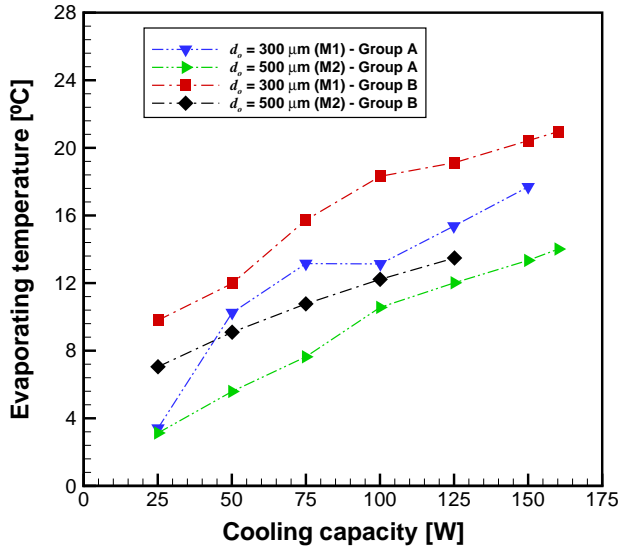
Figure 4.36 – Evaporating temperature as a function of the cooling load (comparison between Matrices 1 and 2 - Groups A and B - $\alpha = 100\%$).

Figure 4.37 – Compressor (electrical) power consumption as a function of the cooling load (comparison between Matrices 1 and 2 - Groups A and B - $\alpha = 100\%$).

Figure 4.38 – Surface temperature as a function of the cooling load (comparison between Matrices 1 and 2 - Groups A and B - $\alpha = 100\%$).
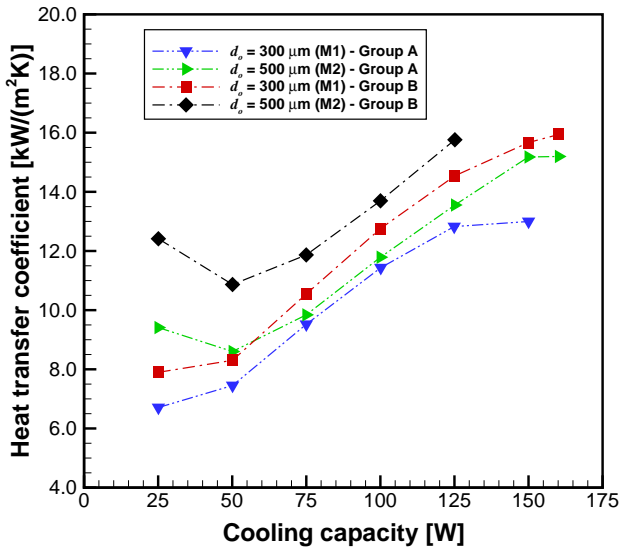
Figure 4.39 – Jet impingement heat transfer coefficient as a function of the cooling load (comparison between Matrices 1 and 2 - Groups A and B - $\alpha = 100\%$).
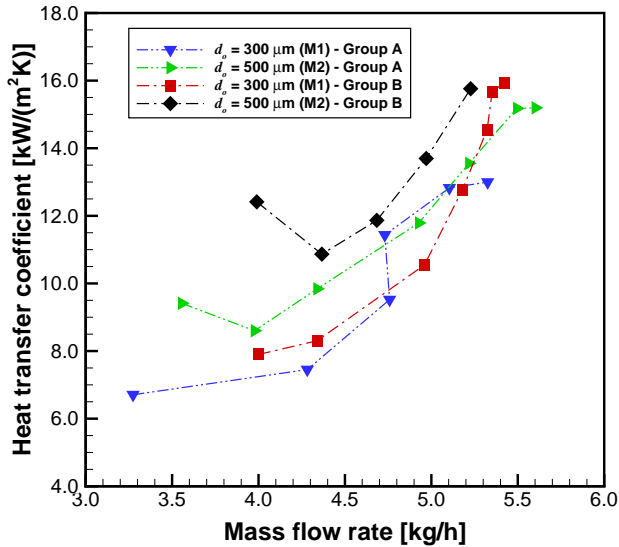
Figure 4.40 – Jet impingement heat transfer coefficient as a function of the refrigerant mass flow rate (comparison between Matrices 1 and 2 - Groups A and B - $\alpha = 100\%$).
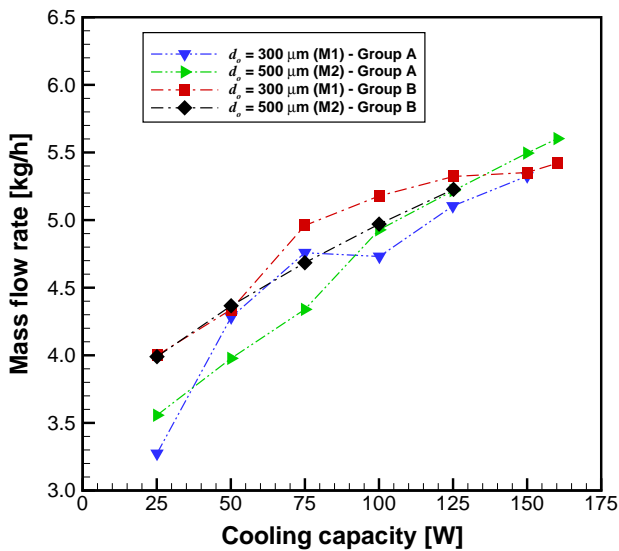
Figure 4.41 – R-134a mass flow rate as a function of the cooling load (comparison between Matrices 1 and 2 - Groups A and B - $\alpha = 100\%$).

4.9   Results for Matrices 1 and 3

This section reports the results of the tests conducted with a smaller jet chamber and compares them with the results of Matrix 1. The jet impingement length was shortened by a factor of approximately 3.0, i.e., from 28.84 mm (Matrix 1) to 9.75 mm (Matrix 3). To facilitate the analysis, the jet cooler parameters are evaluated first, and the system performance is analyzed next.

4.9.1   Jet Cooler Parameters

Considering similar operating conditions (α and $\dot{Q}_c$), Figure 4.42 suggests that the surface temperature is insensitive to the change in the jet impingement length. Nevertheless, it is important to observe that, for the intermediate and full stroke conditions, the reduction of the jet impingement length shifted the point of dryout to lower cooling capacities. This effect was very dramatic, with a maximum reduction of approximately 85 W for the 100% piston stroke in comparison with the tests with a longer jet length.
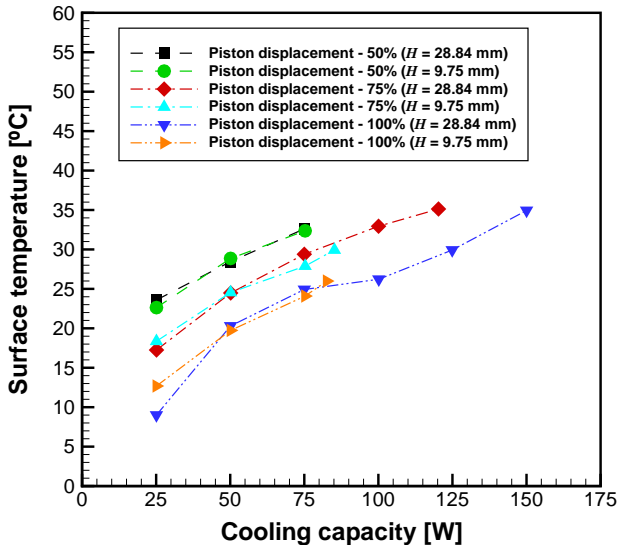
Figure 4.42 – Surface temperature as a function of the cooling load (comparison between Matrices 1 and 3 - Groups A).

The behavior of the evaporating temperature is shown in Figure

4.43. While the results for Matrices 1 and 3 are very similar for $\alpha = 50\%$, the evaporating temperature for Matrix 3 is reduced as the cooling capacity increases for $\alpha = 75\%$ and 100%. Thus, the net effect of the results shown in Figures 4.42 and 4.43 is an increase of the wall superheat as the impingement length is reduced from 28.84 mm to 9.75 mm, as can be seen in Table 4.13.
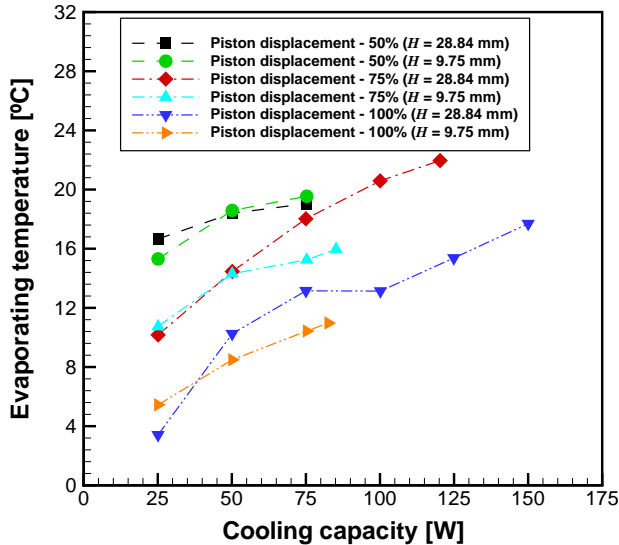
Figure 4.43 – Evaporating temperature as a function of the cooling load (comparison between Matrices 1 and 3 - Groups A).

For a fixed thermal load, the increase in wall superheat is caused by a reduction of the jet impingement heat transfer coefficient. It is believed that jet splattering and droplet atomization are the major factors contributing to the reduction of the heat transfer coefficient shown in Figure 4.44.

Splattering was visually observed to increase considerably when the impingement length was reduced from 28.84 mm to 9.75 mm. The jet impingement (impact) velocity is expected to be greater for the shorter jet length, which promotes a more vigorous atomization of the liquid into droplets ejected from the surface. By having a lower flow rate of liquid as a continuous film on the surface, the heat transfer coefficient of Matrix 3 is reduced in comparison with Matrix 1, as seen in Figure 4.44. In comparison with Matrix 1, the (total) mass flow rate also decreases for the highest heat loads of Matrix 3 for $\alpha = 75\%$

and 100%, as seen in Figure 4.45. Although the reduction is small, it certainly has an effect on the heat transfer coefficient too.

Table 4.13 – Wall superheating values for Matrices 1 (M1) and 3 (M3).

Matrix 1 (M1) and 3 (M3) - Groups A			
α [%]	$\dot{Q}_c$ [W]	M1 - ΔT_s [°C]	M3 - ΔT_s [°C]
50	25.0	6.94	7.31
	50.0	10.06	10.28
	75.0	13.58	12.81
75	25.0	7.08	7.62
	50.0	10.02	10.24
	75.0	11.37	12.64
	85.0	n.a.d.	13.96
100	25.0	5.59	7.24
	50.0	10.05	11.25
	75.0	11.77	13.66
	82.5	n.a.d.	15.02

n.a.d. - no available data.
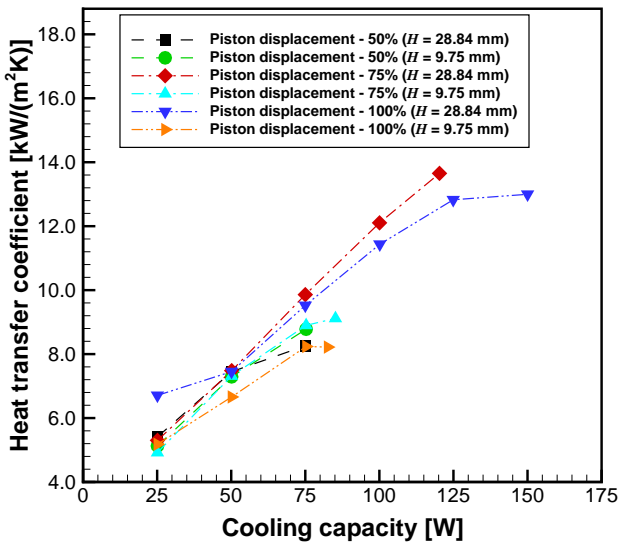
Figure 4.44 – Jet impingement heat transfer coefficient as a function of the cooling load (comparison between Matrices 1 and 3 - Groups A).
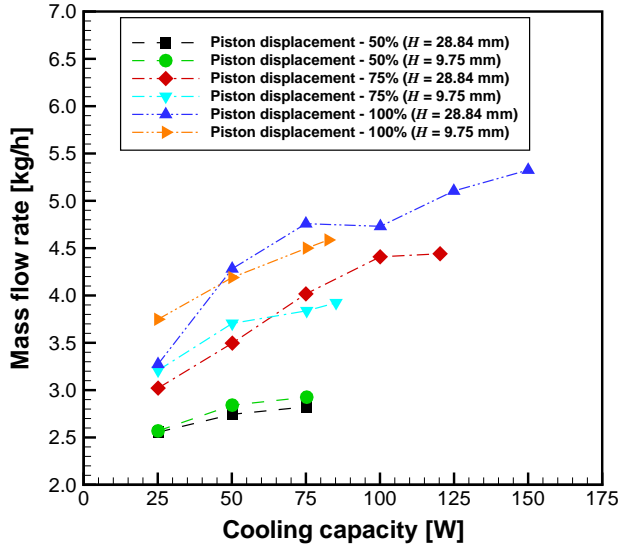
Figure 4.45 – Mass flow rate as a function of the cooling load (comparison between Matrices 1 and 3 - Groups A).

From an operation standpoint, the reduction of the critical heat flux is even more important than the deterioration of the heat transfer coefficient. The effect of this reduction can also be perceived by looking at the behavior of the outlet vapor quality shown in Figure 4.46. While the highest vapor qualities for $\alpha = 75\%$ and 100% in Matrix 3 are approximately 43% and 39%, the corresponding values for Matrix 1 are 50% and 54%, respectively, which means that the latent heat (enthaply) of vaporization of the refrigerant is used much more effectively for an impinging length of 28.84 mm.

Numerical estimates of the flow parameters at the orifice outlet are presented in Table 4.14. The vapor quality at the orifice outlet calculated assuming homogeneous equilibrium flow, x_o, decreases with the cooling capacity for the conditions in Matrices 1 and 3. In some cases, the pressure drop is not enough to generate vapor flashing and the exit condition is still single-phase liquid. The orifice outlet velocity calculated using the model presented in Section 5.3 is generally higher for Matrix 3 as a result of the lower pressure drop along the (shorter) orifice length, as seen in Figure 4.47.
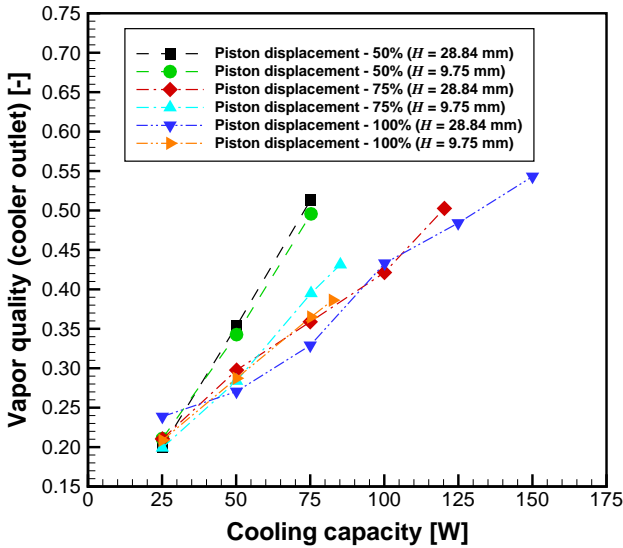
Figure 4.46 – Outlet vapor quality as a function of the cooling load (comparison between Matrices 1 and 3 - Groups A).

Table 4.14 – Fluid flow parameters at the orifice outlet for M1 and M3.

Matrix 1 (M1) and 3 (M3) - Groups A						
α	$\dot{Q}_c{}^{\dagger}$	x_o [-]		V_o [m/s]		$V_{o,cr}$ [m/s]	
[%]	[W]	M1	M3	M1	M3	M1	M3
50	25.0	0.0087	0.0209	11.55	16.76	8.48	11.81
	50.0	l.p.	l.p.	7.27	7.80	540.2	538.8
	75.0	l.p.	l.p.	6.28	6.25	540.6	539.3
75	25.0	0.0479	0.0455	36.92	37.24	19.22	18.71
	50.0	0.0195	0.0211	22.27	24.68	11.33	11.94
	75.0	l.p.	0.0144	9.74	21.02	539.3	10.05
	85.0	n.a.d.	0.0092	n.a.d.	18.11	n.a.d.	8.59
100	25.0	0.0785	0.0671	71.42	67.60	29.34	26.39
	50.0	0.0408	0.0508	46.47	55.76	18.01	21.33
	75.0	0.0228	0.0396	33.61	47.64	12.52	17.89
	82.5	n.a.d.	0.0367	n.a.d.	45.49	n.a.d.	16.99

†Nominal cooling capacities.

n.a.d. - no available data.

l.p. - liquid phase.
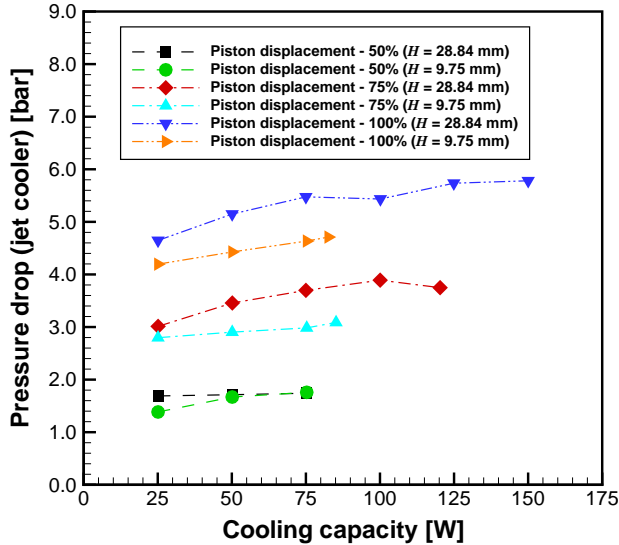
Figure 4.47 – Orifice pressure drop as a function of the cooling load (comparison between Matrices 1 and 3 - Groups A).

Although the impact velocities may be somewhat lower than the exit velocities as a result of flashing and hydrodynamic instabilities that cause the jet to break up into droplets downstream of the orifice, the impact velocities are still expected to be higher for Matrix 3 because of the shorter impingement height. This confirms the visual observations that splattering and atomization are indeed more severe for Matrix 3.

Just for the record, application of the jet instability criteria of Brown and York (1962) as well as Lin and Reitz (1998) predicted a full atomization of the liquid jet for all conditions except that for $\alpha = 50\%$ and $\dot{Q}_c = 75$ W. The criteria are based on a critical Weber number, defined as $We_{l,v} = \rho_{v,o}V_{o,l}d_o\sigma^{-1}$, where σ is the surface tension and $V_{o,l}$ is the velocity of the liquid phase, which is assumed to be equal to V_o according to the homogeneous equilibrium model (GHIAASIAAN, 2008). The atomization regime is reached for $We_{l,v} > 8.0$ (BROWN; YORK, 1962) and $We_{l,v} > 40.3$ (LIN; REITZ, 1998). In this regime, liquid break-up occurs at the nozzle exit and the droplets have much smaller diameters than the jet diameter. The calculated values of $We_{l,v}$ ranged from 47 to 2269. For the remaining case, i.e., $\alpha = 50\%$ and $\dot{Q}_c = 75$ W for which $We_{l,v}$ was calculated as 36.2 and 36.6 for Matrices 1 and 3, respectively, the second wind induced regime ($13 < We_{l,v} <$

40.3) happens, where liquid break-up occurs some nozzle diameters downstream of the nozzle exit and the droplets have smaller diameters than the jet diameter (POLANCO *et al.*, 2010). Nevertheless, given the small impingement length, it is fair to conclude that a fully developed spray was never achieved in the present experiments.

For comparison purposes, Table 4.14 also shows the critical (sonic) flow velocities calculated using Eq. (4.18). As can be seen, apart from the cases where single-phase liquid flow was predicted at the orifice outlet, the velocity results have the same order of magnitude, indicating that conditions at the orifice outlet may be close to critical.

4.9.2   Cooling System Parameters

Figure 4.48 illustrates the effect of the jet length on the refrigeration cycle for $\alpha = 100\%$ and $\dot{Q}_c = 75$ W. A clear shift towards lower condensing and evaporating pressures is observed due to the reduction of the pressure lift, as shown previously in Figure 4.47. Nevertheless, the effect of this shift on the compressor power consumption is rather small, as seen in Figure 4.49.
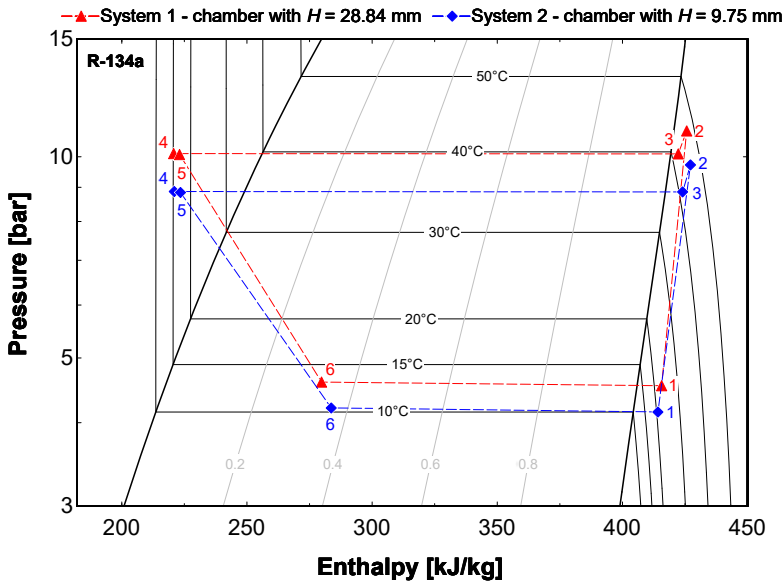
Figure 4.48 – *P-h* diagram: comparison between Matrices 1 and 3 for tests with same piston displacement (100%) and cooling load (75 W).
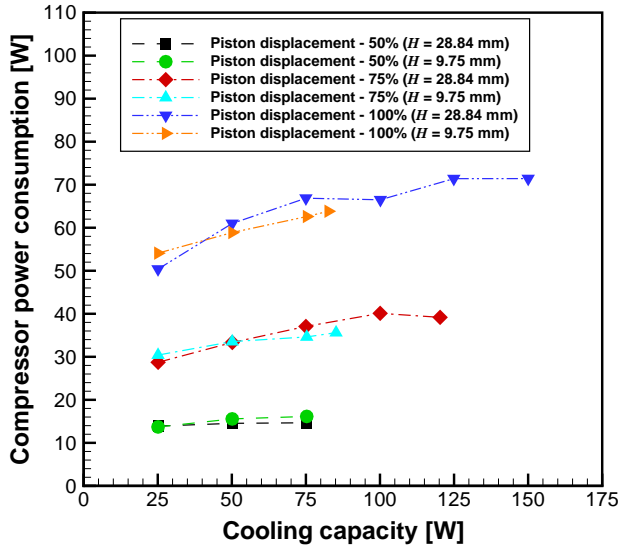
Figure 4.49 – Compressor (electrical) power consumption as a function of the cooling load (comparison between Matrices 1 and 3 - Groups A).

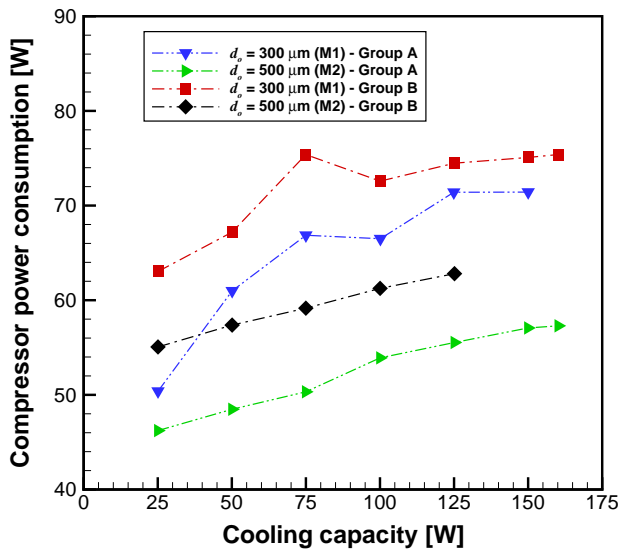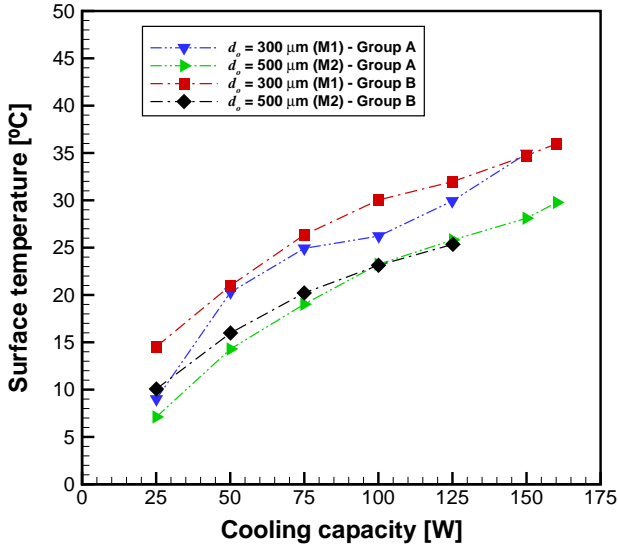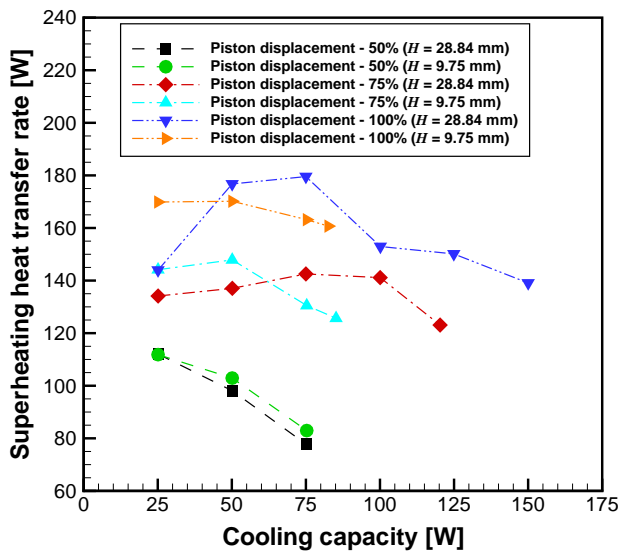

Figure 4.50 – Superheating heat transfer rate as a function of the cooling load (comparison between Matrices 1 and 3 - Groups A).
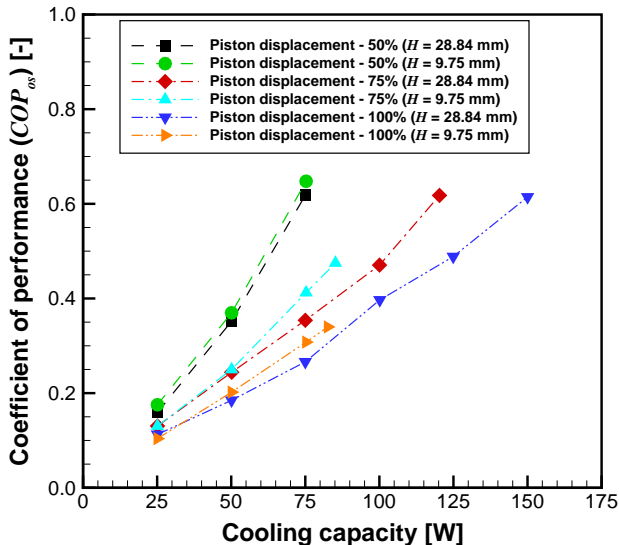
Figure 4.51 – Overall system COP as a function of the cooling load (comparison between Matrices 1 and 3 - Groups A).

When combined with the reduction of the superheating heat transfer rate shown in Figure 4.50 (due to the lower mass flow rates), this provokes a slight decrease in the coefficient of performance, as presented in Figure 4.51.

4.9.3   Influence of The Hot End Temperature

Similarly to the results presented in subsection 4.8.3, the immediate result of operating the refrigeration system at a higher secondary fluid temperature, $T_{w,i}$, is the increase of the condensing temperature as well as of the refrigerant temperature at the condenser outlet, which decreases the sub-cooling degree. The higher pressure lift imposes a higher consumption of the electrical power by the compressor. For the same jet impingement length, $T_{w,i}$ increase weakly affects the surface temperature. As the wall superheat decreases, the heat transfer coefficient becomes higher for a given cooling load. Since the aforementioned trends are quite similar to the ones already presented in subsection 4.8.3, the results of this analysis are presented in Appendix F.

4.10   Results for Matrix 4

Results for the multi-jet impingement cooling are presented in this section. Considering the previous results for the second-law efficiency ratio, the experimental tests were run only at 100% compressor stroke. In addition, cooling capacities lower than 75 W were not performed. The secondary fluid temperature was set at 25℃ and the tests for each multiple jet array started with the same refrigerant mass flow rate. This section is divided in two parts. First, parameters and metrics concerning the influence of the multi-jet on the performance of the refrigeration system as a whole are presented. Second, the heat transfer behavior of the two-phase jet heat sink as a result of the multi-jet cooling strategy is discussed.

4.10.1   Cooling System Parameters

As expected, Figure 4.52 shows that the system mass flow rate increases with the cooling load, however in a virtually linear fashion which differs from the results presented for the single jet cooling case, i.e., particularly for Matrix 1 (see Figure 4.3). This linear trend is also identified for the superheating heat transfer rate decrease, portrayed in Figure 4.53. As can be seen in Figure 4.54, both saturation temperatures increase with the cooling capacity, but the evaporating temperature shows a larger variation (7.0℃) than the condensing temperature (2.1℃). The larger variations in the evaporating temperature are related to the operation of the refrigeration system at a higher hot reservoir temperature, $T_{w,i}$, as already observed in Figures 4.34 and 4.36 (see Group B of Matrix 1). The geometry of the multi-jet arrays seems to affect very weakly the above variables, since no significant differences were observed between the three configurations.

The behavior of the sub-cooling degree at the outlet of the condenser is shown in Figure 4.55. The considerably lower values compared with those observed in the single jet cooling case depicted in Figure 4.35 (Group B of Matrix 1) can be explained by the higher secondary fluid temperature and by the lower restriction imposed by the multiple orifices with a flow area five times larger than that of the single orifice with a diameter of 300 μm. As the condensing temperature for multiple jet array #3 is slightly higher than that for the remaining arrays (see Figure 4.54), this configuration exhibits the larger values for the sub-cooling degree.
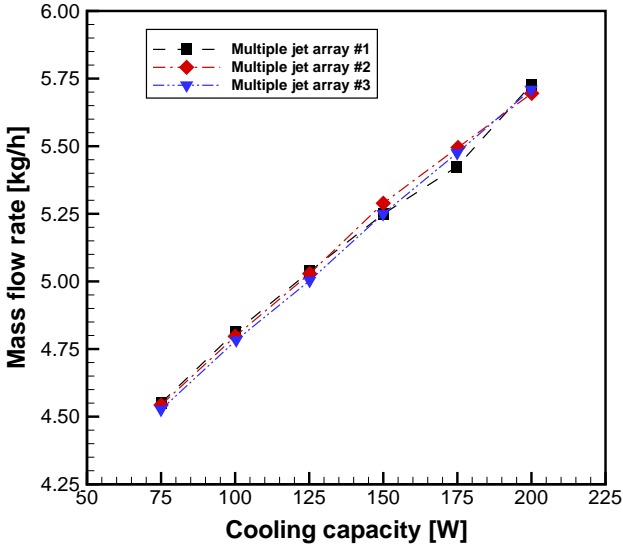
Figure 4.52 – Refrigerant mass flow rate as a function of the cooling load for multi-jet impingement cooling (results for Matrix 4).
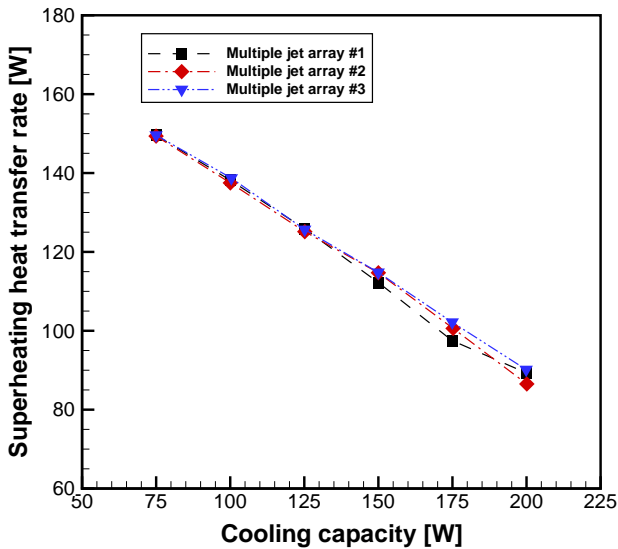
Figure 4.53 – Superheating heat transfer rate as a function of the cooling load for multi-jet impingement cooling (results for Matrix 4).
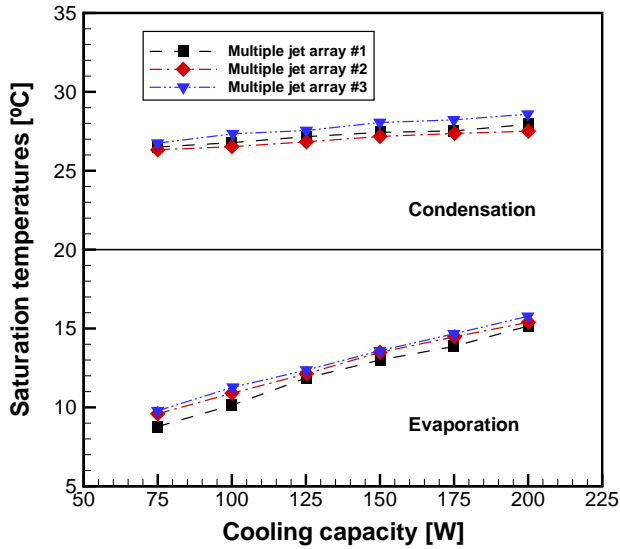
Figure 4.54 – Saturation temperatures as a function of the cooling load for multi-jet impingement cooling (results for Matrix 4).
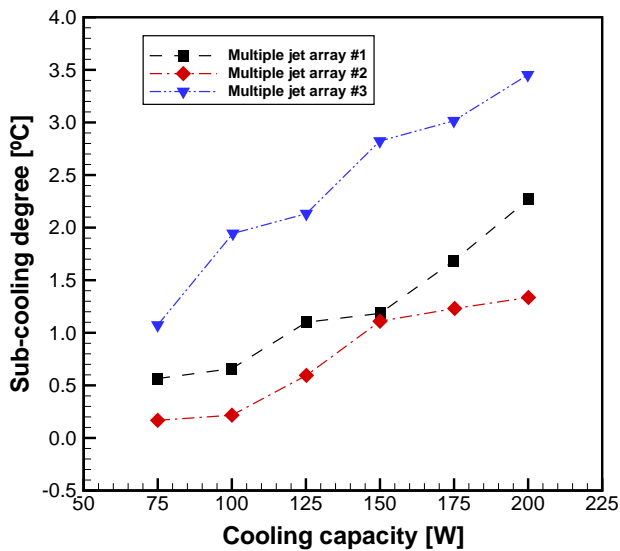
Figure 4.55 – Sub-cooling degree as a function of the cooling load for multi-jet impingement cooling (results for Matrix 4).

Due to the very low sub-cooling degrees observed for the cooling capacities of 75 and 100 W for jet array #2, it is possible that saturation conditions were present at the condenser outlet since ΔT_{sub} is of the order of magnitude of the expanded uncertainty, i.e., $U(\Delta T_{sub}) = 0.17°C$.

The coefficients of performance presented in Figures 4.56 and 4.57 confirm that for higher cooling capacities, a different design strategy such as a multiple jet impingement array decisively contributed for the proposed active cooling system to perform better. As can be seen, besides being capable to remove higher heat loads from the impingement surface (up to 200 W), both overall system and modified (jet-cooler) coefficients of performance are increased compared to the single jet case (Group B of Matrix 1). Again, no noticeable differences are perceived for COP_{os} regarding the multiple jet arrays. On the other hand, the multiple jet array #1 shows lower COP_{jc} values because of the higher electrical power consumption, as depicted in Figure 4.58. Whereas $\dot{W}_{comp}$ shows a small increase with the cooling load, particularly for jet arrays #2 and #3 (maximum of 5 W and 6 W, respectively), $\dot{W}_{ind}$ exhibits a virtually heat-load-independent behavior (maximum decrease of only 1.6 W).
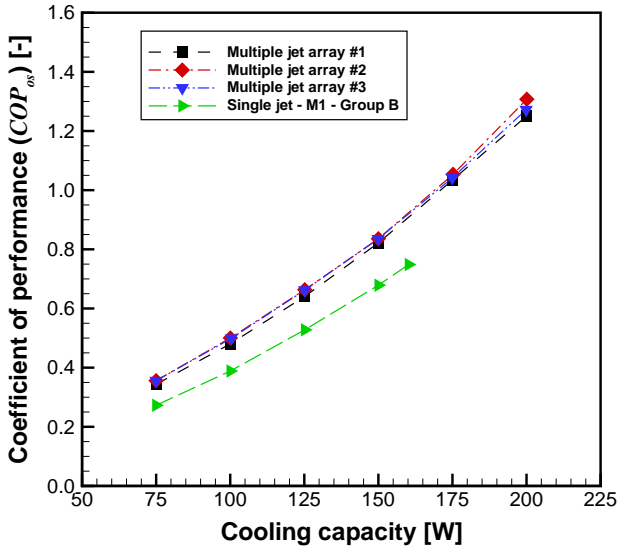
Figure 4.56 – Overall system COP as a function of the cooling load for single (Matrix 1) and multi-jet (Matrix 4) impingement cooling.
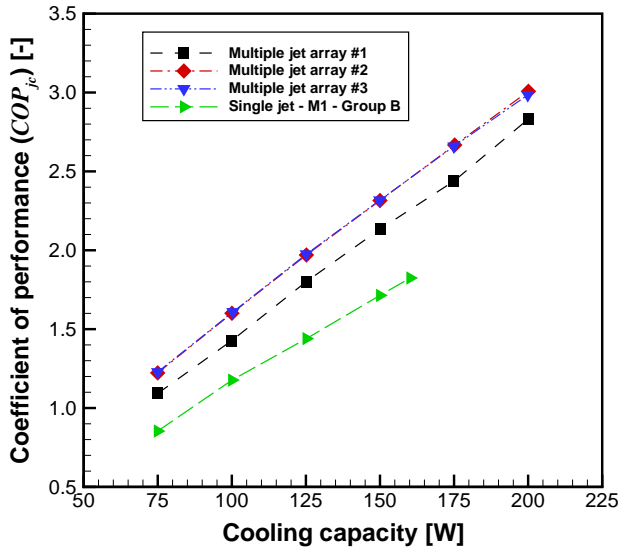
Figure 4.57 – Modified (jet-cooler) COP as a function of the cooling load for single (Matrix 1) and multi-jet (Matrix 4) impingement cooling.
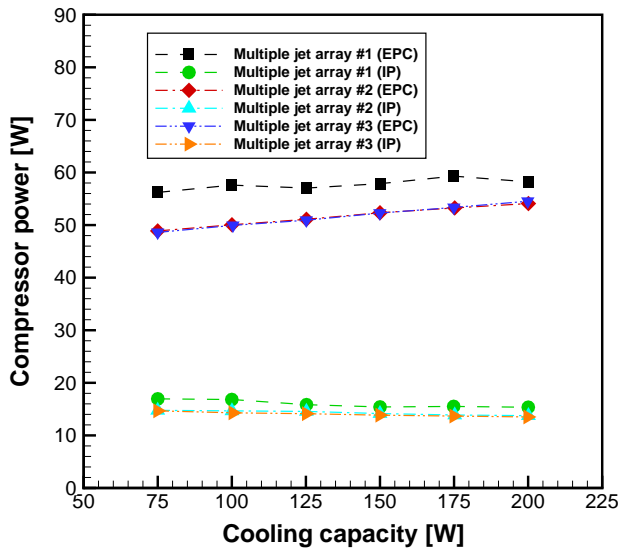
Figure 4.58 – Compressor power as a function of the cooling load for multi-jet impingement cooling (results for Matrix 4). Abbreviations: Electrical Power Consumption (EPC) and Indicated Power (IP).
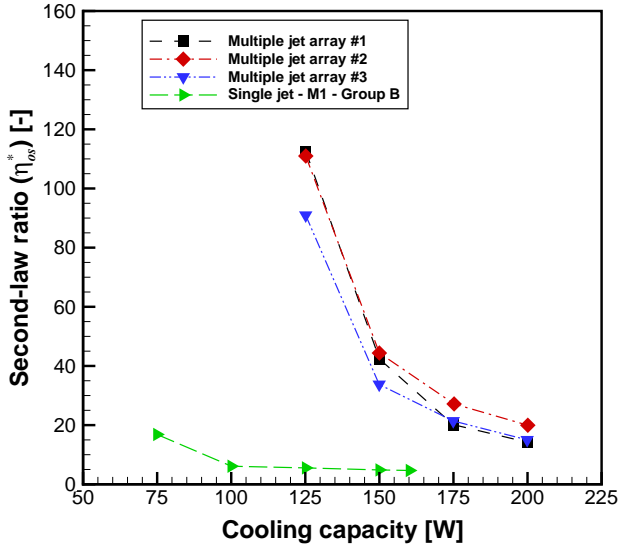
Figure 4.59 – Overall system second-law ratio, η_{os}^*, as a function of the cooling load for single (M1) and multi-jet (M4) impingement cooling.
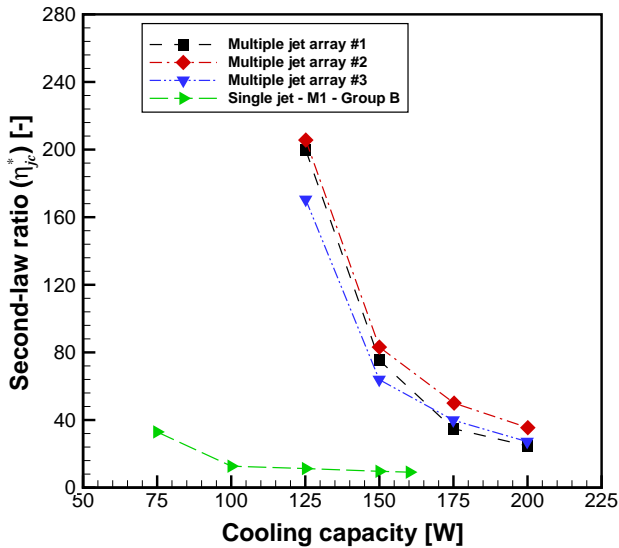
Figure 4.60 – Modified (jet-cooler) second-law ratio, η_{jc}^*, as a function of the cooling load for single (Matrix 1) and multi-jet (Matrix 4) impingement cooling.

The second-law ratio confirms the superior performance of the multiple jet array strategy over the single jet. Figures 4.59 and 4.60 show that both the overall and the modified (jet-cooler) refrigeration system second-law ratios present significantly larger values for the cooling capacity interval. Table 4.15 displays the lower values of the minimal second-law efficiency, η_{min}, as well as of the combined thermal resistance of the hot and cold ends, R_c, for the multiple jet array. The combination of these two factors contribute to the pronounced increase of the second-law ratios presented in the figures. Regarding η_{os}^*, only the data for multiple jet array #2 (higher performance case) and single jet (lower performance case) are shown in Table 4.15. The cases in which $T_s < T_{w,i}$ are not shown in Figure 4.59. When $T_s < T_{w,i}$ and $T_s \approx T_{w,i}$, the second-law ratio assumes a large negative value. The same procedure is applied to η_{jc}^* shown in Figure 4.60, for which only cases of higher and lower performance are presented in Table 4.16.

Table 4.15 – Performance metrics (overall system) for multiple and single jets configurations.

Performance metrics (overall system)					
$\dot{Q}_c$ [W]	R_c [K/W]	R_a [K/W]	η_{os} [%]	η_{min} [%]	$\eta*$ [-]
Results for multiple jet array #2 - Matrix 4					
74.98	0.15	-0.05[†]	2.11	-0.05[†]	-40.94[†]
100.04	0.14	-0.01[⋆]	2.75	-0.01[⋆]	-280.25[⋆]
125.17	0.12	0.01	3.42	0.03	110.98
150.00	0.11	0.03	3.99	0.09	44.37
175.22	0.11	0.04	4.72	0.17	27.16
200.10	0.11	0.06	5.49	0.28	19.95
Results for single jet - Matrix 1 - Group B					
25.09	0.25	-0.40[†]	1.06	-0.78[†]	-1.36[†]
50.11	0.24	-0.07[†]	2.09	-0.30[†]	-7.05[†]
74.98	0.20	0.02	2.83	0.17	16.84
100.06	0.18	0.05	3.79	0.62	6.10
125.17	0.17	0.06	5.19	0.94	5.53
150.00	0.16	0.07	6.55	1.35	4.85
160.22	0.16	0.07	7.19	1.54	4.66

[†]Test for which $T_s < T_{w,i}$.
[⋆]Test for which $T_s < T_{w,i}$ and $T_s \approx T_{w,i}$.

Table 4.16 – Performance metrics (jet-cooler) for multiple and single jets configurations.

$\dot{Q}_c$ [W]	R_c [K/W]	R_a [K/W]	η_{os} [%]	η_{min} [%]	$\eta*$ [-]
Performance metrics (jet-cooler)					
Results for multiple jet array #2 - Matrix 4					
74.98	0.16	-0.05†	7.24	-0.10†	-69.90†
100.04	0.14	-0.01*	8.81	-0.02*	-507.69*
125.17	0.12	0.01	10.15	0.05	205.63
150.00	0.11	0.03	11.06	0.13	83.13
175.22	0.11	0.04	11.95	0.24	49.98
200.10	0.12	0.06	12.63	0.36	35.46
Results for single jet - Matrix 1 - Group B					
25.09	0.35	-0.40†	3.59	-1.55†	-2.31†
50.11	0.32	-0.07†	6.68	-0.53†	-12.70†
74.98	0.27	0.02	8.86	0.27	32.95
100.06	0.24	0.05	11.49	0.91	12.68
125.17	0.21	0.06	14.16	1.26	11.28
150.00	0.20	0.07	16.54	1.71	9.66
160.22	0.19	0.07	17.52	1.92	9.14

†Test for which $T_s < T_{w,i}$.

*Test for which $T_s < T_{w,i}$ and $T_s \approx T_{w,i}$.

4.10.2 Jet Cooler Parameters

Since the multiple jet arrays #2 and #3 differ by a 45° rotation (clockwise or counter-clockwise), it is expected that the heated surface temperatures will present quite close values, as revealed by Figure 4.61. This figure evinces that a more spaced jet array configuration is beneficial to reach lower surface temperatures, particularly at high cooling capacities. Compared to the single jet cooling scheme (Matrix 1 - Group B), the multi-jet impingement arrays enabled the active cooling system to remove higher cooling loads while maintaining the surface temperature well below the conventionally established limit of 85℃ (MUDAWAR, 2001). For cooling loads up to 150 W, it is possible to see that the three multi-jet arrays present close values for the surface temperature. However, a sharp increase is clearly perceived for array #1 at higher cooling loads. This is an immediate consequence of the jet impingement heat transfer coefficient decrease shown in Figure 4.62.
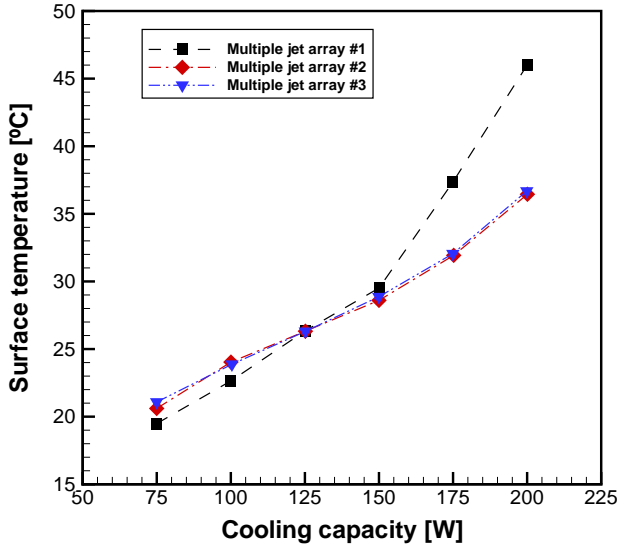
Figure 4.61 – Surface temperature as a function of the Cooling load for multi-jet impingement cooling (results for Matrix 4).
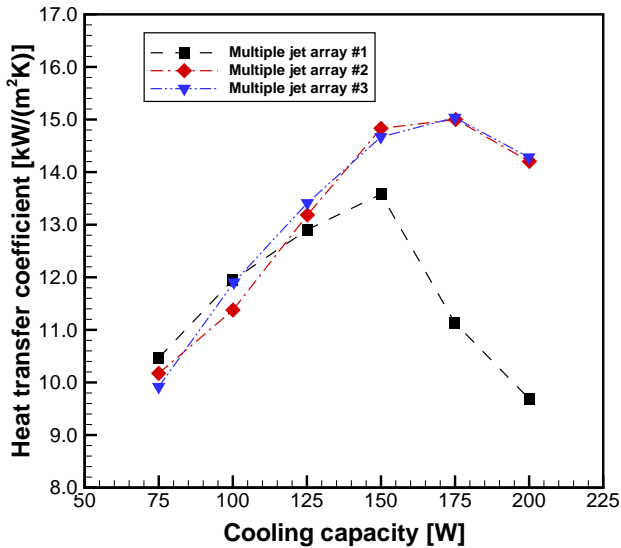
Figure 4.62 – Jet impingement heat transfer coefficient as a function of the cooling load for multi-jet impingement cooling (results for Matrix 4).

After reaching the maximum point at 150 W, the heat transfer coefficient of the multi-jet array #1 abruptly decreases whereas for the remaining arrays the heat transfer coefficient also decreases, but in a far more moderate fashion. Interestingly, the different behavior of the heat transfer coefficient for array #1 is not related to the vapor quality at the outlet of the jet cooler, as illustrated in Figure 4.63. The vapor quality increases steadily, exhibiting very close values for all configurations as well as reaching very high values (up to 75%). An explanation for the heat transfer coefficient behavior for multi-jet array #1 may lie in the fact that in this configuration the jets are positioned closer to each other and the impingement is concentrated at the center of the heated surface; a geometry that resembles the single-orifice impingement from the point of view of the heat transfer interaction.
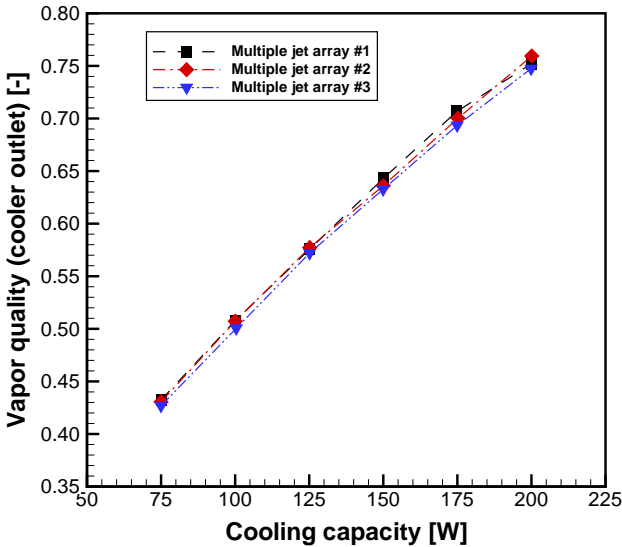
Figure 4.63 – Vapor mass quality at the outlet of the jet cooler as a function of the cooling load for multi-jet impingement cooling (results for Matrix 4).

Another interesting behavior is presented in Figure 4.64, which depicts the pressure drop of the two-phase jet heat sink for single and multiple jet cooling strategies. In addition to being much lower than the pressure drop for Matrix 1, the multiple-jet pressure drop shows the opposite trend compared to the results regarding to Matrix 1, i.e., ΔP_{jc} decreases as the cooling capacity is increased. As more orifices

are present, the refrigerant fluid flow becomes more evenly distributed around the orifices which lowers the restriction imposed by a single orifice with very small size ($d_o = 300~\mu$m). Hence, a lower refrigerant mass is accumulated in the high-pressure components which reduces the pressure upstream of the orifice. The lower pressure drop through the orifice results in a significantly higher pressure downstream (evaporating pressure). The pressure drop magnitude is markedly reduced by a factor of at least 2 as more orifices are used as expansion devices.
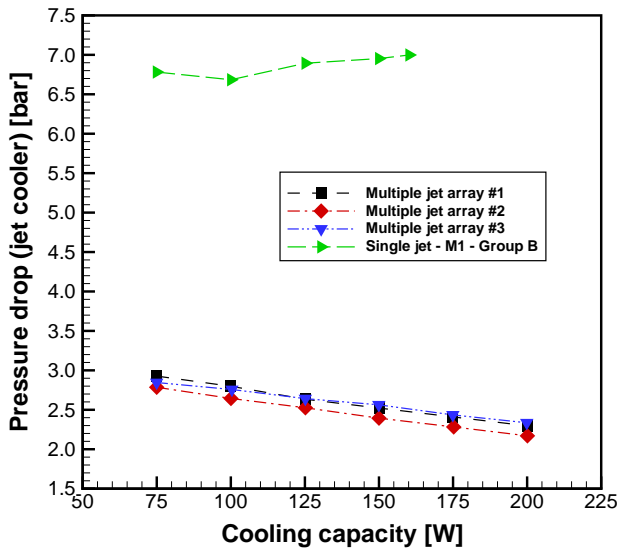
Figure 4.64 – Jet heat sink pressure drop as a function of the cooling load for single (Matrix 1) and multi-jet (Matrix 4) impingement cooling. Note: for Matrix 1, ΔP_{jc} is plotted only for $\dot{Q}_c \geq 75$ W.

5   *Final Considerations*

This thesis presented a novel two-phase jet heat sink that integrates the evaporator and the expansion device into a single cooling unit. The new jet cooler was combined with an active cooling system which operates with a compact oil-free linear motor R-134a compressor to demonstrate the applicability of the system in the removal of highly concentrated heat loads.

5.1   Conclusions

As proposed initially, an experimental apparatus was designed and built to accomplish the objectives of this work. A purpose-built calorimeter was developed to quantify the heat dissipation rate through the compressor shell, thus providing closure for the overall system energy balance. The thermal performance of both the jet impingement cooling module and the vapor compression refrigeration system were evaluated for a variety of operating conditions. In addition, a comprehensive thermodynamic analysis was performed using different performance metrics.

Experiments have been carried out with single and multiple orifice configurations of the jet heat sink. The influence of the following parameters was quantified: (i) applied thermal load, (ii) orifice diameter, (iii) orifice-to-heater distance, (iv) hot reservoir temperature and (v) compressor piston displacement. In addition to the heater surface temperature and two-phase jet impingement heat transfer coefficient, the coefficient of performance and the second-law efficiency were determined. The main conclusions arising from the thesis are as follows:

1. At operating conditions for which the system pressure ratio ranged from 1.4 to 2.2, the two-phase jet heat sink was capable of dissipating cooling capacities of up to 160 W and 200 W from a 6.4-cm^2 surface for single and multiple orifice configurations, which

correspond to the full-stroke tests of Matrix 1 (Group B), Matrix 2 (Group A) and Matrix 4 (multiple jet arrays #2 and #3), respectively. For these cases, the temperature of the impingement surface was maintained lower than 40℃ and the heat transfer coefficient reached values from around 14,000 to 16,000 W/(m²K).

2. Considering the single orifice configuration, for a fixed hot reservoir temperature and a fixed jet length, employing a 500 μm orifice resulted in a better thermodynamic performance than using a 300 μm orifice. The smaller pressure ratio obtained with the larger orifice was the main responsible for the lower compressor power consumption. Moreover, the second-law ratio, was significantly larger than unity only for the compressor strokes of 75% and 100%;

3. The impinging jet heat transfer coefficient was much more affected by the surface heat flux than by the refrigerant mass flow rate which, for a fixed orifice diameter and a constant cooling capacity, increases significantly with the piston stroke. This indicates that nucleate boiling on the heater surface may be an important heat transfer mechanism. Nevertheless, the critical heat flux was significantly affected by the refrigerant mass flow rate;

4. For a fixed orifice diameter, increasing the hot reservoir temperature from 15 to 25℃ causes an increase in both the evaporating and condensing pressures. The net effect of this change is an increase of the heat transfer coefficient resulting from the higher mass flow rate. However, as expected, an increase in the compressor power was observed;

5. Reducing the jet length from 28.84 to 9.75 mm increased jet splattering and droplet breakup. As a result, it reduced the heat transfer coefficient and, more significantly, the critical heat flux. The impact on the compressor power consumption and coefficient of performance, however, was minimal.

6. For a fixed orifice diameter and a fixed jet length, operating the active cooling system with the multiple orifice configurations resulted in a better thermodynamic performance than the single orifice configuration. The combined effect of lower values for the minimal second-law efficiency and for the combined thermal resistance of the hot and cold reservoirs increased the second-law ratio considerably.

5.2   Recommendations for Future Works

Based on the advances presented in this thesis some important recommendations for future works can be listed as follows:

1. Perform a more fundamental study of the impinging jet(s) generated inside the jet heat sink. The idea is to employ high-speed visualization techniques to characterize different heat transfer phenomena, such as jet impingement, film evaporation and nucleate boiling, as well as the interactions between these phenomena for single and multiple jet-based configurations. For a given jet configuration (number of jets, array, orifice diameter and orifice-to-heater distance), the relation between splattering and the surface area actually covered by the impinging jet(s) is an important aspect to be explored in this study;

2. Elaborate and validate a mathematical model for predicting the behavior of the refrigeration system. Particularly, one suggests the evaluation of the applicability of lumped models to describe the heat transfer in the jet cooler, given that such models are less computationally demanding;

3. Perform experimental tests replacing the linear compressor by other small-scale compressors based on different working principles, particularly the rotary technology. The best compression mechanism for active cooling of electronics is still an open topic in the current literature;

4. Compare the thermal performance of the proposed two-phase jet cooler with other high heat flux removal technologies such as microchannels and commercial cold plate evaporators. These components can be easily integrated with the present experimental apparatus by replacing the tubular evaporator in the secondary evaporation circuit. Therefore, two cooling technologies can be tested using the same active cooling system under the same operating conditions, which establishes a fair and robust basis for comparing the results for different competing technologies;

5. Design an efficient thermal solution for providing the superheating thermal energy instead of making use of Joule heating via an electrical supply. As previously mentioned (Chapter 4), this would significantly enhance the overall coefficient of performance of the refrigeration system;

6. Evaluate the thermal performance of the jet cooler for distinct atomization strategies, such as: (i) oblique jets, and (ii) multiple jet impingement atomization, in which angled nozzles generate colliding jets at a particular point along the orifice-to-heater distance, promoting liquid breakup and enhancing droplet formation.

References

AGOSTINI, B.; FABBRI, M.; PARK, J. E.; WOJTAN, L.; THOME, J. R.; MICHEL, B. State of the Art of Heat Flux Cooling Technologies. *Heat Transfer Engineering*, v. 28, n. 4, p. 258–281, 2007.

AMON, C. H. MEMS-BASED THERMAL MANAGEMENT OF HIGH HEAT FLUX DEVICES EDIFICE: EMBEDDED DROPLET IMPINGEMENT FOR INTEGRATED COOLING OF ELECTRONICS. In: ROHSENOW SYMPOSIUM ON FUTURE TRENDS IN HEAT TRANSFER. *Proceedings*. Cambridge, MA: Warren M. Rohsenow Heat and Mass Transfer Laboratory, 2003. p. 1–22. Disponível em: <http://hdl.handle.net/1721.1/7300>.

AMON, C. H.; YAO, S.-C.; WU, C.-F.; HSIEH, C.-C. Microelectromechanical System-Based Evaporative Thermal Management of High Heat Flux Electronics. *Journal of Heat Transfer*, v. 127, n. 1, p. 66–75, jan. 2005.

ANANDAN, S. S.; RAMALINGAM, V. THERMAL MANAGEMENT OF ELECTRONICS: A REVIEW OF LITERATURE. *Thermal Science*, v. 12, n. 2, p. 5–26, dec. 2008.

ASHWOOD, A. C. *Fluid Property Effects on Spray Cooling: An Experimental and Numerical Study*. Dissertação (Mestrado) — University of Wisconsin-Madison, 2006.

ASHWOOD, A. C.; SHEDD, T. A. Spray Cooling with Mixtures of Dielectric Fluids. In: TWENTY THIRD ANNUAL IEEE SEMICONDUCTOR THERMAL MEASUREMENT AND MANAGEMENT SYMPOSIUM. *Proceedings of the 23rd IEEE*

SEMI-THERM Symposium. San Jose (CA): IEEE, 2007. p. 144–148.

AWAD, M. M.; MUZYCHKA, Y. S. Effective property models for homogeneous two-phase flows. *Experimental Thermal and Fluid Science*, v. 33, n. 1, p. 106–113, oct. 2008.

BAILEY, P. B.; DADD, M. W.; STONE, C. R. An Oil-free Linear Compressor for use with Compact Heat Exchangers. In: INTERNATIONAL CONFERENCE ON COMPRESSORS AND THEIR SYSTEMS. *Proceedings*. London, UK, 2009.

BAR-COHEN, A. Completing the Inward Migration - The Transformative Nature of Embedded Cooling. In: ASME 2013 SUMMER HEAT TRANSFER CONFERENCE. *Proceedings of the HT2013*. Minneapolis, MN, 2013. Keynote lecture.

BAR-COHEN, A.; ARIK, M.; OHADI, M. Direct Liquid Cooling of High Flux Micro and Nano Electronic Components. *Proceedings of the IEEE*, v. 94, n. 8, p. 1549–1570, aug. 2006.

BAR-COHEN, A.; HOLLOWAY, C. A. Thermal science and engineering - from macro to nano in 200 years. In: THE 15TH INTERNATIONAL HEAT TRANSFER CONFERENCE (IHTC-15). *Proceedings of the IHTC-15*. Kyoto, Japan, 2014. p. 1–18. Fourier Lecture - Paper IHTC15-FL01.

BARBOSA JR., J. R. RECENT DEVELOPMENTS IN VAPOR COMPRESSION TECHNOLOGIES FOR SMALL SCALE REFRIGERATION APPLICATIONS. In: ASME 2011 9TH INTERNATIONAL CONFERENCE ON NANOCHANNELS, MICROCHANNELS AND MINICHANNELS. *Proceedings of the ICNMM2011*. Edmonton: ASME, 2011. p. 1–13.

BARBOSA JR., J. R.; HERMES, C. J. L. HEAT TRANSFER IN

REFRIGERATION APPLICATIONS. In: HEWITT, G. F. (Ed.). *Heat Exchanger Design Handbook - Heat Exchanger Design Updates*. 1. ed. New York: Begel House, Inc, 2006. v. 13, Chap. 3.26, p. 1–30.

BARBOSA JR., J. R.; RIBEIRO, G. B.; DE OLIVEIRA, P. A. A State-of-the-Art Review of Compact Vapor Compression Refrigeration Systems and Their Applications. *Heat Transfer Engineering*, v. 33, n. 4-5, p. 356–374, 2012.

BARRAU, J.; CHEMISANA, D.; ROSELL, J.; TADRIST, L.; IBAÑEZ, M. An experimental study of a new hybrid jet impingement/micro-channel cooling scheme. *Applied Thermal Engineering*, v. 30, n. 14-15, p. 2058–2066, oct. 2010.

BARRAU, J.; OMRI, M.; CHEMISANA, D.; ROSELL, J.; IBAÑEZ, M.; TADRIST, L. Numerical study of a hybrid jet impingement/micro-channel cooling scheme. *Applied Thermal Engineering*, v. 33-34, p. 237–245, feb. 2012.

BELADY, C. Cooling and Power Considerations for Semiconductors into the Next Century. In: INTERNATIONAL SYMPOSIUM ON LOW POWER ELECTRONICS AND DESIGN. *Proceedings*. Huntington Beach, CA: IEEE, 2001. p. 100–105.

BOGAERT, R.; BÖLCS, A. GLOBAL PERFORMANCE OF A PROTOTYPE BRAZED PLATE HEAT EXCHANGER IN A LARGE REYNOLDS NUMBER RANGE. *Experimental Heat Transfer: A Journal of Thermal Energy Generation, Transport, Storage, and Conversion*, v. 8, n. 4, p. 293–311, sep. 1995.

BRADSHAW, C. R.; GROLL, E. A.; GARIMELLA, S. V. A comprehensive model of a miniature-scale linear compressor for electronics cooling. *International Journal of Refrigeration*, v. 34, n. 1, p. 63–73, jan. 2011.

BRADSHAW, C. R.; GROLL, E. A.; GARIMELLA, S. V. Linear compressors for electronics cooling: Energy recovery and its benefits. *International Journal of Refrigeration*, v. 36, n. 7, p. 2007–2013, nov. 2013.

BRADSHAW, C. R.; GROLL, E. A.; GARIMELLA, S. V. Sensitivity analysis of a comprehensive model for a miniature-scale linear compressor for electronics cooling. *International Journal of Refrigeration*, v. 36, n. 7, p. 1998–2006, nov. 2013.

BROWN, R.; YORK, L. Sprays Formed by Flashing Jets. *American Institute of Chemical Engineers Journal*, v. 8, n. 2, p. 149–153, 1962.

BROWNE, E. A.; JENSEN, M. K.; PELES, Y. Microjet array flow boiling with R134a and the effect of dissolved nitrogen. *International Journal of Heat and Mass Transfer*, v. 55, n. 4, p. 825–833, jan. 2012.

BROWNE, E. A.; MICHNA, G. J.; JENSEN, M. K.; PELES, Y. Microjet array single-phase and flow boiling heat transfer with R134a. *International Journal of Heat and Mass Transfer*, v. 53, n. 23-24, p. 5027–5034, nov. 2010.

BUCHANAN, R. A.; SHEDD, T. A. Extensive Parametric Study of Heat Transfer to Arrays of Oblique Impinging Jets With Phase Change. *Journal of Heat Transfer*, v. 135, n. 11, p. 111017–1 – 111017–13, nov. 2013.

CADER, T.; WESTRA, L. J.; EDEN, R. C. Spray Cooling Thermal Management for Increased Device Reliability. *IEEE Transactions on Device and Materials Reliability*, v. 4, n. 4, p. 605–613, dec. 2004.

CARDENAS, R.; NARAYANAN, V. A Generalized Critical Heat Flux Correlation for Submerged and Free Surface Jet Impingement Boiling. *Journal of Heat Transfer*, v. 136, n. 9, p. 091501–1 – 091501–9, sep.

2014.

CHANG, C.-C.; LIANG, N.-W.; CHEN, S.-L. Miniature Vapor Compressor Refrigeration System for Electronic Cooling. *IEEE Transactions on Components and Packaging Technologies*, v. 33, n. 4, p. 794–800, dec. 2010.

CHEN, S.; LIU, J.; LIU, X.; HOU, Y. An experimental comparison of heat transfer characteristic between R134-a and R22 in spray cooling. *Experimental Thermal and Fluid Science*, v. 66, p. 206–212, sep. 2015.

CHENG, W.-L.; LIU, Q.-N.; ZHAO, R.; FAN, H.-L. Experimental investigation of parameters effect on heat transfer of spray cooling. *Heat and Mass Transfer*, v. 46, n. 8-9, p. 911–921, oct. 2010.

CHIEN, L.-H.; CHANG, C.-Y. An experimental study of two-phase multiple jet cooling on finned surfaces using a dielectric fluid. *Applied Thermal Engineering*, v. 31, n. 11-12, p. 1983–1993, aug. 2011.

CHU, R. C.; SIMONS, R. E.; ELLSWORTH, M. J.; SCHMIDT, R. R.; COZZOLINO, V. Review of Cooling Technologies for Computer Products. *IEEE Transactions on Device and Materials Reliability*, v. 4, n. 4, p. 568–585, dec. 2004.

CHUNQIANG, S.; SHUANGQUAN, S.; CHANGQING, T.; HONGBO, X. Development and experimental investigation of a novel spray cooling system integrated in refrigeration circuit. *Applied Thermal Engineering*, v. 33-34, p. 246–252, feb. 2012.

COLEMAN, H. W.; STEELE, W. G. *Experimentation, Validation, and Uncertainty Analysis for Engineers*. Third edition. [S.l.]: John Wiley & Sons, Inc., 2009.

CREMASCHI, L.; GROLL, E. A.; GARIMELLA, S. V. Performance Potential and Challenges of Future Refrigeration-based Electronics Cooling Approaches. In: GARIMELLA, S. V.; FLEISCHER, A. S. (Ed.). *Proceedings of THERMES 2007 Conference*. Santa Fe, NM, 2007. p. 119–128.

EBADIAN, M. A.; LIN, C. X. A Review of High-Heat-Flux Heat Removal Technologies. *Journal of Heat Transfer*, v. 133, n. 11, p. 110801–1–10801–11, 2011.

FABBRI, M.; JIANG, S.; DHIR, V. K. COMPARATIVE STUDY OF SPRAY AND MULTIPLE MICRO JETS COOLING FOR HIGH POWER DENSITY ELECTRONIC APPLICATIONS. In: ASME 2003 INTERNATIONAL MECHANICAL ENGINEERING CONGRESS AND EXPOSITION. *Proceedings of IMECE'03*. Washington, D. C.: ASME, 2003. p. 1–9.

FABBRI, M.; JIANG, S.; DHIR, V. K. A Comparative Study of Cooling of High Power Density Electronics Using Sprays and Microjets. *Journal of Heat Transfer*, v. 127, n. 1, p. 38–48, jan. 2005.

FABBRI, M.; JIANG, S.; WARRIER, G. R.; DHIR, V. K. HEAT REMOVAL USING NARROW CHANNELS, SPRAYS AND MICROJETS. In: KAKAÇ, S.; VASILIEV, L. L.; BAYAZITOĞLU, Y.; YENER, Y. (Ed.). *Microscale Heat Transfer - Fundamentals and Applications*. The Netherlands: Springer, 2005, (NATO Science Series II: Mathematics, Physics and Chemistry, v. 193). p. 231–254. Proceedings of the NATO Advanced Study Institute on Microscale Heat Transfer - Fundamentals and Applications in Biological and Microelectromechanical Systems.

FERZIGER, J. H.; PERIĆ, M. *Computational Methods for Fluid Dynamics*. [S.l.]: Springer, 2002. 423 p.

GARCÍA-CASCALES, J. R.; VERA-GARCÍA, F.; CORBERÁN-

SALVADOR, J. M.; GONZÁLVEZ-MACIÁ, J. Assessment of boiling and condensation heat transfer correlations in the modelling of plate heat exchangers. *International Journal of Refrigeration*, v. 30, n. 6, p. 1029–1041, sep. 2007.

GARIMELLA, S. V.; RICE, R. A. Confined and Submerged Liquid Jet Impingement Heat Transfer. *Journal of Heat Transfer*, v. 117, n. 4, p. 871–877, nov. 1995.

GHIAASIAAN, S. M. *Two-Phase Flow, Boiling, and Condensation in Conventional and Miniature Systems*. [S.l.]: Cambridge University Press, 2008. 613 p.

GOSNEY, W. B. *Principles of Refrigeration*. [S.l.]: Cambridge University Press, 1982.

GOULD, K.; CAI, S. Q.; NEFT, C.; BHUNIA, A. Liquid Jet Impingement Cooling of a Silicon Carbide Power Conversion Module for Vehicle Applications. *IEEE TRANSACTIONS ON POWER ELECTRONICS*, v. 30, n. 6, p. 2975–2984, jun. 2015.

HE, J.; WU, Y.; CHEN, X.; LU, Y.; MA, C.; DU, C.; LIU, G.; MA, R. Experimental study of a miniature vapor compression refrigeration system with two heat sink evaporators connected in series or in parallel. *International Journal of Refrigeration*, v. 49, p. 28–35, jan. 2015.

HERMES, C. J. L.; BARBOSA JR., J. R. Thermodynamic comparison of Peltier, Stirling, and vapor compression portable coolers. *Applied Energy*, v. 91, n. 1, p. 51–58, mar. 2012.

HERMES, C. J. L.; MELO, C.; KNABBEN, F. T. Algebraic Solution of Capillary Tube Flows: Part I: Adiabatic Capillary Tubes. *Applied Thermal Engineering*, v. 30, n. 5, p. 449–457, 2010.

HEYDARI, A. Miniature vapor compression refrigeration system
for active cooling of high performace computers. In: THE
EIGHTH INTERSOCIETY CONFERENCE ON THERMAL AND
THERMOMECHANICAL PHENOMENA IN ELECTRONIC
SYSTEMS (ITHERM 2002). *Proceedings of the ITHERM 2002.* San
Diego, CA: IEEE, 2002. p. 371–378.

HOU, Y.; LIU, J.; SU, X.; QIAN, Y.; LIU, L.; LIU, X. Experimental
study on the characteristics of a closed loop R134-a spray cooling.
Experimental Thermal and Fluid Science, v. 61, p. 194–200, feb. 2015.

HOWELL, J. R.; BUCKIUS, R. O. *Fundamentals of Engineering
Thermodynamics.* SI version. [S.l.]: McGraw-Hill Book Company,
1987.

HUANG, J.; SHEER, T. J.; BAILEY-MCEWAN, M. Heat transfer
and pressure drop in plate heat exchanger refrigerant evaporators.
International Journal of Refrigeration, v. 35, n. 2, p. 325–335, mar.
2012.

INMETRO. *Avaliação de dados de medição: Guia para a expressão
de incerteza de medição - GUM2008.* Duque de Caxias (RJ), 2012.

JEONG, S. How difficult is it to make a micro refrigerator?
International Journal of Refrigeration, v. 27, n. 3, p. 309–313, may.
2004. Short Communication.

JIN, S.; SUNG, T.; SEO, T.; KIM, J. Characteristics of R-123
two-phase flow through micro-scale short tube orifice for design of a
small cooling system. *Experimental Thermal and Fluid Science*, v. 35,
n. 7, p. 1484–1489, oct. 2011.

JOSHI, S. N.; DEDE, E. M. Effect of sub-cooling on performance
of a multi-jet two phase cooler with multi-scale porous surfaces.

International Journal of Thermal Sciences, v. 87, p. 110–120, jan. 2015.

JOSHI, S. N.; RAU, M. J.; DEDE, E. M. AN EXPERIMENTAL STUDY OF A MULTI-DEVICE JET IMPINGEMENT COOLER WITH PHASE CHANGE USING HFE-7100. In: ASME 2013 INTERNATIONAL MECHANICAL ENGINEERING CONGRESS AND EXPOSITION (IMECE2013). *Proceedings of the IMECE2013*. San Diego, CA: ASME, 2013. p. 1–10. Paper No. 63249.

JOSHI, S. N.; RAU, M. J.; DEDE, E. M.; GARIMELLA, S. V. AN EXPERIMENTAL STUDY OF A MULTI-DEVICE JET IMPINGEMENT COOLER WITH PHASE CHANGE USING HFE-7100. In: ASME 2013 HEAT TRANSFER SUMMER CONFERENCE (HT2013). *Proceedings of the HT2013*. Minneapolis, MN: ASME, 2013. p. 1–9. Paper No. 17059.

KADAM, S. T.; KUMAR, R. Twenty first century cooling solution: Microchannel heat sinks. *International Journal of Thermal Sciences*, v. 85, p. 73–92, nov. 2014.

KANDLIKAR, S. G.; BAPAT, A. V. Evaluation of Jet Impingement, Spray And Microchannel Chip Cooling Options for High Heat Flux Removal. *Heat Transfer Engineering*, v. 28, n. 11, p. 911–923, 2007.

KARAMI, R.; ASHGRIZ, N. Flashing Sprays. In: ASHGRIZ, N. (Ed.). *Handbook of Atomization and Sprays Theory and Applications*. New York: Springer Science+Business Media, 2011. Chap. 10, p. 233–254.

KATTAN, N.; THOME, J. R.; FAVRAT, D. Flow Boiling in Horizontal Tubes: Part 1 – Development of a Diabatic Two-Phase Flow Pattern Map. *Journal of Heat Transfer*, v. 120, n. 1, p. 140–147, feb. 1998.

KATTAN, N.; THOME, J. R.; FAVRAT, D. Flow Boiling in Horizontal Tubes: Part 3 – Development of a New Heat Transfer Model Based on Flow Pattern. *Journal of Heat Transfer*, v. 120, n. 1, p. 156–165, feb. 1998.

KIM, J. Spray cooling heat transfer: The state of the art. *International Journal of Heat and Fluid Flow*, v. 28, n. 4, p. 753–767, aug. 2007.

KLEIN, S. A. *EES - Engineering Equation Solver*. 2004. Professional Version V8.701-3D.

LABUNTSOV, D. A. Heat transfer in film condensation of pure steam on vertical surfaces and horizontal tubes. *Teploenergetika*, v. 4, n. 7, p. 72–79, 1957.

LAMAISON, N.; MARCINICHEN, J. B.; THOME, J. R. Recent advances in on-chip cooling systems: Experimental evaluation and dynamic modeling. In: THE 15TH INTERNATIONAL HEAT TRANSFER CONFERENCE (IHTC-15). *Proceedings of the IHTC-15*. Kyoto, Japan, 2014. p. 1–35. Keynote Lecture - Paper IHTC15-KN06.

LEE, H. *Thermal Design: Heat Sinks, Thermoeletrics, Heat Pipes, Compact Heat Exchangers, and Solar Cells*. New Jersey: John Wiley & Sons, 2010. 630 p.

LEMMON, E. W.; HUBER, M. L.; MCLINDEN, M. *NIST Reference Fluid Thermodynamic and Transport Properties - REFPROP*. 2007. Version 8.0.

LIANG, K.; STONE, R.; DADD, M.; BAILEY, P. A novel linear electromagnetic-drive oil-free refrigeration compressor using R134a. *International Journal of Refrigeration*, v. 40, p. 450–459, apr. 2014.

LIANG, K.; STONE, R.; DAVIES, G.; DADD, M.; BAILEY, P. Modelling and measurement of a moving magnet linear compressor performance. *Energy*, v. 66, n. 1, p. 487–495, mar. 2014.

LIANG, K.; STONE, R.; HANCOCK, W.; DADD, M.; BAILEY, P. Comparison between a crank-drive reciprocating compressor and a novel oil-free linear compressor. *International Journal of Refrigeration*, v. 45, p. 25–34, sep. 2014.

LIENHARD V, J. H. ANNUAL REVIEW OF HEAT TRANSFER. In: *LIQUID JET IMPINGEMENT*. [S.l.]: Begel House, Inc, 1995. v. 6, Chap. 4, p. 199–270.

LIENHARD V, J. H. Heat Transfer by Impingement of Circular Free-Surface Liquid Jets. In: EIGHTEENTH NATIONAL AND SEVENTH ISHMT-ASME HEAT AND MASS TRANSFER CONFERENCE. *Proceedings of the 18th National & 7th ISHMT-ASME HMTC*. IIT Guwahati, India, 2006. p. 1–16.

LIENHARD V, J. H.; HADELER, J. High Heat Flux Cooling by Liquid Jet-Array Modules. *Chemical Engineering & Technology*, v. 22, n. 11, p. 967–970, nov. 1999.

LIN, L.; PONNAPPAN, R. Heat transfer characteristics of spray cooling in a closed loop. *International Journal of Heat and Mass Transfer*, v. 46, n. 20, p. 3737–3746, sep. 2003.

LIN, S. P.; REITZ, R. D. DROP AND SPRAY FORMATION FROM A LIQUID JET. *Annual Review of Fluid Mechanics*, v. 30, p. 85–105, jan. 1998.

LINDEMAN, B. A.; SHEDD, T. A. Comparison of empirical correlations and a two-equation predictive model for heat transfer to arbitrary arrays of single-phase impinging jets. *International Journal*

of Heat and Mass Transfer, v. 66, p. 772–780, nov. 2013.

LONGO, G. A. Refrigerant R134a condensation heat transfer and pressure drop inside a small brazed plate heat exchanger. *International Journal of Refrigeration*, v. 31, n. 5, p. 780–789, aug. 2008.

MADDOX, J. F.; KNIGHT, R. W.; BHAVNANI, S. H. Local Thermal Measurements of a Confined Array of Impinging Liquid Jets for Power Electronics Cooling. In: THIRTY-FIRST SEMICONDUCTOR THERMAL MEASUREMENT, MODELING AND MANAGEMENT SYMPOSIUM (SEMI-THERM 31). *Proceedings of the SEMI-THERM 31*. San Jose, CA: IEEE, 2015. p. 228–234.

MAHMOUDI, S. R.; ADAMIAK, K.; CASTLE, G. S. P. Two-phase cooling characteristics of a saturated free falling circular jet of HFE7100 on a heated disk: Effect of jet length. *International Journal of Heat and Mass Transfer*, v. 55, n. 21-22, p. 6181–6190, oct. 2012.

MALISKA, C. R. *Transferência de Calor e Mecânica dos Fluidos Computacional*. 2. ed. Rio de Janeiro: Livros Técnicos e Científicos Editora, 2004. 453 p.

MANCIN, S.; ZILIO, C.; RIGHETTI, G.; ROSSETTO, L. Mini Vapor Cycle System for high density electronic cooling applications. *International Journal of Refrigeration*, v. 36, n. 4, p. 1191–1202, 2013.

MARCHINICHEN, J. B.; OLIVIER, J. A.; LAMAISON, N.; THOME, J. R. Advances in electronics cooling. *Heat Transfer Engineering*, v. 34, n. 5-6, p. 434–446, 2013.

MEYER, M. T.; MUDAWAR, I.; BOYACK, C. E.; HALE, C. A. Single-phase and two-phase cooling with an array of rectangular jets. *International Journal of Heat and Mass Transfer*, v. 49, n. 1-2, p. 17–29, jan. 2006.

MINER, A.; GHOSHAL, U. Limits of Heat Removal in Microelectronic Systems. *IEEE Transactions on Components and Packaging Technologies*, v. 29, n. 4, p. 743–749, dec. 2006.

MONGIA, R.; MASAHIRO, K.; DISTEFANO, E.; BARRY, J.; CHEN, W.; IZENSON, M.; POSSAMAI, F.; ZIMMERMANN, A.; MOCHIZUKI, M. Small scale refrigeration system for electronics cooling within a notebook computer. In: THE TENTH INTERSOCIETY CONFERENCE ON THERMAL AND THERMOMECHANICAL PHENOMENA IN ELECTRONICS SYSTEMS (ITHERM '06). *Proceedings of the ITHERM '06.* San Diego, CA: IEEE, 2006. p. 751–758.

MUDAWAR, I. Assessment of High-Heat-Flux Thermal Management Schemes. *IEEE Transactions on Components and Packaging Technologies*, v. 24, n. 2, p. 122–141, jun. 2001.

MUDAWAR, I.; BHARATHAN, D.; KELLY, K.; NARUMANCHI, S. TWO-PHASE SPRAY COOLING OF HYBRID VEHICLE ELECTRONICS. In: ELEVENTH INTERSOCIETY CONFERENCE ON THERMAL AND THERMOMECHANICAL PHENOMENA IN ELECTRONIC SYSTEMS. *Proceedings of the ITHERM 2008.* Orlando (FL): IEEE, 2008. p. 1210–1221.

MUSZYNSKI, T.; ANDRZEJCZYK, R. Heat transfer characteristics of hybrid microjet - Microchannel cooling module. *Applied Thermal Engineering*, v. 93, p. 1360–1366, jan. 2015.

NAKAYAMA, W.; SUZUKI, O.; HARA, Y. Thermal Management of Electronic and Electrical Devices in Automobile Environment. In: IEEE VEHICLE POWER AND PROPULSION CONFERENCE (VPPC). *Proceedings of the VPPC '09.* Dearborn, MI: IEEE, 2009. p. 601–608.

OH, C. H.; LIENHARD V, J. H.; YOUNIS, H. F.; DAHBURA, R. S.;

MICHELS, D. Liquid jet-array cooling modules for high heat fluxes. *AIChE Journal*, v. 44, n. 4, p. 769–779, apr. 1998.

OLIVEIRA, P. A.; BARBOSA JR., J. R. Thermal Design of a Spray-Based Heat Sink Integrated with a Compact Vapor Compression Cooling System for Removal of High Heat Fluxes. *Heat Transfer Engineering*, v. 36, n. 14-15, p. 1–15, 2015.

ORTEGA, A.; BIRLE, J. R. The evolution of air cooling in electronic systems and observations about its limits. In: EIGHTEENTH NATIONAL AND SEVENTH ISHMT-ASME HEAT AND MASS TRANSFER CONFERENCE. *Proceedings of the 18th National & 7th ISHMT-ASME HMTC*. Guwahati, India: ASME, 2006. Paper K10.

OZA, R. D. On the Mechanism of Flashing Injection of Initially Subcooled Fuels. *Journal of Fluids Engineering*, v. 106, n. 1, p. 105–109, mar. 1984.

PAN, Y.; WEBB, B. W. Heat Transfer Characteristics of Arrays of Free-Surface Liquid Jets. *Journal of Heat Transfer*, v. 117, n. 4, p. 878–883, nov. 1995.

PARIDA, P. R.; EKKAD, S. V.; NGO, K. Impingement-based high performance cooling configurations for automotive power converters. *International Journal of Heat and Mass Transfer*, v. 55, n. 4, p. 834–847, jan. 2012.

PARK, W. H.; MCCALL, R.; KEN YANG, C. K. Total system power minimization of microprocessors using refrigerated systems for electronic cooling. In: 6TH INTERNATIONAL MICROSYSTEMS, PACKAGING, ASSEMBLY AND CIRCUITS TECHNOLOGY CONFERENCE (IMPACT). *Proceedings*. Taipei: IEEE, 2011. p. 242–245.

PARK, W. H.; YANG, C.-K. K. Effects of Using Advanced Cooling Systems on the Overall Power Consumption of Processors. *IEEE Transactions on Very Large Scale Integration (VLSI) Systems*, v. 21, n. 9, p. 1644–1654, sep. 2013.

PHELAN, P. E.; CHIRIAC, V. A.; LEE, T.-Y. T. Current and Future Miniature Refrigeration Cooling Technologies for High Power Microelectronics. *IEEE Transactions on Components and Packing Technologies*, v. 25, n. 3, p. 356–365, sep. 2002.

POLANCO, G.; HOLDØ, A. E.; MUNDAY, G. General review of flashing jet studies. *Journal of Harzadous Materials*, v. 173, n. 1-3, p. 2–18, jan. 2010.

POULIKAKOS, D. *Conduction Heat Transfer*. New Jersey: Prentice Hall, 1994. 353 p.

PRASHER, R.; CHIU, C.-P. Thermal Interface Materials. In: LU, D.; WONG, C. P. (Ed.). *Materials for Advanced Packaging*. New York: Springer Science+Business Media, 2009. Chap. 13, p. 437–458.

QIU, L.; DUBEY, S.; CHOO, F. H.; DUAN, F. Recent developments of jet impingement nucleate boiling. *International Journal of Heat and Mass Transfer*, v. 89, p. 42–58, oct. 2015.

REITZ, R. D. A Photographic Study of Flash-Boiling Atomization. *Aerosol Science and Technology*, v. 12, n. 3, p. 561–569, 1990.

RIBEIRO, G. B.; BARBOSA JR., J. R.; PRATA, A. T. Mini-Channel Evaporator/Heat Pipe Assembly for a Chip Cooling Vapor Compression Refrigeration System. *International Journal of Refrigeration*, v. 33, n. 7, p. 1402–1412, 2010.

ROYNE, A.; DEY, C. J. Effect of nozzle geometry on pressure drop and heat transfer in submerged jet arrays. *International Journal of Heat and Mass Transfer*, v. 49, n. 3, p. 800–804, jan. 2006. Technical Note.

SAN, J.-Y.; CHEN, J.-J. Effects of jet-to-jet spacing and jet height on heat transfer characteristics of an impinging jet array. *International Journal of Heat and Mass Transfer*, v. 71, p. 8–17, apr. 2014.

SHAH, R. K.; SEKULIĆ, D. P. *Fundamentals of Heat Exchanger Design*. New Jersey: John Wiley & Sons, 2003. 941 p.

SHEDD, T. A. Next Generation Spray Cooling: High Heat Flux Management in Compact Spaces. *Heat Transfer Engineering*, v. 28, n. 2, p. 87–92, 2007.

STARKE, M. R.; AYERS, C. W.; HSU, J. S.; CONKLIN, J. C. *POTENTIAL REFRIGERANTS FOR POWER ELECTRONICS COOLING*. Oak Ridge, Tennessee, oct. 2005. ORNL/TM-2005/219.

SUNG, M. K.; MUDAWAR, I. Single-phase and two-phase cooling using hybrid micro-channel/slot-jet module. *International Journal of Heat and Mass Transfer*, v. 51, n. 15-16, p. 3825–3839, jul. 2008.

SUNG, M. K.; MUDAWAR, I. Single-phase and two-phase heat transfer characteristics of low temperature hybrid micro-channel/micro-jet impingement cooling module. *International Journal of Heat and Mass Transfer*, v. 51, n. 15-16, p. 3882–3895, jul. 2008.

SUNG, M. K.; MUDAWAR, I. CHF determination for high-heat flux phase change cooling system incorporating both micro-channel flow and jet impingement. *International Journal of Heat and Mass Transfer*, v. 52, n. 3-4, p. 610–619, jan. 2009.

SUNG, M. K.; MUDAWAR, I. Effects of jet pattern on two-phase performance of hybrid micro-channel/micro-circular-jet-impingement thermal management scheme. *International Journal of Heat and Mass Transfer*, v. 52, n. 13-14, p. 3364–3372, jun. 2009.

SUNG, T.; LEE, D.; KIM, H. S.; KIM, J. Development of a novel meso-scale vapor compression refrigeration system (mVCRS). *Applied Thermal Engineering*, v. 66, n. 1-2, p. 453–463, may. 2014.

TAKEMORI, C. K.; FAGOTTI, F. Numerical evaluation of performace curves of a high frequency microcompressor. In: INTERNATIONAL COMPRESSOR ENGINEERING CONFERENCE AT PURDUE. *Proceedings*. West Lafayette, IN, 2012. Paper No. 1461.

TAN, Y. B.; XIE, J. L.; DUAN, F.; WONG, T. N.; TOH, K. C.; CHOO, K. F.; CHAN, P. K.; CHUA, Y. S. Multi-nozzle spray cooling for high heat flux applications in a closed loop system. *Applied Thermal Engineering*, v. 54, n. 2, p. 372–379, may. 2013.

TRUTASSANAWIN, S.; GROLL, E.; GARIMELLA, S. V.; CREMASCHI, L. Experimental Investigation of a Miniature-Scale Refrigeration System for Electronics Cooling. *IEEE Transactions on Components and Packaging Technologies*, v. 29, n. 3, p. 678–687, sep. 2006.

TULLIUS, J. F.; VAJTAI, R.; BAYAZITOGLU, Y. A Review of Cooling in Microchannels. *Heat Transfer Engineering*, v. 32, n. 7-8, p. 527–541, 2011.

TÜRKAKAR, G.; OKUTUCU-ÖZYURT, T. Entropy generation analysis and dimensional optimization of an evaporator for use in a microscale refrigeration cycle. *International Journal of Refrigeration*, v. 56, p. 140–153, aug. 2015.

ULSON DE SOUZA, A. G.; BARBOSA JR., J. R. Spray cooling of plain and copper-foam enhanced surfaces. *Experimental Thermal and Fluid Science*, v. 39, p. 198–206, may. 2012.

ULSON DE SOUZA, A. G.; BARBOSA JR., J. R. Experimental evaluation of spray cooling of R-134a on plain and enhanced surfaces. *International Journal of Refrigeration*, v. 36, n. 2, p. 527–533, mar. 2013.

UNGER, R.; NOVOTNY, S. A high performace linear compressor for CPU cooling. In: INTERNATIONAL COMPRESSOR ENGINEERING CONFERENCE AT PURDUE. *Proceedings*. West Lafayette, IN, 2002. Paper No. C23-3.

VERSTEEG, H. K.; MALALASEKERA, W. *An Introduction to Computational Fluid Dynamics: The Finite Volume Method*. [S.l.]: Longman Scientific & Technical, 1995. 257 p.

WANG, W.; TAI, X. Characteristic of a miniature linear compressor. In: INTERNATIONAL COMPRESSOR ENGINEERING CONFERENCE AT PURDUE. *Proceedings*. West Lafayette, IN, 2010. Paper No. 1288.

WANG, Y.; LUO, Q.; CHEN, X. Advanced Electronic Cooling Technologies. In: ASIA PACIFIC CONFERENCE ON POSTGRADUATE RESEARCH IN MICROELECTRONICS & ELECTRONICS (PRIMEASIA). *Proceedings of the PrimeAsia 2009*. Shanghai: IEEE, 2009. p. 149–152.

WANG, Z. Y.; WONG, T. N.; DUAN, F. Submerged Liquid Jet Impingement Cooling. In: 13TH ELECTRONICS PACKAGING TECHNOLOGY CONFERENCE (EPTC). *Proccedings of the 13th EPTC*. Singapore: IEEE, 2011. p. 660–666.

WHELAN, B. P.; KEMPERS, R.; ROBINSON, A. J. A liquid-based system for CPU cooling implementing a jet array impingement waterblock and a tube array remote heat exchanger. *Applied Thermal Engineering*, v. 39, p. 86–94, jun. 2012.

WHELAN, B. P.; ROBINSON, A. J. Nozzle geometry effects in liquid jet array impingement. *Applied Thermal Engineering*, v. 29, n. 11-12, p. 2211–2221, aug. 2009.

WOJTAN, L.; URSENBACHER, T.; THOME, J. R. Investigation of flow boiling in horizontal tubes: Part I – A new diabatic two-phase flow pattern map. *International Journal of Heat and Mass Transfer*, v. 48, n. 14, p. 2955–2969, jul. 2005.

WOMAC, D. J.; RAMADHYANI, S.; INCROPERA, F. P. Correlating Equations for Impingement Cooling of Small Heat Sources With Single Circular Liquid Jets. *Journal of Heat Transfer*, v. 115, n. 1, p. 106–115, feb. 1993.

WU, Z.; DU, R. Design and experimental study of a miniature vapor compression refrigeration system for electronics cooling. *Applied Thermal Engineering*, v. 31, n. 2-3, p. 385–390, feb. 2011.

XIE, J. L.; TAN, Y. B.; WONG, T. N.; DUAN, F.; TOH, K. C.; CHOO, K. F.; CHAN, P. K.; CHUA, Y. S. Multi-nozzle array spray cooling for large area high power devices in a closed loop system. *International Journal of Heat and Mass Transfer*, v. 78, p. 1177–1186, nov. 2014.

XU, H.; SI, C.; SHAO, S.; TIAN, C. Experimental investigation on heat transfer of spray cooling with isobutane (R600a). *International Journal of Thermal Sciences*, v. 86, p. 21–27, dec. 2014.

YAN, Z. B.; DUAN, F.; WONG, T. N. Large Area Spray Cooling by

Inclined Nozzles for Electronic Board. In: 12TH ELECTRONICS PACKAGING TECHNOLOGY CONFERENCE (EPTC 2010). *Proceedings of the EPTC 2010.* [S.l.]: IEEE, 2010. p. 76–78.

YAN, Z. B.; TOH, K. C.; DUAN, F.; WONG, T. N.; CHOO, K. F.; CHAN, P. K.; CHUA, Y. S. Experimental study of impingement spray cooling for high power devices. *Applied Thermal Engineering*, v. 30, n. 10, p. 1225–1230, jul. 2010.

YAN, Z. B.; TOH, K. C.; DUAN, F.; WONG, T. N.; CHOO, K. F. Heat Transfer Characteristics of Impingement Spray Cooling System for Electronic Test Cards. In: THE 2ND INTERNATIONAL CONFERENCE ON COMPUTER AND AUTOMATION ENGINEERING (ICCAE). *Proceedings of the ICCAE 2010.* [S.l.]: IEEE, 2010. p. 326–329.

YUAN, W.; YANG, B.; YANG, Y.; REN, K.; XU, J.; LIAO, Y. Development and experimental study of the characteristics of a prototype miniature vapor compression refrigerator. *Applied Energy*, v. 143, p. 47–57, apr. 2015.

ZHOU, F.; JOSHI, S. N.; DEDE, E. M. Visualization of Bubble Behavior for Jet Impingement Cooling with Phase Change. In: THE FOURTEENTH IEEE INTERSOCIETY CONFERENCE ON THERMAL AND THERMOMECHANICAL PHENOMENA IN ELECTRONIC SYSTEMS (ITHERM). *Proceedings of the ITherm 2014.* Orlando, FL: IEEE, 2014.

APPENDIX A –

Measurement Uncertainty Analysis

This appendix outlines the measurement uncertainty analysis applied to the experimental investigation presented in this thesis. It starts with the introduction of some basic theoretical concepts. Then, the assessing of uncertainties for measured and calculated parameters is separately presented.

A.1 Fundamentals

According to the ISO *Guide to the Expression of Uncertainty in Measurement* (INMETRO, 2012), a standard uncertainty, u, is defined as an estimate of the standard deviation of the parent population from which a particular elemental error originates. The combination of all of the elemental standard uncertainties, u_j, gives the standard uncertainty of a parameter X,

$$u(X) = \sqrt{\sum_{j=1}^{m} u_j^2} \tag{A.1}$$

where $j = 1, 2, .., m$.

The standard deviation of a sample distribution of X composed of N measurements is found from,

$$s(X) = \sqrt{\frac{1}{N-1} \sum_{j=1}^{N} (X_j - \overline{X})^2} \tag{A.2}$$

where the mean value of X is calculated as,

$$\overline{X} = \frac{1}{N} \sum_{j=1}^{N} X_j \tag{A.3}$$

Coleman and Steele (2009) identify two sources of error that influence a parameter X: systematic and random. Systematic error sources do not vary during the measurement period and thus produce the same errors in each measurement. Therefore, the systematic standard uncertainty, $b(X)$, depends mainly on the instrument errors and their influence is not included in $s(X)$. On the contrary, random error sources vary during the measurement period and their effects are included in $s(X)$, which represent the scatter of the parameter X in the measurements.

The elemental standard uncertainties u_i can be conveniently grouped according to this categorization, and the combined standard uncertainty of the variable X can be re-written as,

$$u(X) = \sqrt{b^2(X) + s^2(X)} \tag{A.4}$$

In the case of a parameter ξ defined as a function of multiple variables, such as $\xi = f(X_1, X_2, ..., X_m)$, the Taylor Series Method for uncertainty propagation (COLEMAN; STEELE, 2009) can be employed to obtain the combined standard uncertainty $u(\xi)$,

$$u(\xi) = \sqrt{\sum_{j=1}^{m} \left[\frac{\partial \xi}{\partial X_j} u(X_j) \right]^2} \tag{A.5}$$

The expanded uncertainty, U, is the interval around the best value of a variable of interest, X or ξ, within which it is expected the true value of this variable to lie with a given confidence interval. To obtain the expanded uncertainty, a coverage factor should be used in order to associate a level of confidence with the uncertainty of the variable. Thus,

$$U = k_{95} u \tag{A.6}$$

Considering that the probability distribution of a variable and its combined standard uncertainty are approximately normal and the effective degrees of freedom of the combined uncertainty is of a significant size, the coverage factor calculated for a 95% confidence interval is $k_{95} = 2$ (INMETRO, 2012).

A.2 Uncertainty of the Measured Parameters

 In-house calibration procedures were conducted concerning the following measured parameters: (i) temperature, (ii) absolute pressure, (iii) refrigerant mass flow rate, (iv) secondary fluid volumetric flow rate, (v) superheating input thermal power, and (vi) calorimeter input thermal power.

 The combined standard uncertainty for a parameter X obtained from the calibration process, u_{calibr}, is computed as,

$$u(X) = u_{calibr} = \sqrt{u_{ref}^2 + u_{cf}^2 + \left[\max \frac{s(X_j)}{\sqrt{N}}\right]^2} \qquad (A.7)$$

where $j = 1, 2, ..., NP$. The symbol NP represents the number of points used to generate the curve fit and N is the sample size.

 The reference standard uncertainty, u_{ref}, was obtained from either calibration or catalog provided by the manufacturer according to the following manner: (i) if a calibration process was conducted, a normal distribution is assumed, with a 95% confidence level and infinite degrees of freedom. Hence, $u_{ref} = U_{ref}/2$; (ii) if U_{ref} was evaluated from catalog information, as suggested by INMETRO (2012), a rectangular distribution is assumed with 68% confidence interval and, thus, $u_{ref} = U_{ref}/\sqrt{3}$.

 As the sample standard deviation of the mean, $s(X_j)/\sqrt{N}$, assumes different values for each point of the curve fit, its maximum value was incorporated in Eq. (A.7). The uncertainty related to the linear curve fit, u_{cf}, is determined as,

$$u_{cf} = \sqrt{\frac{1}{NP-2} \sum_{j=1}^{NP} (X_{ref,j} - X_{cf,j})^2} \qquad (A.8)$$

where $X_{ref,j}$ is the value given by the reference measurement equipment for each point of the calibration process and $X_{cf,j}$ is the corresponding value obtained from the linear fit.

 In the present analysis, the systematic uncertainties not corrected by the calibration process are calculated from the uncertainty information provided by the manufacturer. This is the case of the electrical power consumption of the compressor, $\dot{W}_{comp}$. Again, since the manufacturer did not present the confidence interval for the expanded uncertainty of the power meter, a rectangular (uniform) probability

distribution is assumed. Thus, the uncertainty of the active power is calculated as,

$$u(\dot{W}_{comp}) = \frac{1.5}{100\sqrt{3}}[0.5\dot{W}_{comp} + 0.5\text{RNG} + 0.09(f - 10)\dot{W}_{comp}] \quad \text{(A.9)}$$

where RNG represents the input power range and f is the frequency of operation, given in kHz.

A preliminary dimensional analysis of Eq. (A.9) considering the compressor operating conditions showed that the last term on its right-hand side is several orders of magnitude (at least 8) lower than the other terms. Therefore, it was neglected and Eq. (A.9) can be simplified to,

$$u(\dot{W}_{comp}) = \frac{1.5}{100\sqrt{3}}(0.5\dot{W}_{comp} + 0.5\text{RNG}) \quad \text{(A.10)}$$

A.3   Uncertainty of the Calculated Parameters

The uncertainty propagation expression, given in Eq. (A.5), is applied to obtain the uncertainty equations of the calculated parameters introduced in Chapter 4. The following list of equations is divided into three groups: (i) thermodynamic properties, (ii) heat transfer and work rates and (iii) performance metrics.

A.3.1   Thermodynamic Properties

Considering the enthalpy of a specified thermodynamic state, $h = f(P, T)$, the combined standard uncertainty, $u(h)$, can be expressed as:

$$u^2(h) = \left(\frac{\partial h}{\partial P}\right)^2 u^2(P) + \left(\frac{\partial h}{\partial T}\right)^2 u^2(T) \quad \text{(A.11)}$$

where the elemental standard uncertainties $u(P)$ and $u(T)$ are obtained directly from calibration.

The partial derivatives in Eq. (A.11) are numerically approximated by a second-order central-difference scheme (COLEMAN; STEELE, 2009; FERZIGER; PERIĆ, 2002),

$$\frac{\partial h}{\partial P} \approx \frac{h(P_{j+1}, T) - h(P_{j-1}, T)}{2u(P)} \quad \text{(A.12)}$$

$$\frac{\partial h}{\partial T} \approx \frac{h(P, T_{j+1}) - h(P, T_{j-1})}{2u(T)} \tag{A.13}$$

where $P_{j+1} = P + u(P)$, $P_{j-1} = P - u(P)$, $T_{j+1} = T + u(T)$ and $T_{j-1} = T - u(T)$. It should be mentioned that P and T are the sample-averaged pressure and temperature, respectively.

Substituting Eqs. (A.12) and (A.13) in Eq. (A.11) results in,

$$u(h) = \sqrt{\left[\frac{h(P_{j+1}, T) - h(P_{j-1}, T)}{2}\right]^2 + \left[\frac{h(P, T_{j+1}) - h(P, T_{j-1})}{2}\right]^2} \tag{A.14}$$

During some experimental runs, saturation conditions were found at the condenser inlet. In such situations, the vapor enthalpy can be determined either as $h = f(P, x = 1)$ or $h = f(T, x = 1)$. Likewise, the partial derivatives of Eq. (A.11) are numerically computed as,

$$\left.\frac{\partial h}{\partial P}\right|_{sat} \approx \frac{h(P_{j+1}, x = 1) - h(P_{j-1}, x = 1)}{2u(P)} \tag{A.15}$$

$$\left.\frac{\partial h}{\partial T}\right|_{sat} \approx \frac{h(T_{j+1}, x = 1) - h(T_{j-1}, x = 1)}{2u(T)} \tag{A.16}$$

Using Eqs. (A.15) and (A.16) in Eq. (A.11) one obtains the combined standard uncertainty of the saturated vapor enthalpy,

$$u(h)|_{sat} = \left\{\left[\frac{h(P_{j+1}, x = 1) - h(P_{j-1}, x = 1)}{2}\right]^2 + \right.$$

$$\left.\left[\frac{h(T_{j+1}, x = 1) - h(T_{j-1}, x = 1)}{2}\right]^2\right\}^{\frac{1}{2}} \tag{A.17}$$

The enthalpy of the two-phase mixture at the jet cooler outlet, $h_{jc,o}$, is determined by the energy balance shown in Eq. (4.5). The combined standard uncertainty for this calculated parameter is expressed as,

$$u^2(h_{jc,o}) = \left(\frac{\partial h_{jc,o}}{\partial h_{jc,i}}\right)^2 u^2(h_{jc,i}) + \left(\frac{\partial h_{jc,o}}{\partial \dot{Q}_c}\right)^2 u^2(\dot{Q}_c) +$$

$$+ \left(\frac{\partial h_{jc,o}}{\partial \dot{m}_r}\right)^2 u^2(\dot{m}_r) \qquad (A.18)$$

By solving the partial derivatives, the preceding equation is written as,

$$u(h_{jc,o}) = \sqrt{u^2(h_{jc,i}) + \left[\frac{u(\dot{Q}_c)}{\dot{m}_r}\right]^2 + \left[\frac{u(\dot{m}_r)\dot{Q}_c}{(\dot{m}_r)^2}\right]^2} \qquad (A.19)$$

where the computation of $u(\dot{Q}_c)$ is presented in the following subsection.

The vapor quality at the jet cooler outlet, $x_{jc,o}$, is determined by an equation of state which is a function of the two-phase mixture enthalpy, $h_{jc,o}$ and evaporating pressure, $P_{evap} = P_{jc,o}$. Based on the same procedure, the combined standard uncertainty, $u(x)$, is given as follows. The subscript notation jc,o is omitted for convenience.

$$u^2(x) = \left(\frac{\partial x}{\partial P}\right)^2 u^2(P) + \left(\frac{\partial x}{\partial h}\right)^2 u^2(h) \qquad (A.20)$$

Similarly, the numerical treatment of the sensitivity coefficients results in,

$$u(x) = \sqrt{\left[\frac{x(P_{j+1}, h) - x(P_{j-1}, h)}{2}\right]^2 + \left[\frac{x(P, h_{j+1}) - x(P, h_{j-1})}{2}\right]^2} \qquad (A.21)$$

where $h_{j+1} = h + u(h)$ and $h_{j-1} = h - u(h)$. It should be clear that h and $u(h)$ are calculated with Eqs. (4.5) and (A.19), respectively.

Standard uncertainties for condensation, $T_{cond} = f(P_{cond,o})$, and evaporation, $T_{evap} = f(P_{jc,o})$, temperatures are respectively expressed as,

$$u(T_{cond}) = \sqrt{\left[\frac{\partial T_{cond}}{\partial P_{cond,o}} u(P_{cond,o})\right]^2} \qquad (A.22)$$

$$u(T_{evap}) = \sqrt{\left[\frac{\partial T_{evap}}{\partial P_{jc,o}}u(P_{jc,o})\right]^2} \qquad (A.23)$$

In the same manner, the discrete sensitivity coefficients are,

$$\frac{\partial T_{cond}}{\partial P_{cond,o}} \approx \frac{T_{cond}(P_{j+1}) - T_{cond}(P_{j-1})}{2u(P_{cond,o})} \qquad (A.24)$$

$$\frac{\partial T_{evap}}{\partial P_{jc,o}} \approx \frac{T_{evap}(P_{j+1}) - T_{evap}(P_{j-1})}{2u(P_{jc,o})} \qquad (A.25)$$

where $P_{j+1} = P_{cond,o} + u(P_{cond,o})$ and $P_{j-1} = P_{cond,o} - u(P_{cond,o})$ for Eq. (A.24). Concerning to Eq. (A.25), $P_{j+1} = P_{jc,o} + u(P_{jc,o})$ and $P_{j-1} = P_{jc,o} - u(P_{jc,o})$.

Substitution of Eqs. (A.24) and (A.25) into Eqs. (A.22) and (A.23), in the order given, results in the following expressions,

$$u(T_{cond}) = \frac{T_{cond}(P_{j+1}) - T_{cond}(P_{j-1})}{2} \qquad (A.26)$$

$$u(T_{evap}) = \frac{T_{evap}(P_{j+1}) - T_{evap}(P_{j-1})}{2} \qquad (A.27)$$

A.3.2 Heat Transfer and Work Rates

The cooling capacity of the refrigeration system is computed as,

$$\dot{Q}_c = Vi \qquad (A.28)$$

where V is the voltage and i represents the current, both provided by the digital DC power supply.

From Eq. (A.5), the combined uncertainty of the calculated cooling capacity takes the form,

$$u^2(\dot{Q}_c) = \left(\frac{\partial \dot{Q}_c}{\partial V}\right)^2 u^2(V) + \left(\frac{\partial \dot{Q}_c}{\partial i}\right)^2 u^2(i) \qquad (A.29)$$

$$u(\dot{Q}_c) = \sqrt{[iu(V)]^2 + [Vu(i)]^2} \qquad (A.30)$$

where the elemental standard uncertainties $u(V)$ and $u(i)$ are obtained directly from information provided by the manufacturer,

$$u(V) = \frac{(V + 150) \times 10^{-3}}{\sqrt{3}} \qquad (A.31)$$

$$u(i) = \frac{(i + 30) \times 10^{-3}}{\sqrt{3}} \qquad \text{(A.32)}$$

Here, the condenser and superheating heat transfer rates, defined in Eqs. (4.3) and (4.4), as well as the indicated power, introduced in Eq. (4.6), are generically represented by $\dot{Q}_\varphi$. The combined uncertainty of $\dot{Q}_\varphi$ is expressed by,

$$u^2(\dot{Q}_\varphi) = \left(\frac{\partial \dot{Q}_\varphi}{\partial \dot{m}_r}\right)^2 u^2(\dot{m}_r) + \left(\frac{\partial Q_\varphi}{\partial h_i}\right)^2 u^2(h_i) + \left(\frac{\partial \dot{Q}_\varphi}{\partial h_o}\right)^2 u^2(h_o)$$
$$\text{(A.33)}$$

where h_i and h_o are the enthalpies at the inlet and outlet of the corresponding control volume, respectively.

After solving the derivative terms, the expression given above takes the form,

$$u(\dot{Q}_\xi) = \sqrt{[(h_o - h_i)u(\dot{m}_r)]^2 + [\dot{m}_r u(h_o)]^2 + [\dot{m}_r u(h_i)]^2} \qquad \text{(A.34)}$$

The symbol $\dot{Q}_\xi$ designates one of the following three calculated parameters: (i) $\dot{Q}_\varphi = \dot{Q}_{cond}$, (ii) $\dot{Q}_\varphi = \dot{Q}_{sh}$ or (iii) $\dot{Q}_\varphi = \dot{W}_{ind}$. Depending on the parameter, the enthalpy uncertainties $u(h_i)$ and $u(h_o)$ are computed using Eqs. (A.14), (A.17) and (A.19).

A.3.3   Pressure and Temperature Differences

The pressure drop of the jet heat sink is calculated by the following difference: $P_{jc,i} - P_{jc,o}$, i.e., Eq. (4.9). The final form of its uncertainty propagation equation is,

$$u(\Delta P_{jc}) = \sqrt{u^2(P_{jc,i}) + u^2(P_{jc,o})} \qquad \text{(A.35)}$$

where $u(P_{jc,i})$ and $u(P_{jc,o})$ are obtained directly from the calibration of the absolute pressure transducers at the inlet and outlet of the jet cooler, respectively.

Three temperature differences are defined in Chapter 4, i.e., ΔT_{cal}, ΔT_{sup} and ΔT_s. They can be generically represented as,

$$\Delta T_{xy} = T_x - T_y \qquad \text{(A.36)}$$

The combined uncertainty for any of the three calculated tem-

perature differences can be expressed as,

$$u^2(\Delta T_{xy}) = \left(\frac{\partial \Delta T_{xy}}{\partial T_x}\right)^2 u^2(T_x) + \left(\frac{\partial \Delta T_{xy}}{\partial T_y}\right)^2 u^2(T_y) \qquad (A.37)$$

$$u(\Delta T_{xy}) = \sqrt{u^2(T_x) + u^2(T_y)} \qquad (A.38)$$

Thus,

$$u(\Delta T_{cal}) = \sqrt{u^2(T_{room}) + u^2(T_{cal})} \qquad (A.39)$$

$$u(\Delta T_{sup}) = \sqrt{u^2(T_{comp,i}) + u^2(T_{evap})} \qquad (A.40)$$

$$u(\Delta T_s) = \sqrt{u^2(T_s) + u^2(T_{evap})} \qquad (A.41)$$

The elemental standard uncertainty for $T_{comp,i}$ is obtained directly from the calibration procedure of the local RTD. Particularly for T_{room} and T_{room}, the standard uncertainties are given by,

$$u(T_{room}) = \frac{1}{4}\sqrt{\sum_{j=1}^{4} u^2(T_{TC,j})} \qquad (A.42)$$

$$u(T_{cal}) = \frac{1}{5}\sqrt{\sum_{j=1}^{5} u^2(T_{TC,j})} \qquad (A.43)$$

where $u(T_{TC,j})$, is the elemental standard uncertainty provided by the calibration of (i) four T thermocouples outside the calorimeter, used to compute T_{room}, and (ii) five T thermocouples inside the calorimeter, used to calculate T_{cal}, respectively.

For $u(\Delta T_s)$, the elemental standard uncertainty $u(T_s)$ is calculated as,

$$u(T_s) = \left\{ u^2(\overline{T}_{RTD}) + \frac{16}{\pi^2 D^4 k_s^2} \left[\dot{Q}_c^{*^2} u^2(L) + L^2 u^2(\dot{Q}_c^*) + \right.\right.$$

$$\left.\left. \frac{4L^2 \dot{Q}_c^{*^2} u^2(D)}{D^2} + \frac{L^2 \dot{Q}_c^{*^2} u^2(k_s)}{k_s^2} \right] \right\}^{\frac{1}{2}} \qquad (A.44)$$

where $U(L) = U(D) = \pm 0.05$ mm (caliper manufacturer' information) and $u(\overline{T}_{RTD})$ is obtained from,

$$u(\overline{T}_{RTD}) = \frac{1}{5}\sqrt{\sum_{j=1}^{5} u^2(T_{RTD,j})} \tag{A.45}$$

where $u(T_{RTD,j})$, for $m = 1, ..., 5$, is provided by the calibration of the test section RTDs'. It is important to mention that the last term on the right-hand side of Eq. (A.44) has a minute order of magnitude, therefore it is neglected in the present analysis.

Besides, the uncertainty of the corrected cooling capacity, $\dot{Q}_c^*$, is calculated as,

$$u(\dot{Q}_c^*) = \kappa u(\dot{Q}_c) = \kappa \sqrt{[iu(V)]^2 + [V u(i)]^2} \tag{A.46}$$

where κ is the correction factor for the cooling capacity, which assumes a constant value, and the elemental uncertainties $u(V)$ and $u(i)$ are calculated using Eqs. (A.31) and (A.32), respectively.

A.3.4   Heat Transfer Coefficient

Surface heat transfer coefficient, introduced in Eq. (4.7), can also be written as,

$$\hbar_s = \frac{4\dot{Q}_c^*}{\pi D^2 (T_s - T_{evap})} \tag{A.47}$$

Application of the uncertainty propagation expression and algebraic manipulation of the previous equation results in,

$$u(\hbar_s) = \frac{4}{\pi D^2 (T_s - T_{evap})} \left\{ u^2(\dot{Q}_c^*) + \left[\frac{2\dot{Q}_c^* u(D)}{D}\right]^2 + \right.$$

$$\left. \left[\frac{\dot{Q}_c^* u(T_s)}{T_s - T_{evap}}\right]^2 + \left[\frac{\dot{Q}_c^* u(T_{evap})}{D(T_s - T_{evap})}\right]^2 \right\}^{\frac{1}{2}} \tag{A.48}$$

A.3.5   Performance Metrics

Following the same procedure, the combined standard uncertainties for the coefficients of performance previously defined in Chapter 4, Eqs. (4.19) and (4.21), are expressed as,

$$u(COP_{os}) = \left\{ \left[\frac{u(\dot{Q}_c)}{\dot{W}_{comp} + \dot{W}_{fan} + \dot{W}_{sh}} \right]^2 + \right.$$

$$\left[\frac{\dot{Q}_c u(\dot{W}_{comp})}{(\dot{W}_{comp} + \dot{W}_{fan} + \dot{W}_{sh})^2} \right]^2 + \left[\frac{\dot{Q}_c u(\dot{W}_{fan})}{(\dot{W}_{comp} + \dot{W}_{fan} + \dot{W}_{sh})^2} \right]^2 +$$

$$\left. \left[\frac{\dot{Q}_c u(\dot{W}_{sh})}{(\dot{W}_{comp} + \dot{W}_{fan} + \dot{W}_{sh})^2} \right]^2 \right\}^{\frac{1}{2}} \tag{A.49}$$

$$u(COP_{jc}) = \left\{ \left[\frac{u(\dot{Q}_c)}{\dot{W}_{comp} + \dot{W}_{fan}} \right]^2 + \left[\frac{\dot{Q}_c u(\dot{W}_{comp})}{(\dot{W}_{comp} + \dot{W}_{fan})^2} \right]^2 \right.$$

$$\left. + \left[\frac{\dot{Q}_c u(\dot{W}_{fan})}{(\dot{W}_{comp} + \dot{W}_{fan})^2} \right]^2 \right\}^{\frac{1}{2}} \tag{A.50}$$

where $U(\dot{W}_{sh})$ is obtained using the calibration data of the corresponding power line transducer in Eq. (A.7) and $u(\dot{W}_{fan})$ is determined in the following.

The combined standard uncertainty of the electrical power consumed by a particular cooler fan is calculated according to,

$$u(\dot{W}_{fan;j}) = \sqrt{[iu(V)]^2 + [Vu(i)]^2} \tag{A.51}$$

where j represents one of the five cooler fans existent inside the calorimeter (see Chapter 3), V and i are the averaged values of the measured voltage and current, respectively.

As already mentioned in Chapter 3, the electrical power consumption of each fan was determined by voltage and current measurements using a digital multimeter. The manufacturer of the multimeter provides the following information regarding the voltage and current accuracies,

$$u(V) = \frac{0.08V + 2D}{100\sqrt{3}} \tag{A.52}$$

$$u(i) = \frac{0.2i + 4D}{100\sqrt{3}} \tag{A.53}$$

where 2D and 4D represents the 2 and 4 digits of the voltage and current readings, respectively.

Based on Eq. (A.51), the combined standard uncertainty of $\dot{W}_{fan}$, which is the average of the four centrifugal fans, is calculated as,

$$u(\dot{W}_{fan}) = \frac{1}{4}\sqrt{\sum_{j=1}^{4} u^2(\dot{W}_{fan;j})} \qquad (A.54)$$

A.3.6   Calorimeter Parameters

The combined standard uncertainty regarding the electrical power consumption of the five fans inside the calorimeter is determined by,

$$u(\dot{W}_{fans}) = \sqrt{\sum_{j=1}^{5} u^2(\dot{W}_{fan;j})} \qquad (A.55)$$

where $u(\dot{W}_{fan;j})$ is obtained via Eq. (A.51).

Regarding the calibration procedure carried out to determine the cooling capacity of the thermoelectric cooler (described in Chapter 3), the combined standard uncertainty of $\dot{Q}_{TEC}$ is calculated as

$$u(\dot{Q}_{TEC}) = \sqrt{u^2(\dot{W}_{fans}) + u^2(\dot{W}_{ah}) + \left[\max \frac{s(\dot{W}_{ah})}{\sqrt{N}}\right]^2} \qquad (A.56)$$

where $u(\dot{W}_{ah})$ is computed with Eq. (A.7) by providing data from the calibration of the corresponding power line transducer. It should be mentioned that Eq. (A.56) is based on Eq. (3.5) and also takes into consideration the scatter of $\dot{W}_{ah}$ in the repetitions performed during the calibration procedure.

At last, the uncertainties of the heat dissipation rate through the compressor shell calculated with Eqs. (3.4) and (4.40) are given by the following expressions, respectively,

$$u(\dot{Q}_{shell,cal}) = \sqrt{u^2(\dot{Q}_{TEC}) + u^2(\dot{W}_{ah}) + u^2(\dot{W}_{fans})} \qquad (A.57)$$

$$u(\dot{Q}_{shell,eb}) = \sqrt{u^2(\dot{W}_{comp}) + u^2(\dot{W}_{ind})} \qquad (A.58)$$

APPENDIX B –

Leakage Tests

This appendix presents the procedure adopted to perform the leakage tests in the experimental apparatus, which were conducted according to two fronts: (i) tests focusing on the refrigeration circuit, i.e., the discharge line, the suction line and the secondary evaporation circuit altogether, and (ii) tests focusing on the two-phase jet heat sink.

The leakage tests were carried out using compressed nitrogen (N_2), which behaves as an ideal gas. The well-known ideal gas law is (HOWELL; BUCKIUS, 1987),

$$Pv = R_g T \tag{B.1}$$

where v is the specific volume and R_g is the gas constant of N_2 ($R_g = 5.935$ Pa m^3 kg^{-1} K^{-1}).

Based on Eq. (B.1), a relation between pressure and temperature, which is proportional to the mass of the ideal gas, is defined as,

$$\psi = \frac{P}{T} = \frac{R_g}{v} = \rho R_g \tag{B.2}$$

where ψ is the pressure-to-temperature ratio and ρ is the specific mass (density) of the ideal gas.

By measuring the pressure and temperature of the gas at particular points of the experimental facility, it is possible to compute and monitor the behavior of ψ. This reveals what is happening with the gas charge with which the experimental facility (or the jet cooler) was filled. With the aim to minimize the influence of the external ambient in the temperature measurements, the leakage tests were carried out with the experimental facility thermally insulated as well as with the room temperature controlled.

For the first front, the refrigeration circuit was evacuated and filled with a 30-bar N_2 charge and the readings of pressure and temperature of following points were monitored: (2) compressor outlet (discharge); (3) condenser inlet; (4) condenser outlet and (9) tubular evaporator inlet (see Figure 3.1). The pressure value of the charge was chosen as it is the maximum discharge pressure of the compressor (29.57 bar according to the manufacturer). It should be mentioned that as the pressure transducer of the suction line (point 1) operates at a smaller range (0 - 10 bar), measurements at this particular point were not taken with no loss for the leakage analysis since the secondary evaporation circuit is connected to the suction line and any leakage would be indicated by the readings of point 9.

Moreover, the silicone-covered flexible hoses, shown in Figure 3.21, were not considered in the tests because of its smooth-bore PTFE core. PTFE (Teflon) is a permeable material and gases with a very small molecule may migrate through the material. This was verified for nitrogen from the results of preliminary leakage tests. Although a metal hose could easily eliminate this issue, it is not appropriate for systems with constant or severe vibration as is the case. To overcome this limitation, a infrared-based refrigerant leak detector (INFICON D-TEK Select) was used several times during the first experimental tests to search for R-134a leakage points along the hose, particularly at the connections of the hoses with the experimental set up, i.e., ball valves A and G (see Figure 3.1) as well as the compressor connections.

The results for an one-week-period leakage test are presented in Table B.1. They are reported in relative terms of ψ concerning the values at the start and end instants of the test. Thus,

$$\psi_{\%,\mathrm{mp}} = \left| \frac{\psi_{start} - \psi_{end}}{\psi_{start}} \right|_{\mathrm{mp}} \times 100\% \qquad (B.3)$$

where $\psi_{\%,\mathrm{mp}}$ is the pressure-to-temperature ratio given in relative terms for a particular measurement point (mp) at steady-state conditions.

In addition, Figure B.1 shows the behavior of ψ during the first 24 hours (86,400 s) of the leakage test for each measurement point considered. It is clear that after the initial transient, the mass of the system exhibits a plateau-like pattern with small oscillations indicating that no significant leakage is present. The results of Table B.1 confirm that the variation of the gas specific mass during the steady state of the test was insignificant. For completeness, during the experimental runs with the working fluid (R-134a), several inspections were made with the refrigerant leak detector at the hoses and no leakage was detected.

Table B.1 – Results for the leakage test in the refrigeration circuit.

Measurement point	$\psi_{\%,\mathrm{mp}}$ [%]
Point 2	0.18
Point 3	0.24
Point 4	0.21
Point 9	0.05
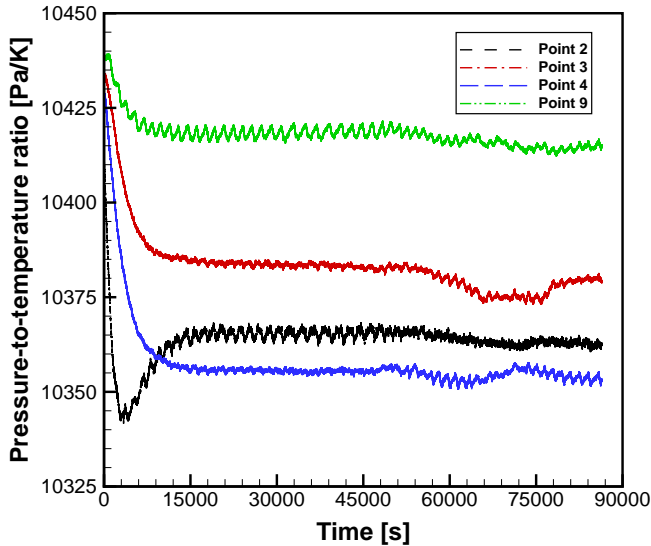
Figure B.1 – Time-dependent behavior of the pressure-to-temperature ratio during the first-front leakage test (refrigeration circuit).

Analogously, for the second-front leakage test, the jet cooler was evacuated and filled with a 10-bar N_2 charge. The duration of the test was 3 days and the time-dependent behavior of ψ during the first 24-hr test (1,440 min) for the inlet (point 5) and outlet (point 6) of the jet cooler is presented in Figure B.2. Likewise Figure B.1, the specific mass reduces markedly during the transient period. As the test tends to steady state, which starts at approximately 750 min, the rate of decay begins to stabilize. For steady-state conditions, the relative variation of the specific mass is $\psi_{\%,\mathrm{mp}} = 0.57\%$ for both points 5 and 6, which is quite a good result considering that sealing gas or vapor in a plastic structure is far more challenging than it is in a metallic structure.
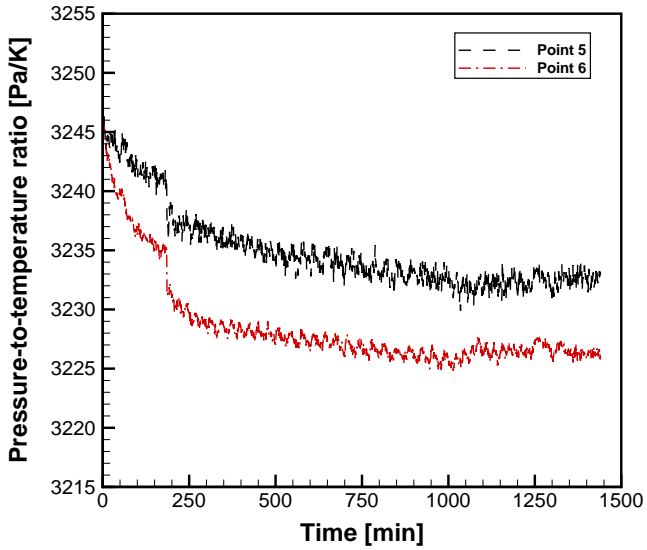
Figure B.2 – Time-dependent behavior of the pressure-to-temperature ratio during the second-front leakage test (two-phase jet heat sink).

APPENDIX C –

Mathematical Deduction of Some Performance Metrics

This appendix outlines the mathematical derivation of Eqs. (4.29) and (4.32), introduced in Chapter 4. First, the definition of the second-law efficiency, η, is repeated here for completeness,

$$\eta = \frac{COP}{COP_{id}} \tag{C.1}$$

where the coefficient of performance, COP, may be computed as COP_{os}, according to Eq. (4.19), or COP_{jc}, given by Eq. (4.21), depending on the focus of the evaluation.

Applying either definitions of COP and the expression for COP_{id}, given by Eq. (4.24), the equation above can be re-written as,

$$\eta = \frac{\dot{Q}_c}{\dot{W}}\left(\frac{T_{cond} - T_{evap}}{T_{evap}}\right) \tag{C.2}$$

where the total electrical power input, $\dot{W}$, is given by Eq. (4.20), in the overall system case, or by the denominator of Eq. (4.21), in the jet cooler case.

Next, the saturation temperatures, T_{evap} and T_{cond}, are written as functions of the thermal resistances of the cold and hot ends, given by Eqs. (4.27) and (4.28), respectively,

$$T_{evap} = T_s - R_{hs}\dot{Q}_c \tag{C.3}$$

$$T_{cond} = T_{w,i} + R_{amb}(\dot{Q}_c + \dot{W}) \tag{C.4}$$

Subtracting Eq. (C.4) from Eq. (C.3) one obtains,

$$T_{cond} - T_{evap} = T_{w,i} + R_{amb}(\dot{Q}_c + \dot{W}) - T_s + R_{hs}\dot{Q}_c \qquad (C.5)$$

$$T_{cond} - T_{evap} = (T_{w,i} - T_s) + (R_{amb} + R_{hs})\dot{Q}_c + \dot{W}R_{amb} \qquad (C.6)$$

The application of Eqs. (C.3) and (C.6) in Eq. (C.2) yields to,

$$\eta = \frac{(T_{w,i} - T_s)\dot{Q}_c + (R_{amb} + R_{hs})\dot{Q}_c^2 + \dot{W}R_{amb}\dot{Q}_c}{\dot{W}T_s - \dot{W}R_{hs}\dot{Q}_c} \qquad (C.7)$$

Defining the temperature difference ΔT_a and the combined thermal resistance of the hot and cold ends, R_c, respectively as,

$$\Delta T_a = T_s - T_{w,i} \qquad (C.8)$$

$$R_c = R_{amb} + R_{hs} \qquad (C.9)$$

and by expanding Eq. (C.7) one obtains,

$$\eta\dot{W}T_s - \eta\dot{W}R_{hs}\dot{Q}_c = -\Delta T_a\dot{Q}_c + R_c\dot{Q}_c^2 + \dot{W}R_{amb}\dot{Q}_c \qquad (C.10)$$

The manipulation of Eq. (C.10) gives,

$$R_c\dot{Q}_c^2 + (\dot{W}R_{amb} + \eta\dot{W}R_{hs} - \Delta T_a)\dot{Q}_c - \eta\dot{W}T_s = 0 \qquad (C.11)$$

$$R_c\dot{Q}_c^2 + [\dot{W}(R_{amb} + \eta R_{hs}) - \Delta T_a]\dot{Q}_c - \eta\dot{W}T_s = 0 \qquad (C.12)$$

where the term into parenthesis on the left-hand side is simplified by,

$$\gamma = \dot{W}(R_{amb} + \eta R_{hs}) \qquad (C.13)$$

Solving Eq. (C.12) and taking its positive square root, since $\dot{Q}_c$ is the cooling capacity imposed to the refrigeration system, i.e., therefore, a positive value, one obtains,

$$\dot{Q}_c = \frac{\Delta T_a - \gamma + \sqrt{4R_cT_s\dot{W}\eta + (\gamma - \Delta T_a)^2}}{2R_c} \tag{C.14}$$

As the apparent thermal resistance of the active cooling system is given by,

$$R_a = \frac{T_s - T_{w,i}}{\dot{Q}_c} \tag{C.15}$$

The substitution of Eq. (C.14) into the previous definition, yields to Eq. (4.29),

$$R_a = \frac{2\Delta T_a R_c}{\Delta T_a - \gamma + \sqrt{4R_cT_s\dot{W}\eta + (\gamma - \Delta T_a)^2}} \tag{C.16}$$

Equating the resistances defined by Eqs. (C.9) and (C.16) gives,

$$R_c = \frac{2\Delta T_a R_c}{\Delta T_a - \gamma + \sqrt{4R_cT_s\dot{W}\eta + (\gamma - \Delta T_a)^2}} \tag{C.17}$$

$$\Delta T_a - \gamma + \sqrt{4R_cT_s\dot{W}\eta + (\gamma - \Delta T_a)^2} = 2\Delta T_a \tag{C.18}$$

$$\sqrt{4R_cT_s\dot{W}\eta + (\gamma - \Delta T_a)^2} = \Delta T_a + \gamma \tag{C.19}$$

Squaring Eq. (C.19) and after some algebraic manipulation, one obtains,

$$4R_cT_s\dot{W}\eta + (\gamma - \Delta T_a)^2 = (\Delta T_a + \gamma)^2 \tag{C.20}$$

$$R_cT_s\dot{W}\eta = \Delta T_a\gamma \tag{C.21}$$

The application of Eqs. (C.8), (C.9) and (C.13) in the above equation gives,

$$(R_{amb} + R_{hs})T_s\dot{W}\eta = (T_s - T_{w,i})\dot{W}(R_{amb} + \eta R_{hs}) \tag{C.22}$$

Expanding Eq. (C.22) and solving it for the efficiency that satisfy this relation, η_{min}, one finally obtains Eq. (4.32),

$$\eta_{min} = \frac{T_s - T_{w,i}}{\left(\dfrac{R_{hs}}{R_{amb}}\right) T_{w,i} + T_s} \tag{C.23}$$

APPENDIX D –

Values of the Controlled Parameters

This appendix presents a series of tables reporting the measured values of the controlled parameters for each experimental test of Matrices 1 to 4. Due to their extension, the tables are shown in the following pages.

Table D.1 – Real input cooling capacity for each experimental test of Matrices 1 to 3.

Bath temperature [°C]				Bath temperature [°C]			
15	15	15	25	15	15	15	25
Piston stroke [%]				Piston stroke [%]			
50	75	100	100	50	75	100	100
Matrix 1							
Test number (t#)				Cooling capacity [W]			
t#1	t#1	t#1	t#1	25.12	25.12	25.09	25.09
t#2	t#2	t#2	t#2	50.16	50.16	50.11	50.11
t#3	t#3	t#3	t#3	75.05	75.00	75.00	74.98
	t#4	t#4	t#4		100.06	100.14	100.06
	t#5	t#5	t#5		120.29	124.92	125.17
		t#6	t#6			149.97	150.00
			t#7				160.22
Matrix 2							
Test number (t#)				Cooling capacity [W]			
t#1	t#1	t#1	t#1	25.08	25.08	25.08	25.08
t#2	t#2	t#2	t#2	50.10	50.10	50.10	50.10
t#3	t#3	t#3	t#3	74.98	74.98	74.98	74.98
t#4	t#4	t#4	t#4	85.14	100.04	100.04	100.04
	t#5	t#5	t#5		120.24	125.15	125.15
		t#6				149.97	
		t#7				160.22	
Matrix 3							
Test number (t#)				Cooling capacity [W]			
t#1	t#1	t#1	t#1	25.10	25.10	25.10	25.10
t#2	t#2	t#2	t#2	50.13	50.13	50.13	50.13
t#3	t#3	t#3	t#3	75.28	75.28	75.28	75.28
	t#4	t#4	t#4		85.18	82.58	100.08
			t#5				107.48

Table D.2 – Controlled input variables for Matrix 1.

Bath temperature [°C]				Bath temperature [°C]			
15	15	15	25	15	15	15	25
Piston stroke [%]				Piston stroke [%]			
50	75	100	100	50	75	100	100
$\Delta T_{sup} = 10.0°C$				$\Delta T_{cal} = 0.0°C$			
10.01	9.88	9.96	9.95	0.02	0.08	0.13	0.25
10.14	10.10	10.13	10.02	0.04	0.13	0.01	0.24
10.06	9.91	9.95	10.06	0.02	0.14	0.11	0.21
	10.09	10.08	10.06		0.06	0.42	0.10
	9.92	10.01	10.00		0.10	0.01	0.10
		10.11	10.01		0.00	0.04	0.10
			9.97				0.15
$T_{room} = 25.0°C$				$T_{cal} = 25.0°C$			
25.03	24.92	24.88	24.74	25.00	25.01	25.00	25.00
24.96	24.88	25.01	24.76	25.00	25.01	25.00	25.00
24.98	25.13	24.89	24.83	25.00	24.99	25.00	25.03
	24.95	25.42	25.10		25.01	24.99	25.00
	25.11	25.00	24.94		25.00	25.00	25.04
		24.97	24.94			25.00	25.04
			24.85				25.00
$T_{w,i} = 15.0°C\ /\ 25.0°C$				$\dot{m}_w = 180.0$ kg/h			
14.8	14.9	14.7	24.6	179.4	179.3	180.1	179.9
14.8	14.9	14.8	24.6	179.3	179.3	180.1	180.2
14.8	14.7	14.8	24.7	179.4	179.9	179.9	180.1
	14.8	14.8	24.6		179.2	179.1	180.1
	14.7	14.8	24.6		179.6	179.4	180.1
		14.9	24.7			179.7	180.1
			24.7				180.3

Table D.3 – Controlled input variables for Matrix 2.

Bath temperature [°C]				Bath temperature [°C]			
15	15	15	25	15	15	15	25
Piston stroke [%]				Piston stroke [%]			
50	75	100	100	50	75	100	100
$\Delta T_{sup} = 10.0°C$				$\Delta T_{cal} = 0.0°C$			
9.99	9.95	10.01	10.05	0.01	0.06	0.15	0.14
10.08	10.01	9.92	9.97	0.03	0.18	0.05	0.09
9.98	10.00	9.99	9.91	0.01	0.19	0.08	0.05
9.96	10.02	10.00	10.08	0.02	0.10	0.11	0.02
	9.99	10.01	10.11		0.08	0.02	0.02
		9.98				0.05	
		10.02				0.02	
$T_{room} = 25.0°C$				$T_{cal} = 25.0°C$			
24.98	24.94	25.21	25.14	24.99	25.00	25.06	25.00
24.97	25.19	25.05	24.91	25.00	25.01	25.01	25.00
25.02	25.19	24.93	24.95	25.01	25.00	25.01	25.00
25.02	25.10	24.90	25.02	25.00	25.00	25.00	25.00
	24.91	25.02	24.98		24.99	25.00	25.00
		24.95				25.00	
		25.02				25.00	
$T_{w,i} = 15.0°C \ / \ 25.0°C$				$\dot{m}_w = 180.0 \ kg/h$			
14.8	14.7	14.8	24.6	179.2	179.3	179.1	179.8
14.7	14.7	14.8	24.6	179.3	179.3	179.2	179.7
14.7	14.7	14.8	24.6	179.4	178.9	179.3	179.8
14.7	14.8	14.8	24.6	179.3	179.5	179.4	179.7
	14.8	14.9	24.6		179.4	179.5	179.8
		15.0				179.4	
		15.0				179.5	

Table D.4 – Controlled input variables for Matrix 3.

Bath temperature [°C]				Bath temperature [°C]			
15	15	15	25	15	15	15	25
Piston stroke [%]				Piston stroke [%]			
50	75	100	100	50	75	100	100
$\Delta T_{sup} = 10.0°C$				$\Delta T_{cal} = 0.0°C$			
9.97	9.99	10.08	9.94	0.14	0.16	0.02	0.21
9.91	10.01	9.99	10.02	0.24	0.12	0.02	0.07
10.06	9.95	10.12	10.01	0.10	0.06	0.11	0.17
	9.97	10.02	9.99		0.14	0.14	0.02
			10.06				0.04
$T_{room} = 25.0°C$				$T_{cal} = 25.0°C$			
25.14	25.16	25.02	25.22	25.00	25.00	25.00	25.01
25.25	25.12	24.98	25.07	25.01	25.00	25.00	25.00
25.10	24.94	25.11	25.17	25.00	25.00	25.00	25.01
	25.15	25.14	25.03		25.00	25.00	25.00
			25.04				25.00
$T_{w,i} = 15.0°C / 25.0°C$				$\dot{m}_w = 180.0$ kg/h			
14.7	14.8	14.8	24.7	179.8	179.8	179.5	180.1
14.8	14.8	14.8	24.8	179.8	179.7	180.1	179.9
14.8	14.8	14.8	24.7	179.8	179.5	180.1	180.3
	14.8	14.9	24.9		179.6	180.1	180.1
			24.8				180.1

Table D.5 – Controlled input variables for Matrix 4 ($\alpha = 100\%$).

	Multiple jet array			Multiple jet array		
	#1	#2	#3	#1	#2	#3
	Test number (t#)			Cooling capacity [W]		
Real input cooling capacity per test	t#1	t#1	t#1	75.01	74.98	74.97
	t#2	t#2	t#2	99.99	100.04	100.37
	t#3	t#3	t#3	125.20	125.17	125.14
	t#4	t#4	t#4	150.02	150.00	149.94
	t#5	t#5	t#5	174.87	175.22	174.93
	t#6	t#6	t#6	200.05	200.10	199.88

Test number (t#)	Multiple jet array			Multiple jet array		
	#1	#2	#3	#1	#2	#3
	$\Delta T_{sup} = 10.0°C$			$\Delta T_{cal} = 0.0°C$		
t#1	10.02	10.05	10.06	0.12	0.03	0.08
t#2	9.97	9.98	10.07	0.16	0.01	0.07
t#3	10.01	10.03	9.97	0.12	0.08	0.13
t#4	10.04	9.96	10.02	0.01	0.01	0.03
t#5	9.96	10.05	10.08	0.25	0.12	0.17
t#6	10.06	10.02	10.02	0.01	0.06	0.06
	$T_{room} = 25.0°C$			$T_{cal} = 25.0°C$		
t#1	24.87	25.02	25.08	24.98	25.00	25.00
t#2	24.79	24.99	25.06	24.95	25.00	25.00
t#3	25.13	24.92	24.87	25.01	25.00	25.00
t#5	24.99	25.01	25.02	25.00	25.00	25.00
t#5	24.81	24.88	25.18	25.06	25.00	25.01
t#6	24.99	25.05	25.06	25.00	25.00	25.00
	$T_{w,i} = 25.0°C$			$\dot{m}_w = 180.0$ kg/h		
t#1	24.67	24.69	24.72	179.72	179.81	179.14
t#2	24.73	24.69	24.74	175.28	179.85	180.04
t#3	24.82	24.70	24.75	179.31	179.65	180.19
t#4	24.94	24.71	24.73	179.59	179.62	180.18
t#5	24.70	24.72	24.71	179.25	179.51	179.96
t#6	24.72	24.71	24.72	179.35	179.54	179.89

APPENDIX E –

Condenser Heat Transfer Model

This appendix describes the model used to compute the overall heat transfer coefficient of the condenser in the proposed refrigeration system. Since the model is particularly oriented to brazed plate heat exchangers (BPHE), the geometric properties of the BPHE are introduced first. Then, the correlations used to calculate the heat transfer coefficients on the refrigerant and WEG sides are presented.

E.1 Geometric Properties of the BPHE

The welded or brazed plate heat exchanger (BPHE) consists of an assembled group of rectangular metal plates made by stamping or embossing a corrugated or wavy surface pattern on a metal sheet. The most common plate geometry is the chevron pattern. Alternate plates are assembled such that the corrugations on successive plates contact or cross each other to provide mechanical support to the plate pack through a large number of contact points. The resulting flow channels are narrow, interrupted and tortuous. Therefore, the heat transfer rate is enhanced and the fouling resistance is decreased by increasing the shear stress, which produces a secondary and highly turbulent flow. The corrugations also improve rigidity of the plates and form the desired spacing. Each plate has four corner ports that provide access to the flow passages on either side of the plate (LEE, 2010).

Figure E.1 exhibits a typical plate inside a BPHE with chevron-type corrugation pattern. The wavelength of the chevron pattern, λ, is the corrugation pitch. The amplitude of the corrugation is represented as $2a$, where a is the amplitude of the sinusoidal corrugation. The plate thickness and width are δ_p and W_p, respectively. The total plate length

(port-to-port channel length) is denoted as L_{pt} and L_p is the effective channel length (LEE, 2010; HUANG *et al.*, 2012).
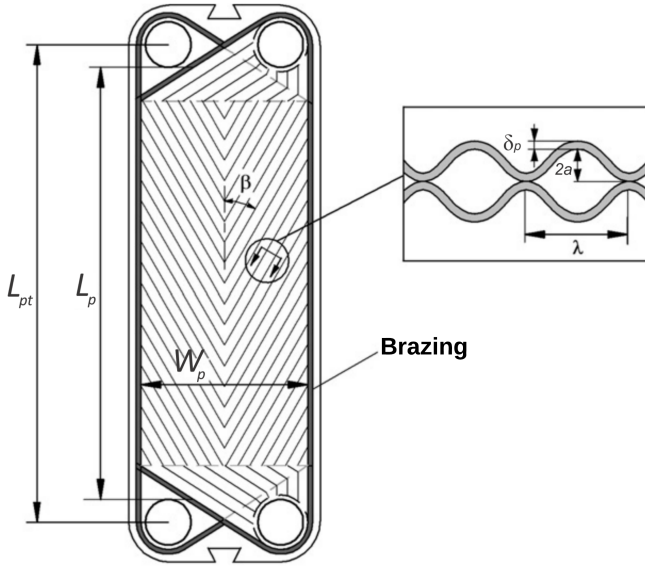

Figure E.1 – Plate with chevron-type corrugation pattern for a BPHE. Adapted from Huang *et al.* (2012).

According to Lee (2010), the number of wavelength per plate, N_λ, is defined as the ratio of the plate width, W_p, and the chevron pattern wavelength, λ,

$$N_\lambda = \frac{W_p}{\lambda} \tag{E.1}$$

The amplitude of the sinusoidal wavelength (corrugation), a, is expressed in terms of the plate heat exchanger height, H_p, the total number of plates, N_t, and the plate thickness, δ_p,

$$a = \frac{1}{2}\left(\frac{H_p}{N_t + 1} - \delta_p\right) \tag{E.2}$$

The BPHE height is computed according to the following expression given by the manufacturer,

$$H_p = \frac{9 + 2.3N_t}{1000} \tag{E.3}$$

The free-flow area in a channel, A_c, is calculated as the equivalent to a rectangular area for taking half of each fluid,

$$A_c = 2aW_pN_c \tag{E.4}$$

where N_c is the number of channels per each fluid (information provided by the manufacturer).

The total heat transfer area for each fluid, i.e., the corrugated area, A_t, is computed as,

$$A_t = 2L_\lambda N_\lambda L_p N_c \tag{E.5}$$

where L_λ is the enlarged length per wavelength, which is obtained using the following expression,

$$L_\lambda = \int_0^\lambda \sqrt{1 + \left(\frac{2\pi a}{\lambda}\right)^2 \cos\left(\frac{2\pi \zeta}{\lambda}\right)^2}\, d\zeta \tag{E.6}$$

It should be pointed out that A_t is the area used to compute the overall thermal conductance in the condenser. The surface waviness can be represented by the surface enlargement factor, Φ, which is defined as the ratio between the corrugated area, A_t, and the projected area. Thus,

$$\Phi = \frac{2L_\lambda N_\lambda L_{pt}N_c}{2W_p L_{pt}N_c} = \frac{L_\lambda N_\lambda}{W_p} \tag{E.7}$$

Using Eq. (E.4) and (E.7), the hydraulic diameter of the BPHE is obtained as follows,

$$d_h = \frac{4A_c}{P_{wet}} = \frac{4(2aW_pN_c)}{2L_\lambda N_\lambda N_c} = \frac{4a}{\Phi} \tag{E.8}$$

where P_{wet} is the wet perimeter.

E.2   Heat transfer Coefficient Correlations

The Nusselt number for the single-phase flow of the WEG mixture is obtained with the correlation proposed by Bogaert and Bölcs (1995),

$$Nu_w = C_1 Re_w^{C_2} Pr_w^{E_1}\left(\frac{\mu_w}{\mu_p}\right)^{E_2} \tag{E.9}$$

where the exponents of the Prandtl number and the viscosity ratio, E_1 and E_2, respectively, are given by the following expressions,

$$E_1 = \frac{1}{3} \exp\left(\frac{6.4}{Pr_w + 30}\right) \tag{E.10}$$

$$E_2 = \frac{0.3}{(Re_w + 6)^{0.125}} \tag{E.11}$$

The Reynolds numbers is defined as,

$$Re_w = \frac{G_w d_h}{\mu_w} \tag{E.12}$$

where the mass flux, G_w, is given as,

$$G_w = \frac{\dot{m}_w}{A_c} \tag{E.13}$$

The hydraulic diameter, d_h, and the free-flow area, A_c, are calculated via Eqs. (E.8) and (E.4), respectively. The mass flow rate of the WEG mixture, is determined as follows,

$$\dot{m}_w = \rho_w \dot{V}_w \tag{E.14}$$

where ρ_w is the mixture density and $\dot{V}_w$ is the measured volumetric flow rate.

For $Re_w > 80$, the coefficients C_1 and C_2 in Eq. (E.9) are $C_1 = 0.26347$ and $C_2 = 0.7152$ (BOGAERT; BÖLCS, 1995; GARCÍA-CASCALES *et al.*, 2007). The dynamic viscosity μ_p was evaluated at the plate temperature, T_p, which is defined as the arithmetic mean of the condensation temperature and the WEG temperatures at the inlet and outlet of the condenser,

$$T_p = \frac{T_{cond} + T_{w,i} + T_{w,o}}{3} \tag{E.15}$$

From definition of the Nusselt number (SHAH; SEKULIĆ, 2003; LEE, 2010), the heat transfer coefficient of the WEG mixture is as follows,

$$\hbar_w = \frac{Nu_w k_w}{d_h} \tag{E.16}$$

where k_w is the mixture thermal conductivity.

It should be mentioned that the thermophysical properties, i.e.,

Pr_w, μ_w, ρ_w and k_w, were obtained from the Brines property library available in EES (KLEIN, 2004) using as inputs the concentration of the mixture (10%) and its average temperature, T_w, calculated with the local measured temperatures at the inlet and outlet of the condenser,

$$T_w = \frac{T_{w,i} + T_{w,o}}{2} \tag{E.17}$$

Longo (2008) proposed the following correlation to compute the heat transfer coefficient of R-134a condensation inside a brazed plate heat exchanger,

$$\hbar_r = 0.943\Phi\left[\frac{k_f^3 \rho_f^2 h_{lv} g}{\mu_f L_{pt}(T_{cond} - T_f)}\right]^{1/4} \tag{E.18}$$

where Φ is given by Eq. (E.7), h_{lv} is the latent heat of vaporization, g is the gravity acceleration and the refrigerant conductivity, density and viscosity, i.e., k_f, ρ_f and μ_f, respectively, were evaluated at the temperature of the condensate film, T_f, defined as follows,

$$T_f = \frac{T_{cond} + T_p}{2} \tag{E.19}$$

Analogously, the refrigerant thermophysical properties were computed via EES (KLEIN, 2004). Finally, the global thermal conductance of the condenser is defined as (SHAH; SEKULIĆ, 2003; LEE, 2010),

$$\hbar_{cond} A_t = \frac{1}{\left(\dfrac{1}{\hbar_r A_r} + \dfrac{\delta_p}{k_p A_p} + \dfrac{1}{\hbar_w A_w}\right)} \tag{E.20}$$

As the corrugated area of the refrigerant and WEG sides are the same, i.e., $A_r = A_w = A_t$, which are equal to the plate area itself, $A_t = A_p$, the previous expression can be simplified in order to determine the overall heat transfer coefficient of the condenser. Thus,

$$\hbar_{cond} = \frac{1}{\left(\dfrac{1}{\hbar_r} + \dfrac{\delta_p}{k_p} + \dfrac{1}{\hbar_w}\right)} \tag{E.21}$$

where the thermal conductivity of the plate material, k_p, was evaluated at the plate temperature, T_p, that is given by Eq. (E.15).

APPENDIX F –

Results for Matrices 1 and 3 - Influence of the Hot End Temperature

This appendix presents the graphs of the variables encompassed in the analysis of the secondary fluid temperature influence concerning the comparison between Matrices 1 and 3. The figures are displayed in the following pages.
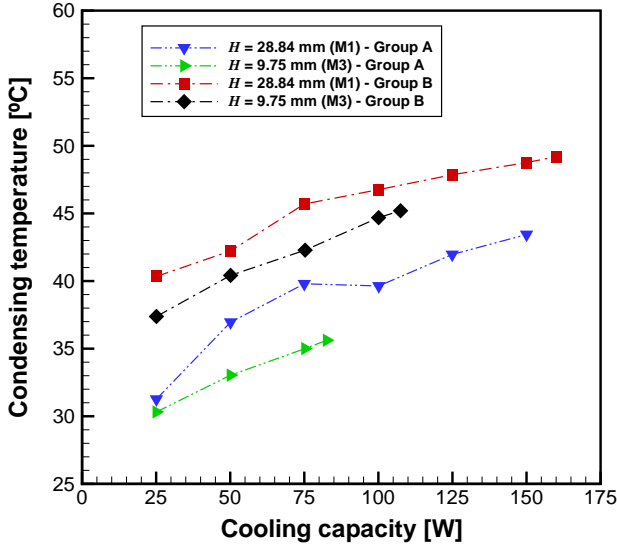
Figure F.1 – Condensing temperature as a function of the cooling load (comparison between Matrices 1 and 3 - Groups A and B - $\alpha = 100\%$).
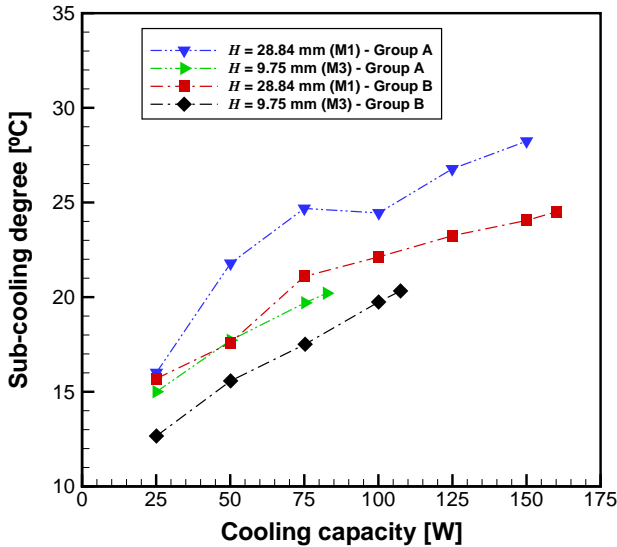

Figure F.2 – Sub-cooling degree as a function of the cooling load (comparison between Matrices 1 and 3 - Groups A and B - $\alpha = 100\%$).
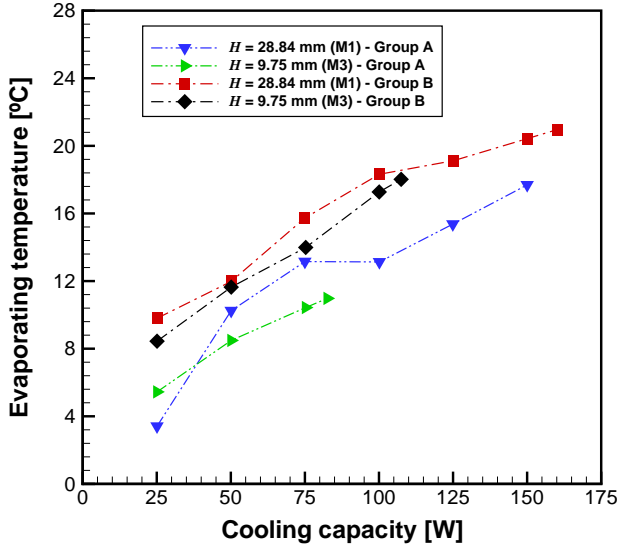
Figure F.3 – Evaporating temperature as a function of the cooling load (comparison between Matrices 1 and 3 - Groups A and B - $\alpha = 100\%$).
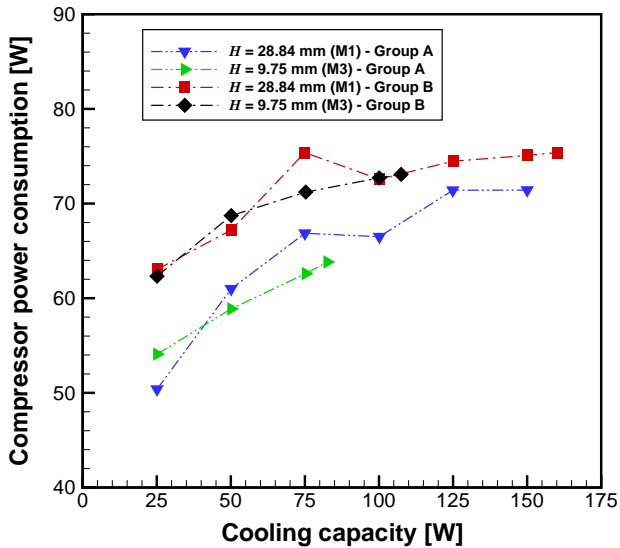

Figure F.4 – Compressor (electrical) power consumption as a function of the cooling load (comparison between Matrices 1 and 3 - Groups A and B - $\alpha = 100\%$).
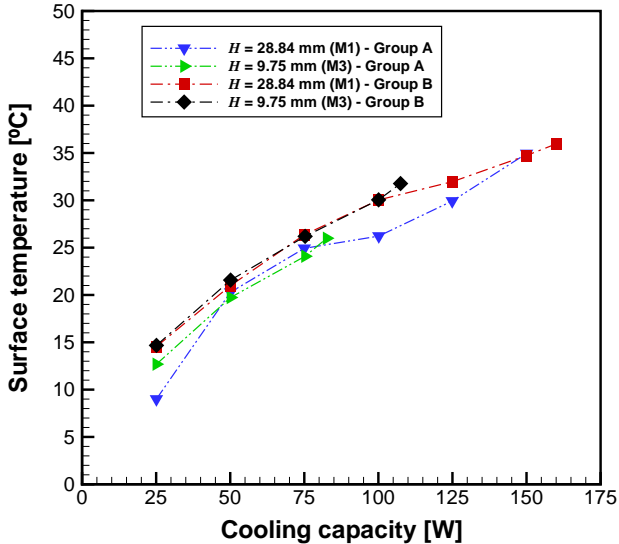
Figure F.5 – Surface temperature as a function of the cooling load (comparison between Matrices 1 and 3 - Groups A and B - $\alpha = 100\%$).
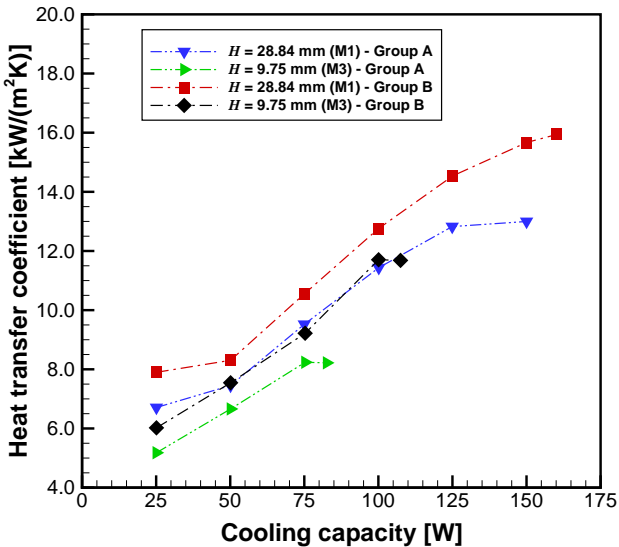

Figure F.6 – Jet impingement heat transfer coefficient as a function of the cooling load (comparison between Matrices 1 and 3 - Groups A and B - $\alpha = 100\%$).